

## ABSTRACT

Title of Dissertation: LASER SWITCHED ELECTRON BEAM  
MODULATION WITH TERAHERTZ  
APPLICATIONS

Jonathan Neumann, PhD 2005

Dissertation Directed By: Dr. Patrick O'Shea, Department of Electrical and  
Computer Engineering

This dissertation describes the exploration of relativistic electron beams modulated at terahertz frequencies using laser driven photoemission. It is divided into three distinct areas: laser beam modulation; electron beam dynamics; and an application of electron beam modulation, the generation of terahertz radiation. The laser modulation portion covers the development of an interferometer system used to control the 266 nm drive laser modulation and the experimental results. The laser pulse is delivered to the photocathode of the accelerator, and is used as a switch that induces an initial electron beam modulation at frequencies between 0.5 and 1.6 terahertz. The electron beam dynamics section includes measurements of the electron beam longitudinal distribution after acceleration to relativistic energy as well as the results obtained from a numerical simulation using the code PARMELA. Both the experimental and numerical results indicate that some of the initial density modulation imposed by the drive laser modulation is retained on the electron beam, although the density modulation that remains, and the frequency of the modulation, falls as a function of increasing charge. Electron beam modulation is achieved between 0.712 and 1.66 terahertz. One application of the deliberate modulation of an electron beam is the generation of coherent radiation, as is seen in many devices ranging from the klystron to the free electron laser. The third section of this work discusses terahertz light generated by transition radiation when a mirror intercepts the modulated electron beam. In this section, transition radiation measured by a bolometric detector is compared to expected results based on the longitudinal electron beam distributions predicted by the PARMELA simulation as well as the measurements from the accelerator system. This dissertation demonstrates that it is possible for an electron beam pre-modulated at the cathode on a subpicosecond time scale to be accelerated to relativistic energy and used for the production of tunable terahertz radiation.

LASER SWITCHED ELECTRON BEAM MODULATION WITH TERAHERTZ  
APPLICATIONS

By

Jonathan G. Neumann

Dissertation submitted to the Faculty of the Graduate School of the  
University of Maryland, College Park, in partial fulfillment  
of the requirements for the degree of  
Doctor of Philosophy  
2005

Advisory Committee:

Dr. Patrick O'Shea, Chair

Dr. Thomas Antonsen

Dr. Chris Davis

Dr. Richard Ellis

Dr. Wolfgang Losert

Dr. Jon Orloff

© Copyright by  
Jonathan G. Neumann  
2005

## Acknowledgements

This work would not have been possible without significant contributions from many people. Many thanks to Professor Patrick O'Shea, who served as my dissertation advisor and has been a tremendous supporter of my professional development as a scientist. Collaboration with other groups was key to the success of this project. Specifically, the Source Development Laboratory at Brookhaven National Laboratory, the National Institute of Standards and Technology, and other groups at the University of Maryland provided insight, equipment, advice, experimental facilities, and motivation. The time and effort from Bill Graves (now at MIT Bates Laboratory), Brian Sheehy, Henrik Loos, Zilu Wu, Yuzhen Shen, Timur Shaftan, Larry Carr, Jim Murphy, and Xijie Wang is very much appreciated. Without their support, none of the experiments could have been conducted at the SDL. My coworkers at the University of Maryland, David Demske, Irving Haber, Martin Reiser, Henry Freund, Kevin Jensen, Rami Kishek, Don and Renee Feldman, Matt Virgo, John Harris, Hui Li, Yupeng Cui, and Anatoly Shkvarunets, not only provided useful discussion and assistance but also continued support and motivation. Ralph Fiorito also provided assistance with experiments and theory. Discussion and support from Professor Chris Davis was essential to the development of the experiment, and David Plusquellic, Karen Siegrist, and Vyacheslav Podobedov from NIST provided tremendous assistance as well. It is also

important to acknowledge all those who donated computer time in order to make the "poor man's massively parallel computing operation" possible. Thanks also to Sandra Biedron and Stephen Milton who provided a set of fresh eyes and much encouragement, and Ruth Neumann who assisted with development of the cover art. And of course, many thanks to my family and friends, especially those I neglected during this process.

Finally, I would like to express tremendous gratitude towards the Army Research Laboratory, the Office of Naval Research, the Directed Energy Professional Society, the Armed Forces Communications and Electronics Association, all of whom supported this research financially.

# Table of Contents

Acknowledgements .....	ii
Table of Contents .....	iv
List of Tables .....	vii
List of Figures .....	viii
Chapter 1: Introduction and Background.....	1
1.1 Introduction.....	1
1.2 History of Accelerator Based Light Source Development .....	5
1.3 Current Terahertz Sources.....	11
1.4 Motivation for a Pre-Modulated Device.....	13
1.5 Background.....	14
Chapter 2: Research Questions and Experimental Overview.....	29
2.1 The Research Questions.....	29
2.1.1 Pulse shape Control .....	30
2.1.2. Electron Beam Dynamics .....	31
2.1.3 Radiation Generated by Electron Beams.....	32
2.2 The Research Tools.....	33
2.2.1 The Source Development Laboratory.....	34
2.2.2 PARMELA Simulations.....	44

2.3 Project Overview .....	46
Chapter 3: Drive Laser Modulation Techniques .....	47
3.1 Theoretical Model for Fabry-Perot Interferometer as a Laser Switch .....	48
3.2. Measurements with the Fabry-Perot Interferometer .....	63
Chapter 4: Electron Beam Dynamics .....	70
4.1 Electron Beam Simulations.....	70
4.2. Longitudinal Profile Measurement Techniques.....	87
4.3 Longitudinal Electron Beam Measurements.....	103
Chapter 5: Terahertz Radiation Generation .....	133
5.1 Theoretical Predictions for Terahertz Radiation From an Electron Beam.....	133
5.1.1. Finite Transition Radiator .....	134
5.1.2 The Transverse Form Factor .....	139
5.1.3 Light Transport System .....	140
5.1.4 Atmospheric Absorption.....	144
5.2 Terahertz Filters .....	145
5.3 Terahertz Radiation Measurements.....	158
Chapter 6: Conclusions and Future Work.....	190
6.1 Drive Laser Modulation.....	190
6.2. Electron Beam Dynamics.....	192
6.3 Terahertz Radiation Measurements.....	194
6.4 Recommendations for Future Work .....	197

Appendix A: Other Laser Modulation Methods .....	198
Appendix B : MATLAB Codes.....	205
B.1 Code used to produce test cases for electron beam modulation.....	205
B.2 Calculation of Fabry-Perot performance.....	207
B.3 Code to demonstrate RF zero phasing issues.....	208
B.4 Calculation of filter performance .....	210
B.5 Theoretical predictions for terahertz emission .....	211
B.5.1. Angular Spectral Density for a Single Electron and a Finite Radiator ...	211
B.5.2. Code for calculating terahertz radiation measured at detector.....	213
References .....	216

## List of Tables

Table 1.1. Various terahertz sources and their capabilities.....	12
Table 1.2. Energy per solid angle radiated at the angle of maximum emission by three different source types for a unbunched and a pre-modulated electron beam.....	27
Table 3.1. Calculated laser form factor, normalized laser energy, and relative measure of terahertz radiation for various mirror reflectances (R) .....	61
Table 5.1. Measured physical properties of meshes used for terahertz filters .....	149
Table 5.2. Summary of filters used for terahertz radiation measurements.....	157

## List of Figures

Figure 1.1. A concept view of electron beam pre-modulation. (Top) The major components in this particular system include, from left to right: a drive laser to cause photoemission, a radio frequency electron gun and accelerating section, and a radiative mechanism. (Middle) A conventional design for a particle accelerator based light source that might be found in a free-electron laser, from left to right : drive laser time profile, electron beam time profile after acceleration, and electron beam profile after a radiative or bunching mechanism such as a wiggler. (Bottom) The proposed design for this accelerator based light source, from left to right: a modulated drive laser profile, which induces a modulated electron bunch in the gun and accelerator. After the radiator, the beam remains bunched. The red arrows indicate the emission of coherent light, which is the goal of both cases. .... 3

Figure 1.2. (Black) Unmodulated electron beam profile used in Equation 1.5. (Blue) Modulated electron beam profile used in Equation 1.5. .... 17

Figure 1.3. (Left) Form factor as a function of frequency for the unmodulated beam in Figure 1.2. (Right) Form factor as a function of frequency for the modulated beam in Figure 1.2. .... 17

Figure 1.4. (Black) Unmodulated electron beam profile used in Equation 1.5. (Blue) Modulated electron beam profile used in Equation 1.5. .... 19

Figure 1.5. (Left) Form factor as a function of frequency for the unmodulated beam in Figure 1.4. (Right) Form factor as a function of frequency for the modulated beam in Figure 1.4.....	19
Figure 1.6. (Left) Angular spectral transition radiation density for pre-modulated electron beam. (Right) From unmodulated electron beam. ....	22
Figure 1.7. Angular spectral density of synchrotron radiation from a single electron. .....	24
Figure 1.8. (Left) Angular spectral synchrotron radiation density for pre-modulated electron beam. (Right) From unmodulated electron beam. Note scale differences. ....	24
Figure 1.9. Angular spectral density for undulator radiation from a single electron. .....	26
Figure 1.10. (Left) Angular spectral undulator radiation density for pre-modulated electron beam. (Right) From unmodulated electron beam. Note scale differences. ....	27
Figure 2.1. Laser system block diagram.....	35
Figure 2.2. (Left) Ti:sapphire laser with stretcher and compressor in background. (Right) Ultraviolet laser transport optics.....	37
Figure 2.3. Cross-Correlator. (Red) 800nm, 100 fs. (Purple) 266 nm (Blue) 400 nm	38
Figure 2.4. Block diagram of the Source Development Laboratory electron accelerator. ....	40

Figure 2.5. Views of the accelerator control area at the Source Development Laboratory..... 41

Figure 2.6. The Source Development Laboratory beamline. The yellow bricks are lead, and are used for radiation shielding. The magnetic spectrometer is at the far end of the picture. The electron gun is off the right hand side in the foreground. .... 41

Figure 2.7. The light enters the light cone near the top of the picture, and travels through the copper pipe. The detector is in the foreground on the left hand side. Though difficult to see, the filter wheel sits just in front of the entrance to the detector. The camera on the right hand side was used to monitor the filter wheel position. .... 42

Figure 2.8. (Left) The filter wheel is placed in front of the detector. These filters are used to discriminate between terahertz light at different frequencies. (Right) The manufacturer also installed several low pass filters in the detector - the one selected for this experiment passes wavelengths longer than 100  $\mu\text{m}$  (frequencies below 3 THz)..... 43

Figure 2.9. Block diagram showing terahertz light collection system..... 44

Figure 3.1. Calculation of transmittance of a Fabry-Perot interferometer in the ultra-violet for two different cavity spacing based on Equation 3.1. .... 50

Figure 3.2. Unmodulated laser spectrum (black) plotted together with "ideal" Fabry-Perot transmittance curve (blue)..... 51

Figure 3.3. (Top) UV laser cross-correlation (black) with input pulse used for calculation (blue) (Bottom) Measured UV laser spectrum (black) with spectrum used for calculation (blue) .....	54
Figure 3.4. Interferometer Structure .....	55
Figure 3.5. Reflectance for UV interferometer mirrors, provided by Scientific Solutions, Inc.....	56
Figure 3.6. Calculated laser time profile based on input with Gaussian envelope. ( $l=200\mu\text{m}$ ).....	58
Figure 3.7. Calculated laser spectrum for Gaussian input ( $l=200\mu\text{m}$ ).....	58
Figure 3.8. Calculated laser time profile based on input with Gaussian envelope. ( $l=100\mu\text{m}$ ).....	59
Figure 3.9. Calculated laser spectrum based on input with Gaussian envelope. ( $l=100\mu\text{m}$ ).....	59
Figure 3.10. (Left) Top view of Fabry-Perot interferometer with UV mirrors mounted. (Right) Side view.....	63
Figure 3.11. Cross-correlation of UV laser pulse. When modulated with the carrier frequency, this is used as the input to the model.....	64
Figure 3.12. (Black) Measured unmodulated UV spectrum (Blue) Calculated UV spectrum based on model.....	65
Figure 3.13. Calculated (Blue) and measured (Black) UV laser profiles for a cavity spacing of $259.8\ \mu\text{m}$ .....	66

Figure 3.14. Calculated (Blue) and measured (Black) UV laser profiles for a cavity spacing of 206.6 $\mu\text{m}$ .....	66
Figure 3.15. "Form Factor" for various UV drive laser pulses at different cavity spacing. The magenta line is the form factor of an unmodulated pulse.....	67
Figure 4.1. Examples of an electron beam longitudinal profiles used as an input distributions for the PARMELA simulations.....	73
Figure 4.2. Electron beam longitudinal profiles for 20 pC after acceleration to 34 MeV. Note the difference in the time scale compared to the initial distribution - the compression is due to off crest injection. ....	74
Figure 4.3. Electron beam longitudinal profiles for 200 pC bunches, after acceleration to 34 MeV. Note the difference in the time scale compared to the initial distribution due to the RF compression.....	75
Figure 4.4. Peak form factor as a function of charge for the input distributions shown in Figure 4.1. In the modulated cases, the form factor value is taken at the peak frequency. For comparison, the form factor for the unmodulated case is taken at 1 terahertz.....	76
Figure 4.5. Beam modulation frequency as a function of charge after acceleration to 34 MeV. The baseline case reports pulse duration as a function of charge. ....	78
Figure 4.6. Form factor of the longitudinal profile of the electron beam for each initial distribution after acceleration to 34 MeV. ....	79
Figure 4.7. Peak form factor values corresponding to the four initial conditions at the	

exit from the electron gun at 4 MeV.....	80
Figure 4.8. Beam modulation frequency as a function of charge after acceleration to 4 MeV at the electron gun exit. The baseline case reports pulse duration as a function of charge. ....	81
Figure 4.9. Form factor of the longitudinal profile of the electron beam for each initial distribution after acceleration to 4 MeV. ....	82
Figure 4.10. Form factor as a function of z for each of the electron beam longitudinal profiles. ....	83
Figure 4.11. Form factor of the unmodulated case for various amounts of charge...	84
Figure 4.12. Peak frequency as a function of z. The baseline plot shows the FWHM pulse duration as a function of z.....	85
Figure 4.13. Form factor and peak modulation frequency as a function of charge for the initial distribution shown in the upper left panel of the previous simulations. In this case, the electron beam is injected at the peak of the RF field instead of 30 degrees off crest.....	86
Figure 4.14. The RF Zero Phasing Technique. Electron beam arrives when there is (A) an RF Upslope (B) an RF Downslope (C) no RF signal.....	89
Figure 4.15. (Left) Example of a longitudinal phase space distribution for an electron beam traveling down the linac. (Right) Projection of this distribution onto the longitudinal coordinate (density distribution) .....	90
Figure 4.16. (Top Left) Electron beam phase space with "A"-style chirp. (Top Right)	

(Blue) Projection of "A" phase space onto longitudinal coordinate (Black)  
 Projection of "A" phase space onto adjusted energy coordinate - the simulated  
 RF zero-phase measurement (Bottom Left) Electron beam phase space with "B"-  
 style chirp. (Bottom Right) (Blue) Projection of "B" phase space onto  
 longitudinal coordinate (Black) Projection of "B" phase space onto adjusted  
 energy coordinate - the simulated RF zero phase measurement. .... 93

Figure 4.17. (Left) Example of a longitudinal phase space distribution for an electron  
 beam traveling down the linac. (Right) Projection of this distribution onto the  
 longitudinal coordinate (density distribution) ..... 94

Figure 4.18. (Top Left) Electron beam phase space with "A"-style chirp. (Top Right)  
 (Blue) Projection of "A" phase space onto longitudinal coordinate (Black)  
 Projection of "A" phase space onto adjusted energy coordinate - the simulated  
 RF zero phase measurement (Bottom Left) Electron beam phase space with "B"-  
 style chirp. (Bottom Right) (Blue) Projection of "B" phase space onto  
 longitudinal coordinate (Black) Projection of "B" phase space onto adjusted  
 energy coordinate - the simulated RF zero phase measurement. .... 95

Figure 4.19. (Left) Example of a longitudinal phase space distribution for an electron  
 beam traveling down the linac. (Right) Projection of this distribution onto the  
 longitudinal coordinate (density distribution) ..... 97

Figure 4.20. (Top Left) Electron beam phase space with "A"-style chirp. (Top Right)  
 (Blue) Projection of "A" phase space onto longitudinal coordinate (Black)

Projection of "A" phase space onto adjusted energy coordinate - the simulated RF zero phase measurement (Bottom Left) Electron beam phase space with "B"-style chirp. (Bottom Right) (Blue) Projection of "B" phase space onto longitudinal coordinate (Black) Projection of "B" phase space onto adjusted energy coordinate - the simulated RF zero phase measurement. .... 98

Figure 4.21. Illustration of algebraic reconstruction technique concept (reprinted with permission from Kak and Slaney) ..... 101

Figure 4.22. (Left, A-F) UV laser cross-correlations of various modulated pulses. (Right, A-F) The corresponding form factor of each laser pulse. .... 106

Figure 4.23. Data corresponds to laser profile A. Total charge is 110 pC. Left hand panels, from top to bottom, correspond to the A-slope of the RF zero-phasing measurement, and show the raw data, the time profile, and the form factor. Right hand panels show the same for the B-slope. .... 107

Figure 4.24. Data corresponds to laser profile A. Total charge is 110 pC. The upper left shows the tomographic reconstruction of the longitudinal phase space. The upper right shows a projection of the phase space onto the axis of time. The solid black curve is from the experimental data while the dotted blue curve is from the simulation. The bottom figure shows the experimental and simulated form factor for this bunch structure. .... 108

Figure 4.25. Data corresponds to laser profile B. Total charge is 60 pC. Left hand panels, from top to bottom, correspond to the A-slope of the RF zero-phasing

measurement, and show the raw data, the time profile, and the form factor.	
Right hand panels show the same for the B-slope. ....	109
Figure 4.26. Data corresponds to laser profile B. Total charge is 180 pC. Left hand panels, from top to bottom, correspond to the A-slope of the RF zero-phasing measurement, and show the raw data, the time profile, and the form factor.	
Right hand panels show the same for the B-slope. ....	110
Figure 4.27. Data corresponds to laser profile B. Total charge is 110 pC (left) and 80 pC (right). From top to bottom are the tomographic reconstructions of the phase space, the projection onto the time axis, and the form factor for each case. Solid black lines correspond to experimental data while dashed blue lines correspond to simulation results. ....	111
Figure 4.28. Data corresponds to laser profile B. Total charge is 60 pC. The upper left shows the tomographic reconstruction of the longitudinal phase space. The upper right shows a projection of the phase space onto the axis of time. The bottom figure shows the form factor for the bunch structure. The solid black curve refers to experimental results while the dashed blue curve refers to simulated results. ....	112
Figure 4.29. Data corresponds to laser profile C. Total charge is 20 pC. Left hand panels, from top to bottom, correspond to the A-slope of the RF zero-phasing measurement, and show the raw data, the time profile, and the form factor.	
Right hand panels, from top to bottom, show the same for the B-slope. ....	113

Figure 4.30. Data corresponds to laser profile C. Total charge is 160 pC. Left hand panels, from top to bottom, correspond to the A-slope of the RF zero-phasing measurement, and show the raw data, the time profile, and the form factor. Right hand panels, from top to bottom, show the same for the B-slope..... 114

Figure 4.31. Data corresponds to laser profile C. Total charge is 160 pC (left) and 130 pC (right). From top to bottom are the tomographic reconstructions of the phase space, the projection onto the time axis, and the form factor for each case. Solid black lines correspond to experimental data while dashed blue lines correspond to simulation results. .... 115

Figure 4.32. Data corresponds to laser profile C. Total charge is 100 pC (left) and 65 pC (right). From top to bottom are the tomographic reconstructions of the phase space, the projection onto the time axis, and the form factor for each case. Solid black lines correspond to experimental data while dashed blue lines correspond to simulation results. .... 116

Figure 4.33. Data corresponds to laser profile C. Total charge is 50 pC (left) and 20 pC (right). From top to bottom are the tomographic reconstructions of the phase space, the projection onto the time axis, and the form factor for each case. Solid black lines correspond to experimental data while dashed blue lines correspond to simulation results. .... 117

Figure 4.34. Data corresponds to laser profile D. Total charge is 60 pC. Left hand panels, from top to bottom, correspond to the A-slope of the RF zero-phasing

measurement, and show the raw data, the time profile, and the form factor.

Right hand panels, from top to bottom, show the same for the B-slope..... 118

Figure 4.35. Data corresponds to laser profile D. Total charge is 145 pC. Left hand

panels, from top to bottom, correspond to the A-slope of the RF zero-phasing measurement, and show the raw data, the time profile, and the form factor.

Right hand panels, from top to bottom, show the same for the B-slope..... 119

Figure 4.36. Data corresponds to laser profile E. Total charge is 180 pC. Top left and

top right show the RF zero phase A and B slope images, respectively.

Immediately below are the tomographic reconstruction of the phase space, and the projection onto the time axis. At the bottom is the form factor of the

longitudinal profile shown in the tomographic reconstruction. .... 120

Figure 4.37. Data corresponds to laser profile F. Total charge is 20 pC. Left hand

panels, from top to bottom, correspond to the A-slope of the RF zero-phasing measurement, and show the raw data, the time profile, and the form factor.

Right hand panels, from top to bottom, show the same for the B-slope..... 121

Figure 4.38. Data corresponds to laser profile F. Total charge is 125 pC. Left hand

panels, from top to bottom, correspond to the A-slope of the RF zero-phasing measurement, and show the raw data, the time profile, and the form factor.

Right hand panels, from top to bottom, show the same for the B-slope..... 122

Figure 4.39. Data corresponds to laser profile F. Total charge is 125 pC (left) and 75

pC (right). From top to bottom are the tomographic reconstructions of the phase

space, the projection onto the time axis, and the form factor for each case.....	123
Figure 4.40. Data corresponds to laser profile F. Total charge is 20 pC. The upper left shows the tomographic reconstruction of the longitudinal phase space. The upper right shows a projection of the phase space onto the axis of time. The bottom figure shows the form factor for the bunch structure. ....	124
Figure 4.41. (Left) Peak form factor at 0.8 terahertz for an unmodulated electron beam. (Right) FWHM pulse duration as a function of charge for an unmodulated beam.....	125
Figure 4.42. (Left) Peak form factor as a function of charge for laser profile B. (Right) Peak modulation frequency as a function of charge for laser profile B.	126
Figure 4.43. (Left) Peak form factor as a function of charge for laser profile C. (Right) Peak modulation frequency as a function of charge for laser profile C.	126
Figure 4.44. (Left) Peak form factor as a function of charge for laser profile F. (Right) Peak modulation frequency as a function of charge for laser profile F.....	127
Figure 4.44. (Left) Phase space simulation for a 20 pC bunch similar to laser profile C. (Right) Phase space simulation for a 300 pC bunch similar to laser profile C. Vertical axis is measured in keV, and represents energy difference from the average particle energy, which is approximately 4 MeV.....	128
Figure 4.45. (Left) Phase space reconstruction for a 20 pC bunch similar to laser profile C. (Right) Phase space reconstruction for a 160 pC bunch similar to laser profile C. Vertical axis is measured in keV, and represents energy difference	

from the average particle energy, which is approximately 38 MeV.....	129
Figure 5.1. Transmission as a function of frequency for vertically polarized (black)	
and horizontally polarized (blue) terahertz light.....	135
Figure 5.2. Demonstration of the finite radiator effect on transition radiation.....	136
Figure 5.3. Spectral density of terahertz radiation.....	137
Figure 5.4. Transverse form factor as a function of frequency.....	139
Figure 5.5. Spectral density of terahertz radiation resulting from an integration over	
the solid angle subtended by the exit aperture.....	141
Figure 5.6. Ray tracing analysis of the light cone collector. (Reprinted with	
permission from John Wiley and Sons, Inc.).....	142
Figure 5.7. Terahertz light transmittance as a function of frequency through the	
copper pipe light transport sections.....	144
Figure 5.8. Transmission of terahertz radiation through 1.5 m of air.....	145
Figure 5.9. Photographs of steel meshes used for terahertz filters. In order of	
decreasing hole size, BE 1401, BE 1000, BE 0805, BE 0600, and BE 0500. The same	
magnification is used for all. A photograph of one of the meshes placed in an	
optical mount is on the bottom right.....	150
Figure 5.10. Views of the FTIR spectrometer at NIST.....	151
Figure 5.11. (Left) Bolometric detector (Right) Close-up of sample and sample holder	
.....	151
Figure 5.12. (Left) Measured terahertz spectrum of mercury arc lamp at NIST.	

(Right) Measured terahertz spectrum of National Synchrotron Light Source (NSLS) on the U-12IR beam line at Brookhaven National Laboratory. Note one of the larger water absorption lines seen clearly in both spectra just above 2 terahertz..... 152

Figure 5.13. (Left) 100 percent lines at various times during the calibration at NIST. (Right) 100 percent lines at various times during the calibration at the NSLS. The black vertical lines denote the area of interest for this experiment..... 153

Figure 5.14. (Left) NIST (blue) calibration of BE 1401 (Right) NIST (blue) and NSLS (red) calibration of BE 1000. Black traces correspond to theoretical predictions. .... 154

Figure 5.15. (Left) NIST (blue) calibration of BE 0805. (Right) NIST (blue) calibration of BE 0600. Black traces correspond to theoretical predictions. .... 154

Figure 5.16. (Left) NIST (blue) calibration of a stack of two sheets of BE 0600. (Right) NIST (blue) and NSLS (red) calibration of BE 0500. Black traces correspond to theoretical predictions. .... 155

Figure 5.17. NSLS (red) calibration of a stack of four sheets of BM-125-01. The black trace corresponds to the theoretical predictions. Note that this material has hexagonal holes compared to circular holes used in the other materials and theoretical calculations. .... 155

Figure 5.18. NSLS calibration of BE 0500 (left) and BE 1000 (right) at various angles. .... 156

Figure 5.19. Laser cross correlation of an unmodulated pulse, corresponding to laser profile A.....	162
Figure 5.20. (Blue) Terahertz energy measured at the bolometer (Black) Terahertz energy predicted using simulation.....	163
Figure 5.21. (Blue) Terahertz energy measured at the bolometer (Red) Terahertz energy predicted using experimentally measured longitudinal electron beam distribution.....	164
Figure 5.22. Simulated terahertz measurements for an unmodulated electron beam. ....	165
Figure 5.23. Comparison of measured (blue), simulated (black), and calculated (red) terahertz measurements for an unmodulated electron beam at 110 pC. ....	166
Figure 5.24. (Left) Simulated spectrum at 110 pC and (right) calculated spectrum for various charge levels for unmodulated electron beams.....	167
Figure 5.25. Laser cross-correlation of pulse corresponding to laser profile B. ....	167
Figure 5.26. (Left) Measurements (blue) compared with simulations (black) for each of the filters. (Right) Calculations (red) compared with measurements (blue) for each of the filters. ....	169
Figure 5.27. Simulated terahertz measurements for an unmodulated electron beam. ....	170
Figure 5.28. Enhancement factor for each filter, for (blue) measured, (black) simulated, and (red) calculated results.....	171

Figure 5.29. Comparison of measured (blue), simulated (black), and calculated (red) terahertz measurements for modulated electron beams generated by laser profile B. ....	173
Figure 5.30. (Black) Simulated spectra of terahertz radiation generated by electron beams from laser profile B. (Red) Calculated spectra of terahertz radiation generated by electron beams from laser profile B. ....	174
Figure 5.31. Additional spectra from simulations of terahertz radiation generated by laser profile B. ....	175
Figure 5.32. Laser cross-correlation of pulse corresponding to laser profile C. ....	175
Figure 5.33. (Left) Measurements (blue) compared with simulations (black) for each of the filters. (Right) Calculations (red) compared with measurements (blue) for each of the filters. ....	177
Figure 5.34. Simulated terahertz measurements for an unmodulated electron beam. ....	178
Figure 5.35. Enhancement factor for laser profile C at 100 pC. ....	179
Figure 5.36. Comparison of measured (blue), simulated (black), and calculated (red) terahertz measurements for modulated electron beams generated by laser profile C. ....	180
Figure 5.37. (Left) Spectra generated from simulations for laser profile C. (Right) Spectra generated from tomographic reconstructions for laser profile C. ....	182
Figure 5.38. Cross correlation of laser profile D. ....	183

Figure 5.39. Comparison of measured (blue), and simulated (black), terahertz measurements for modulated electron beams generated by laser profile D.....	184
Figure 5.40. Spectra generated from simulations for laser profile D.....	185
Figure 5.41. Cross-correlation of laser profile E.....	186
Figure 5.42. (Left) Measured (blue) terahertz energy compared with (red) calculated predictions. (Right) Spectrum predicted by the calculations.....	187
Figure 5.43. PARMELA simulation indicating form factor as a function of charge.	188
Figure 5.44. Total (unfiltered) terahertz energy generated by a modulaed electron beam based on calculations from PARMELA simulations (diamond), calculations from tomographic reconstructions (cross), and actual bolometer measurements (cross). The dashed line is a reference that is defined by a quadratic dependence on charge.....	189
Figure A.1. Schematic of modulation using a physical mask. (A) 300ps pulse @ 800 nm is incident from amplifiers (B) Diffraction grating disperses the beam (C) Second diffraction grating collimates the light (D) This mirror is in the Fourier plane; the mask lines remove some of the frequency components (E) The modulated output pulse emerges from the compressor. ....	199
Figure A.2. Tsunami Ti:sapphire Laser and Mask .....	200
Figure A.3. Cross-correlation of UV laser pulse generated with physical masks....	201
Figure A.4. RF Zero Phasing measurement corresponding to Figure A.3.....	201
Figure A.5. Schematic of the pulse stacker system.....	203

Figure A.5. Optical pulse train produced by the pulse stacker. .... 204

# Chapter 1: Introduction and Background

## *1.1 Introduction*

Particle accelerators have been used to accomplish a variety of goals, including (but not limited to) learning about the nature of the universe<sup>1</sup>, treatment of certain diseases and medical research<sup>2</sup>, and nanoscale device manufacturing<sup>3</sup>.

Electron beam accelerators could even be credited with aiding a societal revolution through their role in television development; Ian Osborne<sup>4</sup> said it well when he noted, "most people own their own particle accelerators. In the back of a television set, electrons are emitted from a cathode and accelerated and maneuvered by electric and magnetic fields toward the phosphor screen." Furthermore, a much larger scale accelerator, the Stanford Synchrotron Radiation Laboratory (SSRL) has even made significant contributions to the development of modern-day LCD flat panel display technology<sup>5,6</sup>.

Most accelerator science and applications result from either the direct use of the accelerated beam (e.g. a particle collider) or an interaction between the beam and another device that causes the generation of radiation (e.g. a free electron laser). This dissertation is an accelerator science study, primarily experimental in nature, of

electron beam longitudinal dynamics that relate to the class of devices that use an electron beam in an accelerator to specifically generate coherent radiation. The study also explores some of the related technology that is necessary for the generation and measurement of the coherent light.

All accelerator based device designers must consider, on some level, the longitudinal distribution of electrons within the electron beam and their dynamics because system performance can vary widely depending on the beam structure. For example, in a particular device, a broad Gaussian distribution of electrons in the beam may cause different effects than a distribution where the electrons are grouped tightly into many well defined bunches. If radiating electrons are bunched properly in an accelerator, the radiating electric fields will be in phase, leading to coherent emission. Since the intensity of the radiation is proportional to the square of the total electric field, and typical electron beams can contain between  $10^8$  and  $10^{10}$  electrons whose fields add in phase, radiating bunched electron beams can serve as high power emitters. Most traditional accelerator based light sources use some type of bunching mechanism, such as a wiggler or bunching cavity, to modulate the electron longitudinal profile after the electron beam has been accelerated in order to generate coherent light. This study explores the possibility of creating a pre-modulated electron bunch train at the accelerator's cathode by using a laser modulated at terahertz frequencies as an optical switch. Figure 1.1 is a diagram that compares the layout of a pre-modulation scheme with that of a traditional free electron laser.

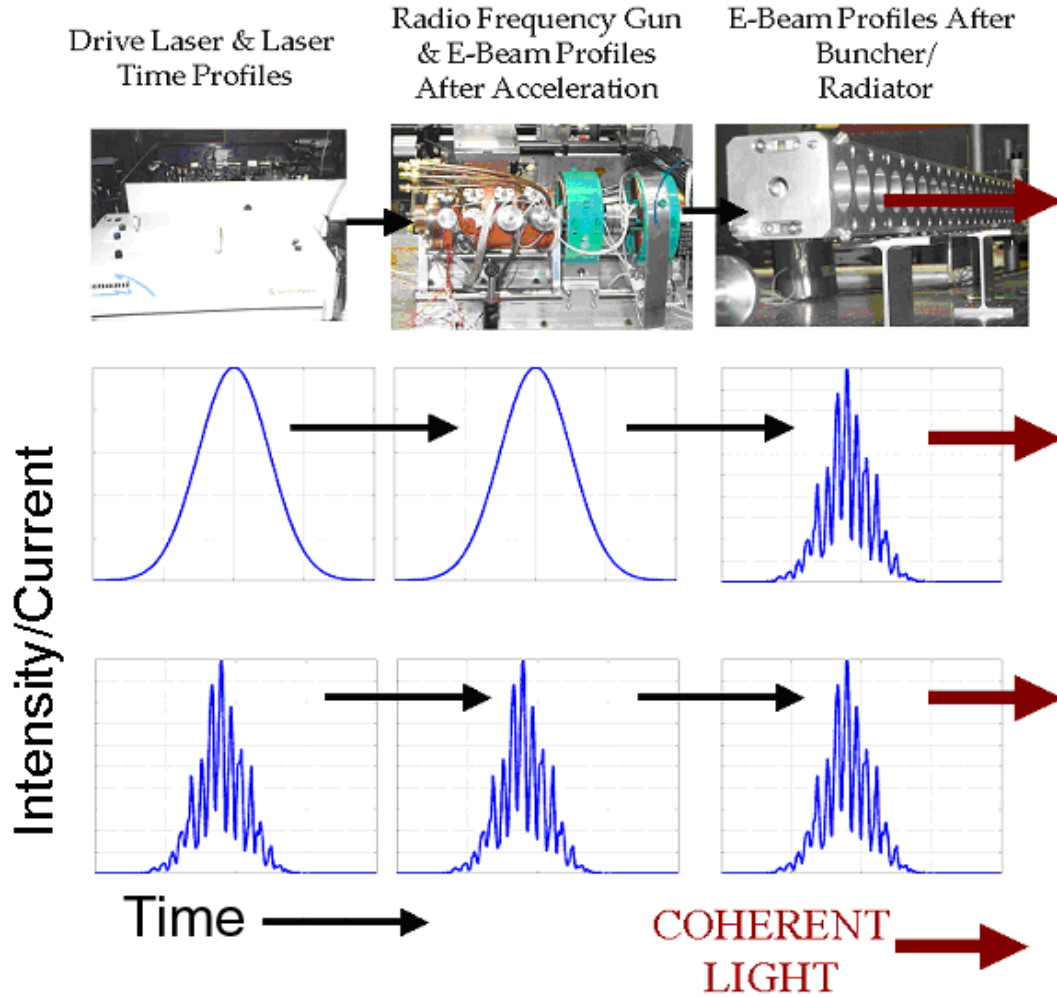


**Figure 1.1.** A concept view of electron beam pre-modulation. (Top) The major components in this particular system include, from left to right: a drive laser to cause photoemission, a radio frequency electron gun and accelerating section, and a radiative mechanism. (Middle) A conventional design for a particle accelerator based light source that might be found in a free-electron laser, from left to right : drive laser time profile, electron beam time profile after acceleration, and electron beam profile after a radiative or bunching mechanism such as a wiggler. (Bottom) The proposed design for this accelerator based light source, from left to right: a modulated drive laser profile, which induces a modulated electron bunch in the gun and accelerator. After the radiator, the beam remains bunched. The red arrows indicate the emission of coherent light, which is the goal of both cases.

This research project consists of three distinct areas of research in order to explore electron beam pre-modulation at the cathode:

- Design and implementation of drive-laser modulation techniques
- Study of electron beam dynamics in the accelerator
- Measurement of terahertz radiation generated by the pre-bunched electron beam.

## *1.2 History of Accelerator Based Light Source Development*

Although this particular implementation of electron beam pre-modulation is new, it is based on a long history of accelerator and light source development. Accelerator technology began with the experiments of J.J. Thomson, who used a small DC accelerator to show the existence of electrons and determine their charge to mass ratio in 1897<sup>7</sup>. During the 1930s and 1940s, devices that extract coherent radiation from bunched electron beams began to mature. In 1937<sup>8</sup>, The Varian brothers, together with William Hansen invented the klystron. The klystron works by accelerating an electron beam from a cathode, and passing it through a cavity whose boundary conditions cause bunching of the electron beam. The separation between groups is equal to the wavelength of radiation that the device emits. At the end of the tube lies a resonant cavity where the electron beam amplifies the microwaves that can be collected and used. In 1940, Boot and Randall invented the cavity magnetron at the University of Birmingham<sup>9</sup>. The magnetron is a crossed-field device also based on cavity structures and electron beam bunching<sup>10</sup>. Both klystrons and magnetrons have many applications, including microwave drivers for radar, radio-frequency particle accelerators, satellite communications, microwave ovens, and television and radio transmission. Today, the klystron, the magnetron, and their relatives in the vacuum tube community such as gyrotrons and traveling wave tubes are the premier sources for microwave radiation, producing kilowatt and

megawatt class power at frequencies 1-100 GHz. An S-Band klystron near 3 GHz has been shown to produce up to 200 MW over  $1\mu\text{s}$ <sup>11</sup>. Klystrons are slow wave devices where the phase velocity of the electromagnetic wave must be close to the velocity of the electron beam for amplification to work. At low energy, this might be quite slow, on the order of half the speed of light in a vacuum. At higher output frequencies, however, slow wave devices like klystrons are not efficient and cannot easily produce high power<sup>12</sup>.

Pursuit of high-energy physics research would eventually lead to new fast-wave devices that allow electromagnetic waves to propagate freely and do not require the boundary conditions imposed by cavities in slow wave devices in order to work. High-energy physicists understood that a circular electron path could allow electrons to accelerate to very high energy in a confined space. The first physicists to build such a device were E.O. Lawrence and M.S. Livingston, who introduced the cyclotron in 1934<sup>13</sup>. The cyclotron works by injecting electrons from a cathode into a strong magnetic dipole field. The Lorentz force due to the magnetic field causes the electrons to travel in a circular orbit. Two D-shaped sections held at different potentials create an accelerating gradient across the gap for longitudinal acceleration. By the time the electrons complete a half turn, the voltage across the gap has shifted such that the electrons can be accelerated again. The electrons gain more energy each time they cross the gap. The initial cyclotron prototype could fit in the palm of a hand, and could accelerate electrons to 80 keV. A larger device, about

25 cm across, accelerated electrons to 1 MeV. Unfortunately, the radius of the electron orbit becomes impractically large as the energy of the electrons increases, and so a different approach had to be used to build a practical high energy electron accelerator.

In an effort to overcome the cyclotron's limitations and increase the energy of the electron beam, scientists developed the synchrotron, another device that accelerates electrons in a circular path through the use of magnets and radio frequency cavities. The main difference between the cyclotron and the synchrotron is that the former uses a constant magnetic field, and the radius of the particle trajectory increases as the particle increases energy; in a synchrotron, the radius of curvature remains constant, but the bend magnet field increases with energy. Interestingly, when highly relativistic electrons pass through magnets that bend their trajectories, they emit radiation<sup>14</sup>. This type of radiation, known as synchrotron radiation, was first observed in 1947 from a 70 MeV electron synchrotron built by General Electric in Schenectady, New York<sup>15</sup>.

With the discovery of synchrotron radiation, the goals of accelerator physicists, who predominantly dealt with high energy physics, nuclear physics, and related machines, began to diverge. The scientists who remained committed to developing clean, high energy electron beams for applications such as high energy colliders considered the radiation an obstacle; radiation losses limited the electrons' energy and resulted in both emittance growth and beam energy spread. Meanwhile,

scientists in the light source community who were searching for sources of short wavelength radiation regarded the discovery of this new light source as a new opportunity and used these machines in a "parasitic" way. These early synchrotrons are sometimes referred to as a "first generation light source," and experiments using the synchrotron radiation were introduced.

Producing intense ultraviolet and x-ray light was easy with a synchrotron, and scientists sought such machines for many applications, such as x-ray crystallography. Synchrotrons designed and built with the expressed purpose of creating x-rays or ultraviolet light (i.e. radiation experiments were no longer parasitic operations), were known as second-generation light sources.

Insertion devices drove the next major improvement in light source development. A device called a wiggler was developed that could be inserted directly into a straight portion of a synchrotron. A wiggler is nothing more than a periodic array of bend magnets that serve to wiggle the beam as it passes through the device. Wigglers are designed to enhance synchrotron radiation from electrons, and provide end users with an extremely bright light source. In 1953, Hans Motz was the first to use a radio frequency electron accelerator with a wiggler in order to produce light<sup>16</sup>. This technique proved to be quite successful, as evidenced by the success of many synchrotron facilities, including (but certainly not limited to) the Advanced Photon Source at Argonne National Laboratory, the National Synchrotron Light Source at Brookhaven National Laboratory, the MAX storage rings at

MAXLAB in Sweden, and the Photon Factory in Japan. Insertion devices at these facilities represent the current state of the art in the field of reliable x-ray generation for the scientific users community and are known as third-generation light sources.

Synchrotrons produce very intense short wavelength light, but it is spread over a broad band, and is not coherent. The next logical step in short wavelength light source development is to produce coherent radiation. When completed, machines that produce intense coherent x-rays are likely to be called fourth generation light sources. One way to accomplish this goal is to bunch the electron beam so that the emitted fields add in phase. Bunching the beam can be accomplished by constructing an optical cavity around the wiggler; the interaction between the feedback radiation and the electron beam causes the beam to bunch. While synchrotrons focused on short wavelength radiation, it was found that wiggler technology could be employed in almost any region of the electromagnetic spectrum. The first demonstration of coherent radiation generation using wiggler technology was the Ubitron, invented by Robert Phillips during the late 1950's<sup>17</sup>. This device worked at microwave frequencies. When this type of device was developed in the optical regime, it became known as a Free Electron Laser (FEL). The modern FEL, as it is understood today, was first proposed by John Madey in 1971<sup>18</sup> and was first demonstrated in 1977<sup>19</sup>. Since then, FEL research has continued to push for operation at higher power and shorter pulses in new regions of the electromagnetic spectrum. To date, the highest average power from an FEL was

recorded in July 2004 at the Jefferson Laboratory FEL, which produced  $>8.5$  kW at  $5.7$   $\mu\text{m}^{20}$ . The FEL community is now developing technology in several areas of the electromagnetic spectrum, and seeks to build a fourth-generation coherent source of x-rays. There are several proposed examples of these, including (but again not limited to) the Linac Coherent Light Source (LCLS) based on the Stanford Linear Accelerator, the Fourth Generation Light Source (4GLS) energy recovery linac at Daresbury Laboratory, and the Accelerator-Radiation Complex for Enhanced Coherent Intense Extended Light (ARC-EN-CIEL - "Rainbow") in France.

Pre-modulation of the electron beam at the cathode has also been attempted in the past as a way to generate coherent light. At low frequencies (RF/microwave regime) there are a few examples of electron beam pre-bunching at the cathode. One example is the klystrode, a microwave amplifier, which produces a modulated electron beam "by application of RF to a grid in close proximity to the cathode surface."<sup>21,22</sup> The principle of operation, in general, is exactly the same as that proposed in this experiment. The electron beam is prebunched at the cathode, and radiation is generated in a microwave cavity. However, the high frequency limit is determined by the electrical circuit driving the grid voltage (and the microwave cavity), and current electronics technology cannot drive the grid at terahertz frequencies.

Optical switching at a photocathode is the only way currently available to explore higher frequency prebunching at the cathode. This idea was also explored

previously in the form of a proposal at the Stanford Linear Accelerator. A device known as a Lasertron<sup>23,24</sup> was proposed, where a laser modulated at RF frequencies illuminated a photocathode. The resulting electron beam is accelerated and a microwave cavity is used to generate radiation. The design frequency was targeted at a range between 3-10 GHz. This device was intended as a replacement for klystrons as microwave sources in future high energy linear colliders.

### *1.3 Current Terahertz Sources*

According to Siegel<sup>25</sup> in 2002, "despite great scientific interest since at least the 1920s, the terahertz frequency range remains one of the least tapped regions of the electromagnetic spectrum." Part of the reason for this may be due to the strong absorption of terahertz radiation by water (see Chapter 5); this problem is important whether using terahertz radiation for wireless communications, radar, or deep tissue imaging. Currently, one of the most prevalent applications of terahertz radiation is spectroscopy of biologically important molecules, including DNA and other various proteins.

Source development is the key to overcoming this problem. Electron beam based sources are currently leading the way. Jefferson Laboratory currently holds the record for a maximum average power for a broadband terahertz source, at nearly

20 W<sup>26</sup>. This is a synchrotron source that creates broadband terahertz radiation by passing a short single bunch through a bend magnet. The large average power is achieved because the repetition rate of the accelerator is extremely high, at 75 MHz. For comparison, the Source Development Laboratory, the primary experimental facility used in for this dissertation, operates at a repetition rate of 2.5 Hz. On the other hand, the free electron laser facility at the University of California, Santa Barbara produces narrow band terahertz radiation at kilowatt peak power levels over tens of microseconds.

While a detailed description of other technologies for terahertz sources are beyond the scope of this dissertation, a good overview is presented by Gallerano and Biedron<sup>27</sup>. Table 1.1 is a summary of some of the sources included in that review.

Source Type	Achieved Power	Frequency
Solid State diodes (Gunn, IMPATT, TUNNET)	100 mW CW 1 mW CW	100 GHz 400 GHz
Gas Laser (methanol)	100 mW CW	2.5 THz
Quantum Cascade Laser	50 mW CW	2.5 THz
Laser Driven Solid State Emitters	~nW- $\mu$ W (av. power)	0.2-2.0 THz
Backward Wave Oscillator	1-100mW	0.03-1.2 THz
UCSB Free Electron Laser	5 kW (av. over 20 $\mu$ s)	0.12-4.8 THz
Jefferson Laboratory ERL (synchrotron radiation)	20 W (av. power)	0.1-3.0 THz
Smith-Purcell FEL	100 $\mu$ W CW	0.3-1.5 THz

**Table 1.1.** Various terahertz sources and their capabilities.

## *1.4 Motivation for a Pre-Modulated Device*

Controlling the electron beam longitudinal profile in a device may be intended to cause sharp, deliberate, longitudinal structure, or may be intended to achieve a particular smooth shape that is different from the Gaussian pulse emitted from many lasers.

Many of the fourth generation light source proposals are based on Free Electron Laser (FEL) technology. Producing high power coherent x-rays requires high-energy (several GeV), high quality electron beams (normalized emittance < 1 $\mu$ m). In order for an x-ray laser to operate, there are strict constraints on the energy spread and emittance (a measure of beam size and divergence) of the electron beam. Current indications suggest that unwanted structure on the electron beam can result in longitudinal beam instabilities, and also cause significant growth in emittance in fourth generation light sources<sup>28,29</sup>. Therefore, those developing these x-ray sources seek to understand, control, and suppress these instabilities in order to enhance x-ray production. In a completely different device, developers of a space charge dominated Cs<sup>+</sup> diode for Heavy Ion Fusion studies used a tailored pulse shape (although thermionically emitted across a pulsed diode) to reduce transients and unwanted structure in an emitted ion beam<sup>30</sup>.

There is also a strong need for powerful terahertz radiation emitter for biomedical imaging, materials science, and sensing technologies<sup>31</sup>. The accelerator

based light source community now has an opportunity to fill this gap with one type of radiator based on longitudinal electron bunching at the cathode. Understanding, controlling, and deliberately seeding longitudinal instabilities on an electron beam can enhance terahertz emission and serve as a powerful source.

Whether the goal is a high-energy accelerator for a Free Electron Laser or a powerful emitter of terahertz radiation, control over the longitudinal profile of the electron beam on a terahertz time scale can enhance performance of the machine. This dissertation explores a system that uses a photoinjecting electron accelerator. In this type of accelerator, a drive laser extracts electrons at a cathode through the photoelectric effect, and the electrons are then accelerated by an electric field. The goal of this work is to evaluate whether terahertz modulation of the drive laser at the cathode can result in controllable modulation of the electron beam.

## 1.5 Background

The total energy radiated by a group of electrons in any system is related to the total energy radiated by one electron in the following way<sup>32</sup>:

$$W_{tot} = W_1 (N_e + N_e(N_e - 1)f(\omega)) \quad (1.1)$$

where  $W_1$  is the energy emitted by one electron,  $N_e$  is the total number of electrons in the electron group, and  $f(\omega)$  is the form factor.  $N_e$  is typically very large. For typical

examples in this experiment, bunches contain about 100 pC of charge. Based on the charge of a single electron, this corresponds to  $\sim 6.3 \cdot 10^8$  electrons. The form factor is a number between 0 and 1, and it is dependent on the geometry of the electron bunch (in both the transverse and longitudinal dimensions) and how this geometry compares to the emitted radiation wavelength.

This experiment seeks to control the form factor for a particular wavelength by controlling the geometry of the electron beam. In cases where emission of radiation is desired, the form factor should be pushed towards 1. As  $f(\omega)$  approaches 1, Equation 1.1 approaches

$$W_{tot} = W_1(N_e^2 f(\omega)) \quad (1.2)$$

On the other hand, as  $f(\omega)$  approaches 0, Equation 1.1 approaches

$$W_{tot} = W_1(N_e) \quad (1.3)$$

Since  $N_e$  is so large for even a modest amount of charge (many experiments use beams with much more charge than 100 pC), the total radiation can be enhanced by many orders of magnitude when the electron bunch geometry is such that the form factor approaches 1.

The form factor itself is computed in the following way<sup>33</sup>:

$$f(\omega) = \left| \int d\vec{r} S(\vec{r}) e^{i \frac{\omega}{c} \hat{n} \cdot \vec{r}} \right|^2 \quad (1.4)$$

where  $S(r)$  is the normalized electron bunch density,  $\omega$  is the angular frequency of the radiation, and  $c$  is the speed of light in the medium that the beam is radiating.

The components for each dimension are often separated:

$$f(\omega) = \left| \iint dydz S_y(y) S_z(z) e^{-i\frac{\omega}{c}y \sin \theta + i\frac{\omega}{c}z \cos \theta} \right|^2 \quad (1.5)$$

Here,  $S_y(y)$  and  $S_z(z)$  are the transverse and longitudinal electron bunch densities, respectively. Note that at this point, most of the calculations in the literature continue by assuming a Gaussian distribution in both the transverse and longitudinal direction, and derive simpler expressions that can be used for the form factor. For this study, however, the analytical analysis stops here; arbitrary experimental or theoretical longitudinal and transverse electron beam distributions can be inserted for  $S_y(y)$  and  $S_z(z)$  and numerically evaluated. Equation 1.5, and its meaning in terms of emitted radiation, is truly the heart of this experiment.

In general, when the electron bunches are small compared to the wavelength, the form factor approaches 1, and consequently, when the bunches are large compared to the wavelength, the form factor approaches zero. Similarly, for a constant bunch size, the form factor is close to 1 for very long wavelengths, but drops to 0 as the wavelength gets smaller. Examining only the on-axis longitudinal component of the form factor, Figures 1.2 and 1.3 compare the form factor of an unmodulated bunch to that of a modulated profile. The unmodulated profile is just

a Gaussian envelope, while the modulated profile uses the same Gaussian envelope multiplied by a  $\sin^2$  wave. The MATLAB code used to calculate these test cases are found in Appendix B.

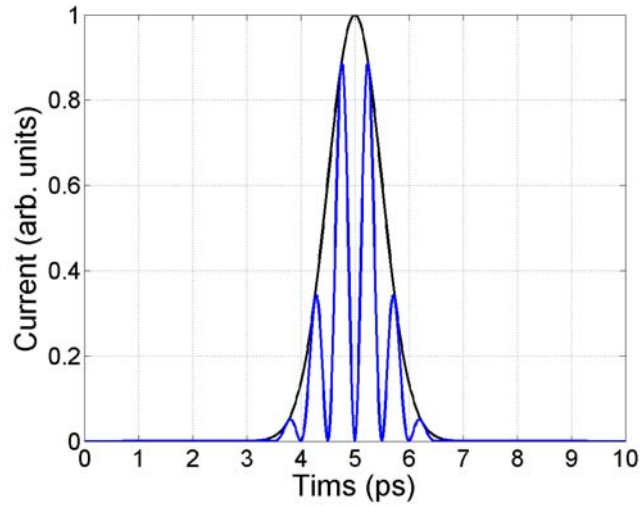


**Figure 1.2.** (Black) Unmodulated electron beam profile used in Equation 1.5. (Blue) Modulated electron beam profile used in Equation 1.5.

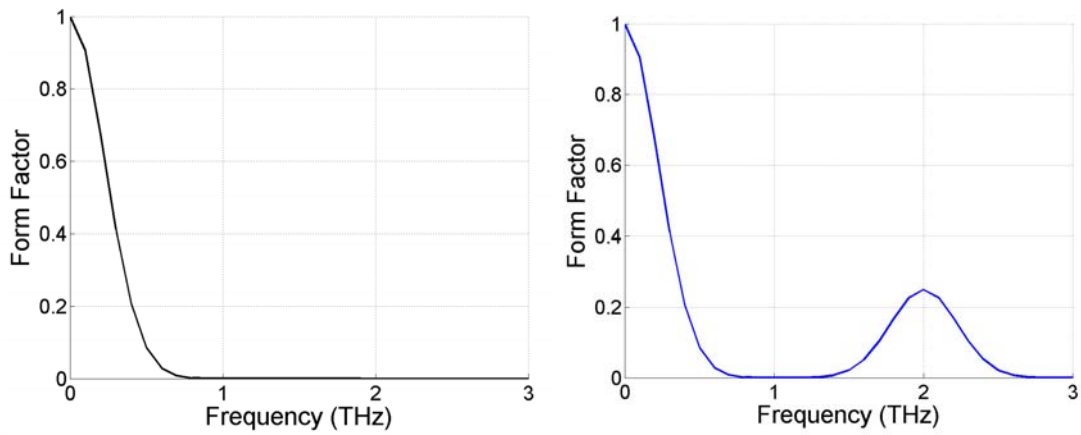


**Figure 1.3.** (Left) Form factor as a function of frequency for the unmodulated beam in Figure 1.2. (Right) Form factor as a function of frequency for the modulated beam in Figure 1.2.

In Figure 1.3, the low frequency characteristics of the form factor are the same. As the radiated frequency goes to zero, or DC, the form factor goes to 1. This is because the wavelength is infinite, and is very large compared to the bunch size in either case. Similarly, as the frequency gets large and the wavelength gets small, the form factor for both cases approaches zero. There is also coherent light at the harmonics of the bunching frequency, but the amplitudes drop because at higher harmonics the wavelength is closer to the bunch size. Near two terahertz, however, there is constructive interference in the modulated case that results in area of a larger form factor. Since there are not very many bunches, and the bunches are not narrow compared to the wavelength at two terahertz, the bandwidth is rather broad, and the light is only partially coherent (i.e. has a form factor of  $\sim 0.25$  instead of 1). If both the modulated and unmodulated cases are assumed to contain 100 pC of charge, and their respective form factors are inserted into equation 1.1, the ratio of energy radiated in the modulated versus the unmodulated case in the band above 1 terahertz is about  $2.3 \times 10^4$ . It is interesting to note, however, that if the same ratio is calculated over the entire bandwidth (from DC to 3 terahertz), the enhancement in the modulated case is only a factor of 1.4. On the other hand, as the bandwidth window is narrowed close to 2 terahertz, this ratio increases, and the value nears the expected peak enhancement of  $\sim 0.25 \times N_e$ , which is near  $1.5 \times 10^8$ . This distinction is extremely important, and will be clearly seen in the experiment. The bandwidth of the detector has an extremely large effect on how relative measurements between the

modulated and unmodulated cases appear in the data.

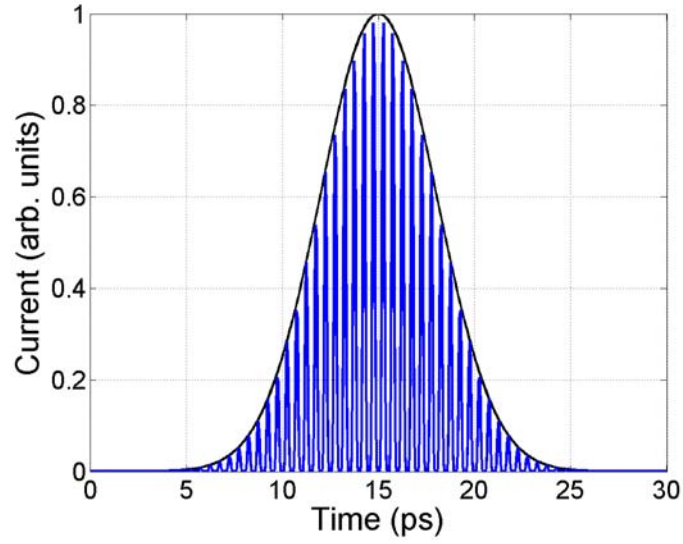


**Figure 1.4.** (Black) Unmodulated electron beam profile used in Equation 1.5. (Blue) Modulated electron beam profile used in Equation 1.5.

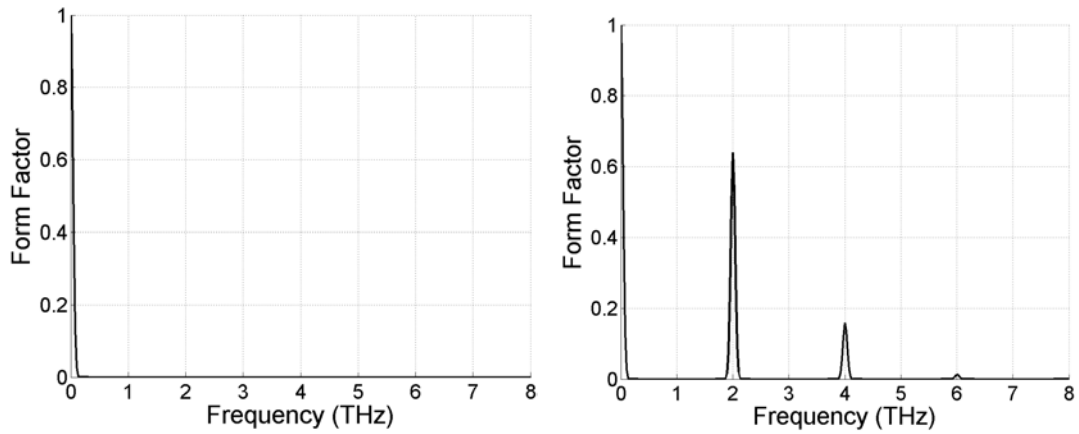


**Figure 1.5.** (Left) Form factor as a function of frequency for the unmodulated beam in Figure 1.4. (Right) Form factor as a function of frequency for the modulated beam in Figure 1.4.

For comparison, Figures 1.4 and 1.5 examine the case where there are a higher number of narrower bunches in order to see the effect on the form factor. In this figure, some of the higher harmonics are shown. Note that the form factor near two terahertz has a higher peak and a narrower bandwidth than that of the previous case. It is precisely this effect that this experiment seeks to exploit.

In order to get an idea of the total energy radiated by the system, not just ratios as determined by the form factor, it is important to explore  $W_l$ . This term is specifically dependent to the type of radiator. Possibilities for radiators are widely varied, but for comparison purposes, a brief look can be taken at transition radiation from a foil, synchrotron radiation from a bend magnet, and radiation from a wiggler.

From the point of view of a terahertz source, the eventual goal is to produce a "table-top" system. Although the experiment that will be described is conducted on a much larger system, for the purposes of exploring an ideal terahertz source, assume that the accelerator is based on a radio frequency electron gun with no additional acceleration (i.e. a room sized system). The electrons will emerge from the gun with an energy of approximately 5 MeV, which corresponds to a  $\gamma$ , or the Lorentz factor in  $E=\gamma mc^2$ , of about 10.8. Each of the major system parameters will be chosen to produce terahertz radiation with this 5 MeV electron beam.

When an electron passes between two media with different dielectric constants, transition radiation is emitted. This occurs when a metal foil intercepts an electron beam in vacuum, and this is the case in the experiment which is described in

further chapters. When the foil is infinitely large, the angular spectral density in the far field is given by<sup>34</sup>

$$\frac{d^2W_1}{d\omega d\Omega} = \frac{q^2 \beta^2}{4\pi^3 \epsilon_0 c} \frac{\sin^2(\theta)}{(1 - \beta^2 \cos^2(\theta))^2} \quad (1.6)$$

where  $q$  is the electron charge,  $\beta$  is the velocity of the electron expressed as a fraction of the speed of light,  $c$  is the speed of light,  $\epsilon_0$  is the permittivity of free space, and  $\theta$  is the angle of observation measured from the direction of propagation of the electron. For comparison purposes, the angular spectral density will be examined at its peak in space, which corresponds to an angle of  $1/\gamma$  where  $\gamma$  is the Lorentz factor. In this case, the angular spectral density at all frequencies is equal to  $2.2659 \cdot 10^{-36}$  J/(rad/s-Solid Angle). Therefore, a transition radiator is a very broadband source.

Imagine now that a 1 nC electron beam was intercepted by the foil. In this case, the angular spectral density would be given by Equations 1.1 and 1.6. For demonstration purposes, this will be calculated for the cases demonstrated in Figure 1.5, and shown in Figure 1.6.

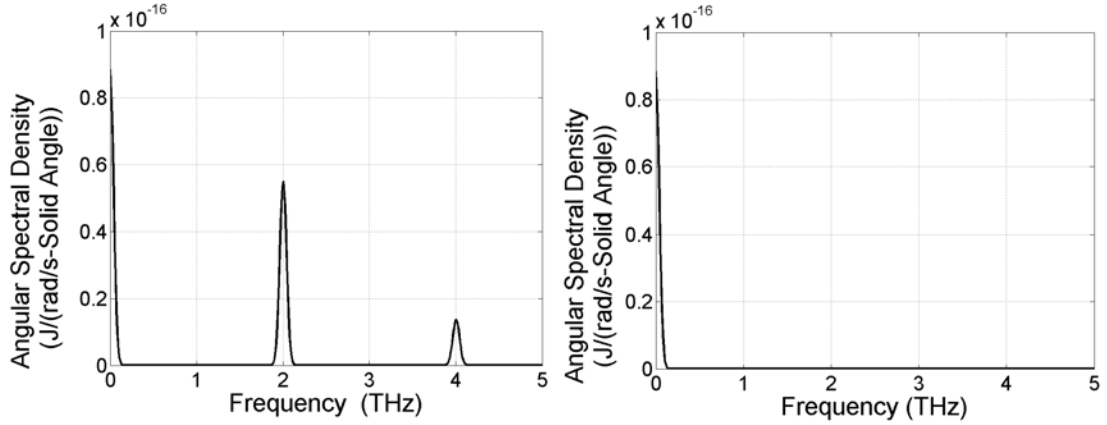


**Figure 1.6.** (Left) Angular spectral transition radiation density for pre-modulated electron beam. (Right) From unmodulated electron beam.

After integrating over the bandwidth up to 5 THz, the unmodulated case is expected to produce 20.82  $\mu\text{J}/\text{solid angle}$ , while the modulated case will produce 62.70  $\mu\text{J}/\text{solid angle}$ . These values are shown along with those from the other sources after they are all discussed, in Table 1.2.

The angular spectral density from synchrotron radiation is given by<sup>35</sup>

$$\frac{d^2W_1}{d\omega d\Omega} = \frac{3q^2\gamma^2}{4\pi^3\epsilon_0 c} \left[ \frac{\zeta^2 K_{2/3}^2(\zeta)}{1 + \gamma^2\phi^2} + \frac{\gamma^2\phi^2\zeta^2 K_{1/3}^2(\zeta)}{(1 + \gamma^2\phi^2)^2} \right] \quad (1.7)$$

where  $q$  is the electron charge,  $\epsilon_0$  is the permittivity of free space,  $c$  is the speed of light,  $K_n(x)$  is the modified Bessel function of the second kind of order  $n$ ,  $\phi$  is the angle of the observer above the plane of orbit, and

$$\zeta = \frac{\omega}{\omega_c} (1 + \gamma^2\theta^2)^{\frac{3}{2}} \quad (1.8)$$

where  $\theta$  is the angle in the plane of electron motion, and  $\omega_c$  is the "critical frequency," which is the highest frequency for which useful synchrotron radiation is emitted, and is given by

$$\omega_c = \frac{3\gamma^3 c}{\rho} \quad (1.9)$$

where  $\rho$  is the radius of the electron orbit. Using the formula defining the radius of the electron trajectory in a magnetic field,

$$\rho = \frac{\gamma m v}{B q} \quad (1.10)$$

where  $m$  is the mass of an electron,  $v$  is the electron velocity,  $B$  is the magnetic field, and  $q$  is the charge on an electron, we find that setting the critical frequency so the spectrum peaks near 1 THz requires a bending radius of 8 cm, and a magnetic field of 0.23 T. The relatively small size and magnet strength (fields of less than 1 T are easily achieved without superconducting magnets) make the synchrotron a viable option for a small-scale device. With these parameters, looking on axis (the maximum for synchrotron radiation) tangential to the velocity of the electron, one sees the angular spectral density given in Figure 1.7.

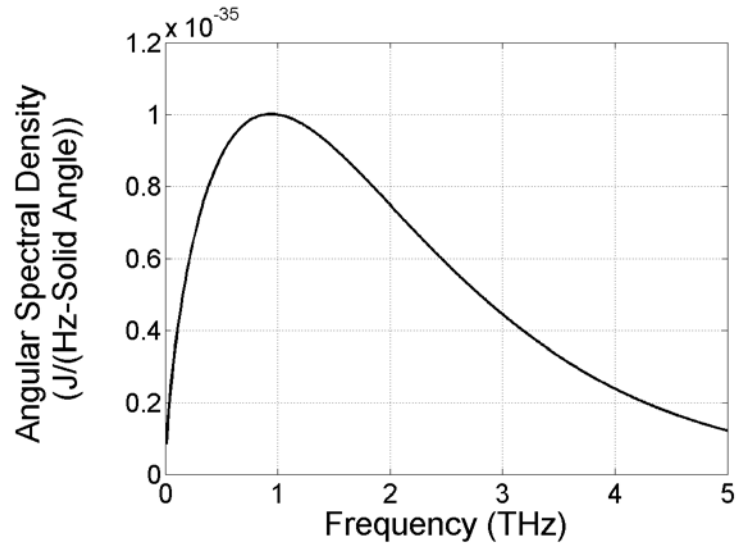


**Figure 1.7.** Angular spectral density of synchrotron radiation from a single electron.

Imagine now that a 1 nC electron beam was passing through this system. In this case, the angular spectral density would be given by Equations 1.1 and 1.7. In a similar way to the case of the transition radiator, this will be calculated for the cases demonstrated in Figure 1.5, and shown in Figure 1.8.

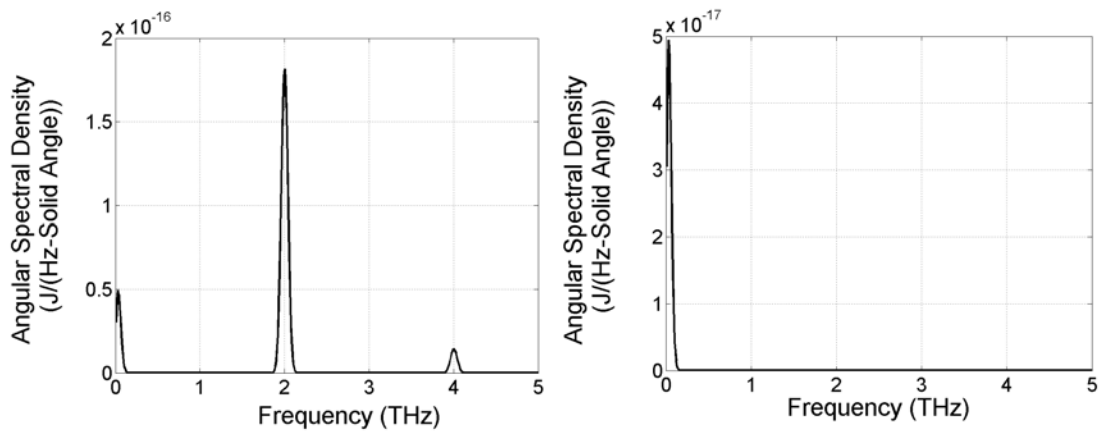


**Figure 1.8.** (Left) Angular spectral synchrotron radiation density for pre-modulated electron beam. (Right) From unmodulated electron beam. Note scale differences.

After integrating over the bandwidth up to 5 THz, the unmodulated case is expected to produce 17.8  $\mu\text{J}/\text{solid angle}$ , while the modulated case will produce 137.4  $\mu\text{J}/\text{solid angle}$ . These values are shown along with those from the other sources after they are all discussed, in Table 1.2.

Instead of using a single bend magnet to generate the radiation, a series of bend magnets can be strung together to form an undulator. This forms a periodic structure with an oscillating magnetic field, and the period of this oscillation is given by  $\lambda_u$ . The emission on axis from a single electron traveling down the undulator is given by<sup>36</sup>

$$\frac{d^2W_1}{d\omega d\Omega} = \frac{q^2 a_u^2 \gamma^2 N_u^2}{2\pi\epsilon_0 c} \left[ \frac{\sin(\pi N_u \Delta k / k_R)}{\pi N_u \Delta k / k_R} \right]^2 \quad (1.11)$$

where  $N_u$  is the number of undulator periods (assumed to be 100),  $k_R$  is the resonant wavenumber given by  $4\pi\gamma^2/\lambda_u$ ,  $\Delta k$  is the deviation from the  $k_R$ , and  $a_u$  is the undulator parameter given by  $qB_u\lambda_u/(2\pi mc)$ . In terms of angular frequency,  $\Delta k/k_R = \Delta\omega/\omega$ .  $B_u$  is the peak magnetic field in the undulator. Given the energy of 5 MeV, the undulator period was calculated to yield a resonant frequency of 2 THz. This yields an undulator period of 3.5 cm. The approximation in Equation 1.11 requires that  $a_u$  must be much less than 1 (but note that the angular spectral density decreases with  $a_u^2$ ). So,  $B_u$  was chosen to be 0.02 T, an order of magnitude smaller than that chosen for the synchrotron radiation source. With these parameters, one sees the angular spectral density from one electron given in Figure 1.9.

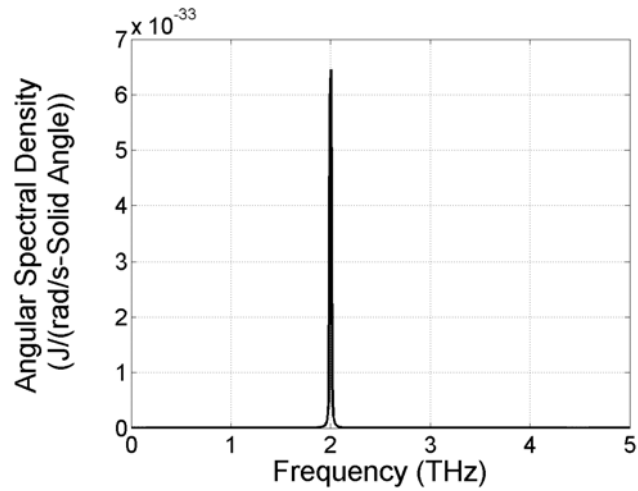


**Figure 1.9.** Angular spectral density for undulator radiation from a single electron.

Notice that in Figure 1.9, the single particle spectrum is quite narrow-band compared to both the transition radiator and synchrotron sources. Also notice that even though the magnetic field is an order of magnitude smaller than that chosen for the synchrotron, the peak undulator radiation is still over two orders of magnitude brighter than the synchrotron radiation (brightness is related to the spectral angular density by a constant).

Now, the same 1 nC electron beams shown in Figure 1.5 passes through this undulator. In this case, as before, the angular spectral density would be given by Equations 1.1 and 1.11. This is demonstrated in Figure 1.10.

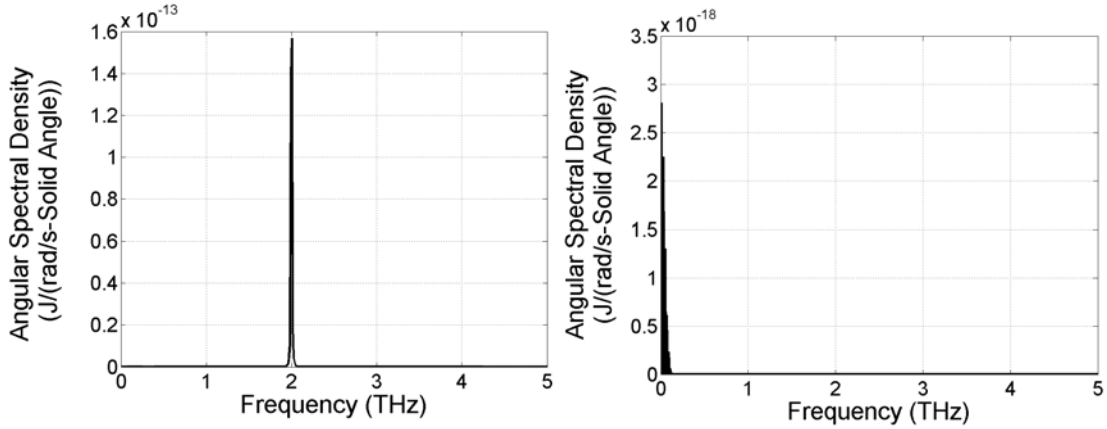


**Figure 1.10.** (Left) Angular spectral undulator radiation density for pre-modulated electron beam. (Right) From unmodulated electron beam. Note scale differences.

After integrating over the bandwidth up to 5 THz, the unmodulated case is expected to produce only 0.37  $\mu\text{J}/\text{solid angle}$ , while the modulated case will produce 21.6 mJ/solid angle. Table 1.2 shows a summary of all of three sources.

Source Type	Transition Radiator	Synchrotron	Undulator
Unbunched	20.82 $\mu\text{J}/\Omega$	17.8 $\mu\text{J}/\Omega$	0.37 $\mu\text{J}/\Omega$
Pre-modulated	62.70 $\mu\text{J}/\Omega$	137.4 $\mu\text{J}/\Omega$	21600 $\mu\text{J}/\Omega$

**Table 1.2.** Energy per solid angle radiated at the angle of maximum emission by three different source types for a unbunched and a pre-modulated electron beam.

Table 1.2 gives an idea of how the total energy per solid angle in the band is affected by pre-modulation. It is clear that undulator radiation provides the most energy in the smallest bandwidth, and is probably the ideal choice for an accelerator

based pre-modulated terahertz source, but for reasons of convenience explained in Chapter 2, a transition radiator was chosen for this proof of principle experiment, which explores the use of electron beam pre-modulation at the cathode to achieve these enhancements in radiation generation.

## Chapter 2: Research Questions and Experimental Overview

The overall goal of this project is to advance the state of the art knowledge on electron beams and particle accelerators so that they can serve as better light sources throughout the electromagnetic spectrum. Specifically, as explained in Chapter 1, controlling the initial longitudinal particle density profile of the electron beam is proposed as a method to enhance coherent radiation for longer wavelengths to serve as a source. Similarly, greater control of the electron beam longitudinal profile could be used to drive the form factor down, which would suppress long wavelength radiation to prevent beam breakup and emittance growth in short wavelength (i.e. x-ray) sources. There are many factors that must be considered when designing any light source, but this project focuses on a few specific research questions, which still turn out to be quite broad.

### *2.1 The Research Questions*

This project looks specifically towards creating deep and defined modulations in the electron beam in order to pursue a tunable, coherent source of terahertz radiation as one application of pre-modulation of the electron beam in a particle accelerator. This project joins varied aspects of physics and engineering research, and serves to enlarge the knowledge base of accelerator based radiation

sources. The terahertz source is based on the idea that an electron beam modulated (or pre-bunched) at terahertz frequencies can radiate coherently at the same frequency. While pre-bunching experiments have been done in the past, this experiment is different because the electron bunches are generated by fast optical switching by a laser modulated at terahertz frequencies at the photocathode of the accelerator.

The various research areas can be categorized in the following way:

- Pulse shape control of high-powered, short-pulse lasers
- Electron beam dynamics in particle accelerators
- Radiation generated by electron beams

### 2.1.1 Pulse shape Control

This experiment proposes that the envelope of the laser incident on a photocathode can control the longitudinal distribution of an electron beam in a photoinjecting linear accelerator. In order to evaluate this statement, it is necessary to control the pulse envelope of the drive laser.

Many varied and widely used techniques exist for laser modulation at megahertz and gigahertz frequencies, but it is more difficult to accomplish terahertz modulation. The first step towards addressing the research questions of this project

required designing, developing, and demonstrating a system that could modulate the laser envelope in an adjustable way, deliver enough laser energy to the photocathode, and be easily integrated into the available experimental systems.

### 2.1.2. Electron Beam Dynamics

Even though the electron beam in a radio frequency linac is subject to extremely high accelerating gradients, space charge forces that come from the Coulomb interaction between electrons may play a large role in beam dynamics before the profile stiffens as the beam becomes relativistic. These space charge forces may cause the modulation placed on the beam by the drive laser to wash out, and can be particularly strong for short microbunches<sup>37</sup>. Since the coherence of the light source is dependent on the sharp density modulation in the electron beam, it will be important to see how well the modulation can be maintained at various frequencies and charge levels, as that will have a direct correlation with the tunability and ultimate power of the terahertz source.

### 2.1.3 Radiation Generated by Electron Beams

Any time a charged particle is accelerated, it will radiate. However, the nature of the radiation produced is dependent on several parameters including the radiative mechanism, the energy of the electron beam, and the distribution of electrons within the beam. Many previous studies that relate electron beam microbunching at high frequency (i.e. larger than the frequency of the injected RF power) and subsequent radiation generation are based on devices such as an FEL wiggler, which intertwine the bunching and radiating mechanisms. This work is different because it will enable the study microbunching independently from a bunching structure that also induces radiation.

Pre-modulating an electron beam is a convenient setup for a radiation source because the beam parameters, radiation mechanism, and bunching characteristics, can all be optimized independently in order to serve as a high power source. Additionally, it is possible to isolate effects on the radiation characteristics such as the spectral or angular density as purely an effect of either the radiator or the structure of the beam.

## 2.2 *The Research Tools*

Various tools were used to answer the research questions, and many of the details of the experimental facilities affect how the data is analyzed. These details will be discussed in further chapters, while this one gives a general overview of the facilities.

The primary experimental facility was the Source Development Laboratory (SDL) at the Brookhaven National Laboratory (BNL), in Upton, New York. Supporting experiments were conducted at the National Synchrotron Light Source (NSLS), also at BNL, and at the National Institute for Standards and Technology (NIST), in Gaithersburg, Maryland. Finally, the University of Maryland Electron Ring (UMER), located at the University of Maryland at College Park, was also used for additional experiments, though in a rather different regime than those conducted at the SDL.

In addition to experimental investigation, some aspects of this experiment were also explored numerically and analytically. Evaluation of the analytical expressions was conducted using the software tool MATLAB, which combines a programming language with powerful mathematics tools and graphics packages. Numerical simulations were conducted using the code PARMELA<sup>38</sup>.

## 2.2.1 The Source Development Laboratory

The Source Development Laboratory is part of the National Synchrotron Light Source (NSLS), located at the Brookhaven National Laboratory. The SDL provided the use of an accelerator system to test the effects of laser pulseshaping on the electron beam. The SDL was constructed as a Free Electron Laser facility, and consists of a 1.6 cell S-band radio frequency photoinjector, an associated drive laser, an accelerating linac, and a wiggler. In the experiment at the SDL, we sought to modulate the drive laser, measure the resultant electron beam, and determine the nature of any radiation coming from the beam.

### 2.2.1.1 The Drive Laser

The electrons in the particle accelerator at the Source Development Laboratory arise in a photocathode-radio frequency gun through the process of photoemission. Under normal operation, the frequency tripled Ti:sapphire drive laser delivers a 5-10 picosecond pulse of 266 nm laser light to the copper photocathode which typically can produce up to 500 pC of charge.

The drive laser subsystem at the Source Development Laboratory is based on a Spectra-Physics Tsunami Ti:sapphire laser that produces a 100 fs laser pulse at 800 nm. A chirped pulse amplification (CPA) scheme, featuring regenerative and single pass amplifiers, is used to increase the energy of the pulse<sup>39</sup>. The infrared pulse is

frequency tripled to the ultraviolet and is delivered to the photocathode. Figure 2.1 shows a basic flow chart for the laser system.

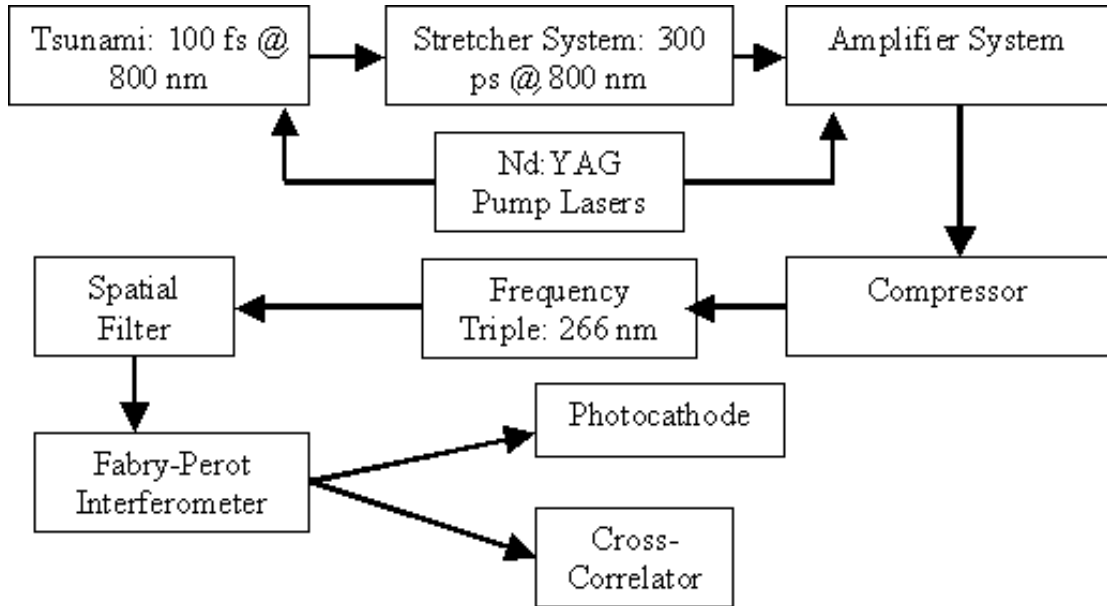


**Figure 2.1.** Laser system block diagram

The chirped pulse amplification system is significant because its effect on the laser pulse is an important factor that enables the laser modulation. The intended purpose of the CPA system is to increase the pulse length of the incident laser such that it can be amplified safely. After amplification, the pulse is recompressed to increase the peak power and reduce the pulse length to the desired point.

In the CPA system, the light is first incident on a diffraction grating. Since the Ti:sapphire laser has a large bandwidth (approximately 7 nm), the different

frequency components of the light will diffract at a different angle after striking the grating. Due to the geometrical arrangement of the system, some frequency components travel across a longer path than others. After passing through the stretcher, the resulting pulse is longer due to the path length differences. Essentially, the stretcher introduces dispersion due to its specific geometry. The dispersion results in a chirped pulse, which means there is a correspondence between frequency and time. After amplification, an analogous system of diffraction gratings will compress the pulse. In a "zero-dispersion" system, the pulse would be compressed back to its original 100 fs pulse length. In this system, the pulse is compressed so that it is still several picoseconds long, and a strong frequency chirp remains on the pulse. This pulse is frequency tripled to 266 nm, so that the photons will have enough energy to overcome the work function of copper. Just prior to delivery to the accelerator, a waveplate/polarizer combination is used to control the amount of laser light that reaches the photocathode. Figure 2.2 shows the Ti:sapphire laser, the stretcher and compressor system, and the ultraviolet transport optics.

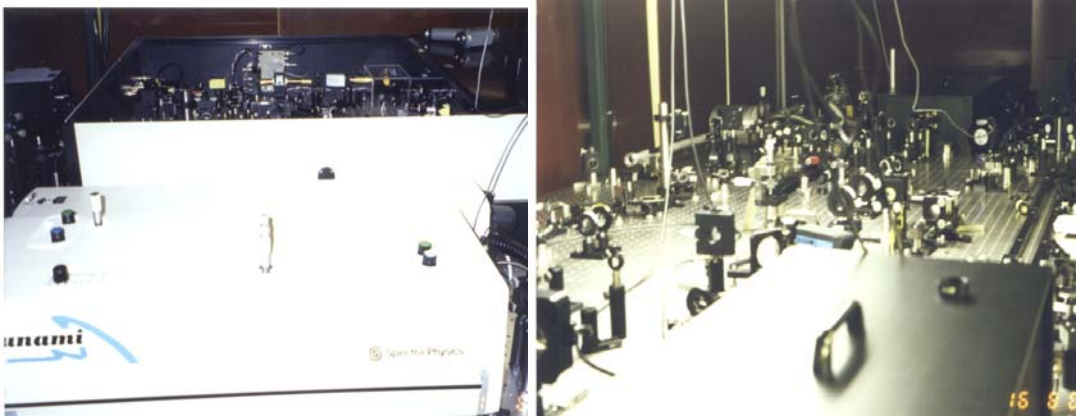


**Figure 2.2.** (Left) Ti:sapphire laser with stretcher and compressor in background. (Right) Ultraviolet laser transport optics.

The primary laser system diagnostics include energy meters, a scanning cross correlator<sup>40</sup>, and a spectrometer. The scanning cross-correlator gives the time profile of the laser beam with 250 fs resolution. The cross correlator works by combining the 100 fs infrared beam and the 266 nm ultraviolet pulse in a Beta-Barium Borate ( $\beta$ -BaB<sub>2</sub>O<sub>4</sub> or BBO) crystal that results in harmonic generation. A delay line scans the short pulse infrared beam (~100 fs) over the long UV pulse in time such that the intensity of the harmonic light represents the time profile of the laser beam over a series of shots. The 250 fs resolution time is a result of different wave propagation velocities for the two light beams inside of the crystal. Figure 2.3 is a photograph of the cross correlator. The infrared delay line works by moving the first set of mirrors back and forth.

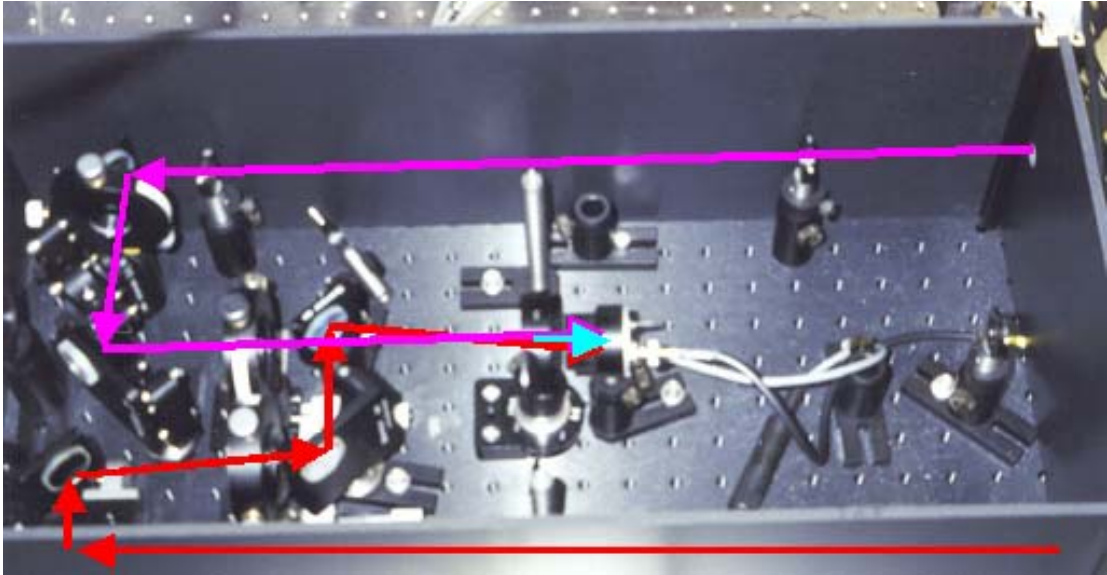


**Figure 2.3.** Cross-Correlator. (Red) 800nm, 100 fs. (Purple) 266 nm (Blue) 400 nm

### 2.2.1.2 The Accelerator

The accelerator at the Source Development Laboratory is named for its intended purpose: the Deep Ultraviolet Free Electron Laser (DUV-FEL). The accelerator begins with a photoinjecting RF electron gun. Many accelerators use a thermionic gun to generate the electrons, where the cathode is heated to a temperature that allows electrons to overcome the work function of the cathode. Instead of using heat, a photoinjecting gun uses a laser whose photons are energetic enough to allow electrons to overcome the work function when they are absorbed. The electron gun is also a microwave resonant structure, specifically at 2856 MHz, or S-Band. A klystron provides RF power at S-Band, which resonates inside the cavity, and provides the large electric field necessary to accelerate the electrons emitted

from the cathode to relativistic energy in a short distance. The cathode in this electron gun is simply the copper that forms the back wall of the cavity. Although copper has a low quantum efficiency (one optimistic measurement quotes the quantum efficiency of copper at  $5 \cdot 10^{-4}$  electrons per photon<sup>41</sup>), it is a very prompt emitter<sup>42</sup> which means that electrons are emitted almost instantaneously (i.e. subfemtosecond) after the arrival of a photon. This quality is essential for this experiment because it allows the longitudinal distribution of electrons emitted at the cathode to match that of the drive laser.

When the electrons leave the photoinjector, they have been accelerated to an energy of approximately 5 MeV. Two accelerating sections, each 3 m long and similar to SLAC accelerating structures, bring the electron beam to 75 MeV. A magnetic bunch compressor is included in the linac, but is not used for this experiment. Two additional SLAC-type accelerating sections follow the bunch compressor, which are used to increase the beam energy to 200 MeV for FEL operations. In this experiment, these additional accelerating sections are not used to provide additional energy to the beam, but rather are used for longitudinal profile diagnostics, which are further explained in Chapter 4. The longitudinal diagnostics also make use of a magnetic spectrometer located after the final accelerating section. Under normal DUV-FEL operation, the electron beam is delivered to a wiggler intended to produce Free Electron Laser light at various wavelengths. After the accelerating sections, however, there is a mirror that could be easily inserted or

removed from the beampipe. This served as a convenient way to intercept the 75 MeV beam, and was used to generate transition radiation. The mirror is placed at a 45 degree angle with respect to the direction of the traveling electron beam. If the mirror were thin enough, forward transition radiation would propagate in the same direction as the electron beam velocity. Backward transition radiation is emitted in a hollow cone with the maximum intensity at an angle of  $1/\gamma$  along the direction of specular reflection from the mirror. This radiation is outcoupled through a window in the beampipe, and this light is transported to the long wavelength diagnostics. Figure 2.4 is a block diagram that shows the structure of the accelerator. Figure 2.5 shows the control area, and Figure 2.6 is a photograph of the beamline itself.

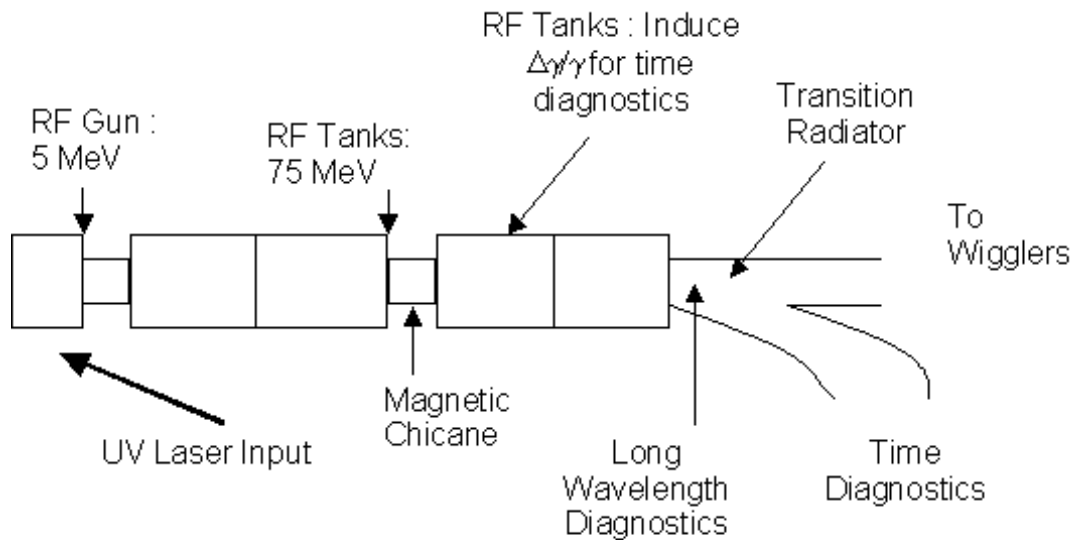


**Figure 2.4.** Block diagram of the Source Development Laboratory electron accelerator.



**Figure 2.5.** Views of the accelerator control area at the Source Development Laboratory.



**Figure 2.6.** The Source Development Laboratory beamline. The yellow bricks are lead, and are used for radiation shielding. The magnetic spectrometer is at the far end of the picture. The electron gun is off the right hand side in the foreground.

### 2.2.1.3. Terahertz Transport and Diagnostics

After exiting the accelerator, a light transport system is used to bring the terahertz light to the detector. The light is collected in a light cone, and passes

through a series of 1/2" copper pipes and reflectors. After exiting the copper pipe, the light passes through a filter designed to discriminate between terahertz light at different frequencies, which will be described further in Chapter 5. Four different filters were mounted on a filter wheel that could be remotely controlled outside the accelerator vault. Once the terahertz light left the accelerator, it was exposed to ambient air. Absorption due to water in the air was a significant effect that needed to be taken into account. The light transport system is shown in Figure 2.7.

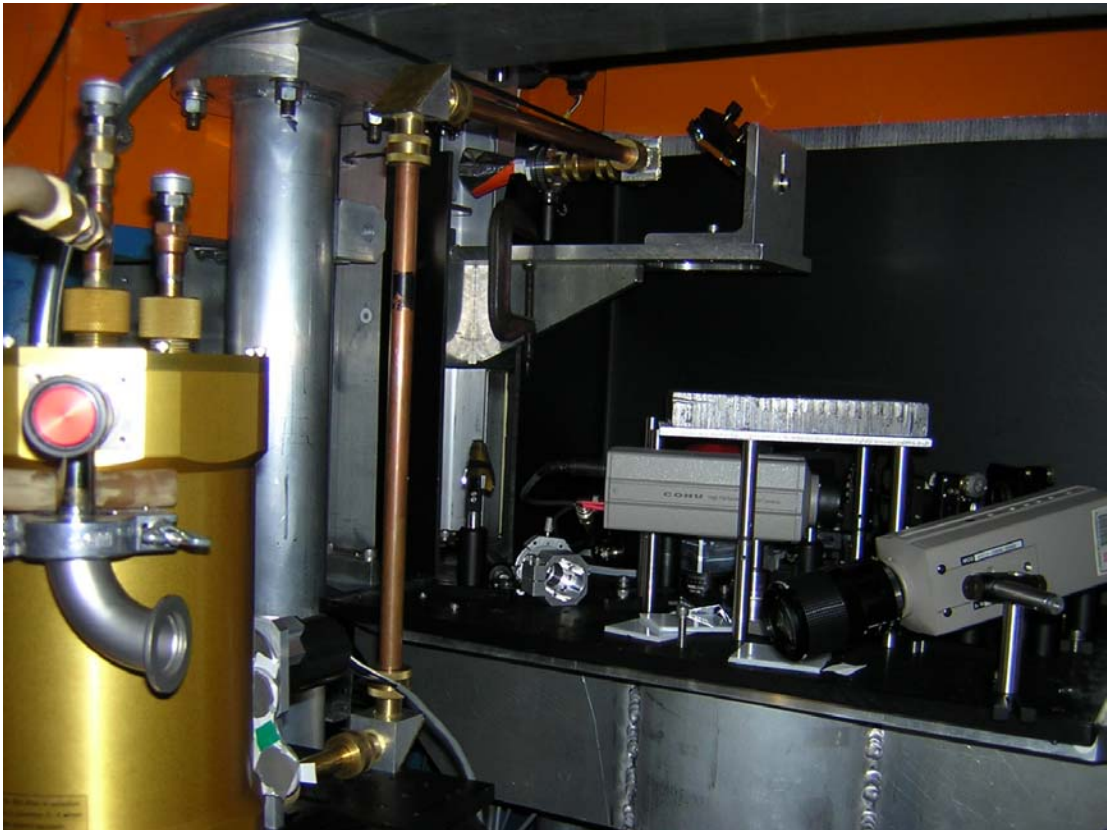


**Figure 2.7.** The light enters the light cone near the top of the picture, and travels through the copper pipe. The detector is in the foreground on the left hand side. Though difficult to see, the filter wheel sits just in front of the entrance to the detector. The camera on the right hand side was used to monitor the filter wheel position.

A helium cooled bolometric detector is used to measure light with wavelengths between 100  $\mu\text{m}$  and 2 mm<sup>43</sup>. The long wavelength limit is determined by the geometry of the system, while a filter installed by the bolometer manufacturer defines the short wavelength limit. The detector is cooled to liquid helium temperature in order to reduce Johnson noise. The responsivity of this detector is  $2.7 \times 10^5 \text{ V/W}^{44}$ , and can be effective for measuring femtojoules of light. The detector has a 300  $\mu\text{s}$  thermal relaxation time, and was operated with a preamplifier gain of 200. Since the electron beam pulse length is on the order of picoseconds, the detector responds to total energy instead of instantaneous power. Figure 2.8 shows different views of the detector. Figure 2.9 shows a block diagram of the entire terahertz collection system, and each part is modeled in detail in Chapter 5.

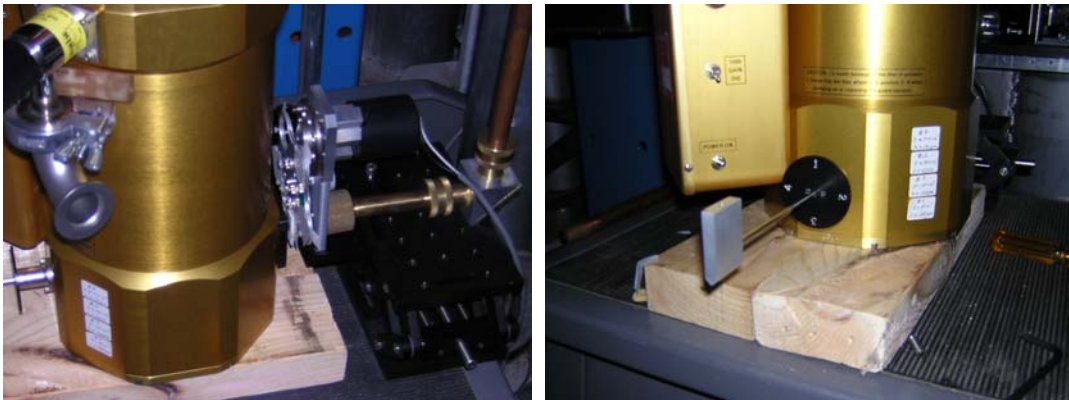


**Figure 2.8.** (Left) The filter wheel is placed in front of the detector. These filters are used to discriminate between terahertz light at different frequencies. (Right) The manufacturer also installed several low pass filters in the detector - the one selected for this experiment passes wavelengths longer than 100  $\mu\text{m}$  (frequencies below 3 THz).

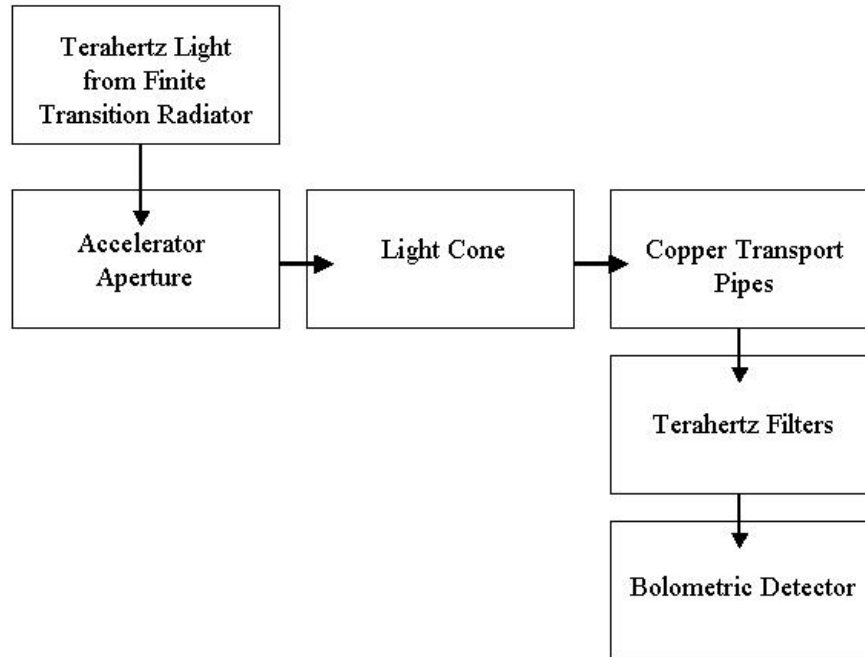


**Figure 2.9.** Block diagram showing terahertz light collection system.

The filter installed by the manufacturer was always placed in position 3 as shown in Figure 2.8. This is close to an ideal low pass filter that rejects frequencies larger than 3 terahertz<sup>45</sup>. Many of the calculations in this dissertation show results up to 5 terahertz for purposes of demonstration, but keep in mind that all calculations that are compared to actual data are integrated only out to 3 terahertz.

### 2.2.2 PARMELA Simulations

Electron beam simulations were used to gain an understanding of how structure on the electron beam can be modified due to space charge forces near the cathode. The primary simulation code used is called PARMELA, which stands for

"Phase and Radial Motion in Electron Linear Accelerators." The simulations do not include any radiative effects.

PARMELA can easily model radio frequency acceleration systems. The computation begins by establishing a 6-D coordinate system to describe the position and momentum of each particle in the x, y, and z directions. The z-direction is that of the beam propagation. PARMELA defines a reference particle whose initial z coordinate and kinetic energy are specified by the input file. The other four coordinates are initialized to zero. The user can define input distributions relative to this reference particle. The beam dynamics calculation begins by calculating space charge. There are two methods available for calculating space charge: a point-to-point method and a space charge mesh method. In the point-to-point method, the Coulomb force is calculated for each particle. This method is both computationally expensive and numerically noisy. Simulations in this work use the space charge mesh method. A separate space charge mesh is defined that lies in the rest frame of the reference particle. All particle coordinates are transformed into the rest frame of the mesh. The software automatically adjusts the space charge mesh size so that all the particles are included. The user defines the mesh resolution. According to the PARMELA documentation, for  $\gamma < 5$ , PARMELA "calculates fields at the mesh corners and interpolates at intermediate locations using these corner fields. For  $\gamma > 5$ , the code calculate the fields at the longitudinal centers of the mesh rings and interpolates at intermediate locations using these points." The space charge impulses

are computed and then the particle coordinates are transformed back to the laboratory frame. PARMELA then uses a matrix transform method to modify individual particle coordinates depending on the beam element in which the particle is located<sup>46</sup>. In this project, PARMELA was used not only to compare experimental results to the simulated ones, but also extract additional information that was not available experimentally.

### *2.3 Project Overview*

The goal of the project is to determine whether or not a pre-modulated electron beam can be accelerated and retain its modulated structure. All of the research tools are used together to help answer this question. The ability to modulate the drive laser and use it as a switch serves as the base for the subsequent work. The longitudinal profile of the electron beam that results from these laser profiles are explored both experimentally and numerically. After acceleration, the amount of transition radiation emitted by the electron beam is measured, calculated from profiles produced by the simulations, and calculated from profiles measured during the experiment at the Source Development Laboratory. Each of the methods used, whether they be experimental, numerical, or analytical, all have benefits and drawbacks, but when used together, yield a clearer picture about the state of the electron beam and the terahertz light.

## Chapter 3: Drive Laser Modulation Techniques

Each drive laser pulse, with a standard length of approximately 5-10 ps, needed to be divided into several smaller pulses, each less than 1 picosecond long in order to generate coherent light at frequencies near 1 terahertz. Instead of using one long, smooth pulse, in this experiment, the cathode is illuminated with a pulse train of shorter pulses. Essentially, the drive laser is used as a switch that would turn the electron beam on and off at terahertz frequencies.

There are many techniques that can be used to accomplish the pulse modulation, and in fact, three different ones were explored for this particular experiment. Each system had several advantages and drawbacks related to ease of integration into the existing laser system, ability to generate laser pulse trains of varying frequency and number of bunches, and the ability to deliver significant laser power to the cathode. The system that seemed the best to create this laser switch based on these criteria was a Fabry-Perot interferometer placed in the path of the UV laser pulse. The interferometer was relatively small, and proper operation depended only on the relative alignment of the interferometer plates, and not the alignment of the incoming laser pulse. Adjusting the rate of the laser switch was a matter of changing the distance between the interferometer plates.

The two other systems considered for use with this experiment were a pulse

stacker, and a spatial filter in the laser compressor. Both were also attempted at various times experimentally. A brief overview of these methods and the experimental results obtained with them can be found in Appendix A.

### *3.1 Theoretical Model for Fabry-Perot Interferometer as a Laser Switch*

Creating a modulated drive laser pulse at a chosen frequency was accomplished with a Fabry-Perot interferometer that was integrated and implemented into the Source Development Laboratory drive laser system. The interferometer is placed after the spatial filter as shown on the laser block diagram, and it consists of two partially reflecting parallel plates separated by an adjustable distance that can be used to control the frequency of modulation. Predicting the performance of the Fabry-Perot system requires consideration of the chirp and short pulse duration of the incident laser, but a more standard approach is useful for explaining the general behavior of this system. When a continuous plane wave is incident on a Fabry-Perot interferometer, the transmission is given by<sup>47</sup>

$$\frac{I_t}{I_i} = \frac{1}{1 + 4R/(1 - R)^2 \sin^2(\delta/2)} \quad (3.1)$$

where  $R$  is the reflectance of the mirrors and  $\delta$  is the phase difference between each of the transmitted waves emerging from the etalon. The phase shift,  $\delta$ , is given by

$$\delta = \frac{4\pi n l \cos \theta}{\lambda_o} + 2\varepsilon \quad (3.2)$$

where  $n$  is the index of refraction inside of the cavity,  $l$  is the cavity spacing,  $\lambda_o$  is the wavelength in vacuum,  $\theta$  is the angle of incidence, and  $\varepsilon$  is the phase shift upon reflection. Following this point, the laser is assumed to be at normal incidence to the interferometer, and so all of the corresponding  $\cos(\theta)$  terms disappear. Below, it is shown how varying the cavity length,  $l$ , can be used to generate laser beam modulation in the time domain.

In general, the two most important parameters that define a Fabry-Perot system are the finesse and the free spectral range (FSR). The finesse is a measure of the sharpness of each of the transmission peaks; in fact, the free spectral range divided by the finesse gives the FWHM of a transmission peak. The free spectral range is a measure of the difference in frequency between the transmission maxima. The finesse and free spectral range at normal incidence are given by

$$F = \frac{\pi\sqrt{R}}{1-R} \quad \Delta\nu = \frac{c_o}{2nl} \quad (3.3)$$

respectively, where  $l$  is the cavity length,  $c_o$  is the speed of light in a vacuum, and  $n$  is the index of refraction inside the cavity. When designing a Fabry-Perot cavity, the reflectance,  $R$ , is essentially fixed because varying  $R$  requires changing the mirrors. However, the free spectral range can be easily changed by varying the cavity length,  $l$ . Figure 3.1 shows the transmittance of a Fabry-Perot interferometer with various

cavity spacing, for a constant mirror reflectance, as a function of frequency. From this plot, it is clear that a Fabry-Perot system acts like a comb filter.

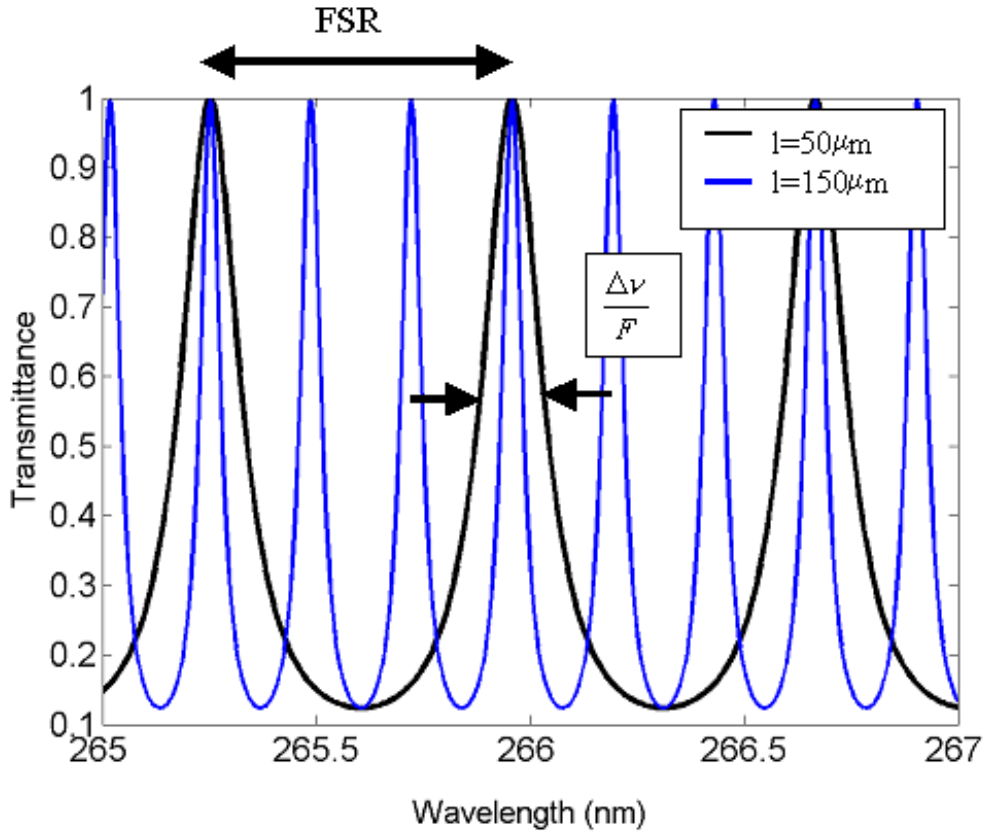


**Figure 3.1.** Calculation of transmittance of a Fabry-Perot interferometer in the ultra-violet for two different cavity spacing based on Equation 3.1.

Since the laser pulse is chirped and there is a correspondence between frequency and time, using a comb filter to modulate the frequency should also result in modulation in the time domain. Additionally, changing the free spectral range should cause a change in the modulation seen in the time domain. Generating several peaks in the time domain requires that the free spectral range should be

small enough such that several transmission maxima fall within the spectrum of the laser pulse. This requirement put the necessary cavity spacing roughly in a range between 50  $\mu\text{m}$  and 500  $\mu\text{m}$ , corresponding to cavity transit times on the order of a picosecond. Note that the total energy transmitted through the interferometer is related to the area under the transmittance curve (multiplied by the laser spectrum). Therefore, sharp peaks in the transmittance (high finesse) correspond to large laser losses due to back reflection from the etalon. Determining the appropriate mirror reflectance for this experiment was important, and this process is described further in this section. To see how the free spectral range should be adjusted to cause modulation, a measured spectrum from the unmodulated laser beam is shown in Figure 3.2 together with a transmittance curve for the etalon as analyzed above.

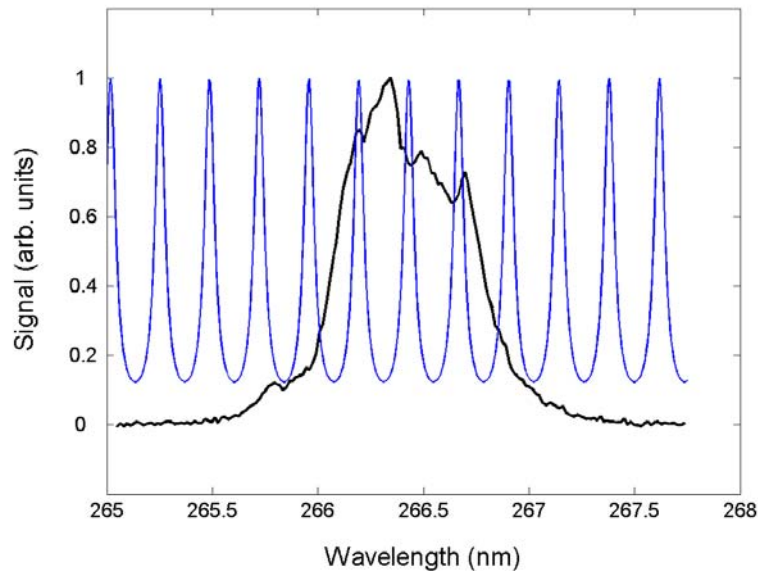


**Figure 3.2.** Unmodulated laser spectrum (black) plotted together with "ideal" Fabry-Perot transmittance curve (blue).

The actual incident ~266 nm laser light has a FWHM of several picoseconds, and is chirped, which means there is a correspondence between frequency and time. However, the above analysis of the Fabry-Perot interferometer makes the assumption that the input pulse is continuous and also that the instantaneous frequency of the pulse does not change with time. In this case described here, the total pulse length is on the order of the cavity spacing, so the cw approximation is not appropriate. Additionally, the variation of frequency with time is not taken into account. It is therefore necessary to perform a new analysis that includes these effects.

The electric field of the incoming UV laser pulse can be modeled in the following way<sup>48</sup>:

$$E(t) = \frac{1}{\sigma\sqrt{2\pi}} \exp\left(\frac{-t^2}{2\sigma^2}\right) \exp(i\omega_o t + i\beta \cdot t^2) \quad (3.4)$$

This model describes a laser pulse with a Gaussian envelope as a function of time,  $t$ , defined by standard deviation  $\sigma$  that has a total instantaneous phase of  $\phi = \omega t + \beta t^2$ .  $\omega$  is the angular frequency of the light, and  $\beta$  is a parameter that describes the chirp. As described in Siegman, the instantaneous frequency of the pulse is given by :

$$\omega_i(t) = \frac{d\phi(t)}{dt} = \omega_o + 2\beta \cdot t \quad (3.5)$$

This formulation models a linear pulse chirp, typically found in a chirped pulse

amplification system, so that the frequency correspondence with time is taken into account. The values for  $\sigma$  and  $\beta$  were chosen such that the bandwidth and pulse length of the model closely match the measured values. Figure 3.3 shows an example of the modeled laser pulse shape and spectrum compared with an example of a measurement, made with the laser cross-correlator and the spectrometer.

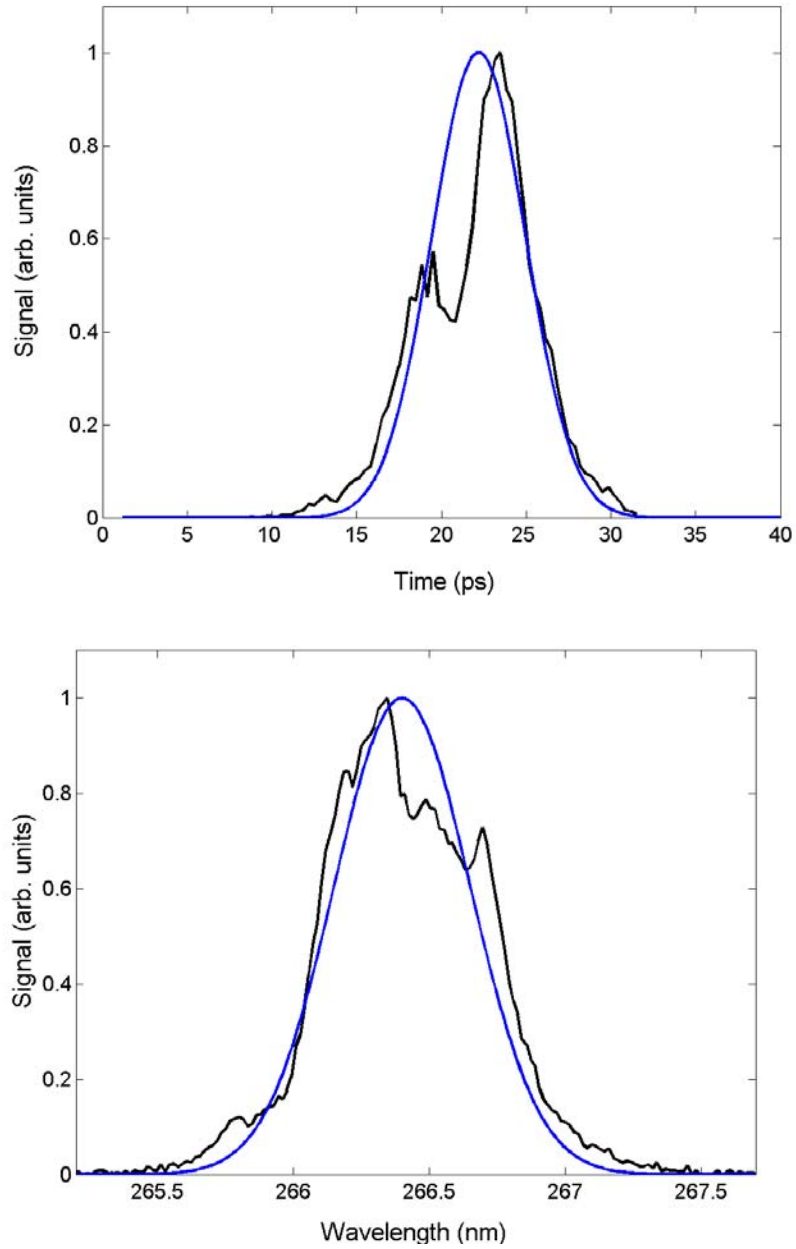


**Figure 3.3.** (Top) UV laser cross-correlation (black) with input pulse used for calculation (blue) (Bottom) Measured UV laser spectrum (black) with spectrum used for calculation (blue)

Note that in Figure 3.3, the cross-correlation measurement of the UV laser pulse is not a smooth Gaussian. The Gaussian approximation just gives an example

of how the interferometer would behave in an ideal case, and was used primarily for guiding the acquisition process of the interferometer. It was necessary to use the cross-correlation measurement modulated at the carrier frequency as an input to this model in order to achieve good agreement between expected and actual behavior. Additionally, the non-Gaussian shapes inherent to this Ti:sapphire system may lead to coherent enhancement, and if this effect is not desired, tailoring the UV laser pulse will be necessary to suppress the emission.

In order to calculate the transmittance of the system, the interferometer was modeled as a multilayered structure that included the two plates separated by an air gap as shown in Figure 3.4.

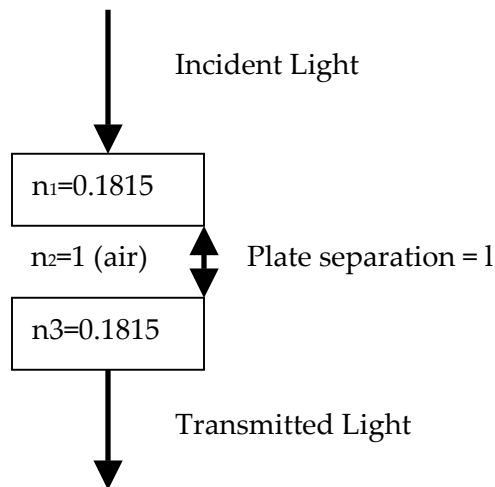


**Figure 3.4.** Interferometer Structure

The edges of the interferometer plates that do not face the air gap are wedged and anti-reflection coated so that their effect on the output pulse is minimized.

The reflectance ( $\rho^2$ ) of the mirrors was measured to be 48% at 266.5 nm (Figure 3.5), and an "effective dielectric constant" was chosen so that the reflectance (and transmittance) would match the measured value achieved by the mirror coating, as calculated from the reflection coefficient

$$\rho = \frac{Z_2 - Z_1}{Z_2 + Z_1}. \quad (3.6)$$

where, assuming normal incidence,  $Z_2=Z_0/n_2$ ,  $Z_1=Z_0/n_1$ , and  $Z_0$  is the impedance of free space ( $376 \Omega$ ).

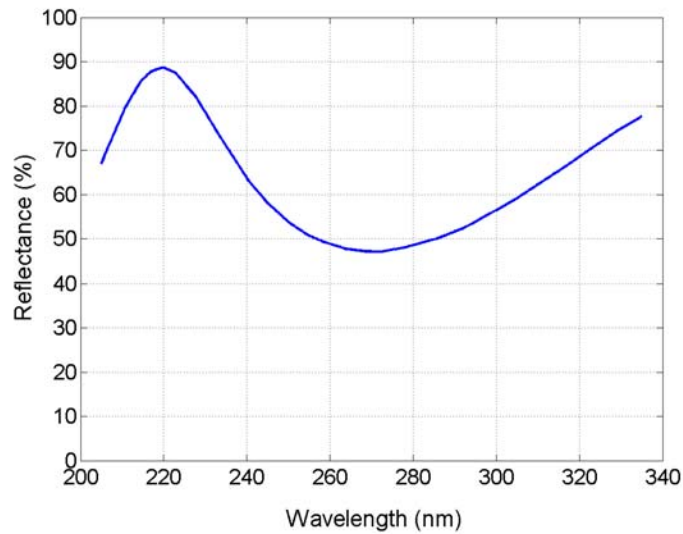


**Figure 3.5.** Reflectance for UV interferometer mirrors, provided by Scientific Solutions, Inc.

The method of impedance transformation<sup>49</sup> was used to calculate the laser output from this multilayered structure. Using this method, the reflection and

transmission coefficient of the entire system can be calculated for each frequency component. The primary interest of this calculation is the transmission coefficient, which is given by

$$\tau(k_2) = \frac{2Z_3'(k_2)}{Z_3'(k_2) + Z_1} \quad (3.7)$$

where

$$Z_3'(k_2) = Z_2 \left( \frac{Z_3 \cos k_2 l + iZ_2 \sin k_2 l}{Z_2 \cos k_2 l + iZ_3 \sin k_2 l} \right) \quad (3.8)$$

and  $k_2 = 2\pi n_2 / \lambda_0$ , and  $Z_n$  is the impedance in region  $n$ .

The calculation proceeds by taking the Fourier transform of the incident laser pulse given by Equation 3.4. Each component is multiplied by its transmission coefficient, which yields the output pulse in the frequency domain. The output signal in the time domain is found by taking the inverse Fourier transform. Figures 3.6, 3.7, 3.8, and 3.9 show a measured and calculated time profile and spectrum of the UV drive laser for two different values of the cavity spacing. Since the real input pulse (and spectrum) is not really Gaussian, like that used for the calculation, the results are not expected to be exactly the same, but are expected to reveal the general

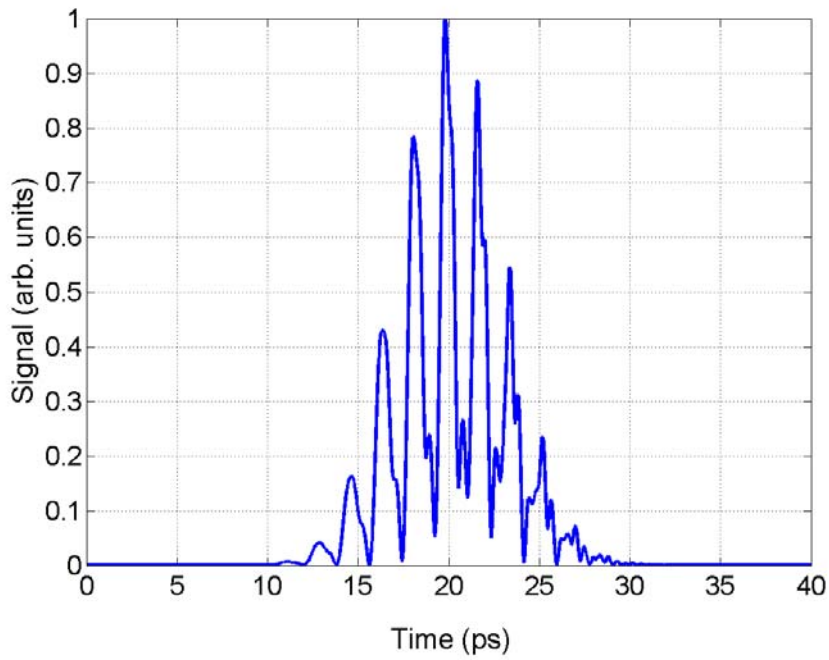


**Figure 3.6.** Calculated laser time profile based on input with Gaussian envelope. ( $l=200\mu\text{m}$ )

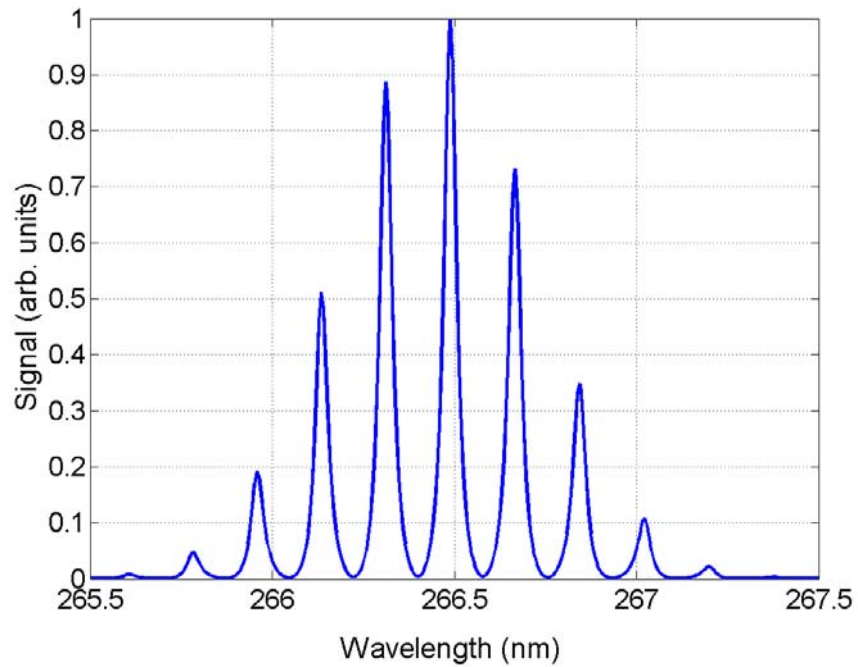


**Figure 3.7.** Calculated laser spectrum for Gaussian input ( $l=200\mu\text{m}$ )

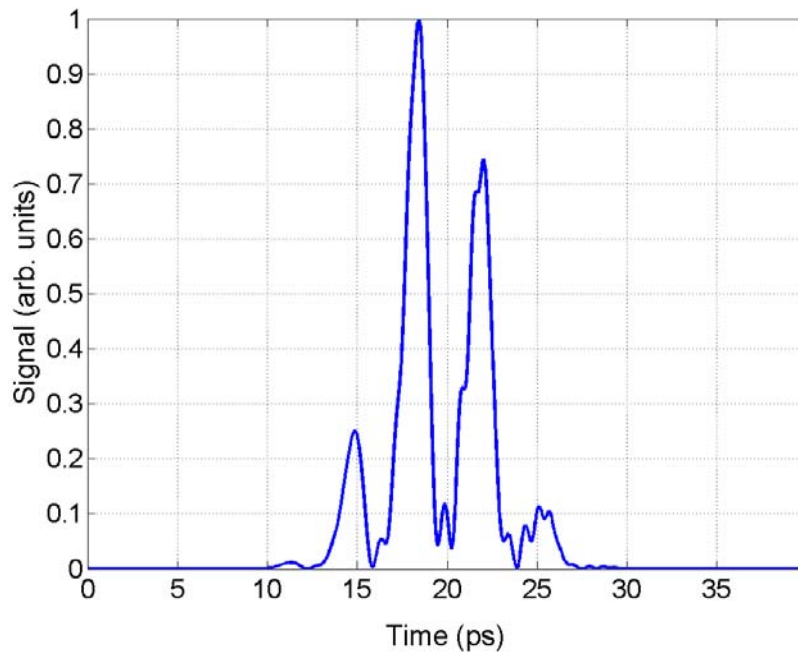


**Figure 3.8.** Calculated laser time profile based on input with Gaussian envelope. ( $l=100\mu\text{m}$ )

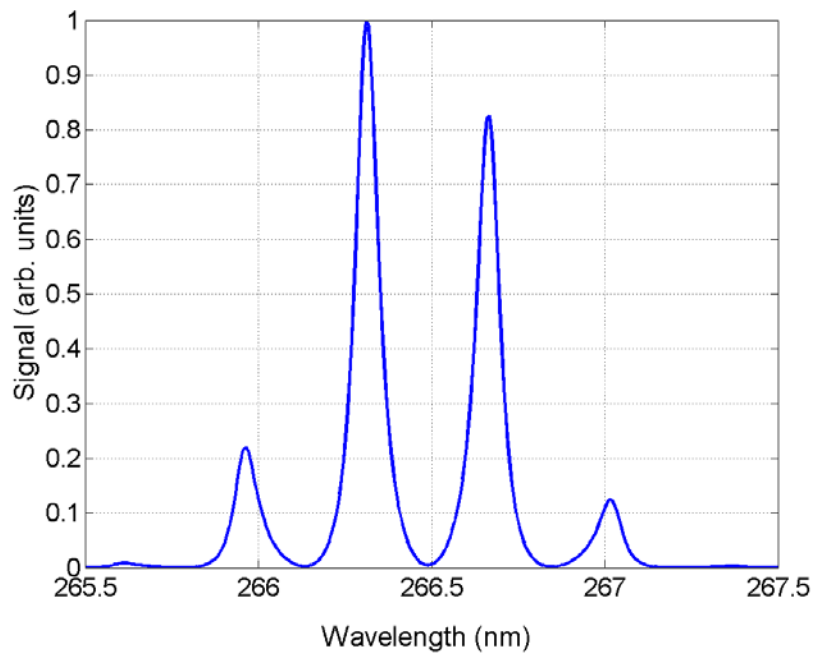


**Figure 3.9.** Calculated laser spectrum based on input with Gaussian envelope. ( $l=100\mu\text{m}$ )

qualitative behavior of the interferometer. The code used to make this calculation can be found in Appendix B.

Figures 3.6-9 demonstrate that the Fabry-Perot interferometer serves as an excellent modulator of the UV laser pulse. As mentioned earlier, this calculation was used to guide the acquisition process of the interferometer, particularly with respect to the reflectivity of the mirrors. The basic design tradeoff was that a higher reflectivity leads to a higher finesse, which leads to sharper peaks. Sharp peaks lead to a high form factor, which leads to more terahertz power. However, since any light not transmitted through the interferometer is back reflected, very little total laser power would be transmitted through a high finesse system, and low laser power translates into low charge in the electron beam. Looking back at Figure 3.2, where the total energy transmitted would be related to the integral of the spectrum multiplied by the transmittance curve, one might imagine that a significant amount of power (even for  $R=0.48$ ) would be back reflected.

As explained earlier, the longitudinal form factor is a measure of the coherence of the light generated by the electron beam. The form factor is the square of the magnitude of the Fourier Transform (i.e. power spectral density) of the density profile of the electron bunch. If the electron beam longitudinal density followed the laser profile exactly, the "form factor" of the laser pulse would indicate how much coherent enhancement of the light radiated from the electron beam could be

achieved at a given frequency. The total amount of terahertz power at a particular frequency would be related to the product of the "form factor" at that frequency and the square of the laser energy (the laser energy is related to the number of electrons in the beam). Table 3.1 lists the form factor, the laser energy normalized to the unmodulated case, and the form factor-energy squared product calculated for different values of mirror reflectance. The cavity spacing is 200 $\mu$ m, the same as that shown in Figure 3.6.

Reflectance	Form Factor	Normalized Laser Energy	FF*Energy <sup>2</sup>
0	~0	1	~0
0.1	0.12	0.55	0.035
0.2	0.19	0.44	0.036
0.3	0.20	0.37	0.027
0.4	0.19	0.31	0.018
0.5	0.16	0.25	0.010
0.6	0.12	0.20	0.005
0.7	0.08	0.005	0.002

**Table 3.1.** Calculated laser form factor, normalized laser energy, and relative measure of terahertz radiation for various mirror reflectances (R)

As can be seen in Table 3.1, it turns out that as the reflectance increases, the form factor does not necessarily go up. While examination of the spectrum indicates that the finesse in fact increases with reflectance, as expected, the reconstruction in the time domain does not necessarily yield a nice pulse train. The result is that according to this calculation, the best form factor can be achieved at a reflectance of 30%. Above this value, the total terahertz power and total laser power are predicted

to decrease. According to Table 3.1, a reflectance of 20% would optimize the system for maximum terahertz power. In addition to terahertz power, total transmitted laser energy was a primary concern, because in addition to generating terahertz light, this experiment reveals how space charge affects an electron beam pre-modulated at the cathode. Therefore, it was important to be sure that enough charge could be generated in order to clearly see the space charge effects. Optimizing for maximum laser energy clearly results in an even further reduction of the mirror reflectance.

Specifying a mirror reflectance turned out to be somewhat subjective because the way the pre-modulated electron beam would propagate was not known (hence this experiment - see further explanations in Chapter 4). It was not known how much laser power would be required to observe the space charge effects. So, it was unclear which operating point in Table 3.1 would yield maximum utility from the interferometer in terms of electron beam dynamics and terahertz experiments (for instance, it may have been possible that at 30% reflectance, there would not be enough laser energy to clearly observe how the space charge would affect the electron beam). Additionally, while the general relationships described in Table 3.1 were known, there was no experimental data to use as a comparison with the model (the previous calculations suggested an optimum value near 55%, but later comparison with experimental data led to the discovery that the model could be better implemented).

### 3.2. Measurements with the Fabry-Perot Interferometer

A mirror with a reflectance of 55% was chosen, hoping that it would strike a good balance between the form factor and total laser energy. Unfortunately (or as it turns out for the details of this situation, fortunately), the manufacturer thought the request was for 50%, and actually even undershot that with a measured reflectivity of 48%. Now hindsight (i.e. Table 3.1) indicates that a reflectance near 30% may have been a slightly better choice. Figure 3.10 shows a top and side view of the interferometer plates mounted inside a Burleigh RC-110 Fabry-Perot system.

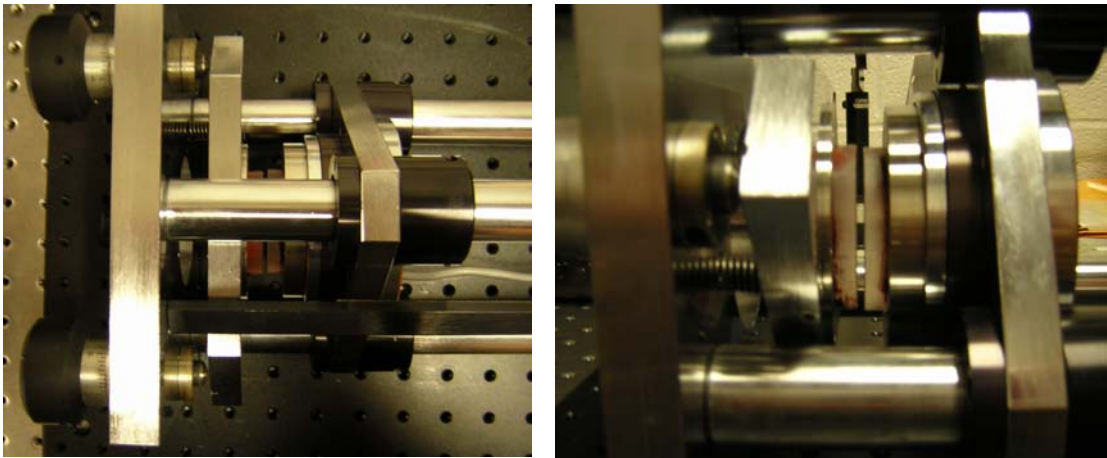


**Figure 3.10.** (Left) Top view of Fabry-Perot interferometer with UV mirrors mounted. (Right) Side view.

As it turns out, the UV laser pulse incident on the interferometer is not smooth, as expected, and as is shown in Figure 3.3. In order to compare

experimental data with the theoretical model, the measured unmodulated laser pulse was used as an input. So, another example of a measured input pulse envelope is shown in Figure 3.11. This pulse envelope is multiplied by the term containing the carrier frequency and the chirp. The parameter  $\beta$  was optimized by minimizing the mean square error between the calculated and measured spectrum. The best value for  $\beta$  was calculated to be  $-1.2893 \times 10^{24}$  radians/sec<sup>2</sup>, which yielded a correlation coefficient of 0.9843. Figure 3.12 shows the calculated and measured unmodulated laser spectrum using this optimized value of  $\beta$ .

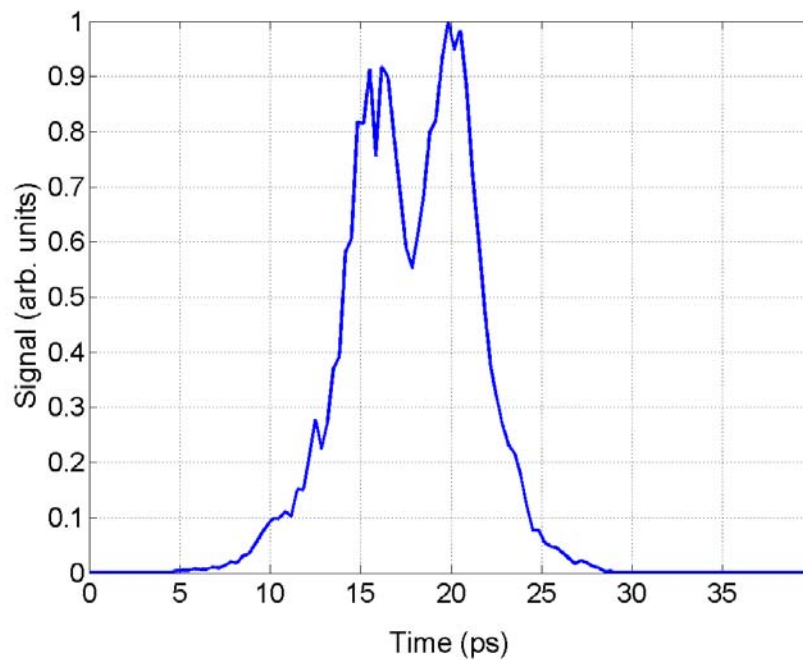


**Figure 3.11.** Cross-correlation of UV laser pulse. When modulated with the carrier frequency, this is used as the input to the model.

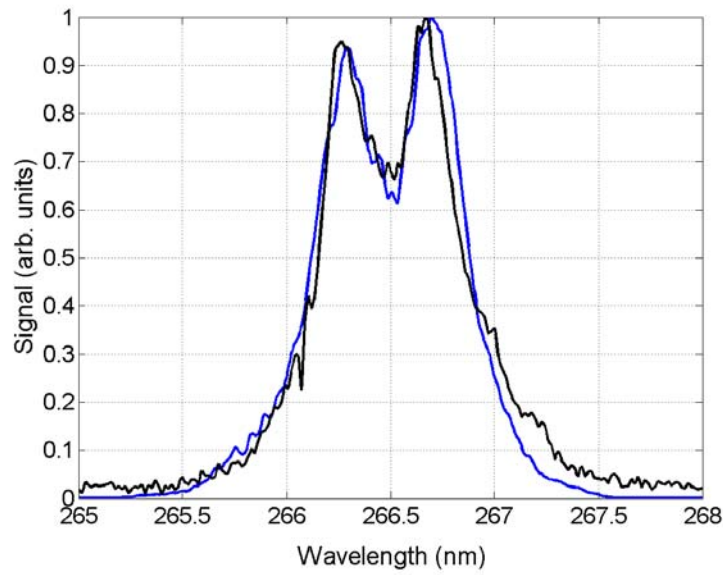


**Figure 3.12.** (Black) Measured unmodulated UV spectrum (Blue) Calculated UV spectrum based on model

Unfortunately, it was not possible to easily measure the cavity spacing experimentally due to the construction of the interferometer and the small distances involved (tens to hundreds of micrometers). Therefore, the cavity spacing,  $d$ , was also optimized by minimizing the mean square error in order to best match the experimental data. The optimum cavity spacing was determined to be 259.8  $\mu\text{m}$ , and the correlation coefficient with the measured laser profile is 0.81. Figures 3.13 and 3.14 show a comparison of experimental and calculated laser pulse trains delivered to the cathode for two different cases. In the first case, the optimum cavity spacing was calculated to be 259.8  $\mu\text{m}$ , and the correlation coefficient with respect to the measured laser pulse is 0.8132. In the second case, the optimum cavity spacing was 206.6  $\mu\text{m}$ , and the correlation coefficient was 0.9143.

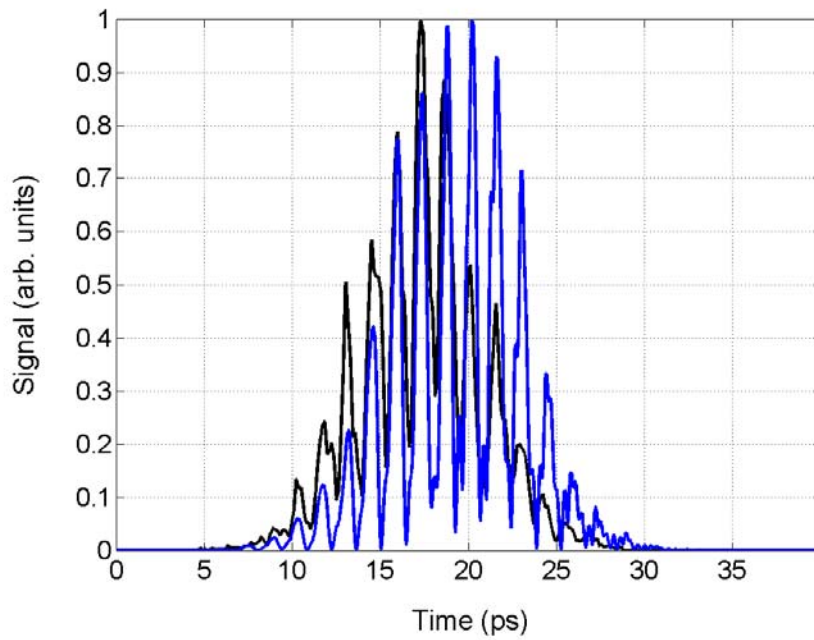


**Figure 3.13.** Calculated (Blue) and measured (Black) UV laser profiles for a cavity spacing of 259.8  $\mu\text{m}$ .

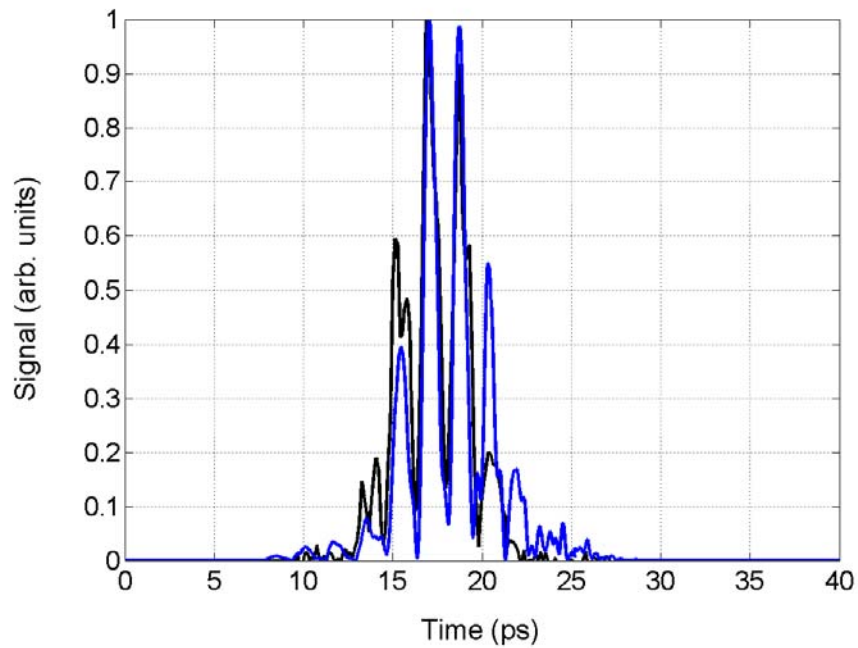


**Figure 3.14.** Calculated (Blue) and measured (Black) UV laser profiles for a cavity spacing of 206.6  $\mu\text{m}$ .

Much of the previous discussion included references to the laser "form-factor". Rather than present all of the various cross correlation measurements here, Figure 3.15 represents the form factor (or power spectral density) as a function of frequency for selected experimentally measured UV pulses that represent the range of laser tunability achieved in this experiment. Additional cross correlation measurements will be presented together with their corresponding electron beam and terahertz data in later sections.

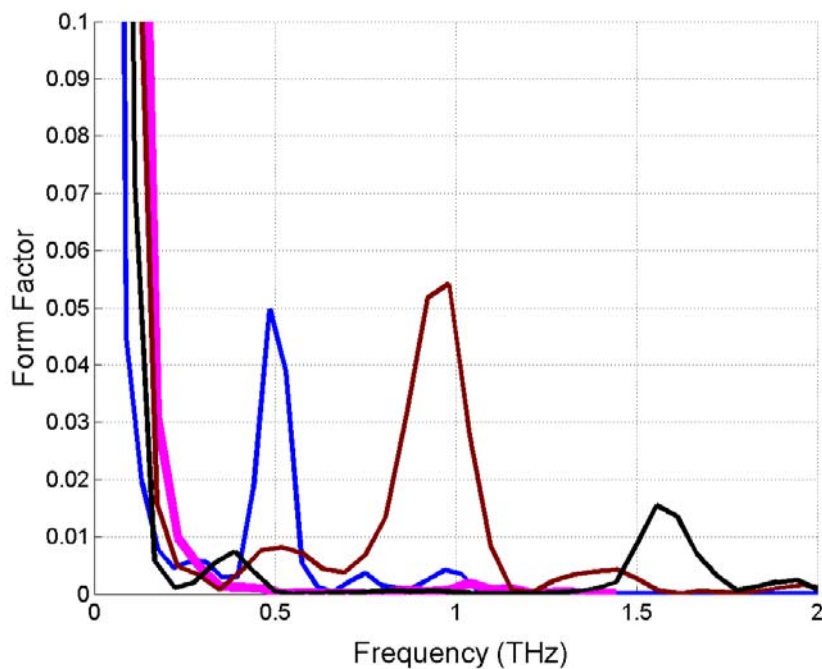


**Figure 3.15.** "Form Factor" for various UV drive laser pulses at different cavity spacing. The magenta line is the form factor of an unmodulated pulse.

Varying the cavity length in the interferometer causes the peak frequency to shift. If the electron beam profile matched the laser profile exactly, this is the form factor that one uses to calculate the total terahertz energy as presented in Chapter 1. As Figure 3.15 shows, the modulation frequency was tunable between ~0.5 terahertz and ~1.6 terahertz. When the laser is modulated at high frequencies, the form factor begins to fall off. This is because as the cavity length gets longer (the free spectral range gets shorter and the modulation frequency gets higher) the amount of pulse overlap inside the cavity is reduced. Therefore, the interference effects of the Fabry-Perot system are reduced and the effective finesse will drop, which will also lead to a drop in the form factor. The thick magenta line represents the power spectral density for an unmodulated laser profile. Note that while the form factor is still small at the peak frequencies, remember that it is leveraging an  $N^2$  term, which is quite large.

One of the main thrusts of this experiment was to determine whether or not the electron beam modulation could be maintained through acceleration. As is discussed in Chapter 4, the electron beam profile does in fact change, primarily due to factors such as RF velocity bunching and space charge forces. The RF velocity bunching generally causes an increase in the modulation frequency, but the space charge forces cause the density modulation to wash out. Therefore, the expected electron beam form factors will likely peak at higher frequencies than that shown in

Fig. 3.15, but the peak value will likely have an upper bound determined by the laser profile form factor.

The UV laser energy transmitted through the interferometer was sufficient to conduct an experiment to probe longitudinal space charge effects in a pre-modulated electron beam. The system was able to deliver tens of microjoules of UV power to the cathode, resulting in bunch trains containing up to ~200 pC total charge.

## Chapter 4: Electron Beam Dynamics

One of the main research questions addressed during this project was whether or not the longitudinal density distribution of an electron beam pre-modulated at the cathode could be sustained through acceleration to relativistic energy. This question was addressed both numerically and experimentally. At the Source Development Laboratory, the drive laser profiles described above were used to create a pre-modulated electron beam that was accelerated through the linac at the SDL. After acceleration, the longitudinal bunch profile of the electron beam was measured. Simulations of this experiment were conducted with the code PARMELA. This chapter focuses specifically on electron beam pre-modulation, while the terahertz radiation from these beams is discussed in Chapter 5.

### *4.1 Electron Beam Simulations*

Numerical simulations were used in order to predict how the pre-modulated electron beam longitudinal profiles would change as the beam was accelerated. The primary simulation code used is called PARMELA, which stands for "Phase and Radial Motion in Electron Linear Accelerators." As is in the case with all simulators, only the physical principles programmed by the authors are included. This package

does not include mechanisms for radiation emission. However, the state of the electron beam is easy to obtain at any point in the accelerator simulation (whereas experiments tend to be very under-diagnosed). Additionally, simulations can be used to explore a domain that is not readily accessed experimentally.

The PARMELA simulations use the experimentally achieved laser profiles as initial electron beam longitudinal distributions. The model includes the electron gun and the solenoid used for emittance compensation, as well as the first accelerating section, which brings the electron beam to approximately 34 MeV. The electron gun is about 14 cm long, while the entire simulated system is approximately 4 m long. The model used in the PARMELA simulations is the same as the one currently being developed and used for other experiments at the Source Development Laboratory<sup>50</sup>; the primary difference is the modulated input distributions.

Four different laser profiles were converted into a particle distribution that could be used effectively with PARMELA, one unmodulated case, and three different examples of pre-modulation. In each case, 30,000 particles were used for various levels of charge, ranging from 20 pC to 1 nC. The space charge mesh is divided into 500 mesh intervals, though the size of the longitudinal mesh changes size dynamically as the beam is accelerated. Significantly increasing the number of mesh intervals, time step, or number of particles dramatically increases the amount of time to complete the simulation to the point of impracticality. Tests against short runs with finer parameters indicate that this level of refinement is acceptable. As in

the experiment, the electron beam was not injected at the point of maximum RF power in the gun; rather, the electron beam was injected 30 degrees off the crest, which provides some longitudinal focusing due to the slope of the RF field. In fact, varying the injection phase is another way to tune the modulation frequency. Although this was not carried out during the experimental phase, the simulations clearly show this is possible, and the effect of RF compression is well known<sup>51,52</sup>.

In order to run the simulations, many assumptions were made, including the initial spot size on the cathode, the solenoid current used for emittance compensation, and the peak electric field inside the electron gun. As a result, although the simulation results are compared directly with the experimental data, it is important to remember that the simulations represent an approximate model of the real accelerator and initial beam conditions. This section discusses some of the general trends that the simulations predict. Specific results that compare each of the laser profiles with their corresponding experimental cases are discussed in section 4.3. Figure 4.1 shows the four initial electron longitudinal profiles that were used for this part of the analysis. All of the simulation results will be shown in panels of four images that correspond in location to the initial electron beam longitudinal distributions shown in Figure 4.1. Where space allows, the initial laser distribution will be shown as a small subplot inside each graph. However, the simulation results will always be displayed in the same order as Figure 4.1.

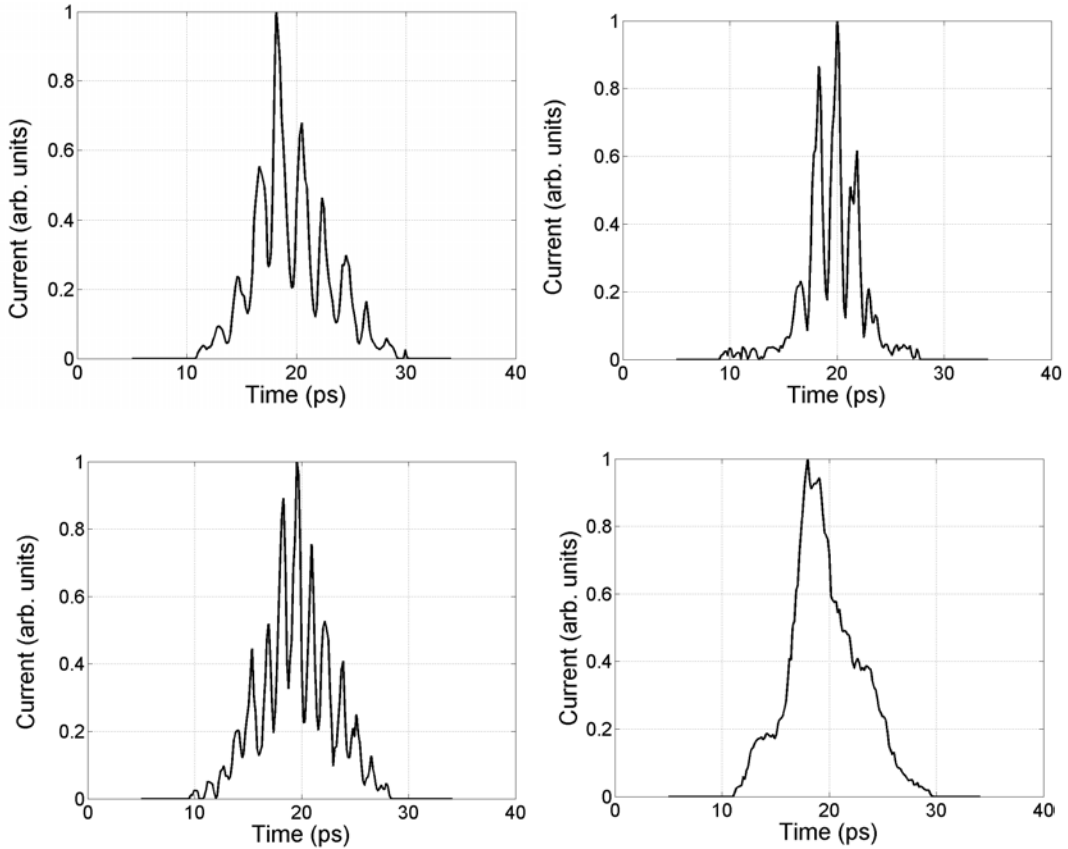


**Figure 4.1.** Examples of an electron beam longitudinal profiles used as an input distributions for the PARMELA simulations.

As expected, varying the charge caused varying levels of washout for the modulation in the electron beam. Figure 4.2 shows the electron beam longitudinal profile at 20 pC after each initial distribution had been accelerated to 34 MeV, at the end of the first accelerating section. For comparison, Figure 4.3 shows the same profiles for 200 pC. From these figures, it is clear that the amount of charge in the beam has a strong effect on the longitudinal profile of the accelerated electron bunch.

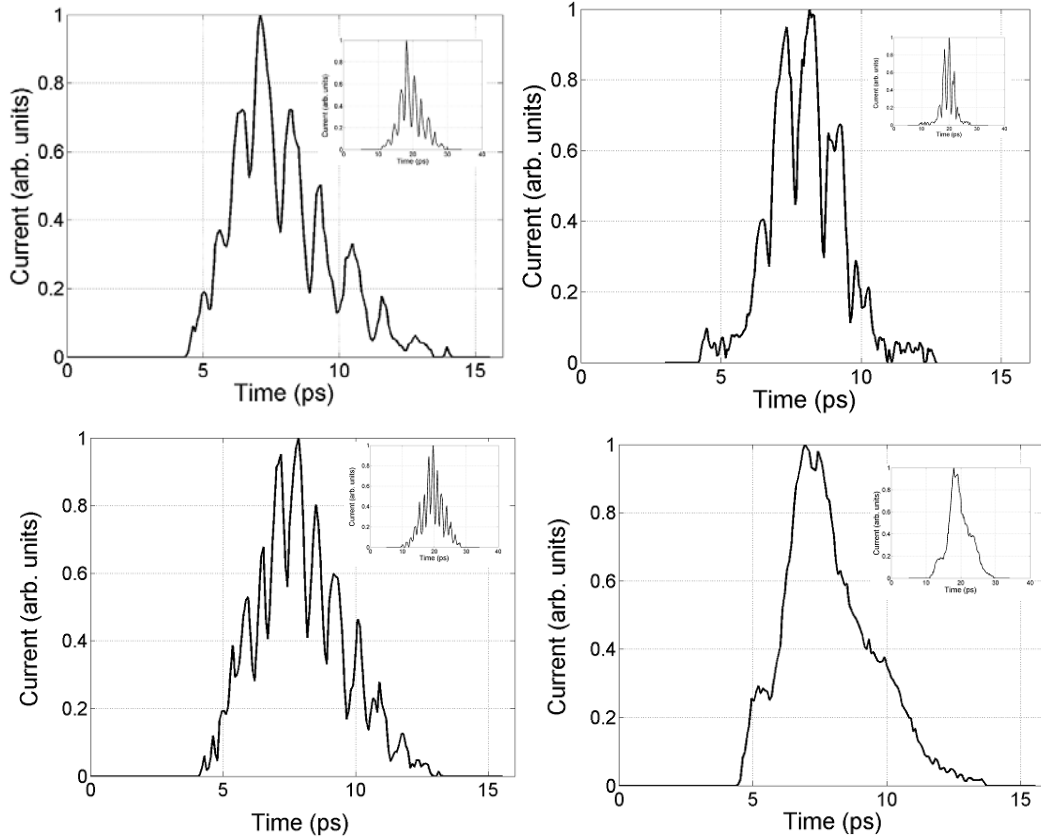


**Figure 4.2.** Electron beam longitudinal profiles for 20 pC after acceleration to 34 MeV. Note the difference in the time scale compared to the initial distribution - the compression is due to off crest injection.

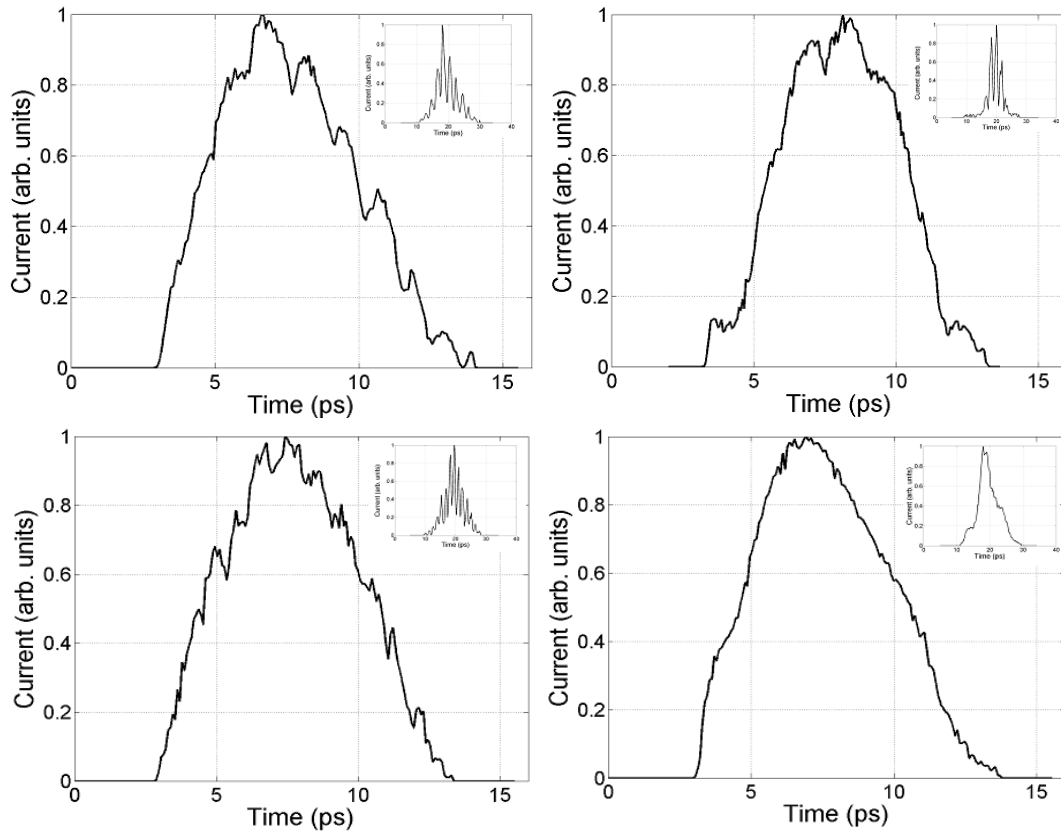


**Figure 4.3.** Electron beam longitudinal profiles for 200 pC bunches, after acceleration to 34 MeV. Note the difference in the time scale compared to the initial distribution due to the RF compression.

Generally speaking, at low charge, the initial modulation on the beam survives the acceleration nearly intact. At higher charge, the modulation washes out, causing a reduction in the form factor. Figure 4.4 shows how the simulations predict the value of the form factor at its peak frequency (ignoring the low frequency component) to change as a function of charge for the input distribution shown in Figure 4.1 after the beam has been accelerated through the electron gun and first accelerating section to 34 MeV.

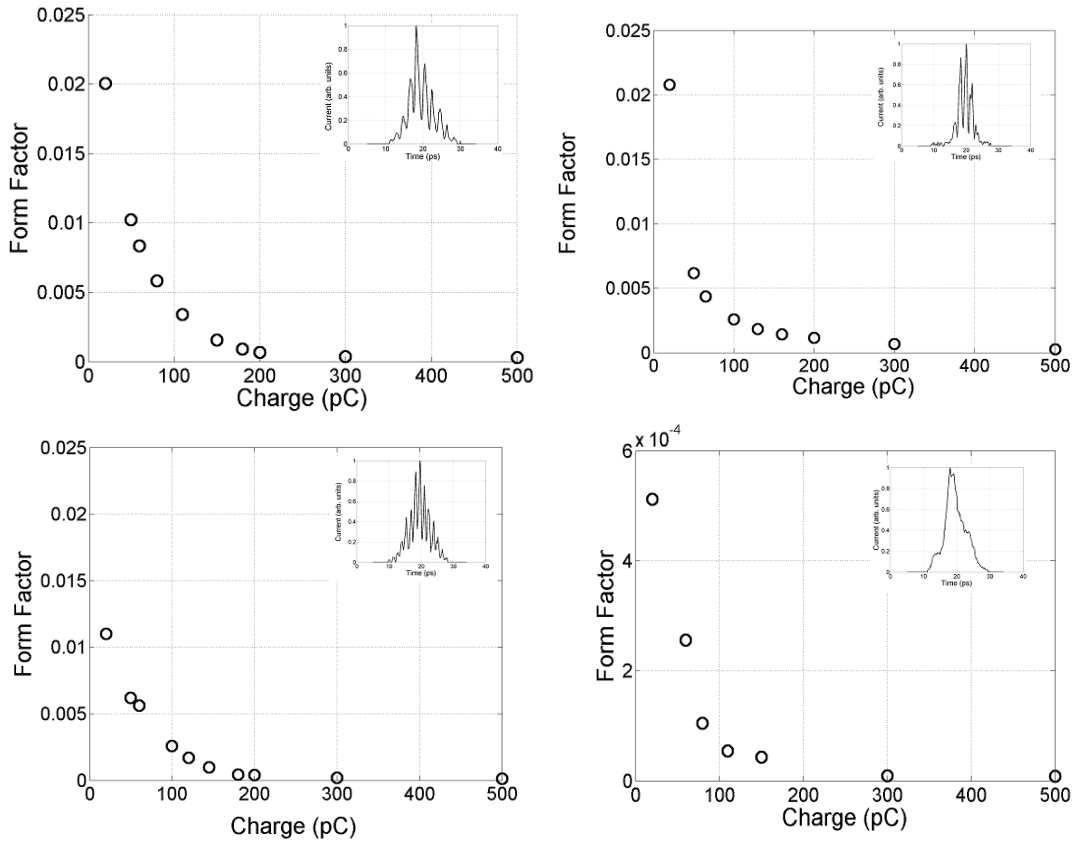


**Figure 4.4.** Peak form factor as a function of charge for the input distributions shown in Figure 4.1. In the modulated cases, the form factor value is taken at the peak frequency. For comparison, the form factor for the unmodulated case is taken at 1 terahertz.

As can be seen in Figure 4.4, the form factor falls very quickly as charge increases. This is typical for all of the modulated electron beams. In Chapter 1, it was noted that the total energy from a coherent bunch of electrons is proportional to  $f(\omega)N^2$ , where  $N$  is the number of electrons in the bunch train, and  $f(\omega)$  is the form factor. In many experiments that test for coherent radiation from an electron beam,  $N$  is varied, and the radiated energy is expected to have a quadratic dependence on

charge. In this case, since the form factor should really be given by  $f(\omega, N)$ , this is not necessarily the case for this experiment. It is important to note that the experimentally achievable range of charge falls between 20 pC and 180 pC - which is the region where the form factor varies the fastest. This issue contributes to the counter-intuitive situation where increasing the charge in the beam can actually reduce the total radiated power. The implications of this will be explored further in Chapter 5.

It also turns out that the frequency at which the maximum form factor occurs also varies as a function of charge. Since higher charge causes the beam to expand, the frequency of modulation effectively drops. Figure 4.5 shows how the peak frequency changes as a function of charge. Since discussing the modulation frequency of an unmodulated beam does not have much meaning, the full width half maximum (FWHM) of the electron beam is plotted as a function of charge for the baseline case to indicate beam expansion. In contrast to the modulation frequency, the pulse width varies directly with charge.

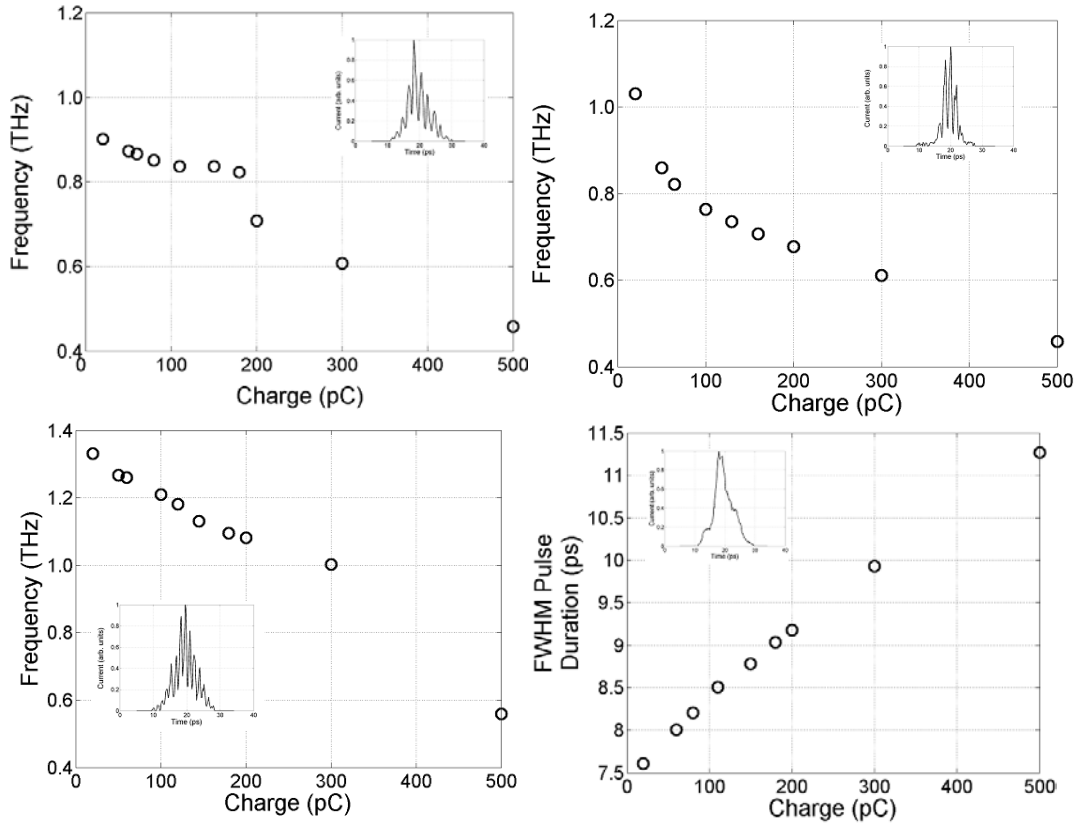


**Figure 4.5.** Beam modulation frequency as a function of charge after acceleration to 34 MeV. The baseline case reports pulse duration as a function of charge.

Another look at the same phenomenon is taken in Figure 4.6. In this case, instead of plotting the form factor and frequency as a function of charge, the entire form factor as a function of frequency is plotted in the same graph for a few of the selected cases. In this Figure, it is more difficult to see exactly how the form factor varies as a function of charge, but it is easier to see an overall picture of how the power spectral density changes.

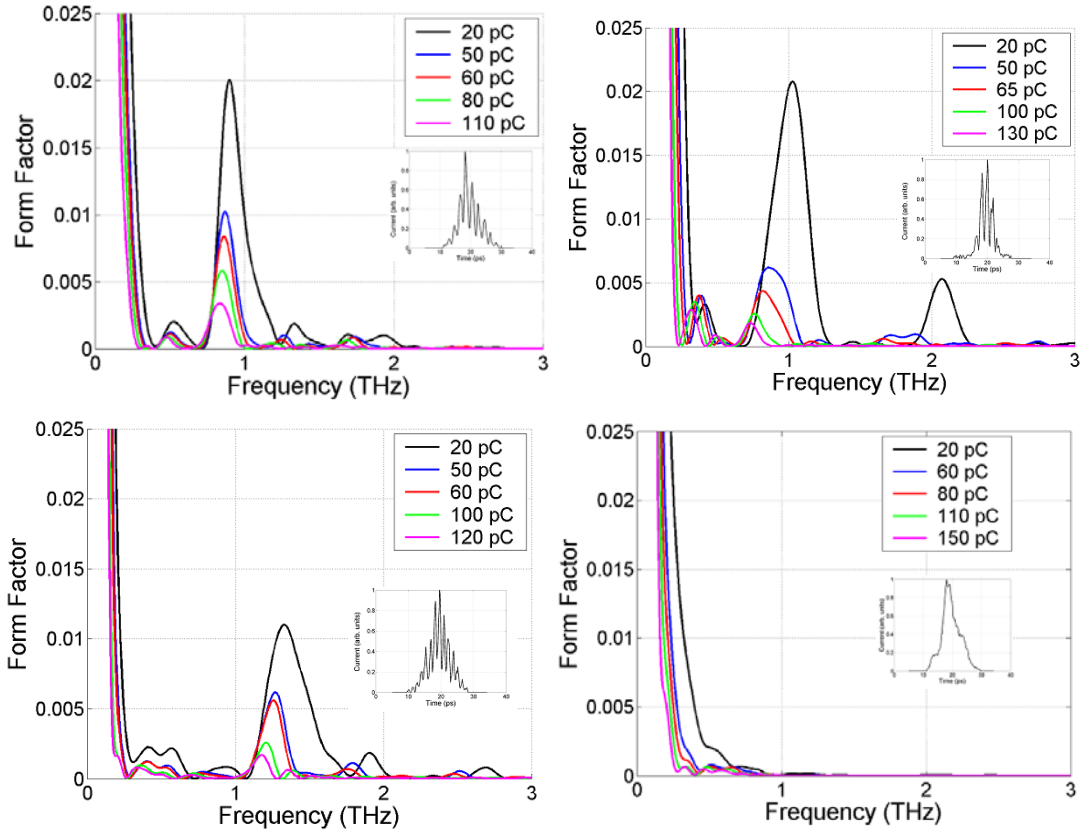


**Figure 4.6.** Form factor of the longitudinal profile of the electron beam for each initial distribution after acceleration to 34 MeV.

In a realistic implementation of this system as a terahertz source, the goal would be to build a compact device, rather than a large accelerator. In fact, a terahertz source based on this technology would likely use the electron gun by itself, with no additional accelerating sections attached. At the exit from the electron gun, the beam energy is about 4 MeV.

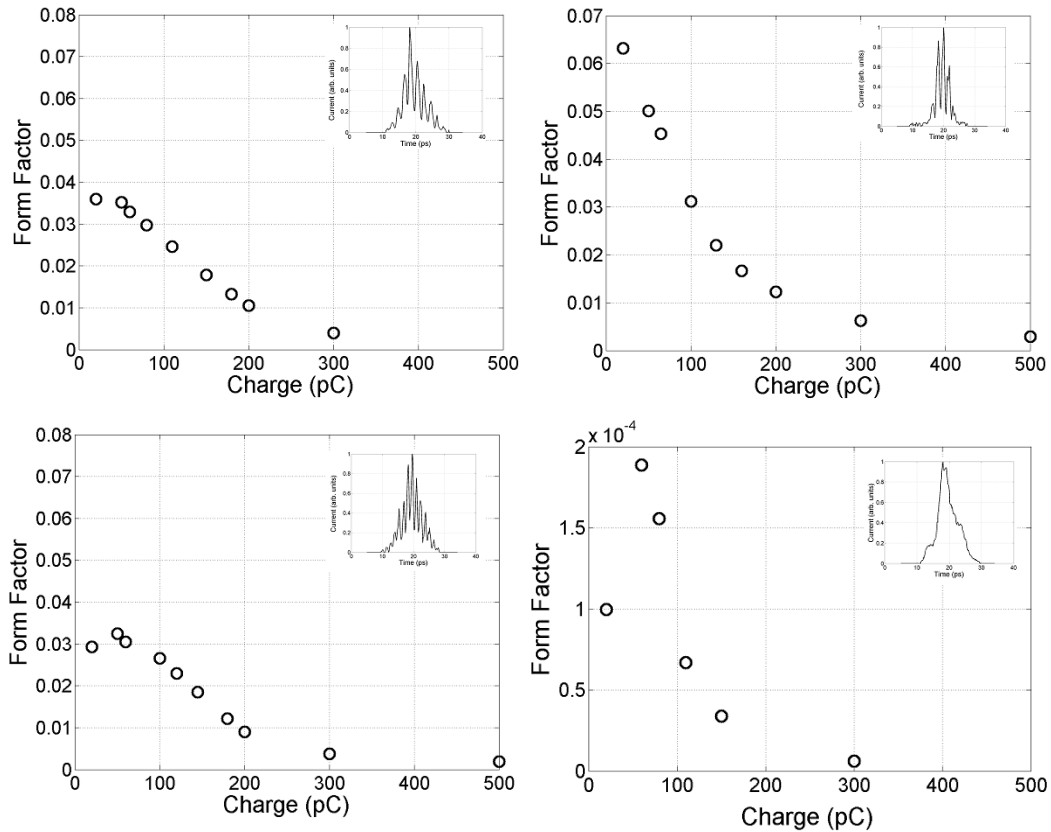


**Figure 4.7.** Peak form factor values corresponding to the four initial conditions at the exit from the electron gun at 4 MeV.

Although simulations are not perfect models of actual experiments, the ability to diagnose the state of the electron beam at any point in the beamline is a major advantage over typical experimental equipment. While the experiment conducted for this research did not have longitudinal diagnostics near the electron gun, the simulation has the ability to provide information about the state of the electron beam in this region. Taking advantage of that capability, Figure 4.7 shows the form factor for each of the electron beam longitudinal distributions after they

have been accelerated to the exit of the electron gun. In general, the form factor for all cases is several times larger than those found after the beam has been accelerated. This indicates a further advantage for a compact source, in that the form factor, and therefore the spectral brightness, in such a system will benefit over that of a larger system. Figure 4.8 also shows how the peak frequency changes as a function of charge at the electron gun exit. Figure 4.9 shows the plot of the entire form factor as a function of frequency at various levels of charge.

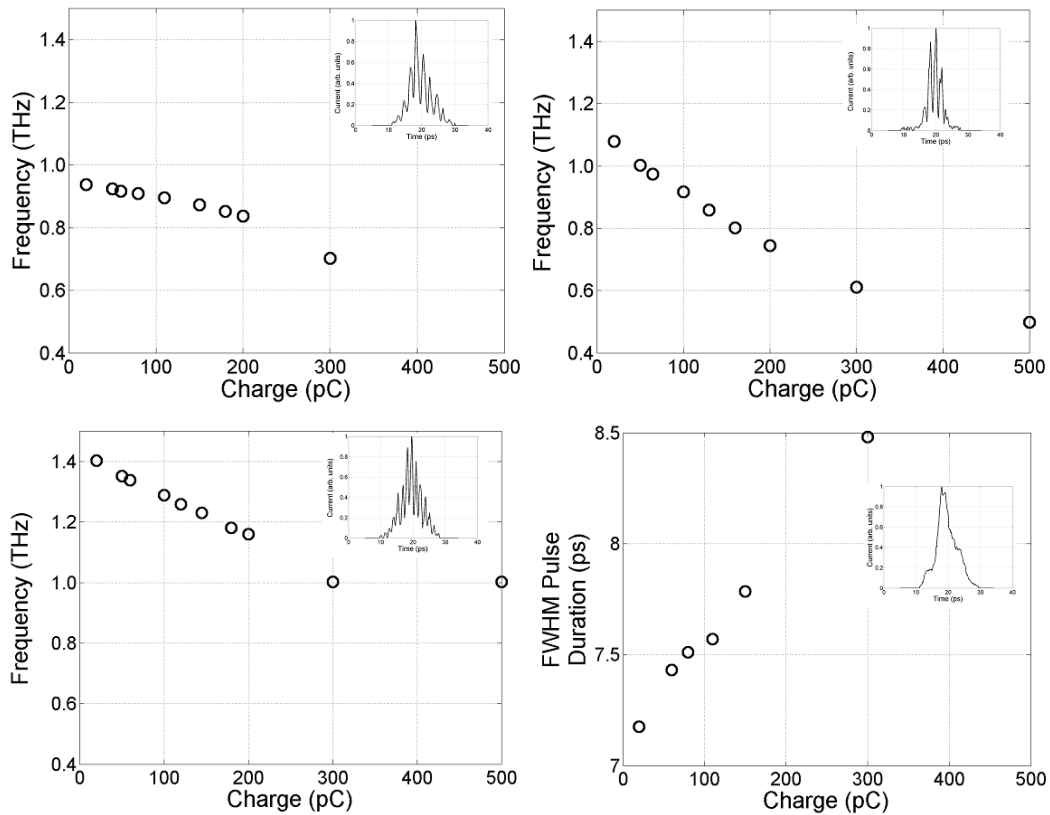


**Figure 4.8.** Beam modulation frequency as a function of charge after acceleration to 4 MeV at the electron gun exit. The baseline case reports pulse duration as a function of charge.

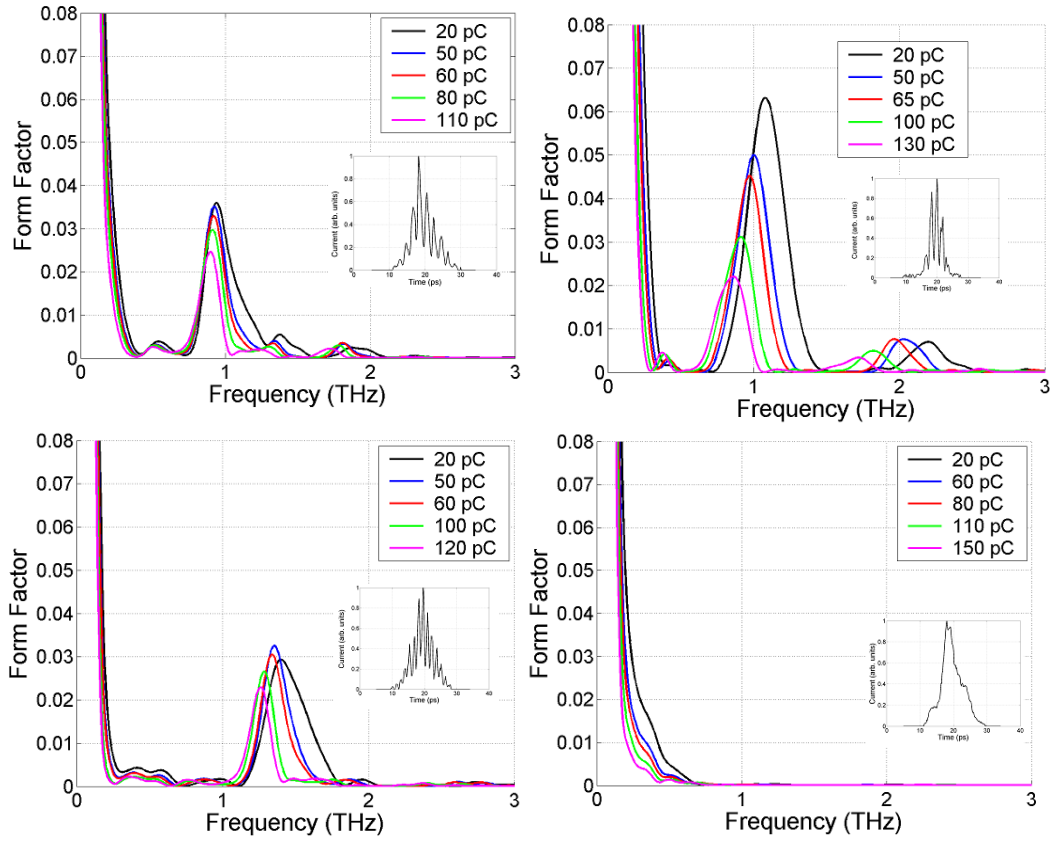


**Figure 4.9.** Form factor of the longitudinal profile of the electron beam for each initial distribution after acceleration to 4 MeV.

Noting that the longitudinal profile of the electron beam is different at the gun exit compared to the end of the first accelerating section, it is interesting to look at how the modulation changes as a function of  $z$  as the beam travels through the accelerator. Even after acceleration to relativistic energies, the pre-modulation imposed on the electron beam continues to wash out. As mentioned, this is an extremely important point for a compact terahertz source; higher form factors at

higher charges may be available to compact devices since the electron beam modulation does not have as much of a chance to be diminished. Figure 4.10 shows how the peak form factor value changes as a function of  $z$  at various levels of charge for each of the initial electron beam distributions.

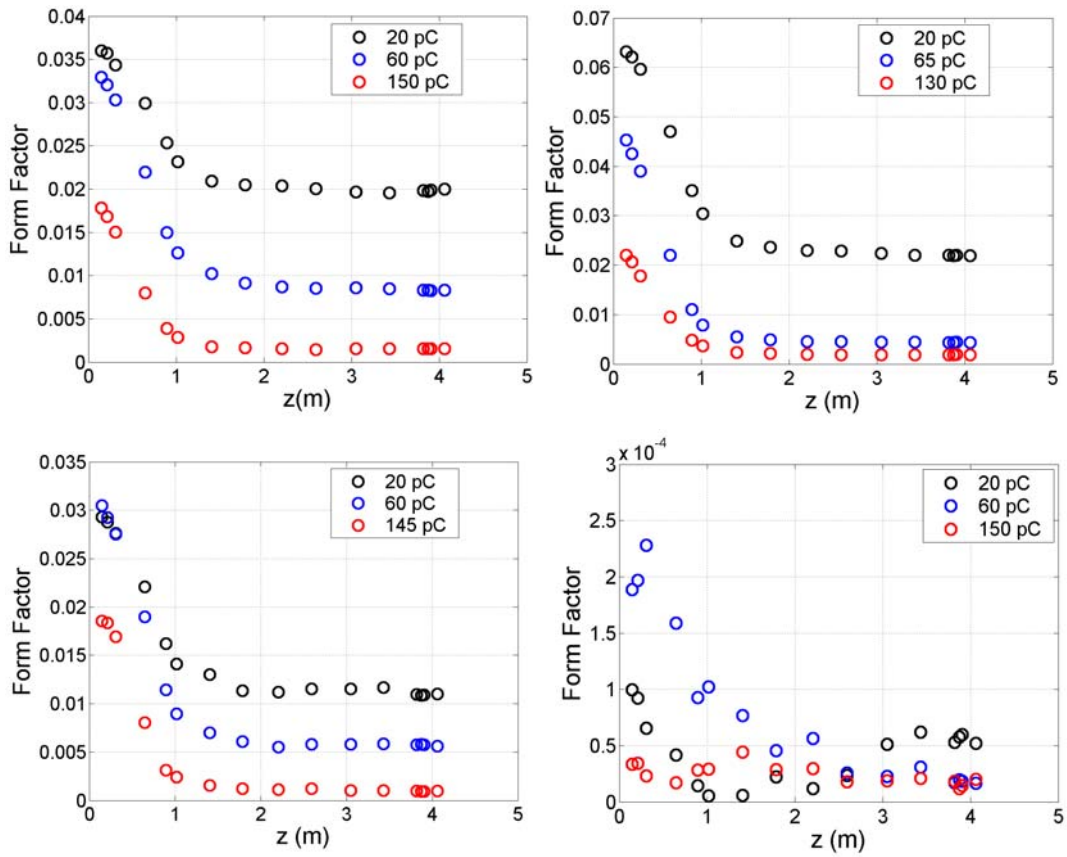


**Figure 4.10.** Form factor as a function of  $z$  for each of the electron beam longitudinal profiles.

The form factors for the modulated cases seem to stop falling near 1.4 m when the beam is at approximately 9 MeV. It is not unexpected that this should

occur, since the space charge forces decrease with increasing energy. It is also interesting to note there is a relatively large drift section at the gun exit prior to the first accelerating section where the modulation can be affected by space charge forces. The form factor values for the baseline case are not as consistent as the others. A closer look at the baseline form factor, in Figure 4.11, in the region of interest explains why.

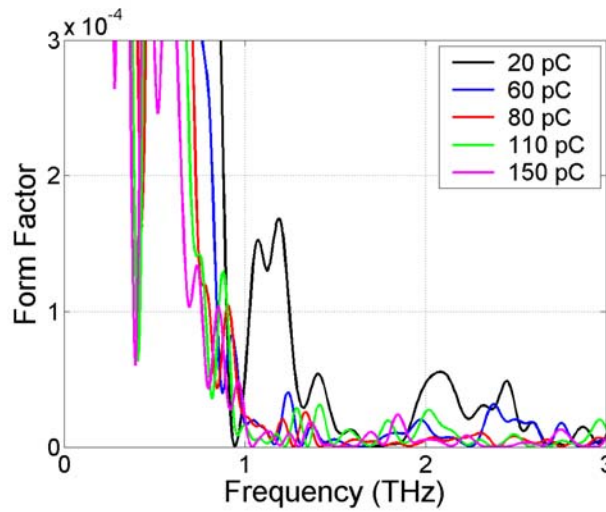


**Figure 4.11.** Form factor of the unmodulated case for various amounts of charge.

If the unmodulated case were an ideal Gaussian, its form factor would have a smooth Gaussian tail as well (the Fourier transform of a Gaussian is also a Gaussian), and would drop very quickly increasing pulse width (which increases with  $z$ ). For comparison, the longitudinal form factor for a Gaussian is given theoretically<sup>53</sup> by

$$f(\omega) = e^{-\left(\frac{\omega \cos \theta \sigma_z}{c}\right)^2} \quad (4.1)$$

where  $c$  is the speed of light,  $\theta$  is the angle of observation, and  $\sigma_z$  is the standard deviation of the Gaussian bunch. The form factor for an 8 ps bunch at 1 terahertz is very nearly zero. Figure 4.12 shows how the modulation frequency shifts as a function of  $z$ .

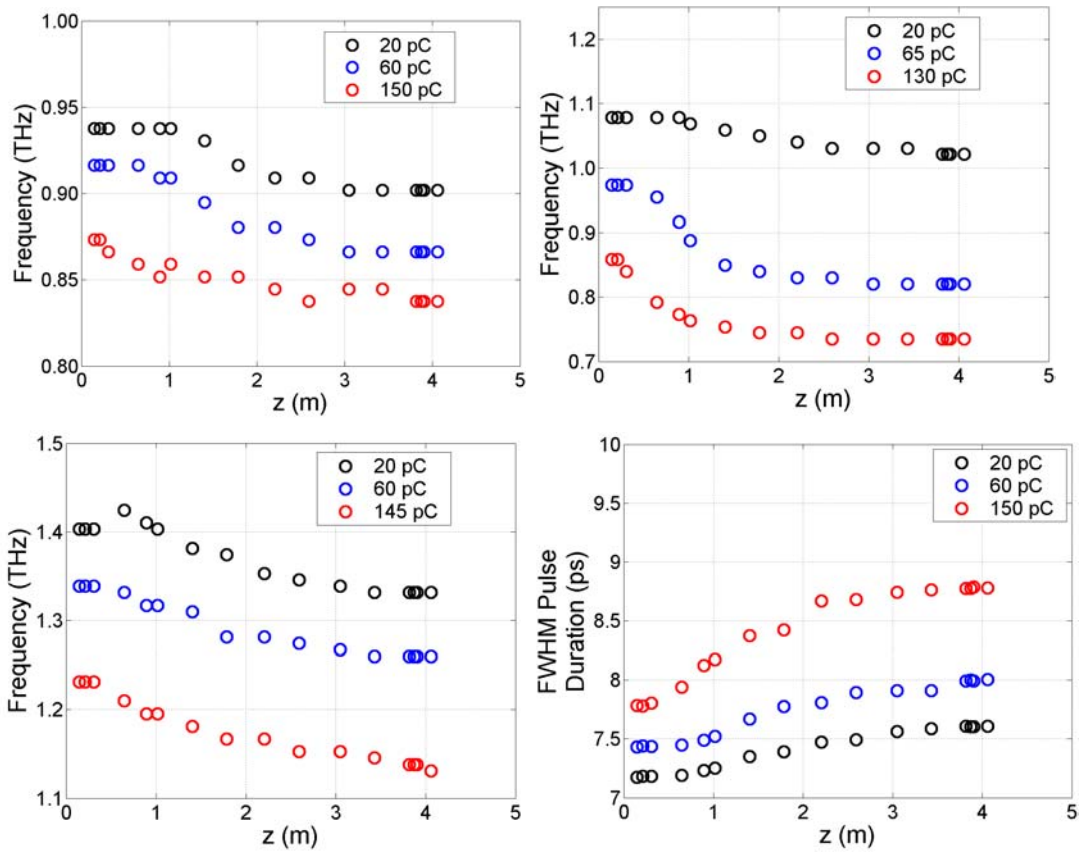


**Figure 4.12.** Peak frequency as a function of  $z$ . The baseline plot shows the FWHM pulse duration as a function of  $z$ .

Finally, Figure 4.13 shows the results of a simulation with the upper left initial longitudinal profile, but is injected at the peak of the RF field rather than 30

degrees off crest. This beam is accelerated to a slightly higher energy, but does not experience the compression seen by beams that are injected off crest. The result of changing the injection phase is essentially a trade off between form factor peak value and modulation frequency. When the beam is injected at the crest of the RF, the form factor values remain higher at all charge levels compared to the case of off crest injection. However, since there is no compression due to off crest acceleration, the frequency of modulation is significantly lower. However, similar to changing the amount of charge in the beam, this effect could be used as a feature; the modulation frequency could be easily tuned by varying the RF injection phase.

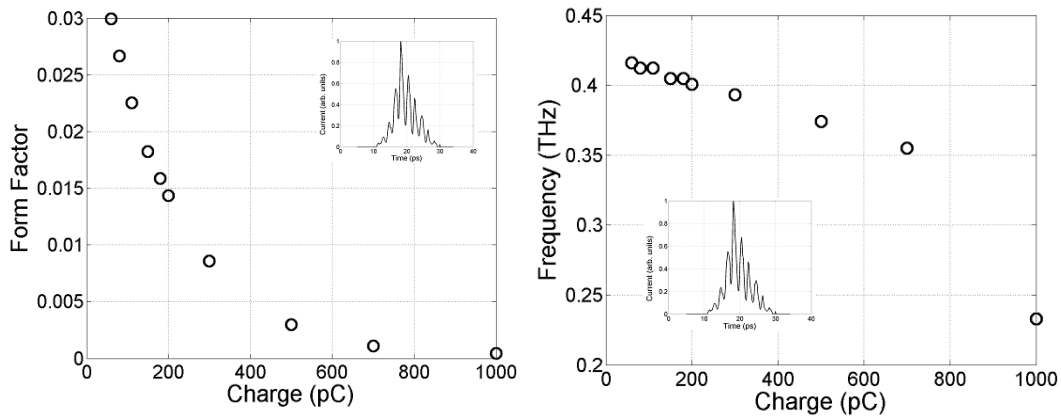


**Figure 4.13.** Form factor and peak modulation frequency as a function of charge for the initial distribution shown in the upper left panel of the previous simulations. In this case, the electron beam is injected at the peak of the RF field instead of 30 degrees off crest.

Overall the PARMELA simulations indicate that electron beam pre-modulation can be maintained with varying levels of success through acceleration depending on the initial conditions. In general, as charge goes up, the peak modulation frequency and form factor value both shift down. In fact, the level of charge could be used as an additional way to tune terahertz radiation in an application. For pre-bunched electron beams, the modulation seems to fill in, reducing the form factor until the beam reaches approximately 9 MeV. However, the beam continues to expand as a whole throughout the simulation. The simulations predict significant enhancement in the longitudinal form factor near terahertz frequencies when the beam is properly pre-modulated, which should lead to corresponding enhancements in the terahertz radiation that is generated in the experiment.

#### *4.2. Longitudinal Profile Measurement Techniques*

Electron beams are often described in terms of phase space, a six dimensional coordinate system that describes the  $i^{\text{th}}$  particle's position as  $(x_i, y_i, z_i)$  and momentum as  $(p_{x_i}, p_{y_i}, p_{z_i})$ <sup>54</sup>. In this particular work, the focus is on the longitudinal phase space, describing the beam in terms of  $(z_i, \Delta E)$ , using an energy coordinate instead of momentum. The energy spectrum is found by projecting the phase space onto the energy coordinate, and is done experimentally with a magnetic spectrometer.

Measuring the longitudinal density distribution, or the projection of the longitudinal phase space onto the position coordinate, is more difficult to do experimentally when the electron beam is so short (i.e. sub-picosecond). The measurement techniques used to measure the longitudinal profile of the electron beam work by manipulating the phase space so that a difficult measurement (the longitudinal profile) can be inferred from a measurement that is possible to make (an energy spectrum).

Two techniques were used to measure the longitudinal profile of the accelerated bunch train experimentally, both of which are related. The first is based on the RF zero-phasing technique<sup>55</sup>. The idea is to introduce an energy spread on the electron beam by passing it through an accelerator cavity while the field is ramping rapidly up or down. This occurs near the "zero-crossing" of the RF field used to accelerate the electrons, and it also happens to be nearly linear; if the length of the electron beam is considered in terms of degrees of RF phase at 2.856 GHz, a 5 picosecond electron bunch corresponds to approximately 5 degrees of phase. In the small angle approximation, a sin wave is still nearly linear out to 5 degrees. This causes a linear correspondence between time and energy. This is known as a linear chirp, and is really the same conceptually as that described in Chapter 3. If the center of the electron beam arrives at the zero crossing, the head of the beam will have a larger energy, the tail of the beam will have a smaller energy, and the energy at the center of the beam will remain unchanged. If this electron beam is then passed

through a dipole magnetic energy spectrometer, the energy spectrum can be recorded on a screen. The energy axis can easily be converted to the time axis, allowing the longitudinal profile to be observed. The SDL uses the two accelerating sections after the bunch compressor to implement the chirp. The time resolution of this technique is basically limited by the initial energy spread on the beam, the total beam energy, and the time derivative of the electric field in the cavity (the chirp). At the SDL, the time resolution is approximately 8 fs<sup>56</sup>. Using the RF zero phasing method involves taking three images of the beam. Two images at the energy spectrometer can be taken when the beam arrives at the upslope or the downslope of the RF field. A third image is taken with the RF input off, which reveals the intrinsic energy spread of the beam. A diagram of the proper phasing for this technique is shown in Figure 4.14.

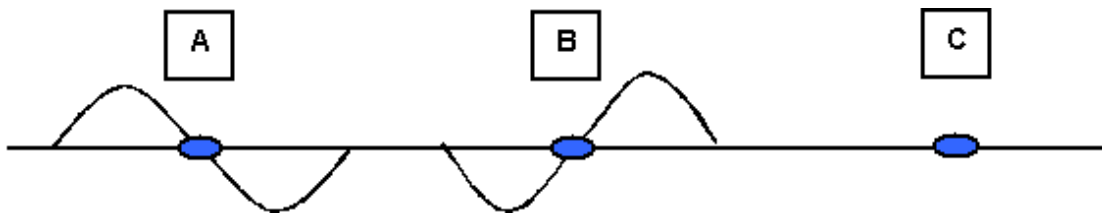


**Figure 4.14.** The RF Zero Phasing Technique. Electron beam arrives when there is (A) an RF Upslope (B) an RF Downslope (C) no RF signal.

There are some differences expected between the images taken in case (A) and in case (B). Assuming there is some energy spread inherent on the beam such that the head is at a higher energy than the tail, case (A) results in expansion of the resulting image because the total energy spread is magnified. In case (B) the

inherent energy spread is first neutralized and then reversed, which results in a different image at the detector.

In order to properly indicate how this technique works (and more importantly, why and when it can sometimes fail), it is important to illustrate this method using a "thought experiment". This follows essentially the same argument made by Huang and Shaftan<sup>57</sup> and Loos<sup>58</sup>, but is specifically applied to this experiment. Imagine in the longitudinal  $z$ - $\Delta E$  space, an electron beam that is traveling down the accelerator might look like that shown in Figure 4.15. The longitudinal coordinate is referred to simply as "x" in order to emphasize that it could represent time, distance, or phase. The "real" density distribution for this arbitrary phase space is found by projecting the phase space onto the longitudinal coordinate, and is shown next to the phase space diagram.

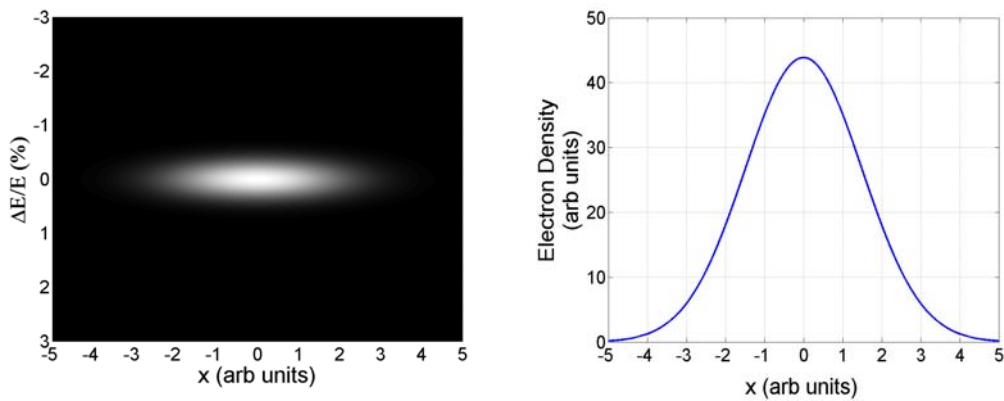


**Figure 4.15.** (Left) Example of a longitudinal phase space distribution for an electron beam traveling down the linac. (Right) Projection of this distribution onto the longitudinal coordinate (density distribution)

The plot on the right hand side of Figure 4.15, the longitudinal profile of the electron beam, is the datum of interest, but it is very difficult to measure directly with the required sub-picosecond resolution. However, the projection onto the energy coordinate is easy to measure with the spectrometer. Without any chirp, the projection of the beam onto the energy coordinate will reveal the energy spread, which refers to the "C" case in Figure 4.14. In the RF zero-phasing method, a large chirp is placed on the beam such that the new  $\Delta E/E$  ( $\Delta E$  is the energy deviation from the average) is much larger than the intrinsic energy spread in the electron beam. The longitudinal measurement is made by then taking the projection on the energy axis (via the spectrometer). If the chirp is assumed to be linear, the energy axis can be converted to the longitudinal coordinate (i.e. distance, time, or phase) through multiplication by a conversion factor, which is the inverse of the slope of the chirp. The amplitude of the projection is also adjusted by dividing by the cosine of the angle in phase space imposed by the chirp.

In Figure 4.16, a large linear chirp is applied to this electron bunch (for both the "A" and "B" cases), the phase space is projected onto the energy coordinate, and the energy axis is adjusted to appear in the units of the longitudinal coordinate. It is important to remember that although the energy axis is converted to represent position, the acquired data is still a projection on the energy axis. This will be an essential point when describing how this measurement technique can be deceptive, especially when trying to accomplish the experiments of the type presented in this

project. Meanwhile, in this particular case, as demonstrated by Figure 4.16, the RF-zero phasing technique works quite well. The blue "real" distributions are almost indistinguishable from the black "measured" distributions, with the exception of a few small excursions due to the finite number of pixels in the array used to store the phase space and the rather crude method used to apply the chirp (no attempt to suppress the errors caused by the pixelation is made) (Appendix B contains the MATLAB code used to carry out this procedure, and can be examined more closely there).

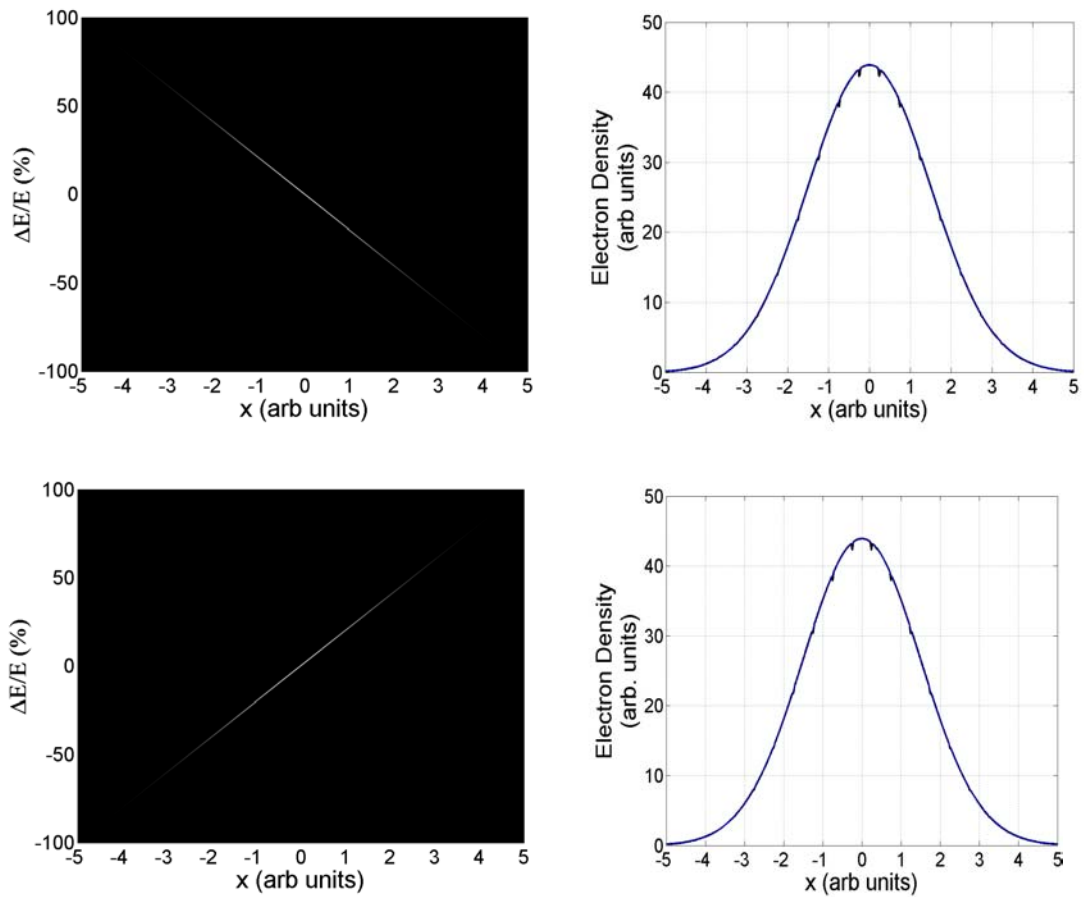


**Figure 4.16.** (Top Left) Electron beam phase space with "A"-style chirp. (Top Right) (Blue) Projection of "A" phase space onto longitudinal coordinate (Black) Projection of "A" phase space onto adjusted energy coordinate - the simulated RF zero-phase measurement (Bottom Left) Electron beam phase space with "B"-style chirp. (Bottom Right) (Blue) Projection of "B" phase space onto longitudinal coordinate (Black) Projection of "B" phase space onto adjusted energy coordinate - the simulated RF zero phase measurement.

Note also in Figure 4.16 the change in scale on the energy axis of the phase space diagrams. If the scales were the same, the phase space of the electron beam would look like it had been rotated nearly 90 degrees. This is the essential idea of the RF-zero phasing technique - the electron beam is rotated in phase space so that

the projection desired can be recovered in a relatively simple way. But, it is important to explore what might happen in a different case, when the energy spread of the electron beam is comparable to the chirp.

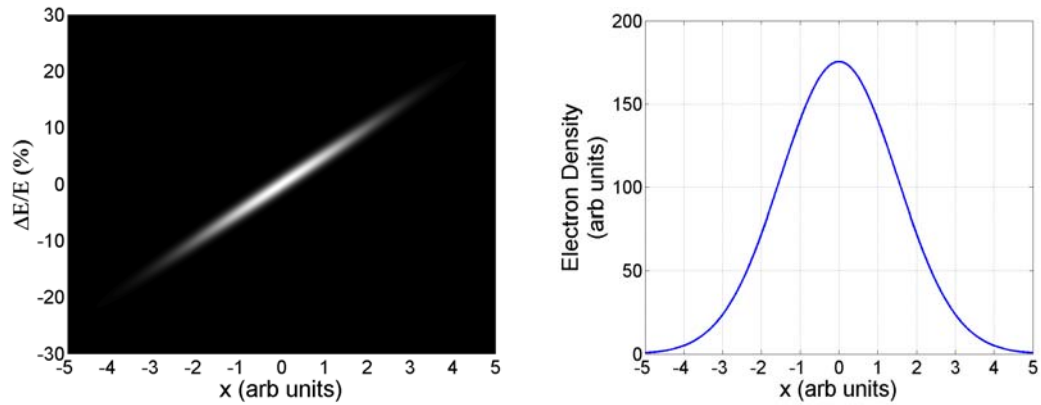


**Figure 4.17.** (Left) Example of a longitudinal phase space distribution for an electron beam traveling down the linac. (Right) Projection of this distribution onto the longitudinal coordinate (density distribution)

Figure 4.17 shows a longitudinal phase space diagram that describes a beam with a different energy at the head and the tail. This might be due to space charge or RF curvature if the beam is even a few degrees of the RF wavelength. In addition to this energy slew, there is also a larger local energy spread at each point longitudinally along the beam compared to the one described in Figure 4.15. The RF zero phase measurement that would result from this situation is compared to the actual longitudinal profile in Figure 4.18.

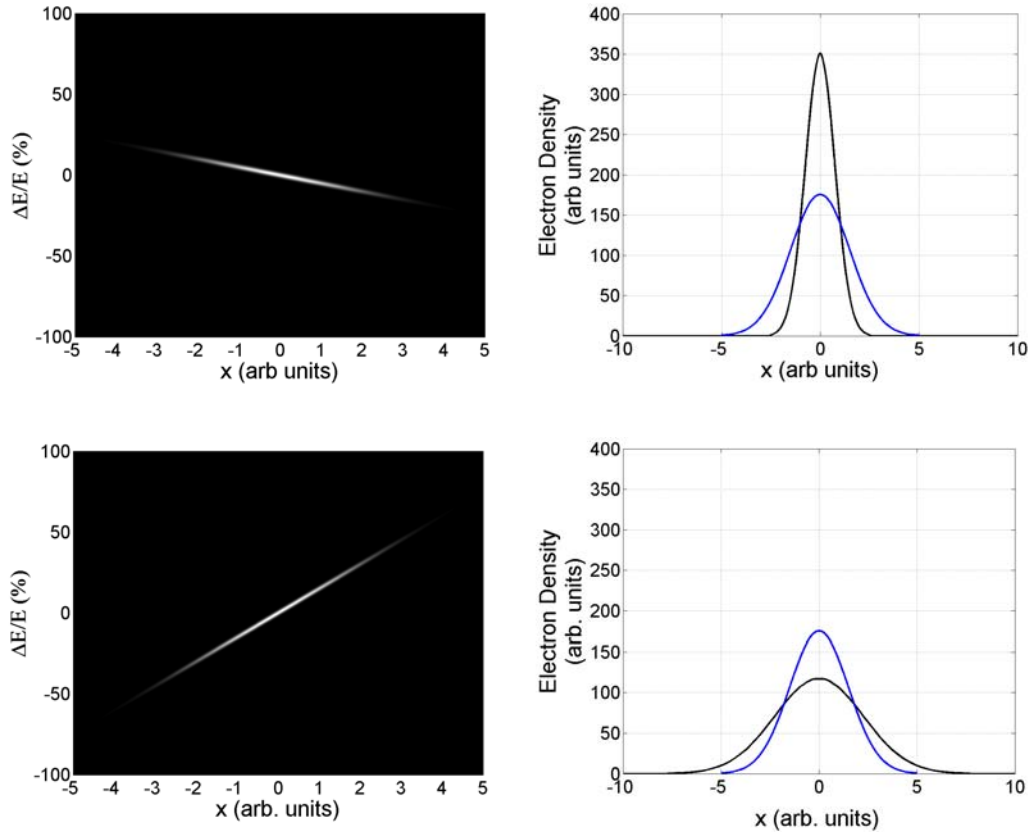


**Figure 4.18.** (Top Left) Electron beam phase space with "A"-style chirp. (Top Right) (Blue) Projection of "A" phase space onto longitudinal coordinate (Black) Projection of "A" phase space onto adjusted energy coordinate - the simulated RF zero phase measurement (Bottom Left) Electron beam phase space with "B"-style chirp. (Bottom Right) (Blue) Projection of "B" phase space onto longitudinal coordinate (Black) Projection of "B" phase space onto adjusted energy coordinate - the simulated RF zero phase measurement.

As Figure 4.18 shows, the projections do not look the same for the "A" and "B" slope because of the issue of the energy spread. Notice also that the "real" distribution in Figure 4.18 is exactly the same as that in Figure 4.16 and Figure 4.15. The only difference between the two cases is that the local energy spread (near one particular longitudinal point) and the longitudinally correlated energy spread were

increased. The result of this increase in energy spread is that the projection onto the energy coordinate cannot be easily converted to the time coordinate without a priori knowledge of the longitudinal phase space (and if one knew this, there would be no reason to take the measurement in the first place). One way to alleviate this problem, however, is to use one of the accelerating sections to remove any correlated energy spread that might be on the beam (that is why the RF zero phasing method requires two accelerating sections, as described earlier).

Now, imagine this one bunch is one part of a larger bunch train. If the bunch has a phase space distribution that looks like Figure 4.17, the RF zero phase measurement may show erroneous shortening or lengthening of the bunch, as shown in Figure 4.18. But, in the case of a bunched beam, the correlated energy does not change linearly with the longitudinal coordinate, and is therefore impossible to remove using the tools presently available at the SDL.

To demonstrate this problem, one more RF zero phasing case will be examined. In this case, Figure 4.19 shows the phase space of an electron beam bunch train that might be produced in this experiment. There are a series of bunches, and each one is modeled by an ellipse in longitudinal phase space. Each ellipse is also tilted like the one in Figure 4.17, to approximate the effect of space charge.

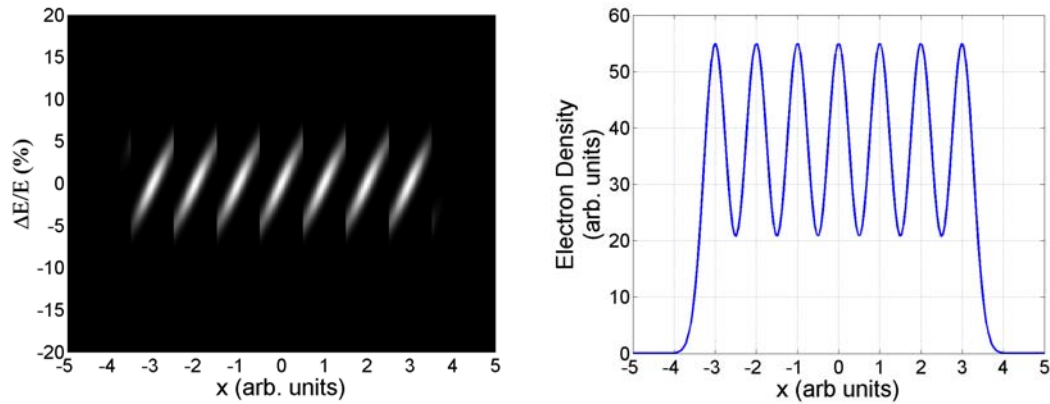


**Figure 4.19.** (Left) Example of a longitudinal phase space distribution for an electron beam traveling down the linac. (Right) Projection of this distribution onto the longitudinal coordinate (density distribution)

Each bunch is centered around zero in the energy coordinate. This is because the accelerating section can be used to remove the overall chirp from the bunch, but cannot remove the correlated energy spread in each individual bunch. The "real" density distribution in Figure 4.19 clearly shows a density modulation, but some of the density modulation is beginning to wash out. But, note in the phase space diagram, that there is also an energy modulation on the electron beam (i.e. in Figure 4.17 energy increases linearly with position, but in Figure 4.19 energy is periodic with position). This energy modulation can lead to errors in the RF zero phase measurement similar to that seen in Figure 4.18, but in this case, the effects are quite dramatic, as seen in Figure 4.20.

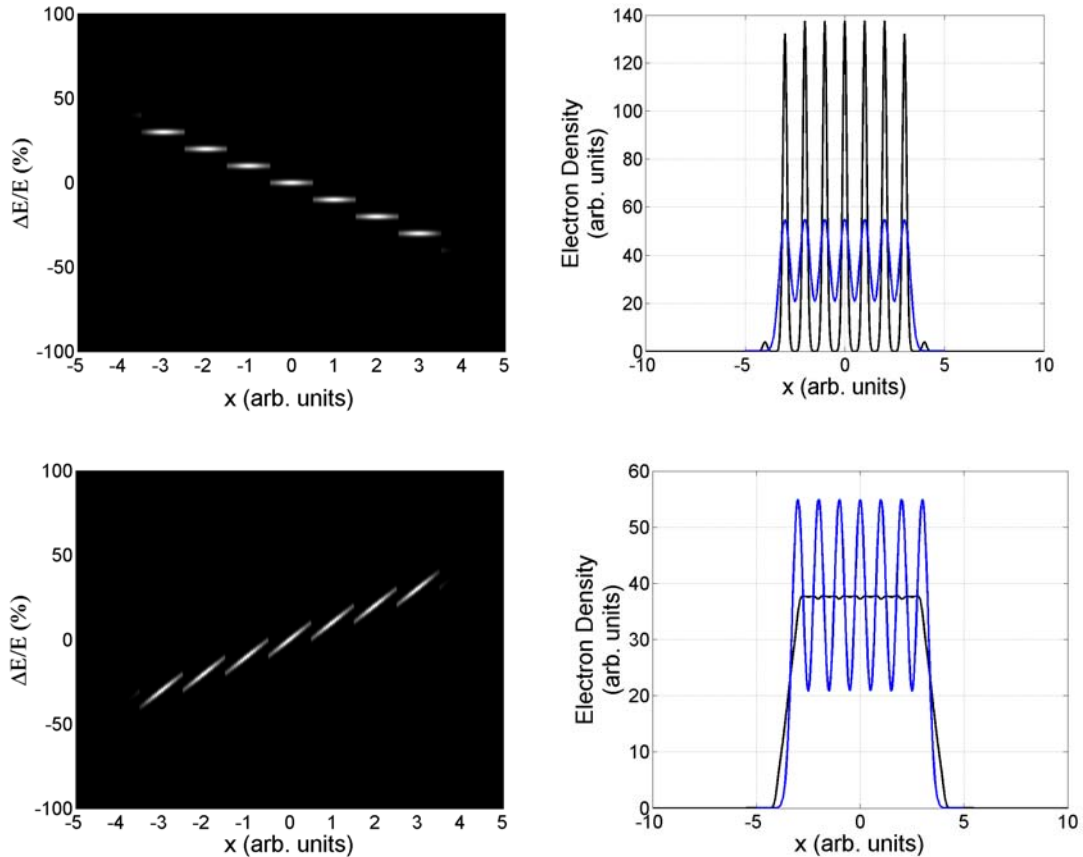


**Figure 4.20.** (Top Left) Electron beam phase space with "A"-style chirp. (Top Right) (Blue) Projection of "A" phase space onto longitudinal coordinate (Black) Projection of "A" phase space onto adjusted energy coordinate - the simulated RF zero phase measurement (Bottom Left) Electron beam phase space with "B"-style chirp. (Bottom Right) (Blue) Projection of "B" phase space onto longitudinal coordinate (Black) Projection of "B" phase space onto adjusted energy coordinate - the simulated RF zero phase measurement.

The simulated RF zero phase measurements in Figure 4.20 are somewhat troublesome; the "A" case indicates deeper density modulation than actually exists in the real longitudinal profile, while in the "B" case, the measurement indicates that all of the density modulation has washed out. This is a particularly troublesome issue

for this experiment, where one of the main goals is to determine whether or not an accelerated electron beam can keep its initial modulation! Although this thought experiment used an arbitrary phase space diagram to illustrate the points, the real electron beam in the SDL linac has been shown to exhibit this type of behavior in previous experiments. In fact, apparent density modulation due to energy modulation has appeared in RF zero phase measurements when almost no density modulation at all actually exists<sup>59</sup>.

There is a way to overcome this problem. Since each RF zero phase measurement is a different projection of a two dimensional longitudinal phase space onto the energy coordinate, it may be possible to reconstruct the original two dimensional picture from a set of several projections. The Simultaneous Algebraic Reconstruction Technique (SART) is a useful algorithm for this purpose, and has been implemented by the staff at SDL for use with their accelerator to reconstruct longitudinal phase space diagrams.

Kak and Slaney<sup>60</sup> describe the algorithm concept very well, and their interpretation is paraphrased here. The first step is to assume that the two dimensional image can be represented by an array of pixels, where the value of each pixel is constant (this lends itself very nicely for use with computers, which exhibit exactly this property in their handling of images). Each pixel is labeled  $f_j$ , and  $N$  is the total number of pixels. Next, a ray is drawn, with some finite width, and at some arbitrary angle, across the image. The image can be projected onto an axis

perpendicular to this line by performing a line integral, or in this discrete case, a sum, along this line. The complete projection from the image is computed from a series of parallel rays. The value of this sum is labeled  $p_i$ . This sum is actually computed in the following way:

$$\sum_{j=1}^N w_{ij} f_j = p_i \quad i = 1, 2, \dots, M \quad (4.2)$$

where  $M$  is the total number of rays in all projections. The weighting factor,  $w_{ij}$ , is calculated by computing the fractional area of the  $j^{\text{th}}$  pixel intercepted by the  $i^{\text{th}}$  ray. So, there are  $M$  equations and  $N$  unknowns. The illustration in Figure 4.21 makes this process easier to visualize.

The parallel  $p_i$ 's form the projections, and many projections are taken from various angles around the image. Experimentally, this is done by varying the chirp of the RF field in the accelerating section, which serves to rotate the image rather than rotate the rays. Then, the projection onto the energy axis is performed by the spectrometer. So, the  $p_i$ 's are measured experimentally, and the  $w_{ij}$ s can be calculated based on the image size and the known amount of chirp, which leaves solving this set of linear equations for the  $f_j$ s to reconstruct the image.

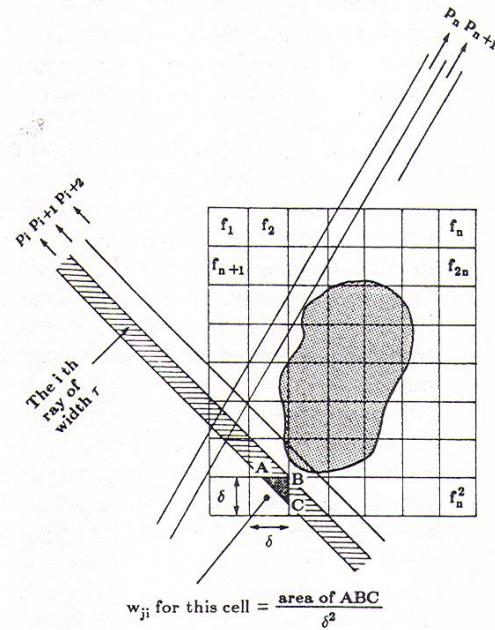


**Figure 4.21.** Illustration of algebraic reconstruction technique concept (reprinted with permission from Kak and Slaney<sup>61</sup>)

Kak and Slaney suggest an iterative approach to reduce computation time due to the large matrix size required for this computation. The data for each longitudinal profile collected from the SDL, for example, consists of 19 projections onto the energy coordinate, each with 640 points, corresponding to an M-value (the number of *p*'s) of 12,160. Requesting a reconstructed image of 200 X 200 pixels yields an N of 40000. Of course an MXN matrix of this particular size cannot be directly inverted anyway, but the point is that the computational problem is quite large.

The specific implementation for this algorithm at the SDL was accomplished by Loos<sup>62</sup>. In this case, the various projections are actually made by varying the

phase of one of the accelerating sections. The same procedure applies as above, except the chirp now varies linearly with the sin of the phase, and the weighting functions are determined by appropriately tracing each phase space pixel onto the energy axis. The implemented SART algorithm uses some different numerical techniques, including the use of bilinear elements to make the computation of the weighting functions easier, to create a more accurate reconstruction than the basic Algebraic Reconstruction Technique described above. The basic concept, however, is still the same. As a result, the formula<sup>63</sup> used uses  $g_j$  for the image and  $a_{ij}$  for the weighting functions, since they are calculated in a different way.

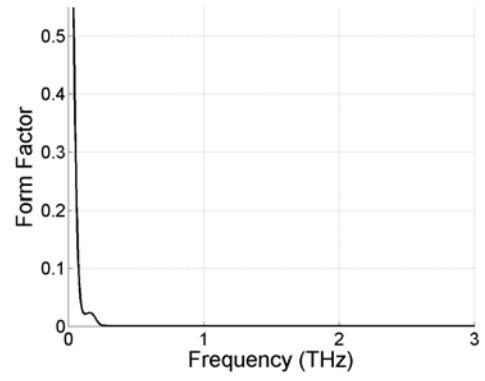
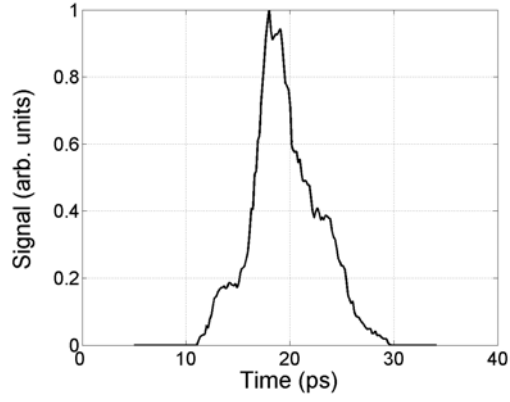
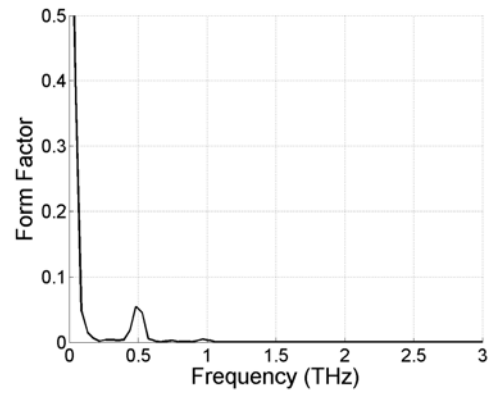
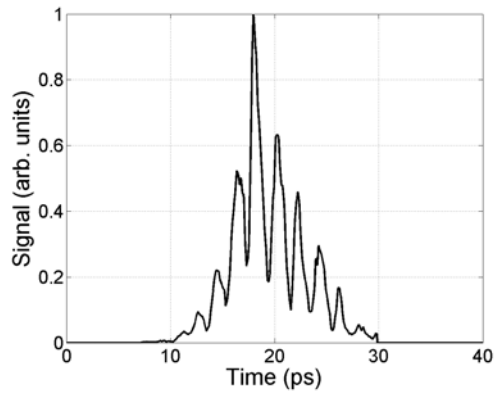
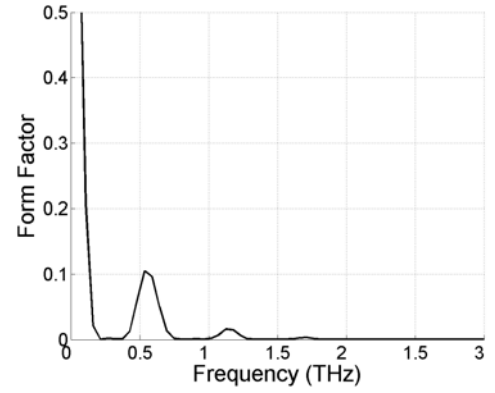
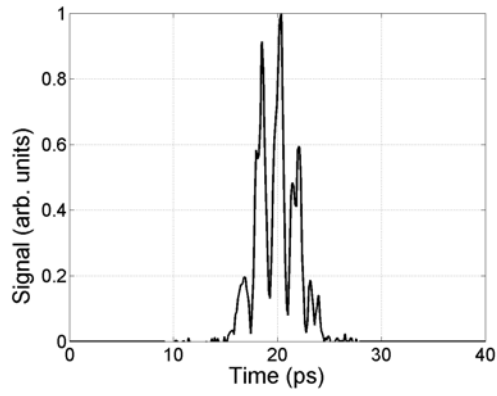
$$g_j^{(k+1)} = g_j^{(k)} + \frac{\sum_i \left[ \frac{a_{ij} \left( p_i - a_i \vec{g}^{\rightarrow T \rightarrow(k)} \right)}{\sum_{j=1}^N a_{ij}} \right]}{\sum_i a_{ij}} \quad (4.3)$$

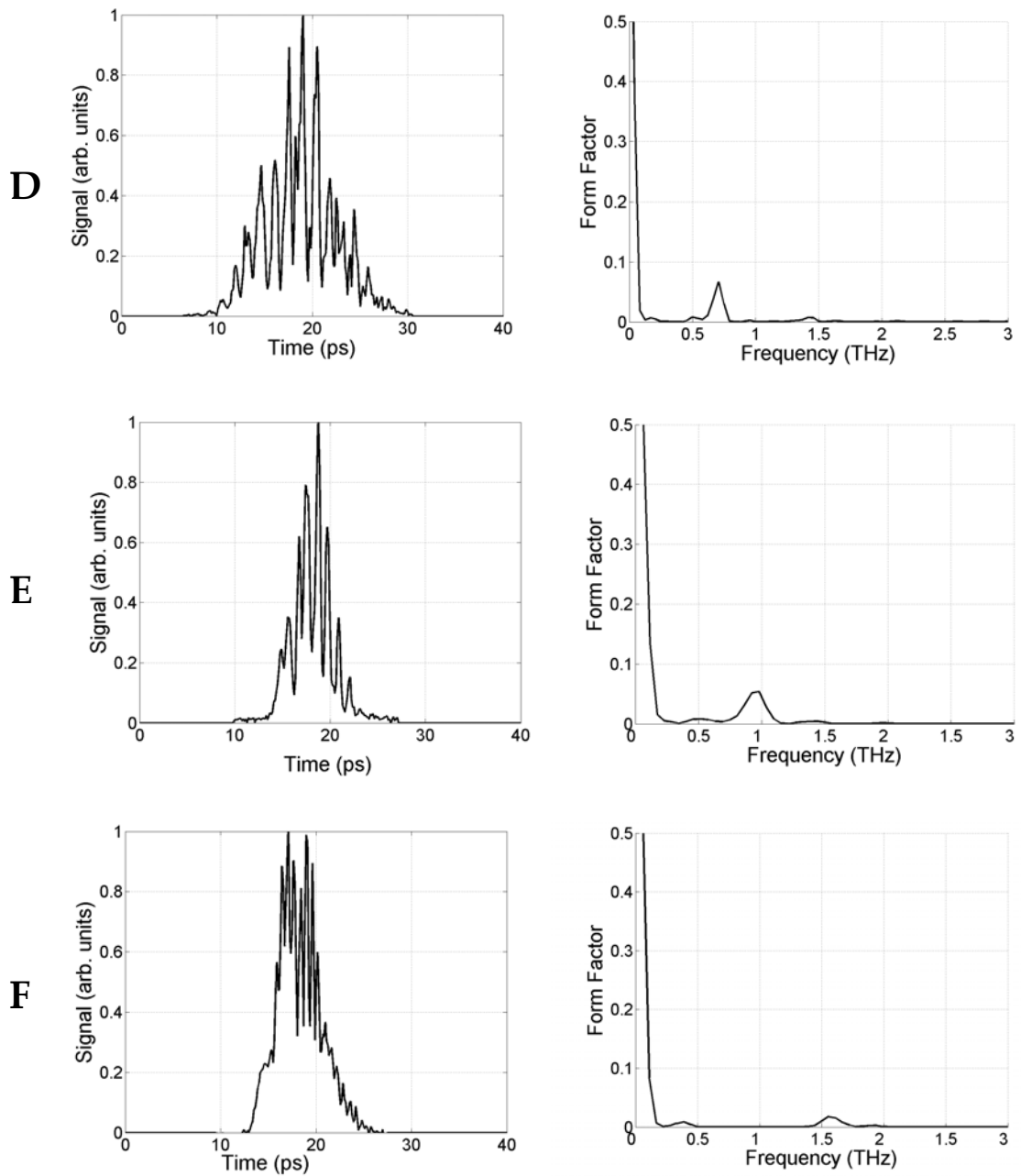
Sufficient data for tomographic reconstruction was available for some, but not all, of the experiments performed at the SDL. Keeping the above discussion in mind, the RF zero phase measurements of the longitudinal profile will be presented for all of the relevant experimental cases, while the tomographic reconstructions will also be presented where available.

### *4.3 Longitudinal Electron Beam Measurements*

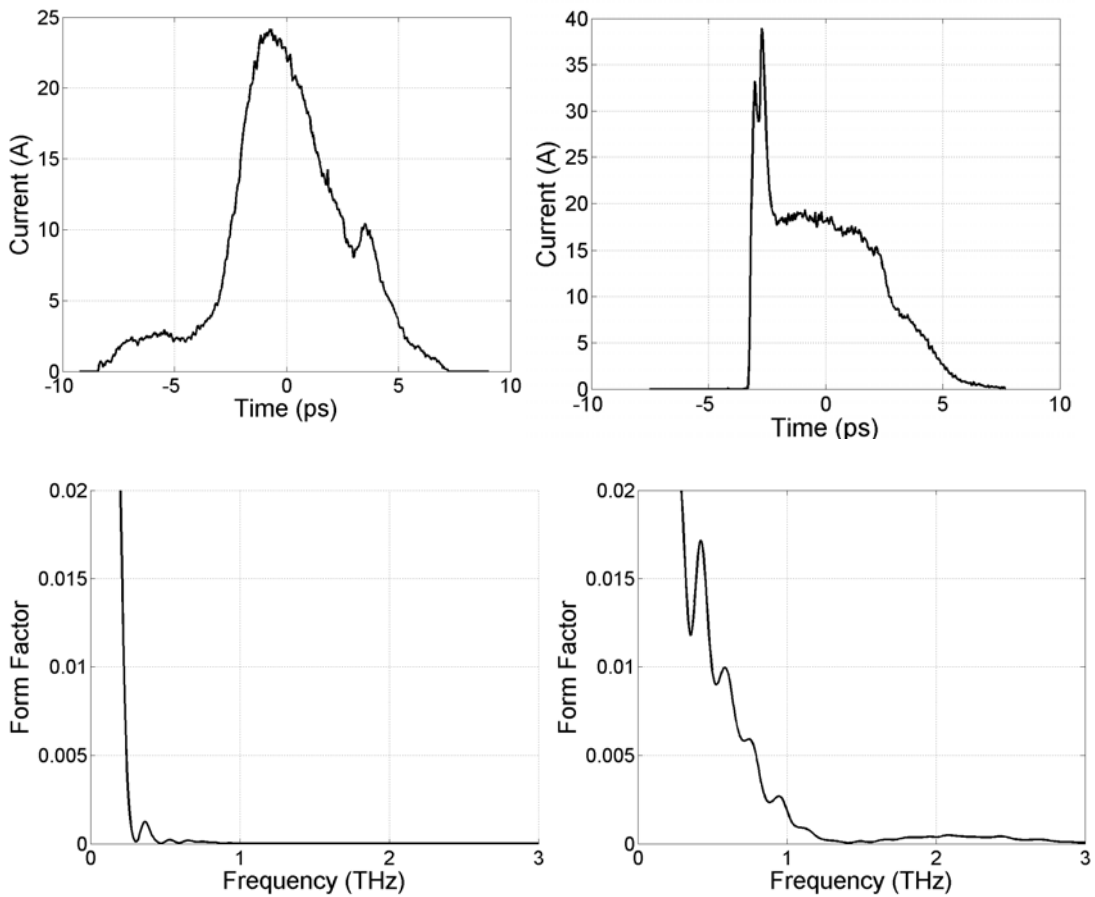
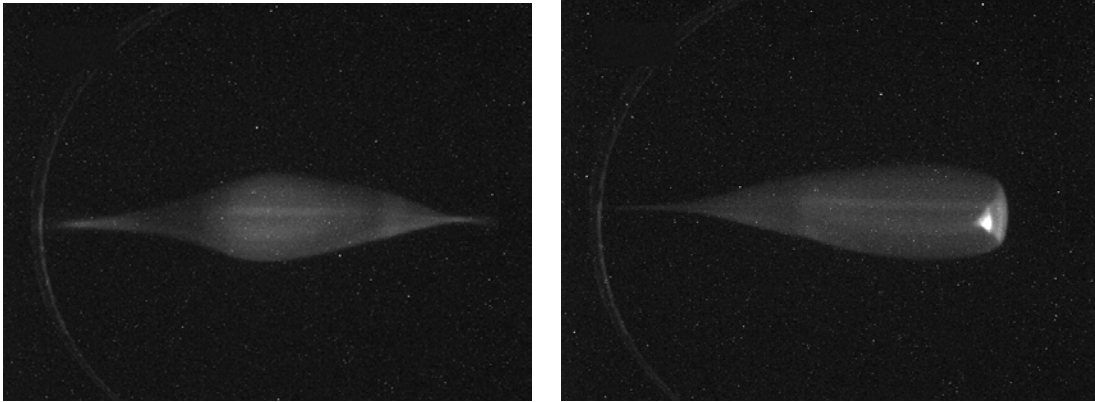
Electron beam longitudinal measurements were made for several different laser profiles. The laser modulation frequency and the laser energy were varied in order to explore the effects of these parameters on the measured electron beam. Figure 4.22 shows a representative unmodulated baseline measurement, and each of the laser profiles used to generate an electron beam in this experiment along with their corresponding form factors. The profiles are marked with letters, A-F, which will be used for reference with the electron beam longitudinal measurements. Each data set includes a laser cross-correlation, the total charge in the bunch train (related directly to UV laser energy), the RF zero-phase projections (from the spectrometer screen and across a slice). For each laser profile, some of the RF zero phase measurements are shown along with the available tomographic reconstructions of the longitudinal phase space and their corresponding longitudinal profile projections. Both the RF zero phase measurements and reconstructions are shown with their respective form factor. Where available, results from the PARMELA simulations are compared to the tomographic reconstructions. While a great deal of RF zero phase data exists, it is of limited use due to the issues discussed in the previous section. Considering this, and the fact that the RF zero phase measurements have peak form factor values significantly larger than the initial laser profile used to generate them, it is likely that the RF zero phase profiles are much

less indicative of the actual longitudinal profile of the electron beam than the tomographic reconstructions or the simulation results. Some of the data from the RF zero phase measurements are included in order to provide an overview of all of the information that was recorded, and to supplement the experimental reconstructions and simulation results. The RF zero phase measurements should be thought of more as an energy spectrum of the chirped electron beam than as a time profile, even though they are labeled as such. Therefore, only results from the tomographic reconstructions are compared with the simulation results, and the RF zero phasing results will not be used as part of any further analysis.

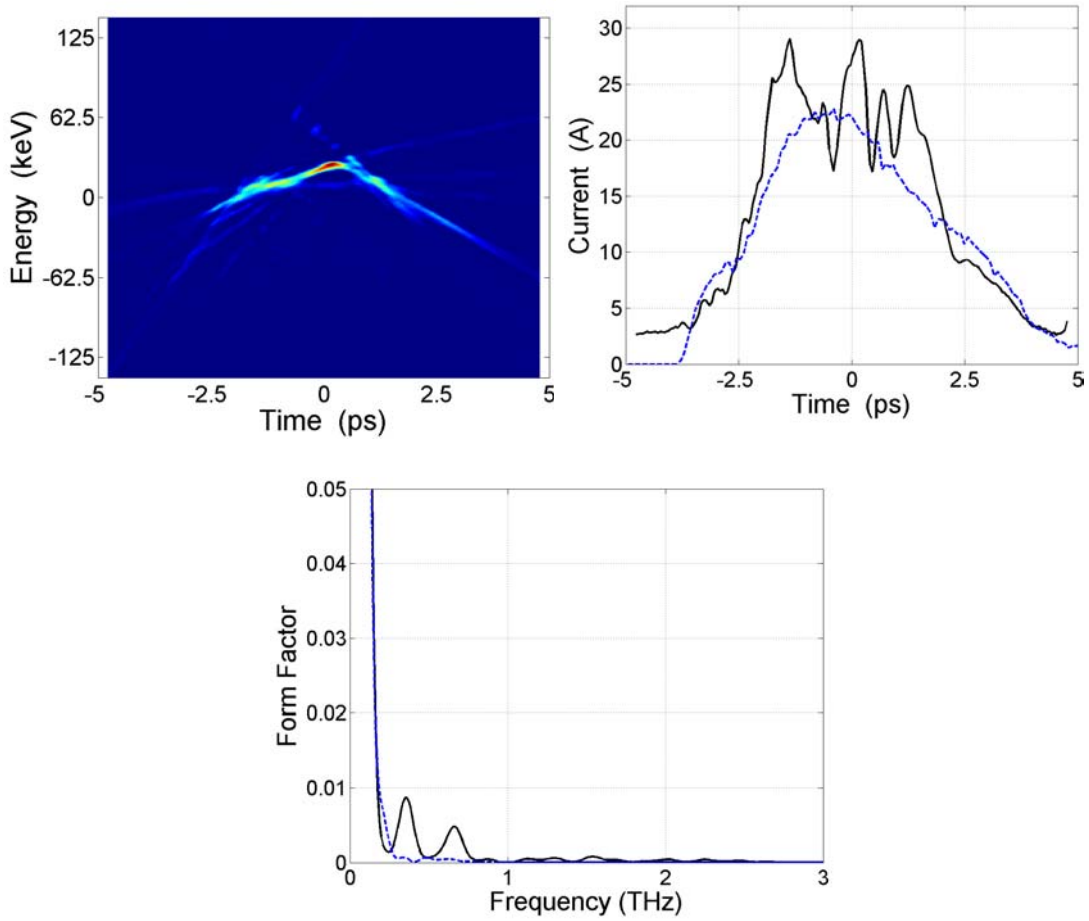
**A****B****C**



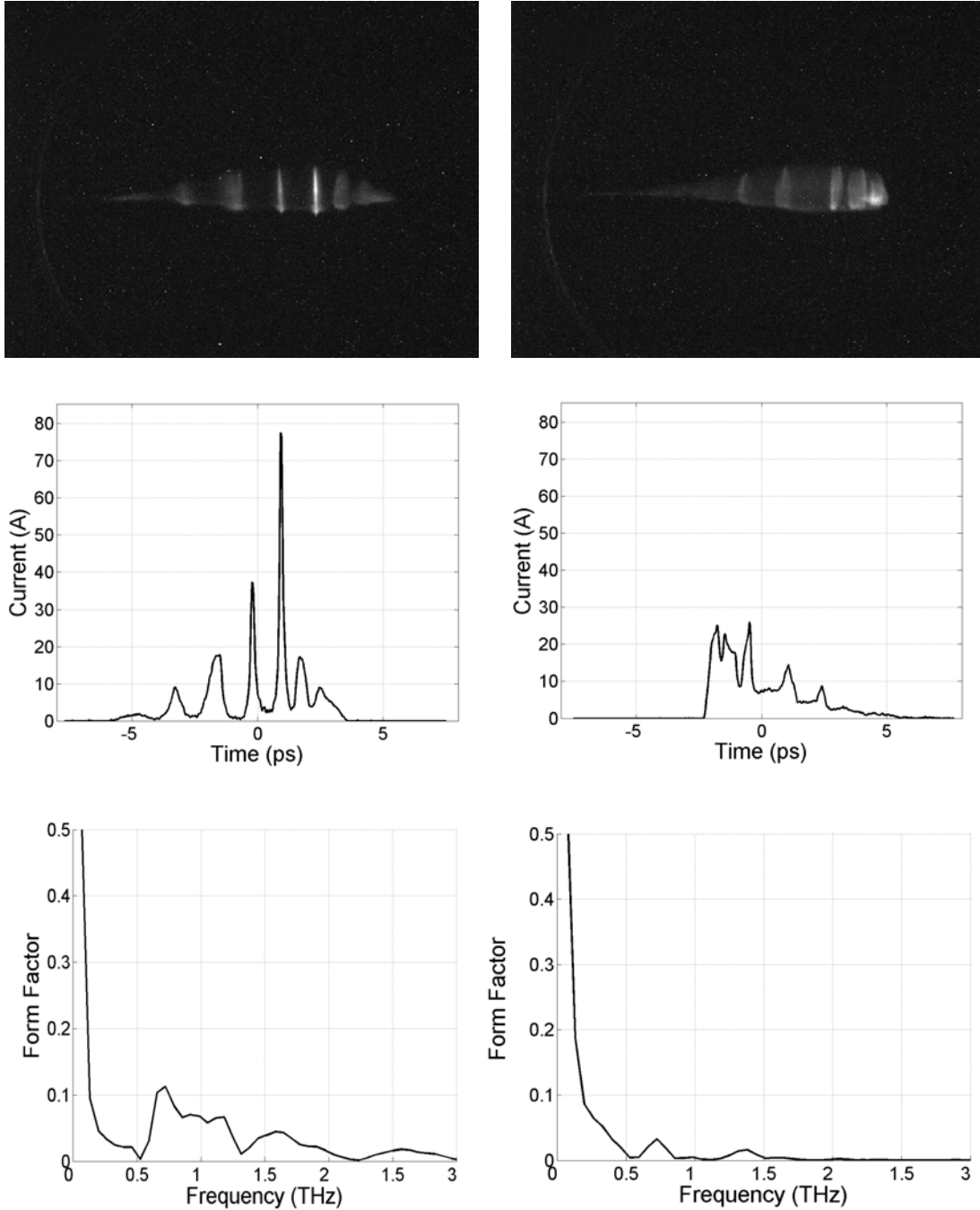
**Figure 4.22.** (Left, A-F) UV laser cross-correlations of various modulated pulses. (Right, A-F) The corresponding form factor of each laser pulse.



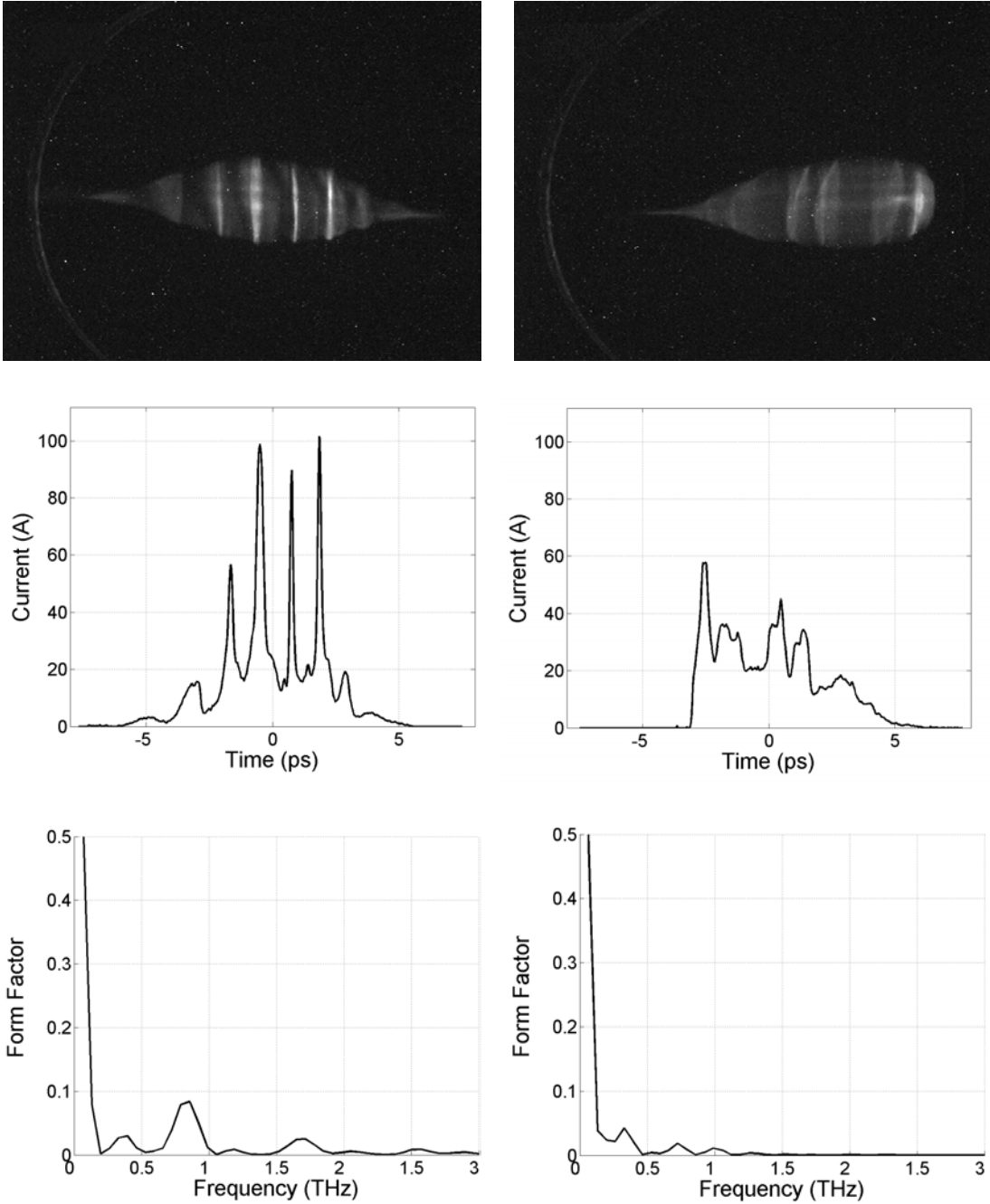
**Figure 4.23.** Data corresponds to **laser profile A**. Total charge is **110 pC**. Left hand panels, from top to bottom, correspond to the A-slope of the RF zero-phasing measurement, and show the raw data, the time profile, and the form factor. Right hand panels show the same for the B-slope.



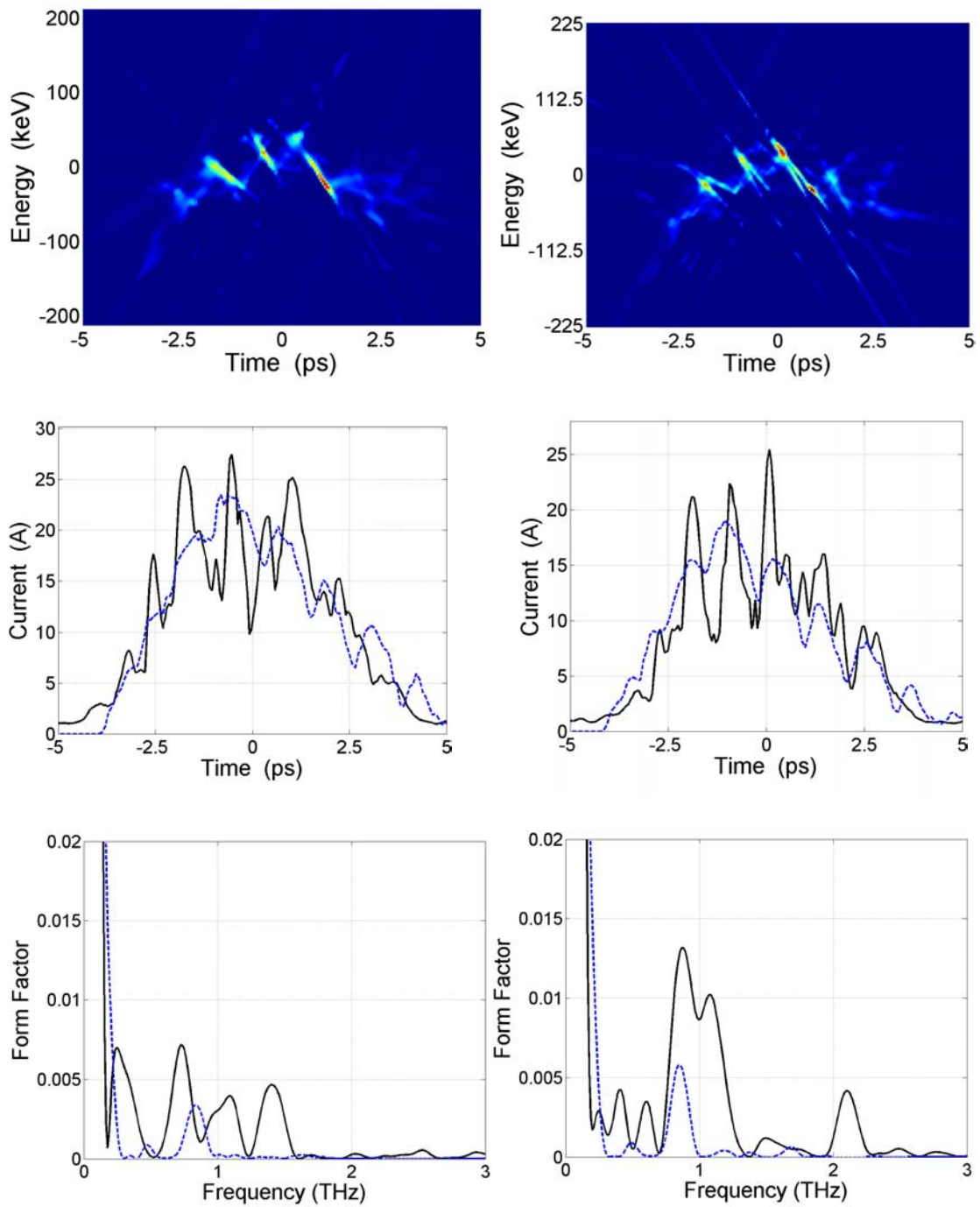
**Figure 4.24.** Data corresponds to **laser profile A**. Total charge is **110 pC**. The upper left shows the tomographic reconstruction of the longitudinal phase space. The upper right shows a projection of the phase space onto the axis of time. The solid black curve is from the experimental data while the dotted blue curve is from the simulation. The bottom figure shows the experimental and simulated form factor for this bunch structure.



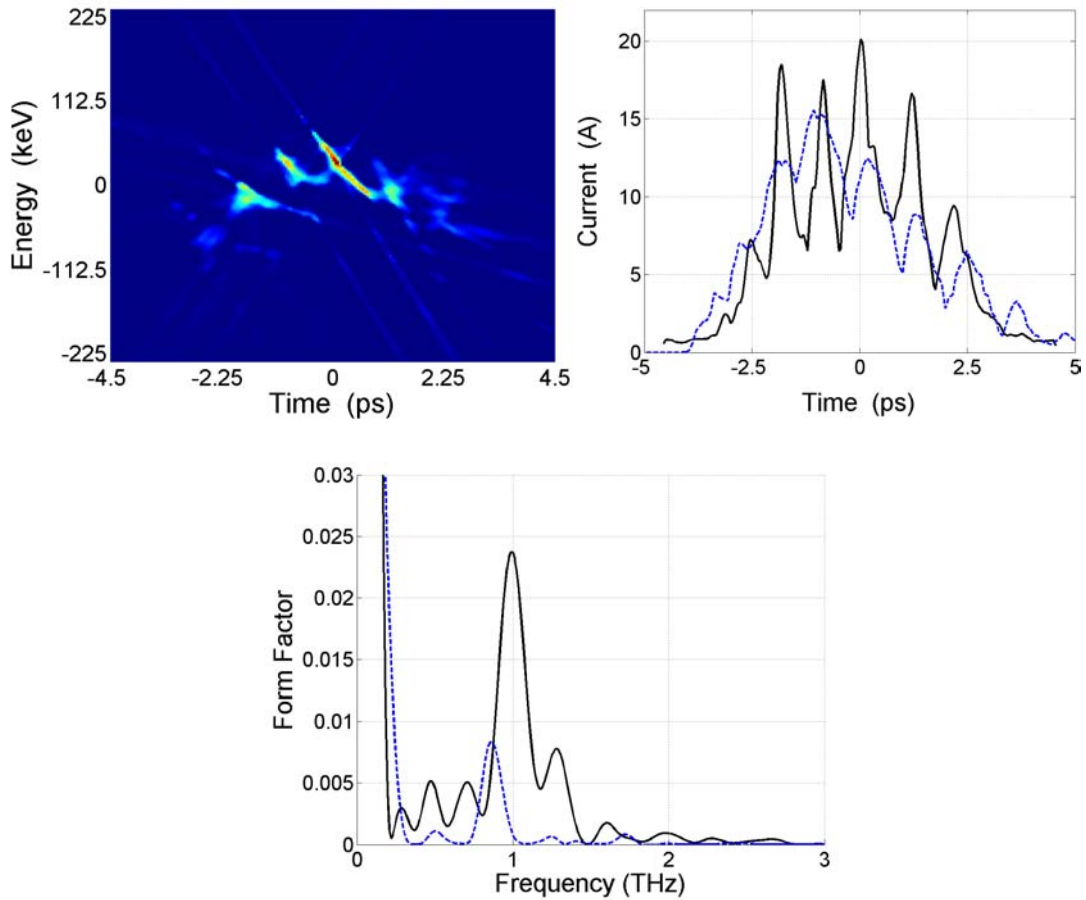
**Figure 4.25.** Data corresponds to **laser profile B**. Total charge is **60 pC**. Left hand panels, from top to bottom, correspond to the A-slope of the RF zero-phasing measurement, and show the raw data, the time profile, and the form factor. Right hand panels show the same for the B-slope.



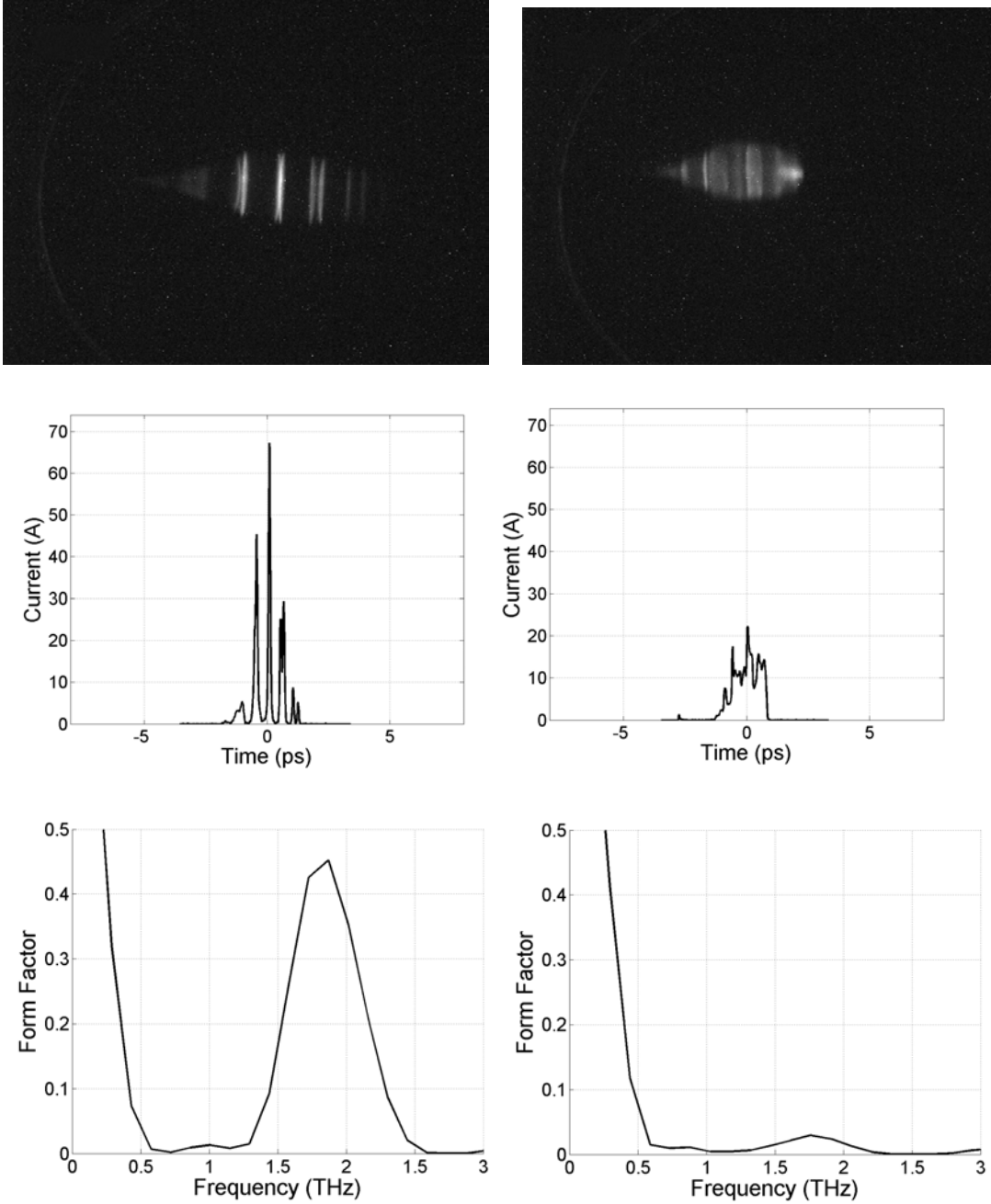
**Figure 4.26.** Data corresponds to **laser profile B**. Total charge is **180 pC**. Left hand panels, from top to bottom, correspond to the A-slope of the RF zero-phasing measurement, and show the raw data, the time profile, and the form factor. Right hand panels show the same for the B-slope.



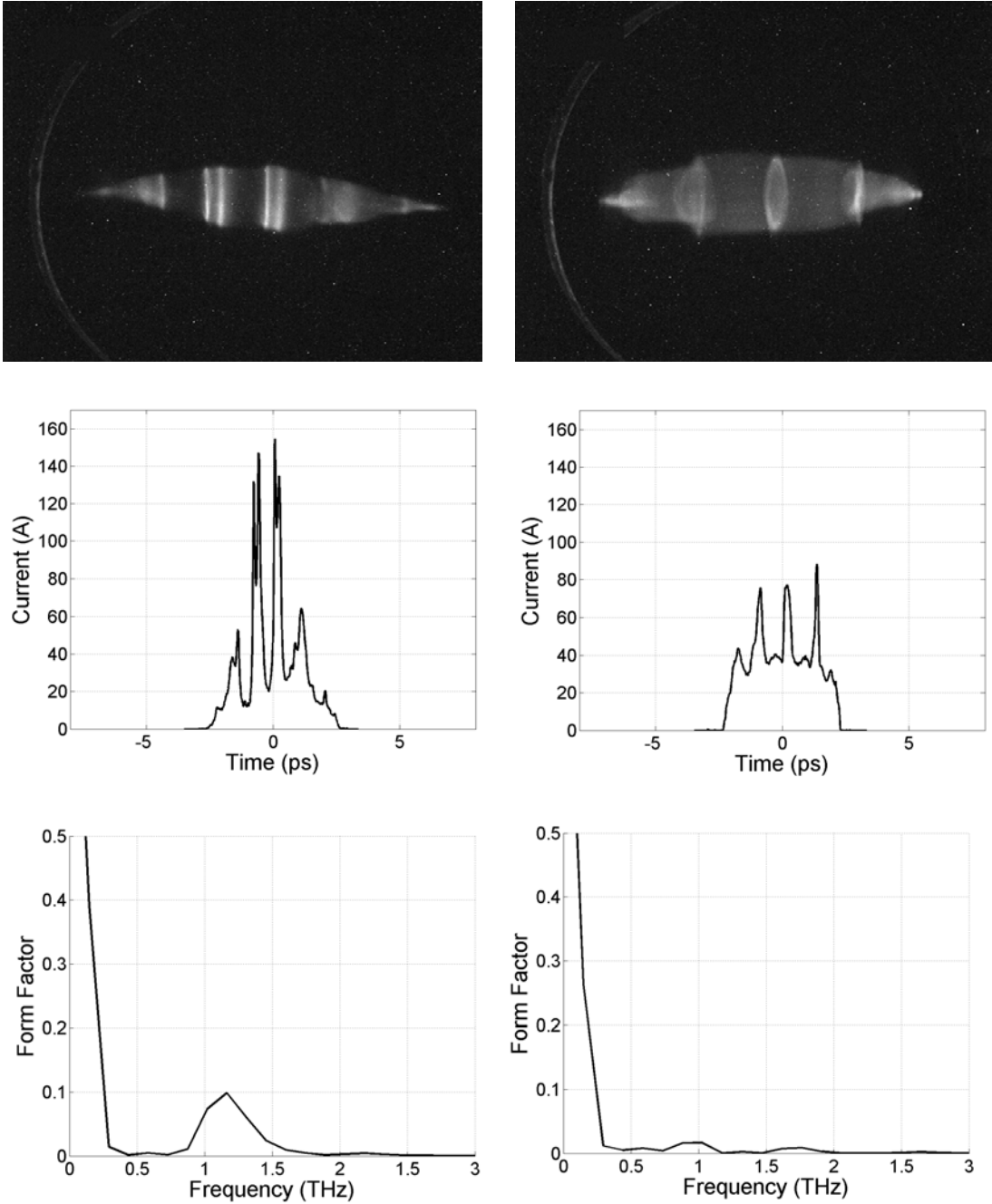
**Figure 4.27.** Data corresponds to **laser profile B**. Total charge is **110 pC (left)** and **80 pC (right)**. From top to bottom are the tomographic reconstructions of the phase space, the projection onto the time axis, and the form factor for each case. Solid black lines correspond to experimental data while dashed blue lines correspond to simulation results.



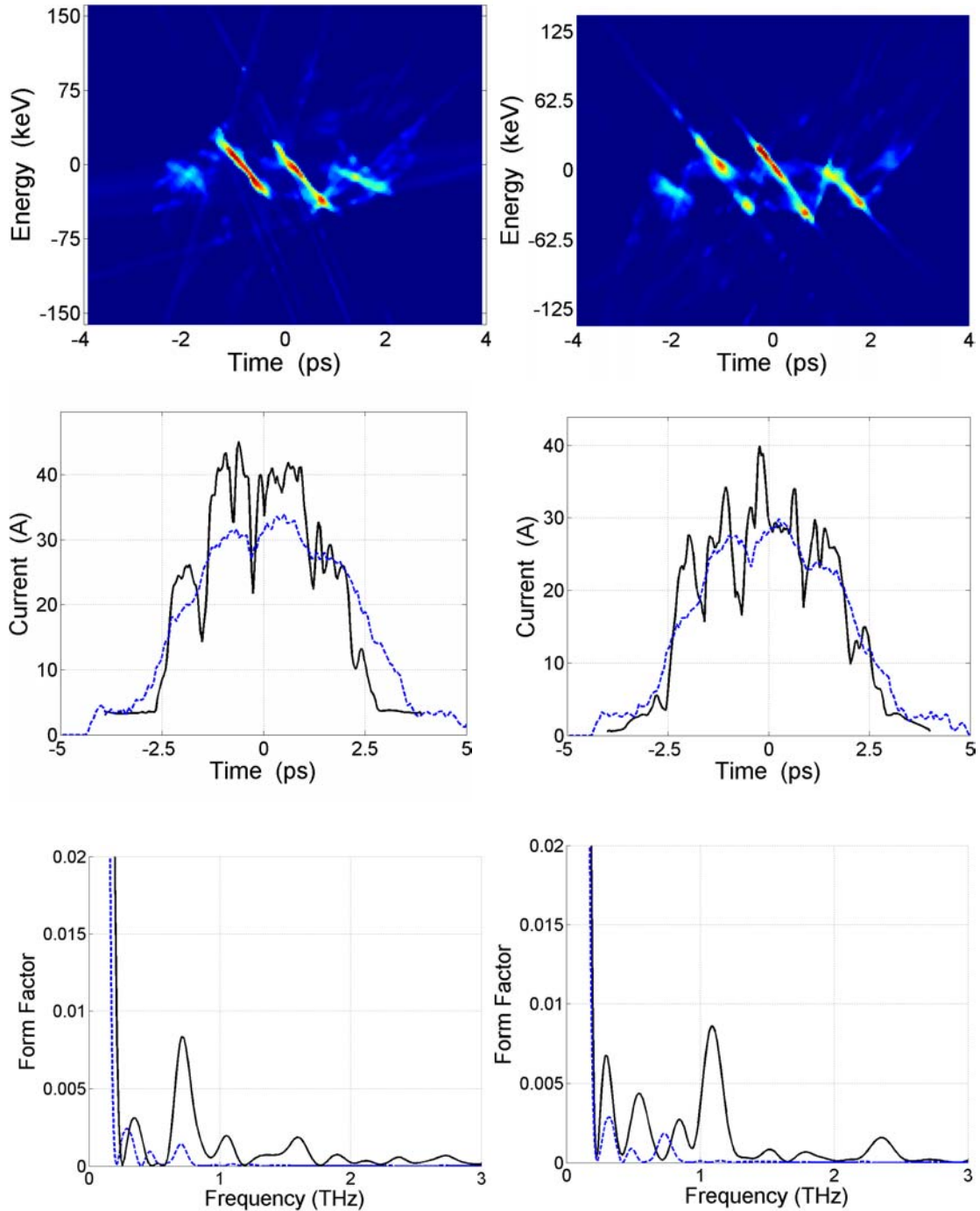
**Figure 4.28.** Data corresponds to **laser profile B**. Total charge is **60 pC**. The upper left shows the tomographic reconstruction of the longitudinal phase space. The upper right shows a projection of the phase space onto the axis of time. The bottom figure shows the form factor for the bunch structure. The solid black curve refers to experimental results while the dashed blue curve refers to simulated results.



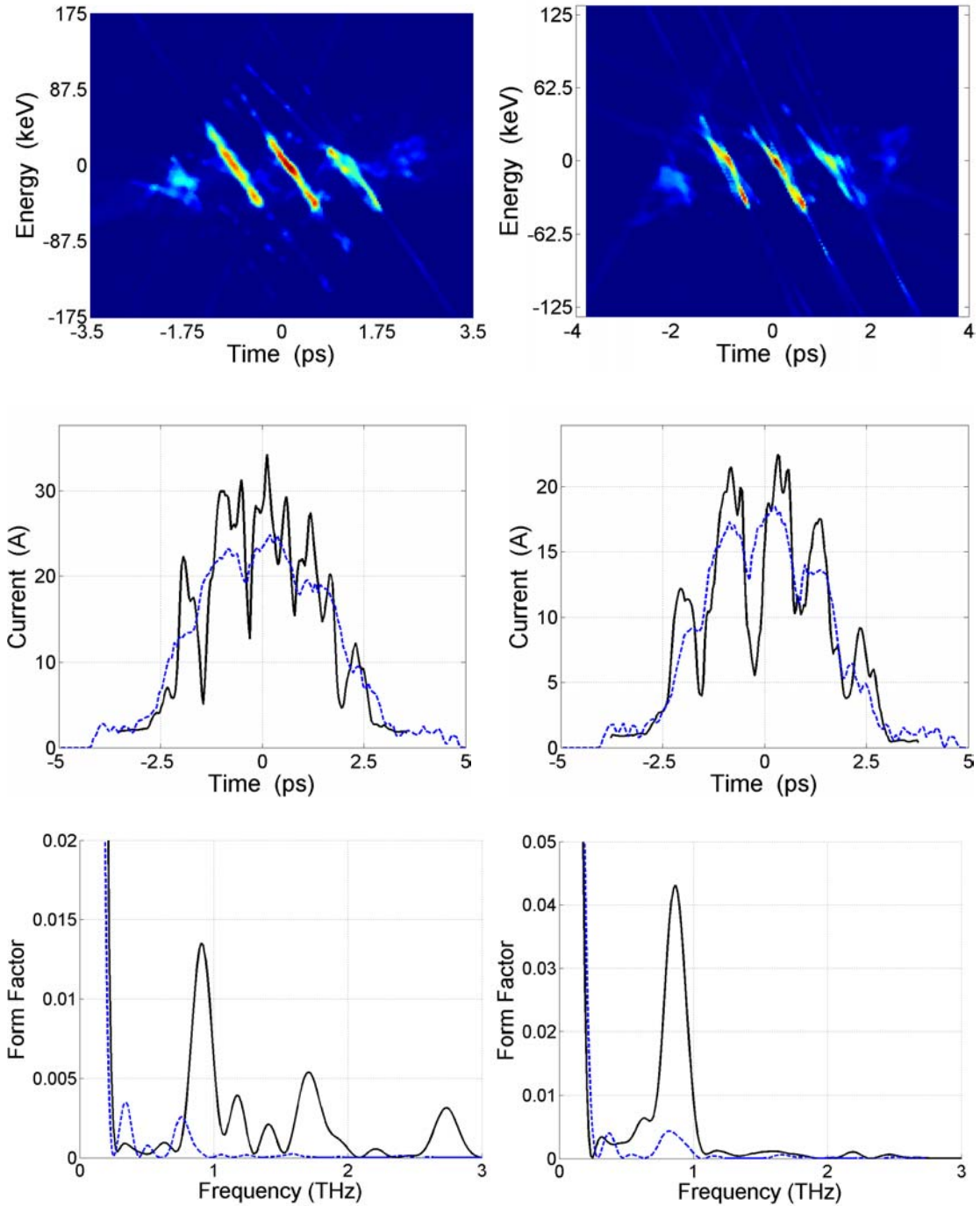
**Figure 4.29.** Data corresponds to **laser profile C**. Total charge is **20 pC**. Left hand panels, from top to bottom, correspond to the A-slope of the RF zero-phasing measurement, and show the raw data, the time profile, and the form factor. Right hand panels, from top to bottom, show the same for the B-slope.



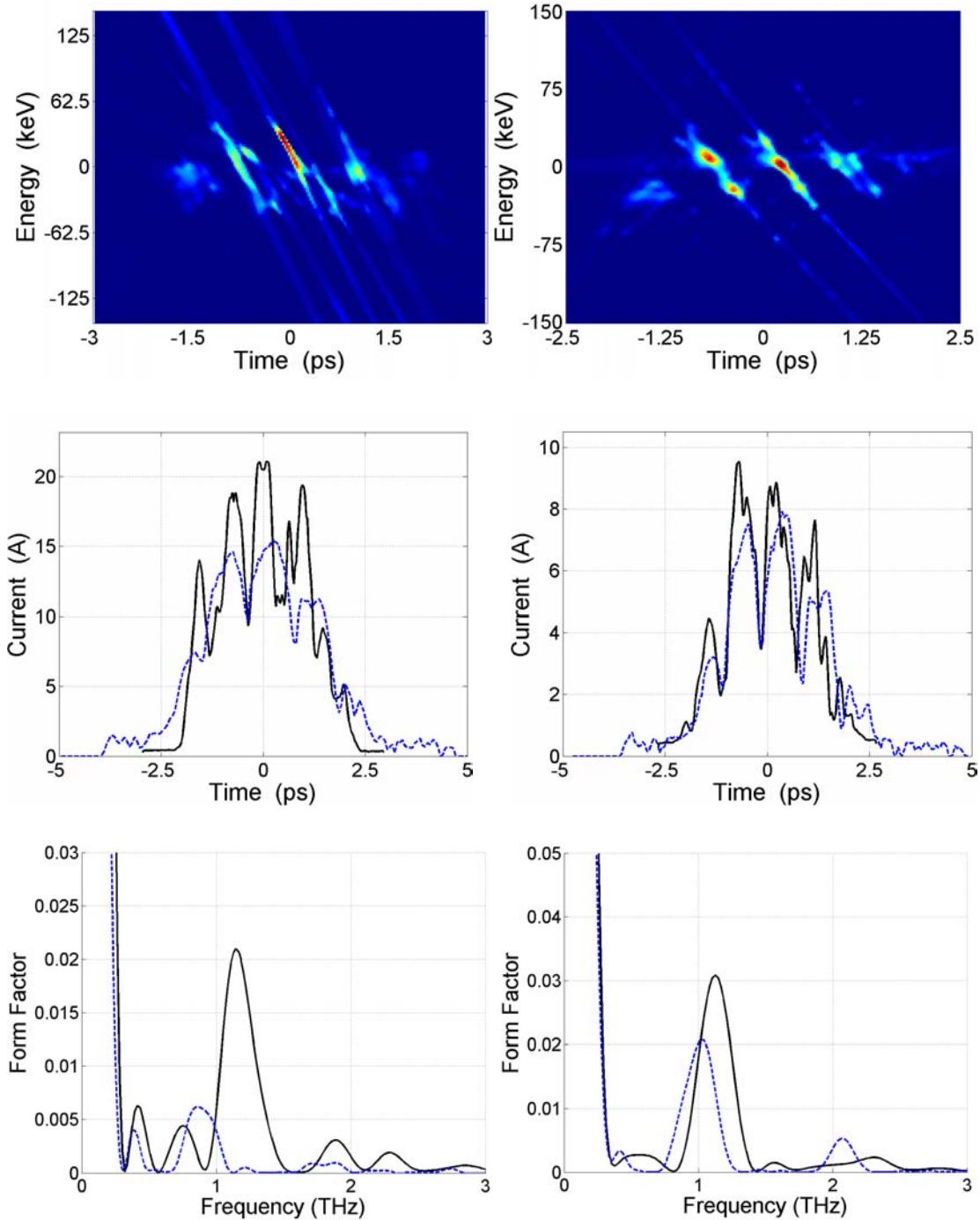
**Figure 4.30.** Data corresponds to **laser profile C**. Total charge is **160 pC**. Left hand panels, from top to bottom, correspond to the A-slope of the RF zero-phasing measurement, and show the raw data, the time profile, and the form factor. Right hand panels, from top to bottom, show the same for the B-slope.



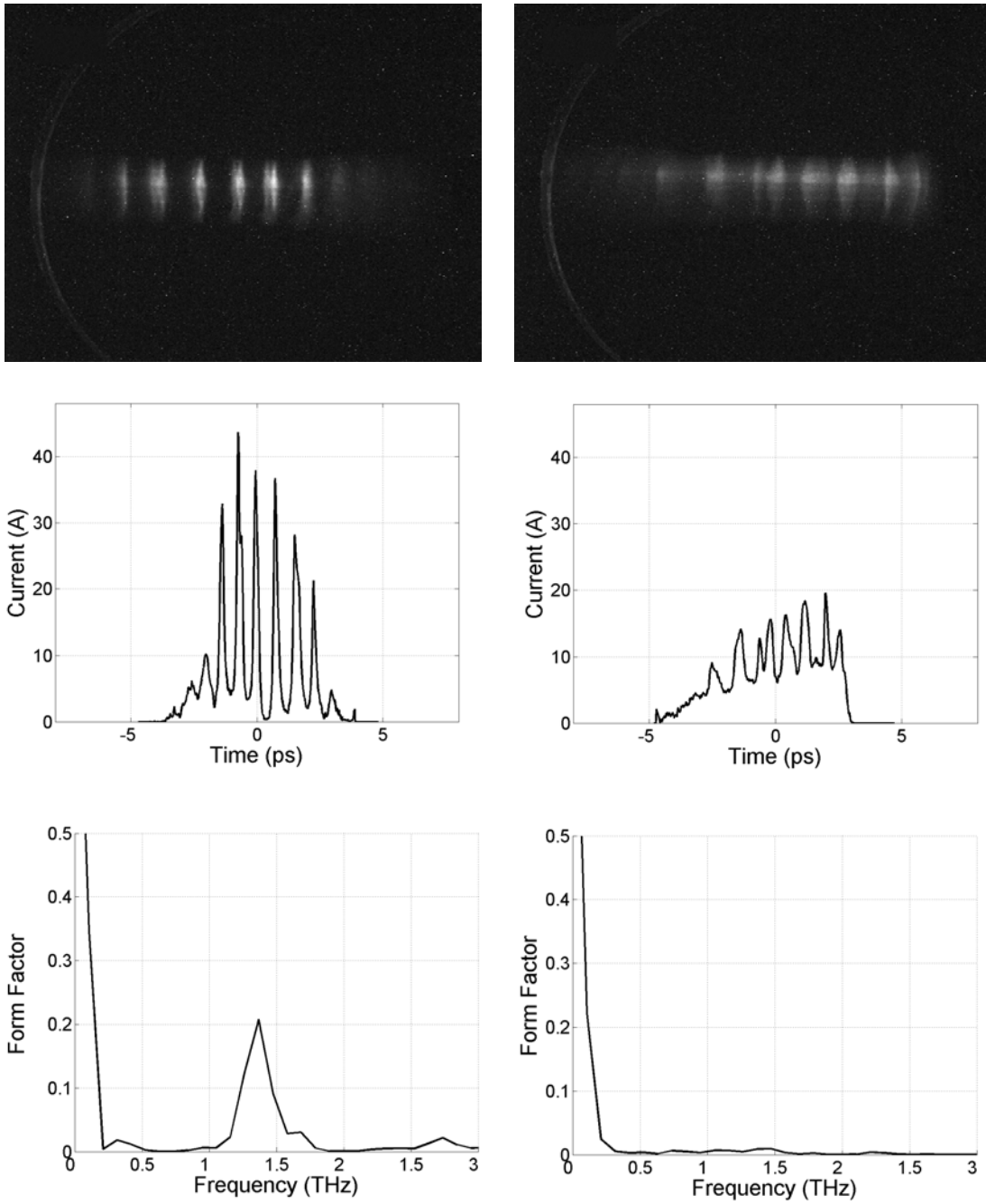
**Figure 4.31.** Data corresponds to **laser profile C**. Total charge is **160 pC (left)** and **130 pC (right)**. From top to bottom are the tomographic reconstructions of the phase space, the projection onto the time axis, and the form factor for each case. Solid black lines correspond to experimental data while dashed blue lines correspond to simulation results.



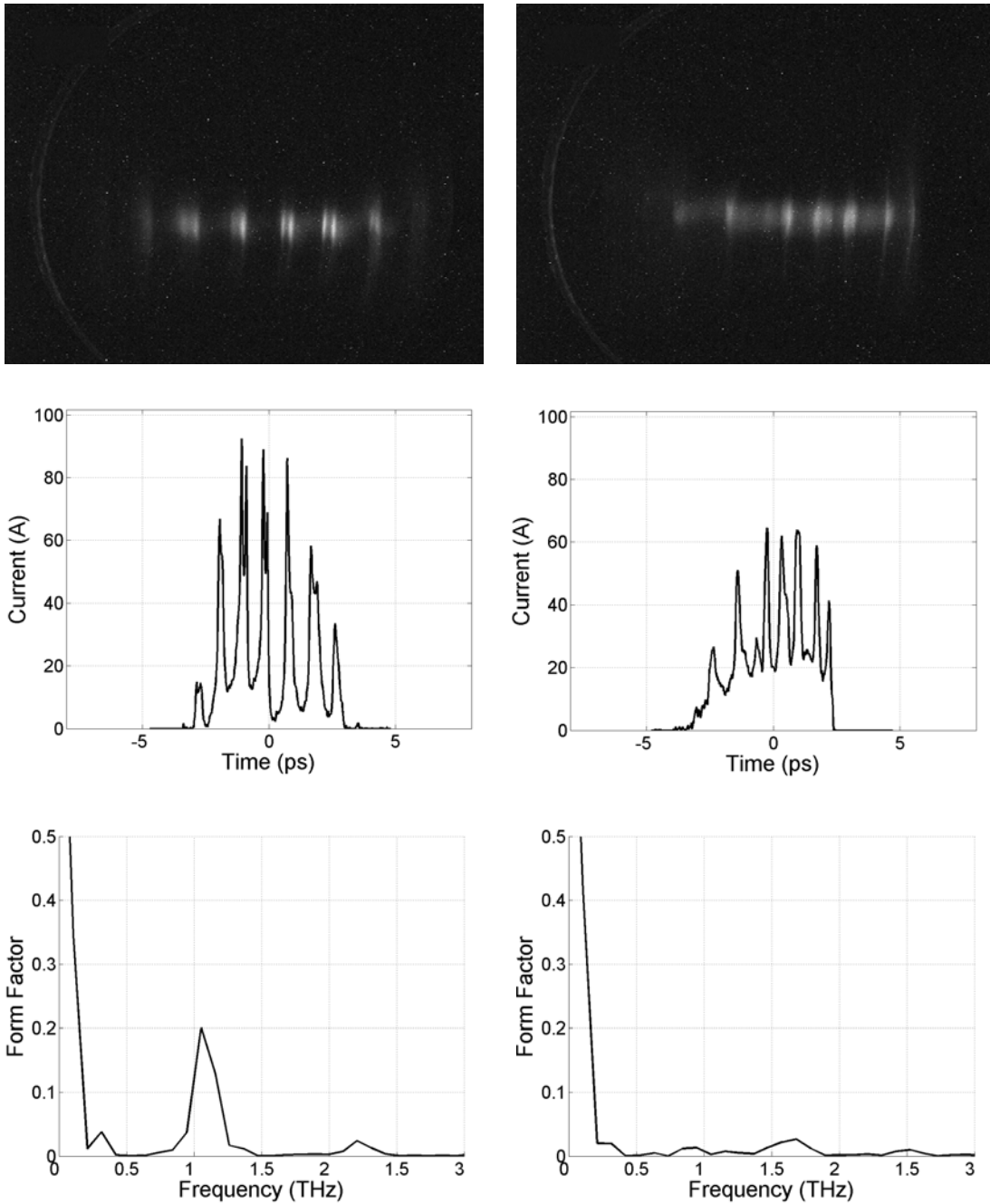
**Figure 4.32.** Data corresponds to **laser profile C**. Total charge is **100 pC (left)** and **65 pC (right)**. From top to bottom are the tomographic reconstructions of the phase space, the projection onto the time axis, and the form factor for each case. Solid black lines correspond to experimental data while dashed blue lines correspond to simulation results.



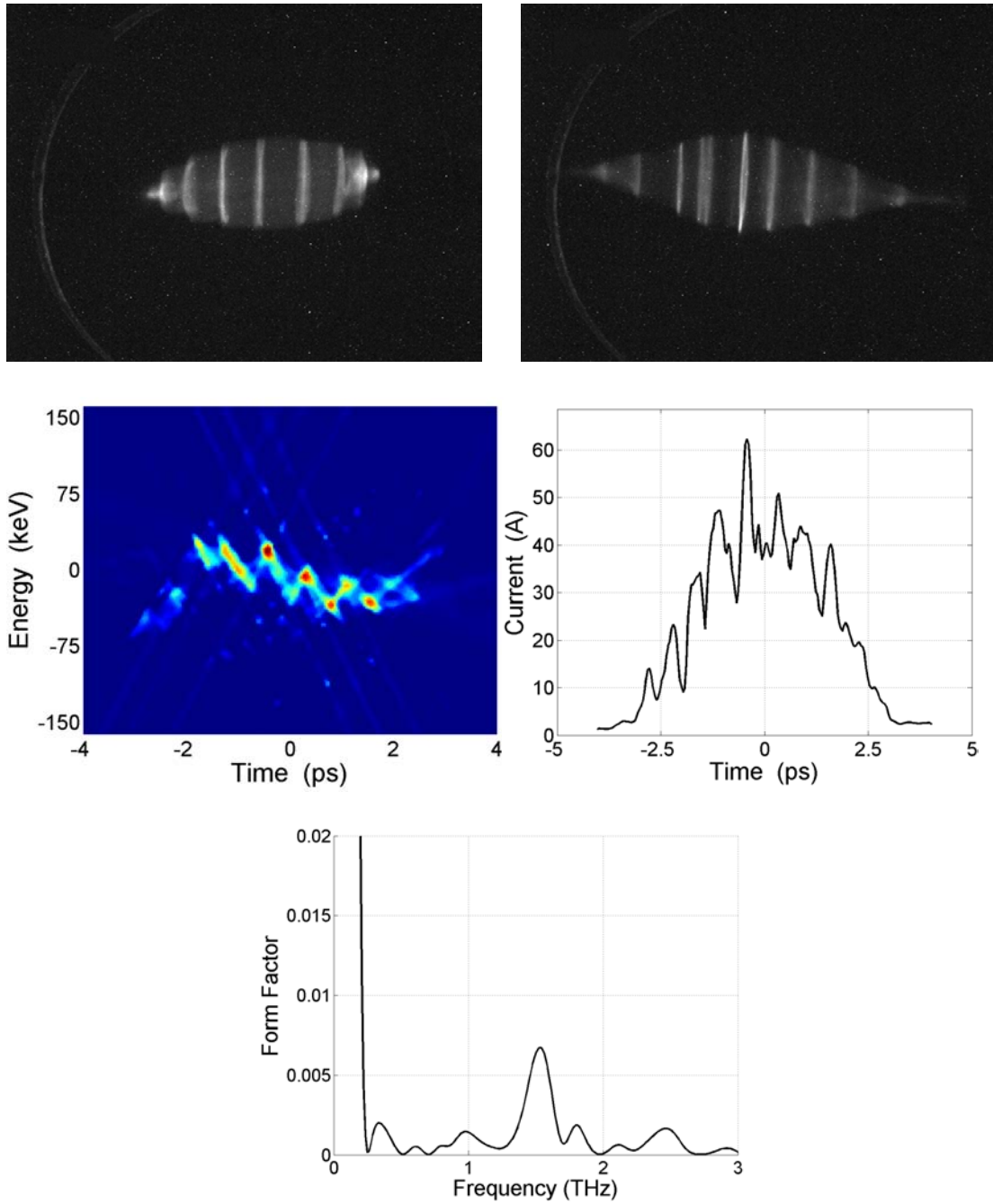
**Figure 4.33.** Data corresponds to **laser profile C**. Total charge is **50 pC (left)** and **20 pC (right)**. From top to bottom are the tomographic reconstructions of the phase space, the projection onto the time axis, and the form factor for each case. Solid black lines correspond to experimental data while dashed blue lines correspond to simulation results.



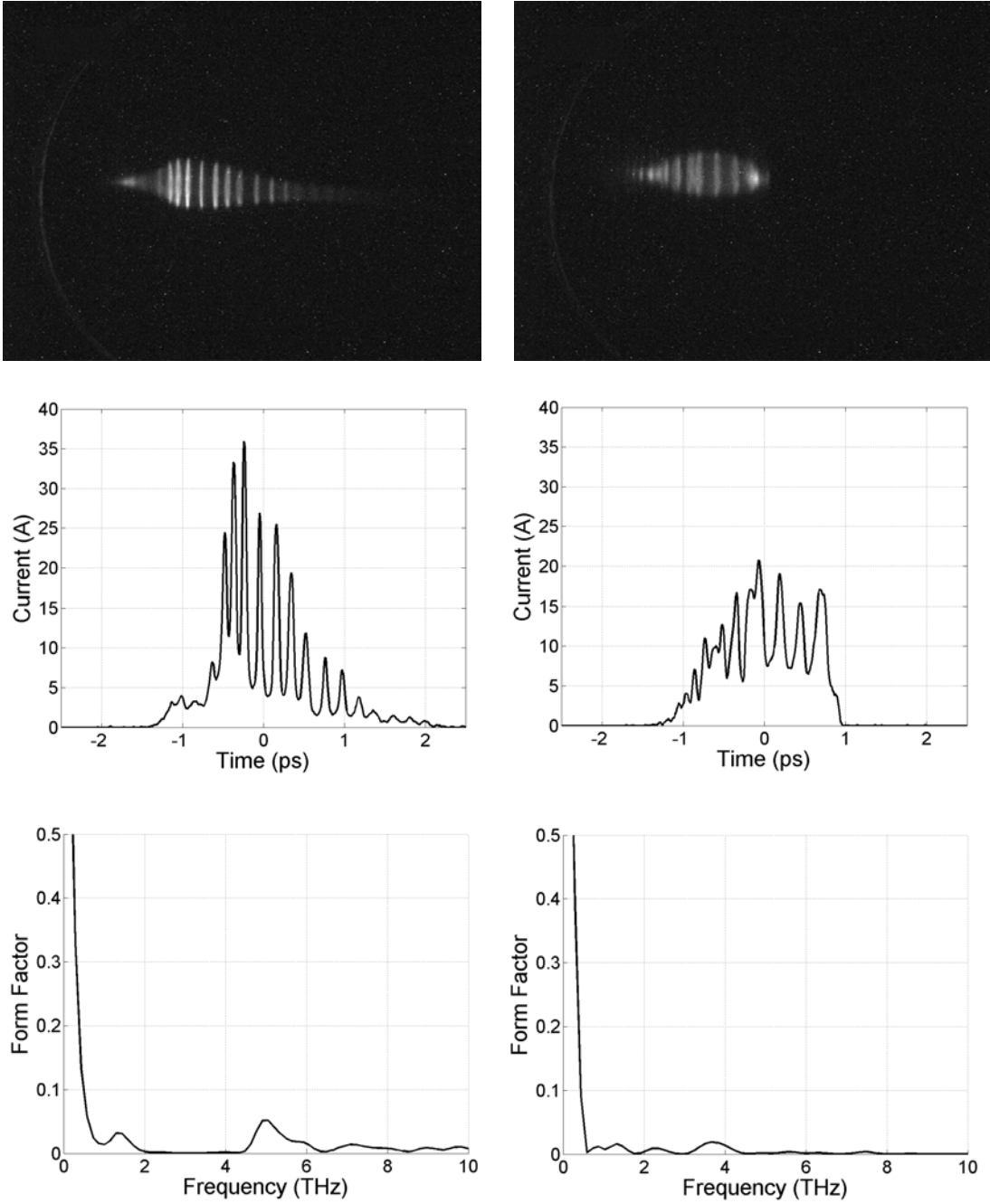
**Figure 4.34.** Data corresponds to **laser profile D**. Total charge is **60 pC**. Left hand panels, from top to bottom, correspond to the A-slope of the RF zero-phasing measurement, and show the raw data, the time profile, and the form factor. Right hand panels, from top to bottom, show the same for the B-slope.



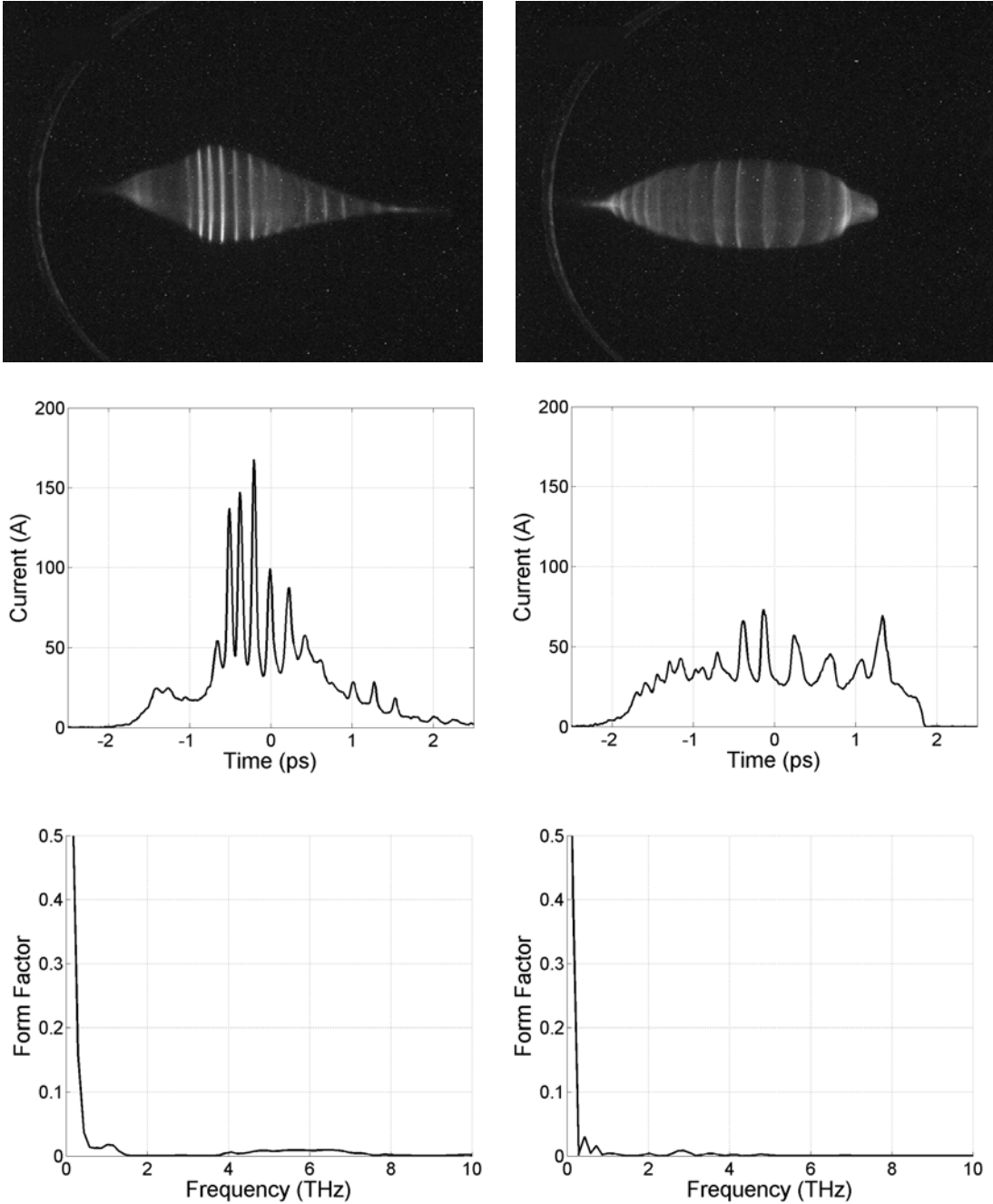
**Figure 4.35.** Data corresponds to **laser profile D**. Total charge is **145 pC**. Left hand panels, from top to bottom, correspond to the A-slope of the RF zero-phasing measurement, and show the raw data, the time profile, and the form factor. Right hand panels, from top to bottom, show the same for the B-slope.



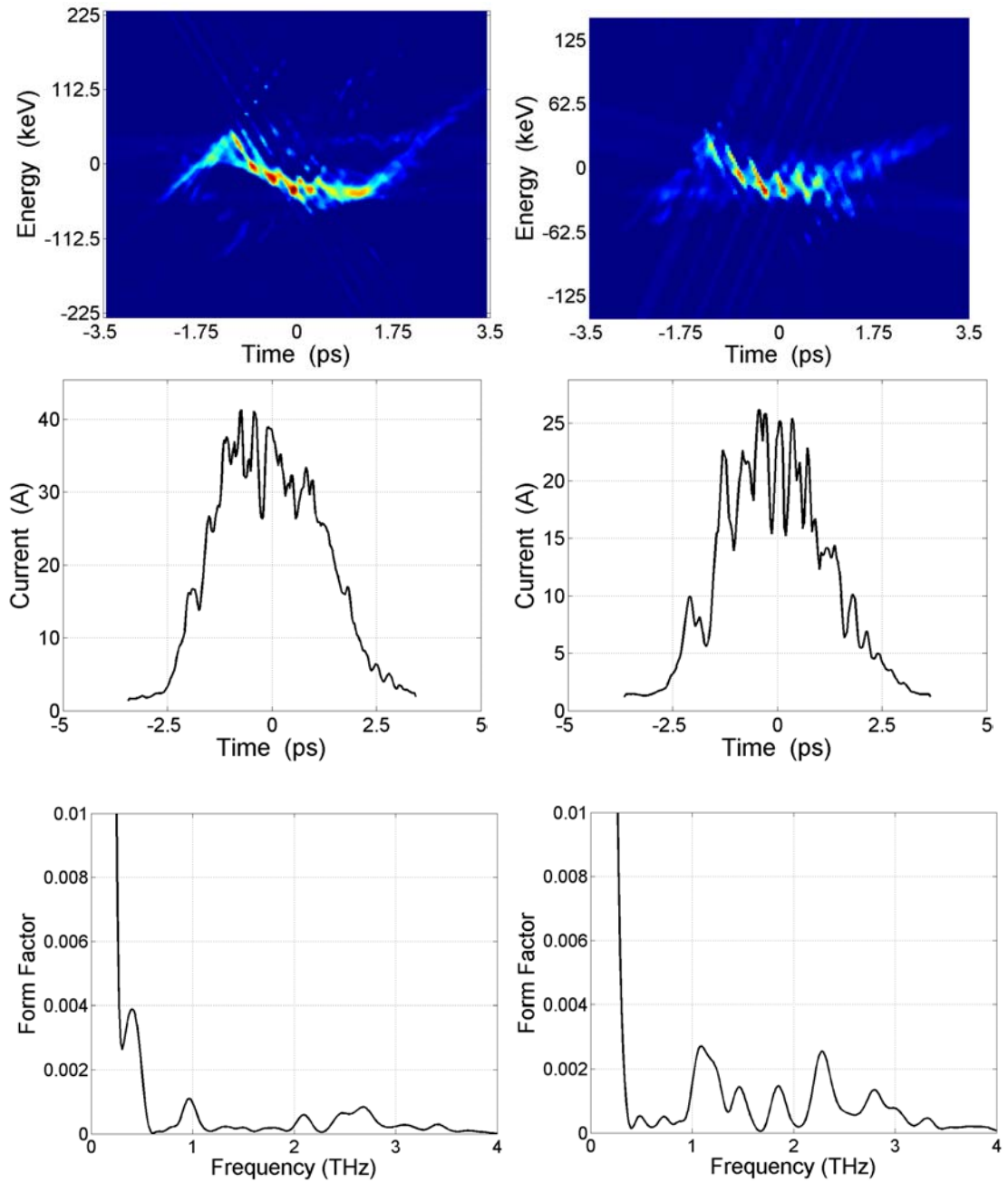
**Figure 4.36.** Data corresponds to **laser profile E**. Total charge is **180 pC**. Top left and top right show the RF zero phase A and B slope images, respectively. Immediately below are the tomographic reconstruction of the phase space, and the projection onto the time axis. At the bottom is the form factor of the longitudinal profile shown in the tomographic reconstruction.



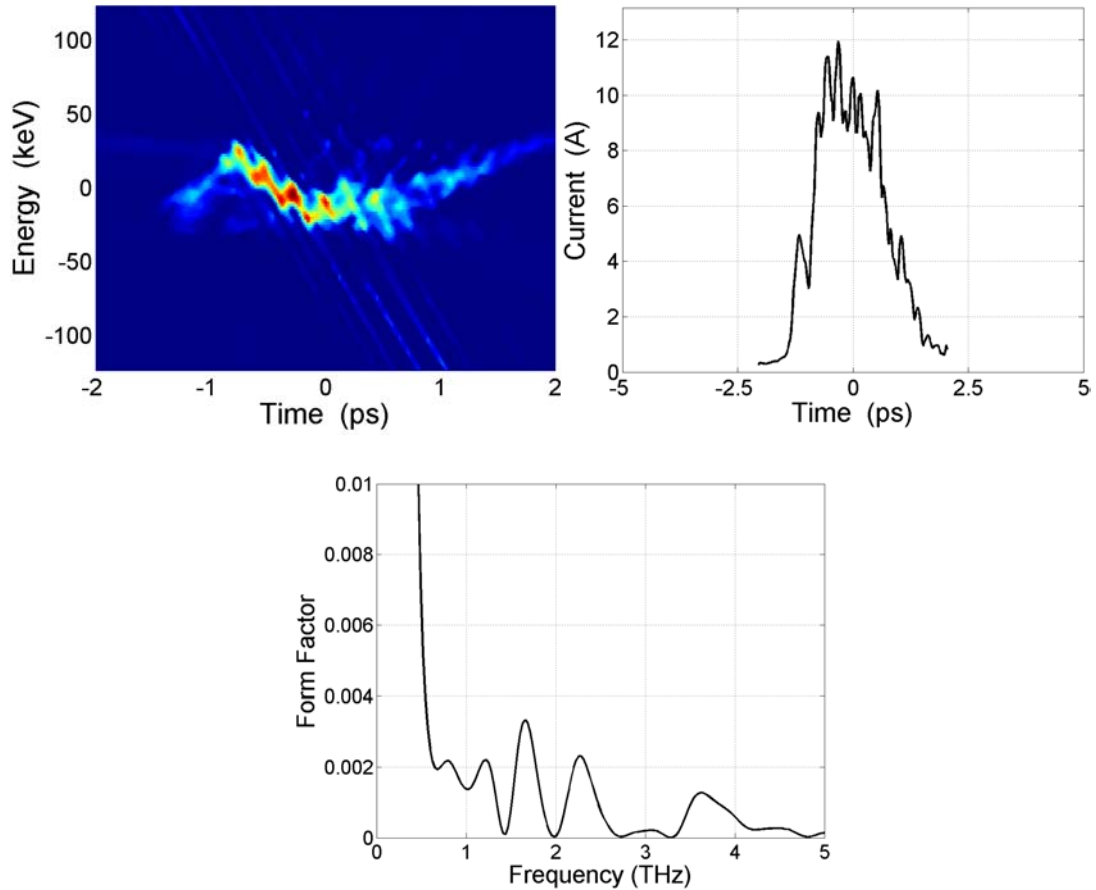
**Figure 4.37.** Data corresponds to **laser profile F**. Total charge is **20 pC**. Left hand panels, from top to bottom, correspond to the A-slope of the RF zero-phasing measurement, and show the raw data, the time profile, and the form factor. Right hand panels, from top to bottom, show the same for the B-slope.



**Figure 4.38.** Data corresponds to **laser profile F**. Total charge is **125 pC**. Left hand panels, from top to bottom, correspond to the A-slope of the RF zero-phasing measurement, and show the raw data, the time profile, and the form factor. Right hand panels, from top to bottom, show the same for the B-slope.



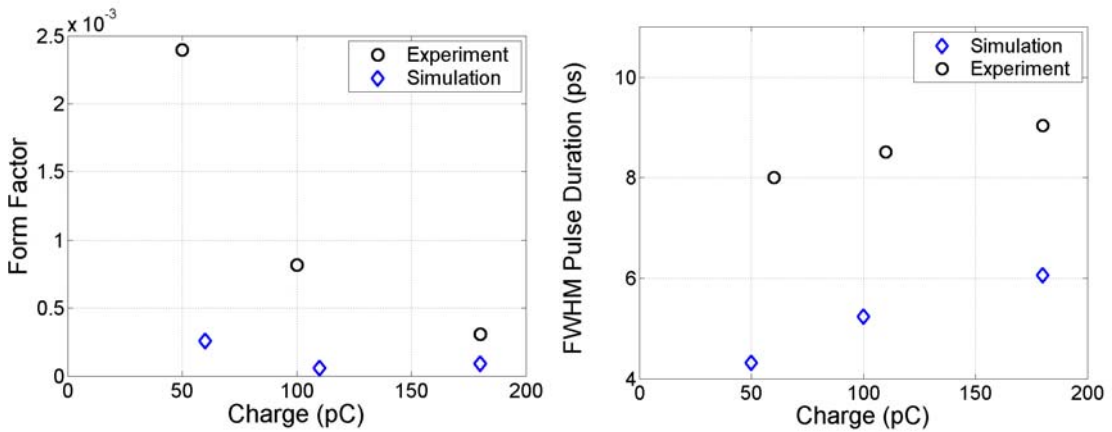
**Figure 4.39.** Data corresponds to **laser profile F**. Total charge is **125 pC (left)** and **75 pC (right)**. From top to bottom are the tomographic reconstructions of the phase space, the projection onto the time axis, and the form factor for each case.



**Figure 4.40.** Data corresponds to **laser profile F**. Total charge is **20 pC**. The upper left shows the tomographic reconstruction of the longitudinal phase space. The upper right shows a projection of the phase space onto the axis of time. The bottom figure shows the form factor for the bunch structure.

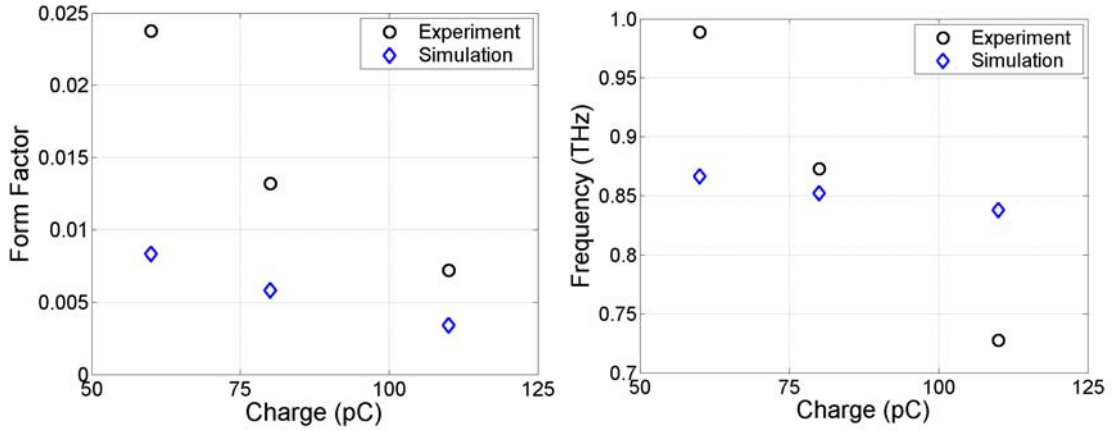
The simulations were useful for predicting trends related to the form factor as a function of charge and distance through the accelerator. Although fewer data points exist, it is still useful to see how well the experimental data matches the trends predicted by the simulations. Figure 4.41 shows the peak form factor value and the FWHM pulse duration for an unmodulated beam. It is important to note in this case

that the simulated initial longitudinal distribution is not the same as the experimental data points. However, the trends are similar, as expected; the peak form factor is small, and decreases with increasing charge, while the FWHM pulse width increases as a function of charge.



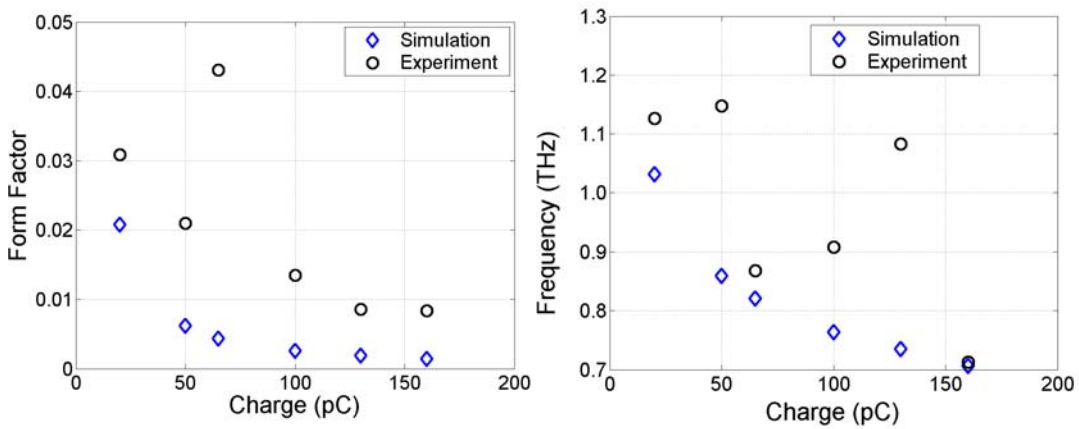
**Figure 4.41.** (Left) Peak form factor at 0.8 terahertz for an unmodulated electron beam. (Right) FWHM pulse duration as a function of charge for an unmodulated beam.

Figure 4.42 shows the peak form factor and peak modulation frequency for laser profile B. The trend of decreasing form factor and decreasing modulation frequency is noted for this case as well.



**Figure 4.42.** (Left) Peak form factor as a function of charge for laser profile B. (Right) Peak modulation frequency as a function of charge for laser profile B.

The results for laser profile C are a slightly more scattered. Figure 4.43 shows that the peak form factor seems to have the same downward trend as a function of charge with the exception of one data point. The experimental data for the peak modulation frequency does not match up as well.



**Figure 4.43.** (Left) Peak form factor as a function of charge for laser profile C. (Right) Peak modulation frequency as a function of charge for laser profile C.

Laser profile D is used for the terahertz radiation studies, but there are no tomographic reconstructions available. Profiles E and F are a result of pushing the limits of the Fabry-Perot system, and only the one data point is available for profile E. Figure 4.44 shows the peak form factor and modulation frequency as a function of charge for laser profile F. In this case, the experimental data continues to follow the trends of decreasing form factor and peak modulation frequency as a function of charge. Note that the absolute value of the peak form factor is nearing those seen in the unmodulated case, which is consistent with the washout seen in the longitudinal profiles. However, the peak frequency is recorded as high as 1.66 THz.

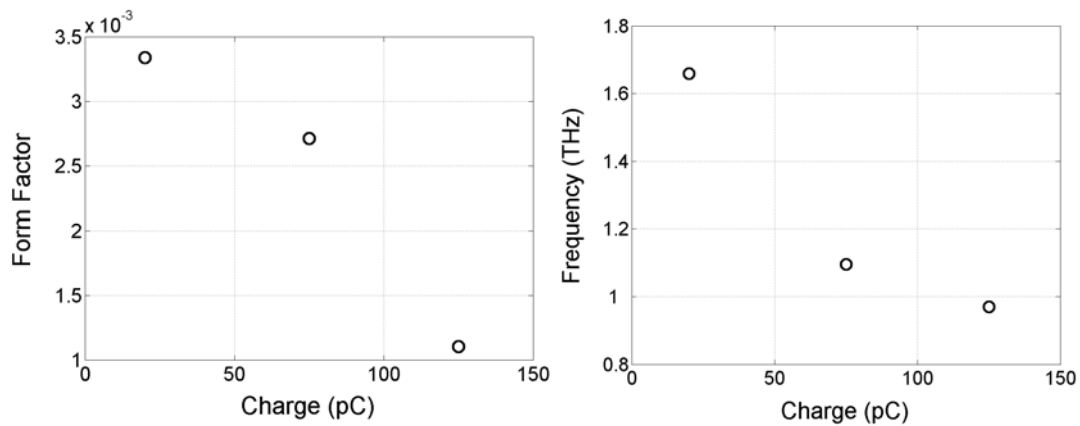


**Figure 4.44.** (Left) Peak form factor as a function of charge for laser profile F. (Right) Peak modulation frequency as a function of charge for laser profile F.

Even when the longitudinal density modulation washes out, there is still significant energy modulation on the electron beam. Studies have shown that even small amounts of density modulation can be transformed into energy modulation, including other experiments at the Source Development Laboratory<sup>64</sup>.

Indeed, the PARMELA simulations and the tomographic reconstructions of the longitudinal phase space show energy modulation is present on the beam even when significant density washout has occurred. Figure 4.44 shows the phase space and for two simulated cases that are similar to laser profile C, at 20 pC and 300 pC, at the exit of the electron gun. The average energy is approximately 4 MeV.

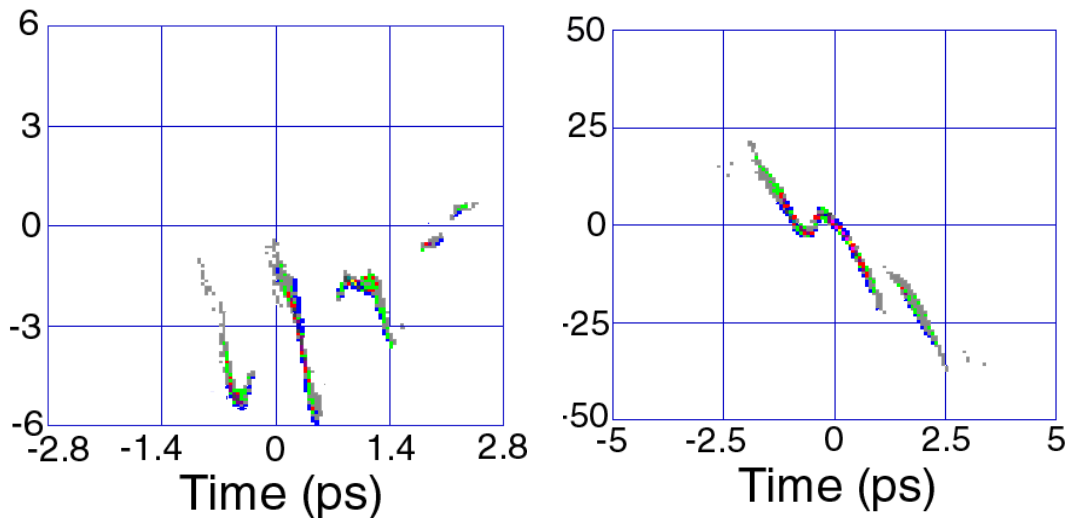


**Figure 4.44.** (Left) Phase space simulation for a 20 pC bunch similar to laser profile C. (Right) Phase space simulation for a 300 pC bunch similar to laser profile C. Vertical axis is measured in keV, and represents energy difference from the average particle energy, which is approximately 4 MeV.

The areas with low particle densities in the simulated phase space plots have been cleared so that the high density areas are easier to see. In both the 20 pC case and the 300 pC case, there is energy modulation in the phase space (i.e. energy varies in a periodic way with the longitudinal coordinate, or at least does not monotonically increase or decrease). In the 300 pC case, the density modulation undergoes significant washout (recall the form factor plots). However, in the 20 pC case the density washout is not significant.

Figure 4.45 shows the tomographic reconstruction of the longitudinal phase space for two cases similar to laser profile C, at 20 pC and 160 pC. In this case, the average energy is 38 MeV.

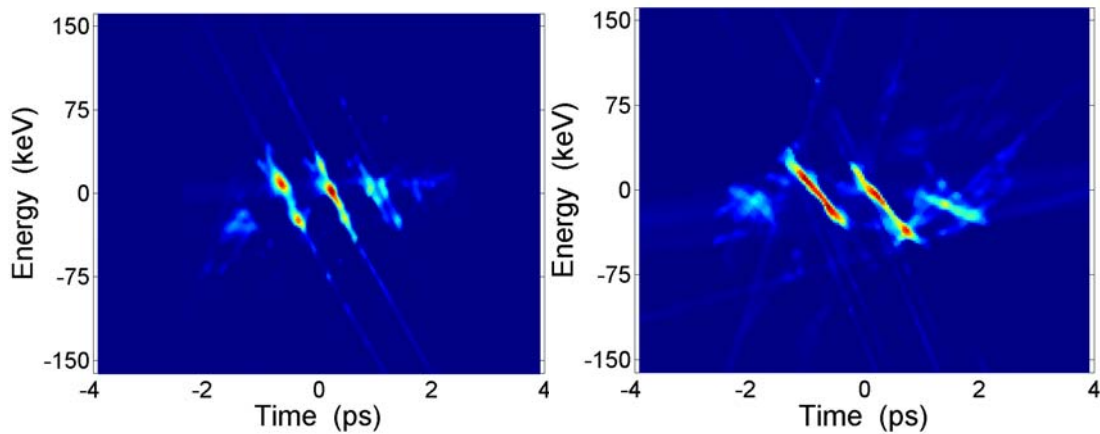


**Figure 4.45.** (Left) Phase space reconstruction for a 20 pC bunch similar to laser profile C. (Right) Phase space reconstruction for a 160 pC bunch similar to laser profile C. Vertical axis is measured in keV, and represents energy difference from the average particle energy, which is approximately 38 MeV.

Washout occurs because the phase space of each of the bunches grows in both the longitudinal and energy coordinate, such that when projected onto the longitudinal coordinate, their ends overlap. The individual bunches appear to be rotated as charge increases. If the rotated bunches could be set upright once again, their ends would no longer overlap in a projection on the longitudinal coordinate, and the density modulation would be recovered. This type of rotating action may be made possible by passing the electron beam through a bend magnet. In this case, dispersion due to path length differences in the bend causes low energy particles to lag behind while high energy particles will gain position. Shifting the positions of the various particles in this way would cause the phase space bunches to become upright once again, restoring the density modulation. In fact, simulations have shown that an energy modulation can be imposed on an electron beam by placing a physical mask in the middle of a chicane buncher. A typical chicane buncher consists of four bend magnets. A large energy spread is deliberately placed on the electron beam prior to entering the chicane. In the middle of the chicane, the electron bunch is arranged such that energy increases linearly as a function of the transverse length coordinate due to the particle path differences as a result of the energy spread. The physical mask, in this case a wire grid, removes some of the particles in a periodic way, and leaves a modulated energy spectrum. After passing through the remainder of the chicane, the particles are reorganized back onto the original axis of propagation. After the beam passes through the final bend magnets

in the buncher, the energy modulation is successfully converted to density modulation<sup>65</sup>.

It can be seen in the preceding data that information from the drive laser modulation is clearly carried on the electron beam through acceleration. The results indicate that electron beam modulation is tunable in several ways; by changing the initial drive laser profile, by changing the injection phase in the accelerator, and adjusting the amount of charge in the beam. Tunable modulation appears to have been achieved experimentally between 700 GHz and 1.6 THz. There are differences, however, between the longitudinal profiles measured using the tomographic reconstructions and the simulations. While the simulations do not have the exact initial conditions as the experiment, and do not necessarily include all of the relevant physics, the tomographic reconstruction technique is also not perfect. The reconstructed phase space is a best fit to the data collected by the RF zero phasing technique; computing the projections from the calculated phase space that would be measured in the experiment reveals a close, but certainly not exact comparison. Different algorithms and various numerical tricks can also reveal quite different solutions. In addition, the reconstruction is sensitive to timing jitter in the accelerator. If the beam arrives earlier or later than expected, the chirp imposed by the RF on the electron beam will be different from what is expected and cause errors in the reconstruction. Generating terahertz light from a modulated electron beam for other experiments is a useful application of this technology, but the terahertz light

can also be used as a diagnostic for the beam. In Chapter 5, the terahertz radiation generated from these modulated electron beams will be analyzed to help determine whether the actual electron longitudinal beam distribution is more closely related to the simulation results or the tomographic reconstructions.

## Chapter 5: Terahertz Radiation Generation

Generating terahertz light is one application for modulating the electron beam at the photocathode. As described in Chapter 1, the coherence of the terahertz light will depend on the longitudinal structure of the electron beam. Therefore, measuring the terahertz radiation, and comparing it to calculations for expected values, not only demonstrates this application, but also can be used to provide further evidence to confirm or refute the electron beam longitudinal measurements. This chapter provides a closer look at how the expected amount of terahertz radiation can be calculated for this particular experiment

### *5.1 Theoretical Predictions for Terahertz Radiation From an Electron Beam*

The description of transition radiation presented in Chapter 1, while valid for general comparison with other radiative devices, does not take into account many of the particular details associated with this experiment, as it represents an ideal situation. In order to compare the actual measured values with theoretical predictions, these details must be considered. The primary effects that need to be considered are those related to the finite size of the transition radiator, the geometrical construction of the accelerator and the transport system, and absorption

of terahertz radiation in the air.

### 5.1.1. Finite Transition Radiator

The calculations in Chapter 1 assume an infinitely large transition radiator is used to produce the light. The radiator does not appear infinite, however, when its radius is less than  $\gamma\lambda$  ( $\gamma$  is the Lorentz factor and  $\lambda$  is the radiated wavelength).

Assuming the beam arrives at normal incidence to the target, the backwards transition radiation can be calculated in the far field to be<sup>66</sup>

$$\frac{d^2W_1}{d\omega d\Omega} = \frac{q^2 \beta^2}{4\pi^3 \epsilon_0 c} \frac{\sin^2(\theta) A^2}{(1 - \beta^2 \cos^2(\theta))^2} \quad (5.1)$$

where

$$A = \frac{\int_{-\pi}^{\pi} d\alpha \int_0^u t dt K_1(t) \cos(\alpha) \exp(-it\gamma \cos(\alpha) \sin \theta)}{\int_{-\pi}^{\pi} d\alpha \int_0^{\infty} t dt K_1(t) \cos(\alpha) \exp(-it\gamma \cos(\alpha) \sin \theta)} \quad (5.2)$$

and

$$u = \frac{a\omega}{v_z \gamma} \quad (5.3)$$

where  $a$  is the radius of the radiator,  $\omega$  is the angular frequency of the emitted radiation,  $v_z$  is the electron velocity in the  $z$  direction,  $\theta$  is the angle from the direction of specular reflection, and  $K_1$  is the first order modified Bessel function of

the second kind. Equation 5.1 is an approximation that the beam hits the target at normal incidence. In this experiment, the beam actually hits the target at a 45 degree angle. The main result of the tilt is that the fields are not azimuthally symmetric due to the physical geometric effects of the tilt. The SDL staff has also developed a software package that uses numerical techniques to simulate terahertz radiation production<sup>67</sup>. Although it was not used extensively in this work, it is useful to look at one result, shown in Figure 5.1 which shows the transmission of terahertz radiation as a function of frequency from the source to the exit port of the accelerator beam pipe for the horizontally and vertically polarized light.

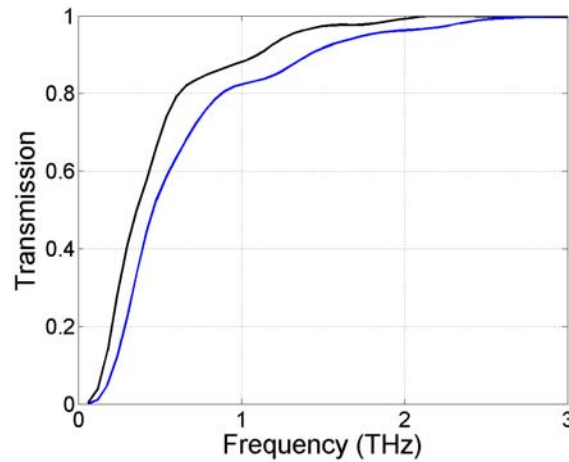


**Figure 5.1.** Transmission as a function of frequency for vertically polarized (black) and horizontally polarized (blue) terahertz light.

Integrating over the spectrum, the energy radiated into the two polarizations, given the parameters in this particular experiment, are different by 7.5%. The

calculations used in this work take an average target radius between the two effective sizes seen by the different polarizations in order to approximate the effect of the tilt, allowing the normal incidence approximation to be used. The result is equation 5.1.

Figure 5.2 shows the angular spectral distribution of terahertz radiation from a single electron calculated at various frequencies for the electron energy used in this experiment ( $\gamma=143$ ) and a 7.6 mm radiator (which is the effective size due to the actual incidence angle of 45 degrees).

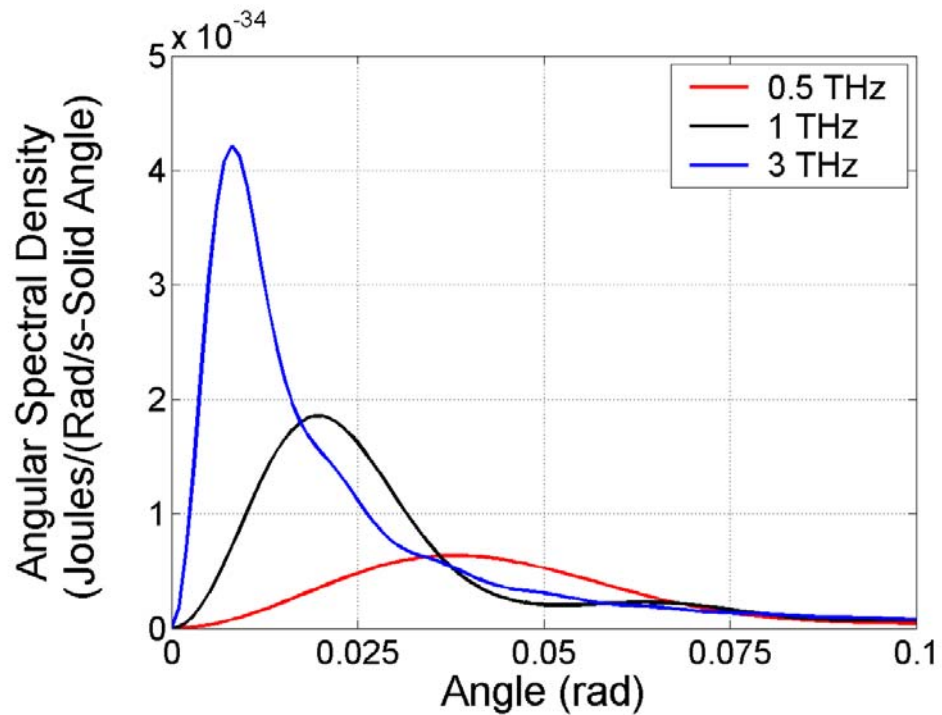
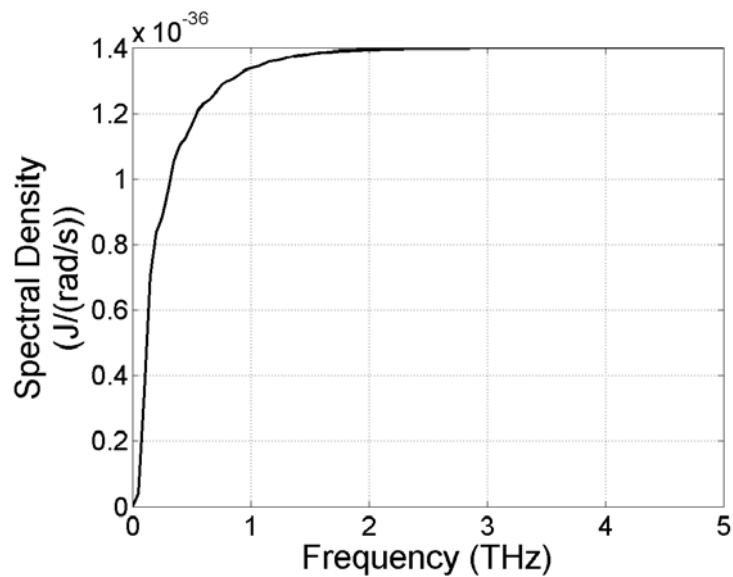


Figure 5.2. Demonstration of the finite radiator effect on transition radiation.

In Figure 5.2, as the frequency increases (i.e. the radiator becomes larger compared to the radiation), the angular spectral distribution approaches that of the infinite radiator, with the peak of the radiation at an angle of  $1/\gamma$ , which in this experiment corresponds to 0.007 radians. Even at 3 THz, the effects of the finite radiator size can still be seen. Examining lower radiation frequencies, one sees a lower angular spectral density at the peak, and that peak occurs at a much larger angle. Although the parameters chosen for calculating these properties are those for this particular experiment, the behavior of the plots follows that shown in other experiments<sup>68</sup>. Recall that most of the experimental data lies in these lower frequencies. Figure 5.3 shows the spectral density after integrating over entire calculated solid angle.



**Figure 5.3.** Spectral density of terahertz radiation.

Recalling the flat spectrum for transition radiation calculated in Chapter 1, it is evident from Figure 5.3 that the combination of the finite radiator size and exit aperture in the accelerator act like a high-pass filter and suppresses the long wavelength radiation. In the area of interest of this experiment, between 0.5 THz and 2 THz, this effect is significant. The MATLAB code for the calculation of the angular spectral density from one electron is given in Appendix B.5.

It is important to also note that Equation 5.1 is a far field approximation for the light generated by the transition radiation. Consistent with standard optics, when transition radiation emerges from the finite aperture, it proceeds first through a region that can be described by near field approximations, and transitions to a region that can be described by far-field approximations. According to Dobrovolsky and Shul'ga<sup>69</sup>, the radiation field approaches the far field form when the distance from the target,  $r$ , is greater than  $2\gamma^2c/\omega$ . In this experiment, the detector sits approximately 2 m from the source. Therefore, the far field approximations are valid for frequencies near 1 terahertz and higher. The near field approximations are only valid for frequencies much lower than 1 terahertz; calculating the angular spectral density in this region requires an exact expression. Since the electron beam modulation is near 1 terahertz in this experiment, the far field approximations are used.

### 5.1.2 The Transverse Form Factor

The effect of the longitudinal form factor on the spectrum of the radiation produced has been discussed extensively so far. In Chapter 1, the transverse component of the form factor was briefly mentioned. For this experiment, the transverse distribution is assumed to be Gaussian, which leads to a simple analytical expression for the form factor, given by

$$f(\omega) = e^{-\left(\frac{\omega \sin \theta \sigma_x}{c}\right)^2} \quad (5.4)$$

Unfortunately, the transverse beam size was not measured for every case, but was measured at various points to be between 400 and 800  $\mu\text{m}$ . Note that on axis, when  $\theta=0$ , the transverse form factor approaches 1. Figure 5.3 shows the transverse form factor at the angle of  $1/\gamma$ , where the transition radiation peak is found in the far field.

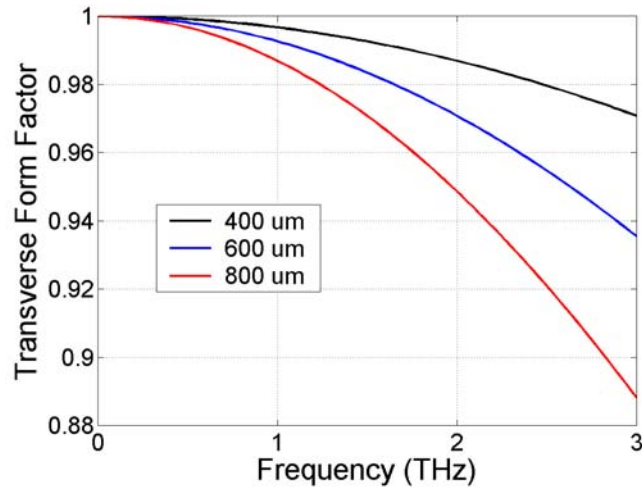


**Figure 5.4.** Transverse form factor as a function of frequency.

Figure 5.4 shows that the transverse form factor does not have an extremely large effect near 1 terahertz, where most of the beam modulation occurs in this particular experiment. In the terahertz radiation calculation, an average size of 600  $\mu\text{m}$  was used for determining the transverse form factor.

### 5.1.3 Light Transport System

The geometry of the light transport system also has an effect on the spectrum of radiation that emerges from the window of the accelerator. The window serves as an aperture that subtends 0.0169 steradians. In Figure 5.2, it can be seen that the peak of the angular spectral density as a function of angle depends on the frequency. Thus, an aperture will block the lower frequencies that appear at larger angles, while it will pass the higher frequencies that appear closer to the axis. Integrating the angular spectral density over the solid angle subtended by the exit aperture yields a slightly different spectral density compared to the one integrated over the larger set of angles. This effect is seen in Figure 5.5.

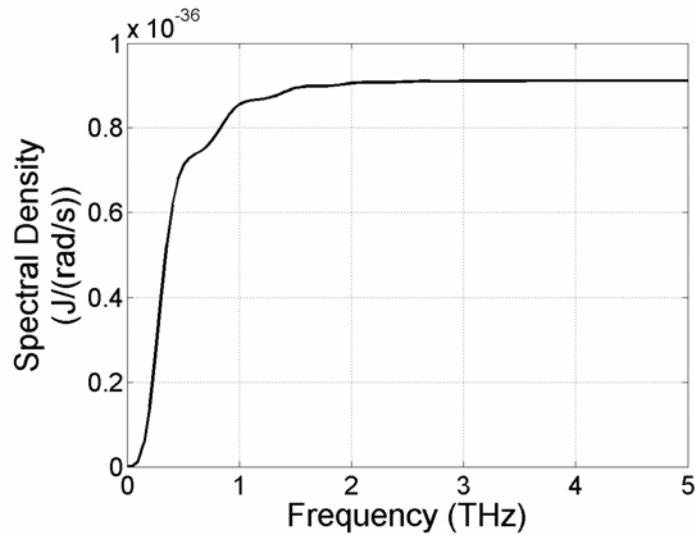


**Figure 5.5.** Spectral density of terahertz radiation resulting from an integration over the solid angle subtended by the exit aperture.

After the terahertz light exits the accelerator, it is collimated by a lens and collected by a light cone. A simple ray diagram, Figure 5.6, shows how the light cone works<sup>70</sup>. The light cone itself is defined as *abcd*. Crossing a boundary, say into *abef*, represents a reflection. The rays within the aperture of the beam pipe proceed unaffected by the cone. The rays near the outside bounce off the wall, and reflect at the appropriate angle, and become skew rays inside of the light pipe (ray *BB*). Light rays at extreme angles (ray *AA*) may be prevented from entering the light pipe at all. In early versions of the experiment, the light would proceed from the light cone, through the copper waveguide, and directly into the detector aperture. However, in this experiment, the filters and filter wheel were placed in an open area between the end of the light pipe and the final detector aperture. The geometry of this setup is

such that the skew rays are not accepted at the detector. Unfortunately, this essentially defeats the purpose of having the light cone in the first place. In order to accommodate this, the terahertz radiation was integrated over a smaller solid angle compared to the case where the light pipe ends at the detector aperture. This is one of the reasons why less terahertz energy was recorded in recent experiments compared with previous experiments<sup>71</sup>.

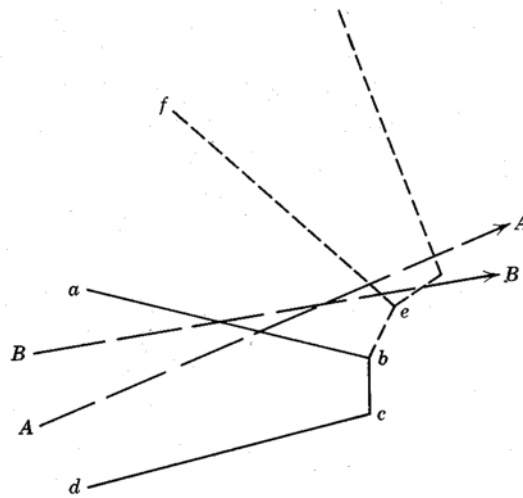


**Figure 5.6.** Ray tracing analysis of the light cone collector. (Reprinted with permission from John Wiley and Sons, Inc.<sup>72</sup>).

After being collected by the light cone, the terahertz radiation is guided to the detector by approximately 1 meter of copper pipe. The attenuation of TE and TM electromagnetic waves in circular guides are given, in nepers/meter, by<sup>73</sup>

$$\alpha_{TMnl} = \frac{R_s}{a\eta} \frac{1}{\sqrt{1 - \left(\frac{f_c}{f}\right)^2}}$$

and

$$\alpha_{TE_{nl}} = \frac{R_s}{a\eta} \frac{1}{\sqrt{1 - \left(\frac{f_c}{f}\right)^2}} \left[ \left(\frac{f_c}{f}\right)^2 + \frac{n^2}{p'_{nl}{}^2 - n^2} \right] \quad (5.5)$$

where  $a$  is the radius of the pipe,  $\eta$  is the impedance of free space, and  $p'_{nl}$  is the  $l^{\text{th}}$  root of  $J'_{nl}(x)$ .  $R_s$  is the surface resistivity of copper, given at  $2.61 \cdot 10^{-7} \sqrt{f}$ . The cutoff frequency,  $f_c$ , is given by

$$\frac{p'_{nl} c}{2\pi a}$$

It turns out that because the pipe is so large compared to the wavelength, it supports a large number of modes. Since the mode structure of the transition radiation is not known in this experiment, the attenuation in the waveguide is approximated considering  $f$  to be much larger than  $f_c$ . Additionally, the TE modes are generally attenuated less than the TM modes (the term involving  $p'_{nl}$  is less than 1, while the  $f_c/f$  term goes to zero), so the attenuation can be approximated by  $R_s/a\eta$ . Figure 5.7 shows the approximation used for attenuation of the terahertz light in the copper pipe. Although using a different method to arrive at the solution, this is close to the transmittance curve for large light pipes found by others<sup>74</sup>.

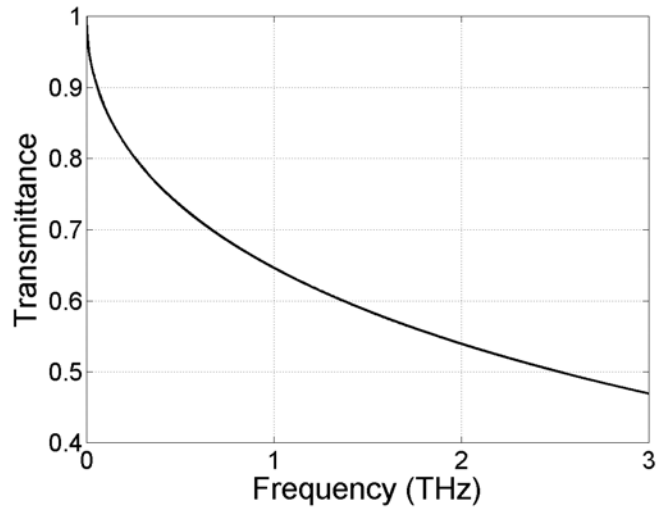


**Figure 5.7.** Terahertz light transmittance as a function of frequency through the copper pipe light transport sections.

The copper pipe itself was broken into three sections to properly steer the light to the detector. Each of the sections are connected by a corner reflector. These are known to be lossy across the entire spectrum in question, but the total amount of loss was not known<sup>75</sup>. This was left as a free parameter in the calculation, and was eventually set at 40%.

#### 5.1.4 Atmospheric Absorption

This experiment was conducted in open air. Most experiments involving terahertz radiation are either conducted under vacuum or in a dry nitrogen environment in order to remove water vapor, because it absorbs significant amounts

of terahertz radiation. In this experiment however, absorption of the terahertz light due to water vapor had to be taken into account. The transmission curve for terahertz light traveling through the atmosphere, shown in Figure 5.8, was provided by NIST<sup>76</sup>, and represents the distance traveled by the light in this experiment, from the accelerator exit aperture, past the lens and light cone, and through the copper pipe, at 296 K and 30% humidity.

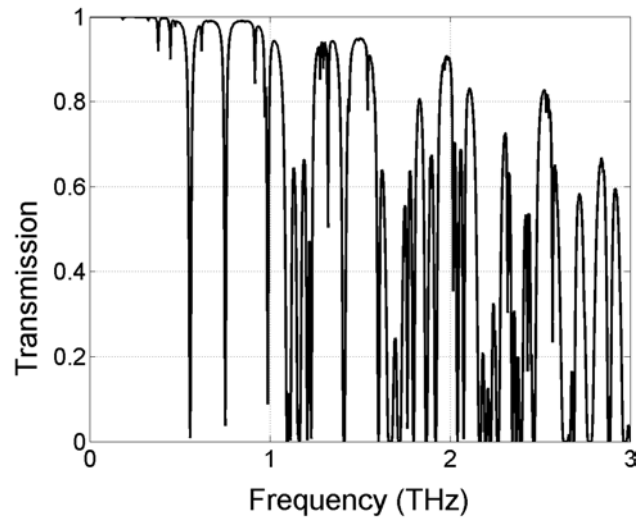


**Figure 5.8.** Transmission of terahertz radiation through 1.5 m of air.

## 5.2 Terahertz Filters

The spectrum and energy of the generated terahertz light are considered to be very important characteristics. These measurements not only help to characterize the light as a source, but also serve to confirm the longitudinal structure of the

electron beam in the accelerator. The energy of the light pulse was measured with the bolometer, which will be discussed further in the next section. A scanning Michelson interferometer adapted with optics for the terahertz frequency regime was available to measure the spectrum, but it required a great deal of time in order to use it due to the shot to shot fluctuations of the accelerator. Since the available experimental time was extremely limited, it was necessary to develop a faster technique to measure the spectral content of the terahertz signal.

Several different filters, which are described below, were employed in order to glean information about the spectral content of the terahertz light. A separate measurement was made for each filter that was placed individually in front of the bolometer. This experimental measurement was compared to the theoretical model described above, and reasonable agreement should indicate the spectrum actually present in the experimental case. Although this is not the ideal method for determining the spectral content of the terahertz light, a similar type of analysis was made by Leemans<sup>77</sup> for their terahertz source.

The design of the terahertz filters was based on ideas first developed for microwave filters<sup>78</sup>. More recently, these ideas were used for terahertz applications<sup>79</sup>. The filters are constructed from a perforated metal sheet, i.e. an array of uniformly spaced apertures, with either Cartesian or hexagonal symmetry. The finite thickness of the sheet results in the filter having resonance and waveguide-like characteristics. Light at wavelengths much smaller than the hole will transmit through the mesh,

while light with large wavelengths will be reflected, resulting in a high pass filter.

The frequency characteristics of these filters are dependent on the hole size, the spacing between the holes, and the thickness of the material. As given by Chen<sup>80</sup>, the transmission coefficient for such a filter is given by

$$T = \frac{1}{1 - i \cdot \left( A + B \tanh\left(\frac{1}{2} i\beta l\right) \right)} - \frac{1}{1 - i \cdot \left( A + B \coth\left(\frac{1}{2} i\beta l\right) \right)} \quad (5.6)$$

where

$$A = 12 \sqrt{\frac{4}{3} \left(\frac{\lambda}{s}\right)^2 - 1} \left[ \frac{J_1'(x)}{1 - \left(\frac{x}{1.841}\right)^2} \right]^2 - \frac{12}{\sqrt{\frac{4}{3} \left(\frac{\lambda}{s}\right)^2 - 1}} \left[ \frac{J_1(x)}{x} \right]^2$$

$$x = \frac{2\pi d}{s\sqrt{3}}$$

$$B = 0.21 \left(\frac{s}{d}\right)^2 i\beta\lambda$$

$$\beta(\nu) = \frac{2\pi\nu}{c} \sqrt{1 - \left(\frac{p_{nm}c}{\pi d\nu}\right)^2}$$

where  $\nu$  is the frequency,  $\lambda$  is the wavelength,  $c$  is the speed of light,  $d$  is the hole diameter,  $l$  is the thickness of the filter, and  $s$  is the spacing between the holes (in a hexagonal close packed structure). Equation 5.6 is actually an approximation valid for the TE<sub>11</sub> mode, so  $p_{nm}=1.841$ .

These equations were used as a guide when purchasing materials to use for the terahertz filters. Perforated stainless steel screens manufactured by Buckbee-Mears are sold as stock items for other purposes by Internet, Inc., but were well suited for use as a terahertz filter. There are two different types of screens available: photo-chemically etched stainless screens, and electroformed nickel meshes. Each type can be specified by thickness, hole size, and hole spacing, although they are not necessarily independent of each other due to the manufacturing process. In the case of the photo-chemically etched meshes, the thickness of the material needs to be on the order of the hole size because the etch works in all directions. Additionally, the holes are tapered as a result of this process. The company claims +/- 15% accuracy for the specified hole diameter, but some were measured to be less accurate than that. In the case of the electroformed meshes, the hole spacing is related to the combination of the wire thickness and hole diameter, and the thickness is defined by that of the wire. The holes in the electroformed meshes are also hexagonal rather than circular.

A variety of products were chosen to test as filters, including those with stock numbers BE 1400, BE 1000, BE 0806, BE 0600, BE 0500 (photo-etched), and BM 125-01 (electroformed). The photo-chemically etched screens are made from steel, and the electroformed mesh is made from nickel. Although InterNet, Inc. publishes the physical properties of the meshes online<sup>81</sup>, the published values of the hole diameters and hole spacing were sometimes found to be erroneous by more than 20%. Table

5.1 shows the relevant parameters for each of these materials as measured with a profilometer. The profilometer essentially scans a stylus across the surface in and measures the relative height of the surface features. The diameter of the hole can be easily measured from the surface profile. The published values of the thickness were confirmed to be correct with a set of calipers.

Material Stock Number	Hole Size (d) ( $\mu\text{m}$ )	Distance Between Holes (s) ( $\mu\text{m}$ )	Thickness ( <i>l</i> ) ( $\mu\text{m}$ )
BE 1401	595.1	1049.9	355.6
BE 1000	299.1	555.3	254.0
BE 0805	277.8	393.4	203.2
BE 0600	200.5	253.0	152.4
BE 0500	173.3	280.5	127.0
BM 125-01	169.9	203.2	33.3

**Table 5.1.** Measured physical properties of meshes used for terahertz filters

Photographs taken with an optical microscope and digital camera of the various photo-chemically etched screens at the same magnification are shown in Figure 5.9.

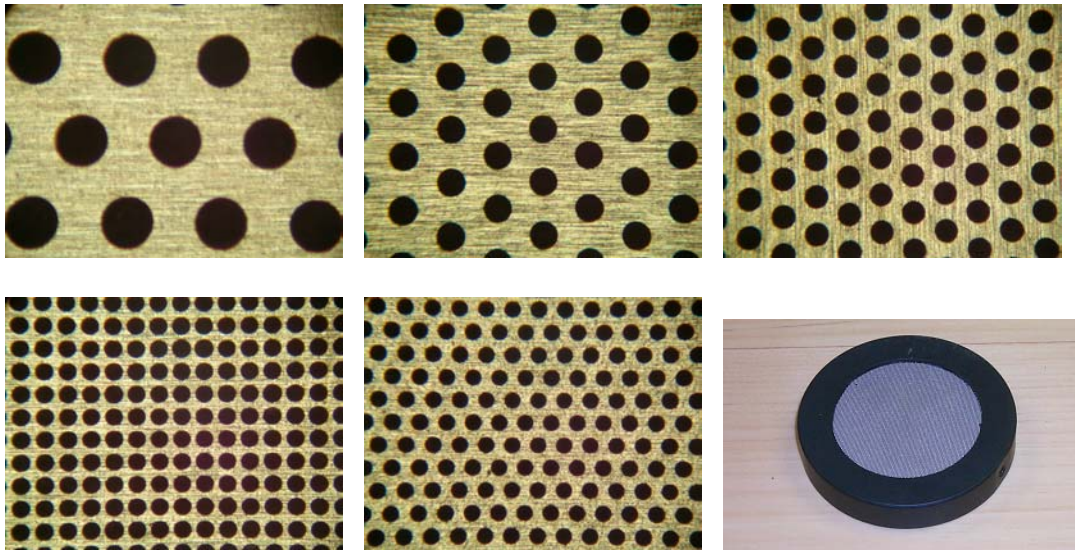


**Figure 5.9.** Photographs of steel meshes used for terahertz filters. In order of decreasing hole size, BE 1401, BE 1000, BE 0805, BE 0600, and BE 0500. The same magnification is used for all. A photograph of one of the meshes placed in an optical mount is on the bottom right.

The transmission characteristics of the filters were calibrated with two different light sources, the National Synchrotron Light Source (NSLS) at Brookhaven National Laboratory, and at the National Institute for Standards and Technology (NIST). The NSLS is a synchrotron light source and the terahertz band was used to illuminate the filters, whereas at NIST, a mercury arc lamp was used.

Both setups used the same diagnostic, a Fourier Transform Infrared (FTIR) spectrometer. In an FTIR system, the incident broadband light passes through a Michelson interferometer before entering the sample chamber, and then passes through to a detector. The data is taken by adjusting the length of one of the delay arms, and recording the detector signal at each point. The result is called an

interferogram, and the spectrum is found by taking the Fourier transform of the interferogram. Figures 5.10 and 5.11 show the layout of the FTIR system at NIST, the bolometric detector, and how the sample is placed in front of the detector.



**Figure 5.10.** Views of the FTIR spectrometer at NIST.



**Figure 5.11.** (Left) Bolometric detector (Right) Close-up of sample and sample holder

The system is first used to take a baseline spectrum, which is the spectrum of the source. When the sample is placed in front of the detector, the transmission (and absorption) characteristics are determined by taking the ratio of the measured spectrum to the baseline spectrum. Figure 5.12 show the reference spectrum for both the mercury arc lamp at NIST as well as the synchrotron light source at BNL.

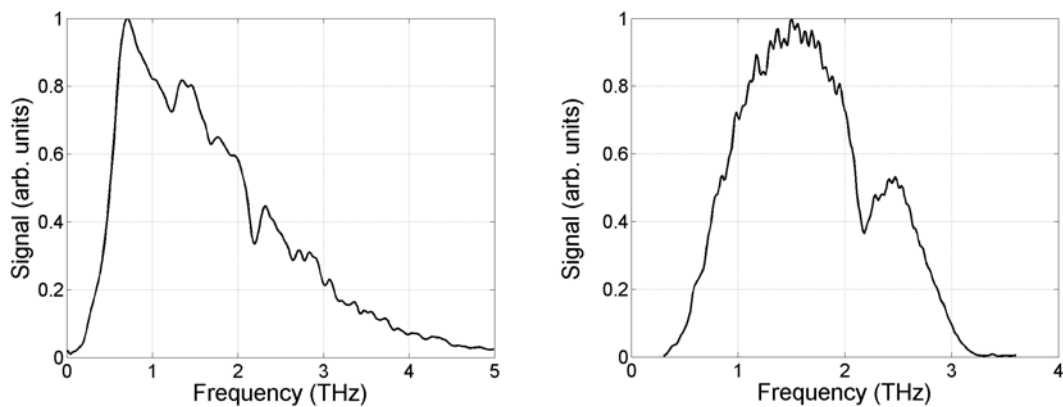


**Figure 5.12.** (Left) Measured terahertz spectrum of mercury arc lamp at NIST. (Right) Measured terahertz spectrum of National Synchrotron Light Source (NSLS) on the U-12IR beam line at Brookhaven National Laboratory. Note one of the larger water absorption lines seen clearly in both spectra just above 2 terahertz.

The test source spectra are not uniform across the area of interest (i.e. 0.5-3 THz), and drop off significantly at the edges of this region, and eventually cannot be discerned from noise. The sources exhibit temporal variation in output, particularly at the edges of the region of interest. One commonly used technique to determine the region of valid data is by taking a "100 percent line." This calls for the examination of the ratios of various reference spectra taken at different times. In

regions where the source is stable, the ratio of two reference spectra will be near 1, or 100%. In regions that are dominated by noise, the ratio will deviate from this value. Figure 5.13 shows 100 percent lines at various times during calibration with the mercury arc lamp at NIST as well as the synchrotron source at the NSLS. The vertical black lines denote the spectral area of interest. It is interesting to note that the synchrotron source seems to be much more stable than the mercury arc lamp in the low terahertz region.

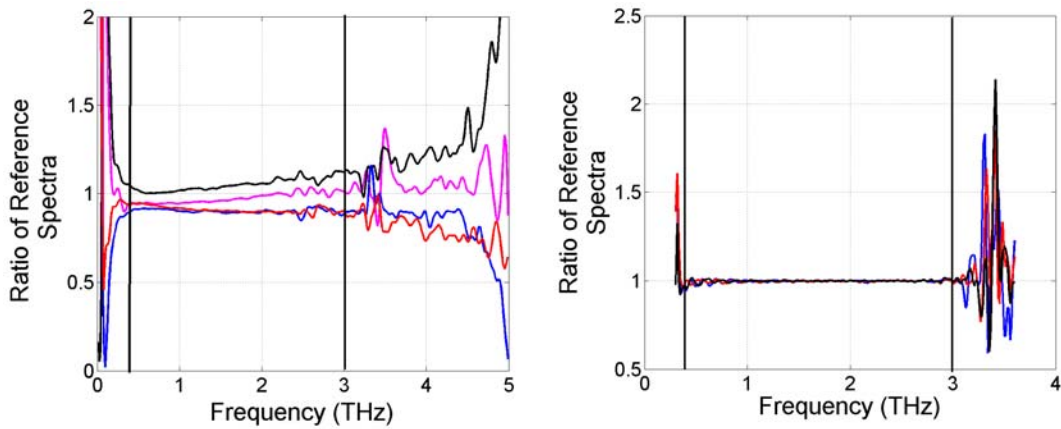


**Figure 5.13.** (Left) 100 percent lines at various times during the calibration at NIST. (Right) 100 percent lines at various times during the calibration at the NSLS. The black vertical lines denote the area of interest for this experiment.

Figures 5.14-17 shows the calibrations for each of the filters. Black traces represent the theoretical predictions based on Chen's model, blue traces represent calibrations at NIST, and red traces represent calibrations at the NSLS. Sample code to calculate the theoretical traces can be found in Appendix B.

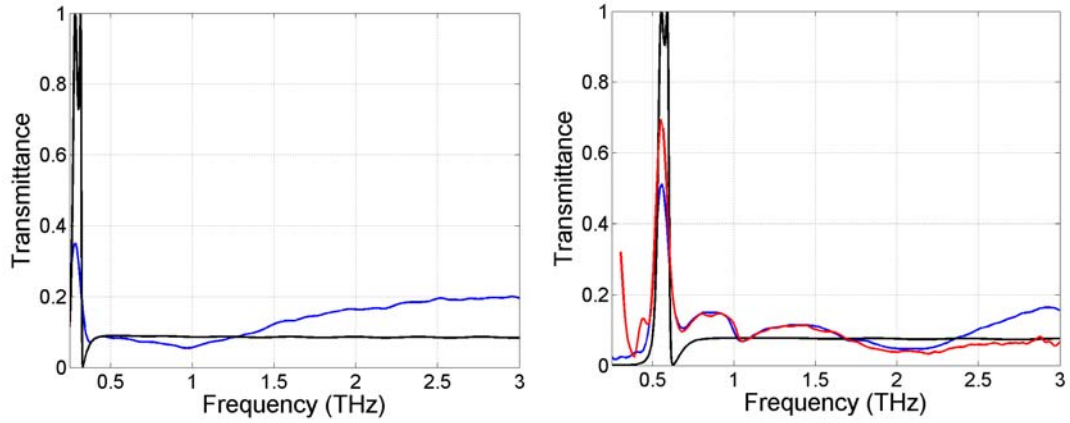


**Figure 5.14.** (Left) NIST (blue) calibration of BE 1401 (Right) NIST (blue) and NSLS (red) calibration of BE 1000. Black traces correspond to theoretical predictions.

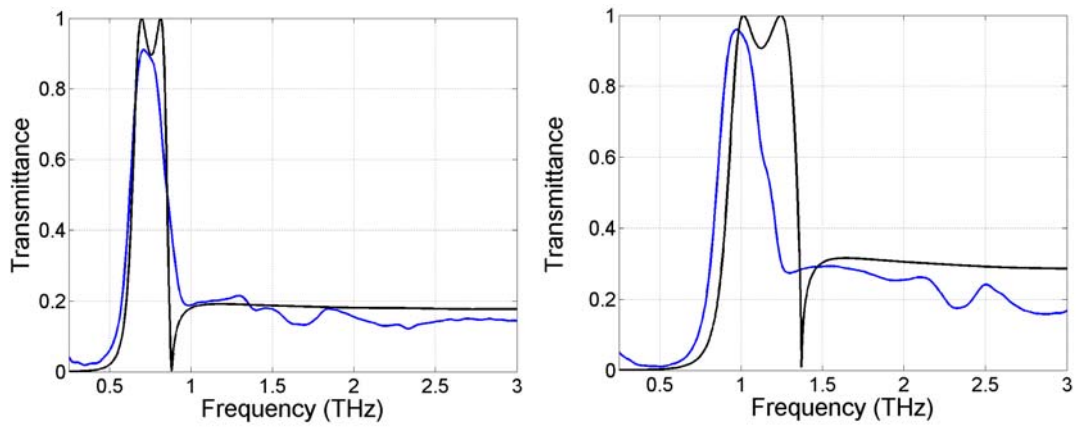


**Figure 5.15.** (Left) NIST (blue) calibration of BE 0805. (Right) NIST (blue) calibration of BE 0600. Black traces correspond to theoretical predictions.

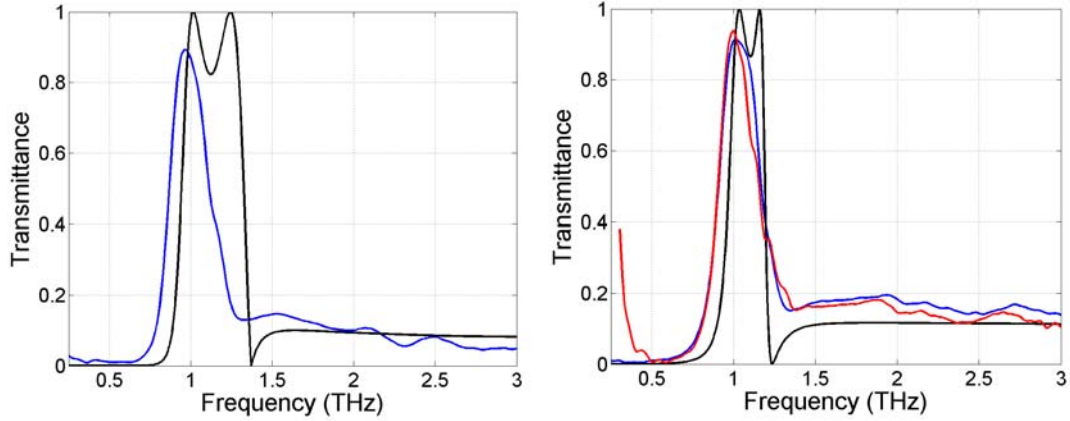


**Figure 5.16.** (Left) NIST (blue) calibration of a stack of two sheets of BE 0600. (Right) NIST (blue) and NSLS (red) calibration of BE 0500. Black traces correspond to theoretical predictions.

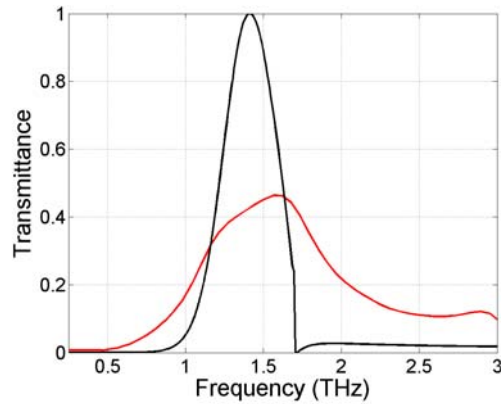


**Figure 5.17.** NSLS (red) calibration of a stack of four sheets of BM-125-01. The black trace corresponds to the theoretical predictions. Note that this material has hexagonal holes compared to circular holes used in the other materials and theoretical calculations.

Generally speaking, the measured transmittance of the mesh filters corresponds well to the theoretical curves, with the exception of the electroformed mesh. This is likely because the shape of the hole is not round. Additionally, when calibrations were available from both NSLS and NIST, they agree with each other

quite well. This degree of correlation between experiment and theory is about the same as that seen by Winnewisser<sup>82</sup>.

In addition to calibrating the filters at normal incidence, the calibration was done for two of the filters at various angles. Figure 5.18 shows the measured angular dependence of the transmittance.

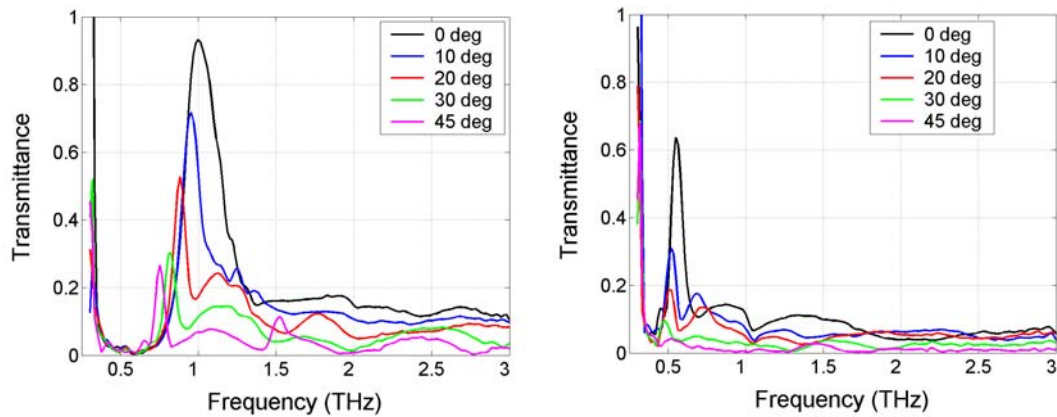


**Figure 5.18.** NSLS calibration of BE 0500 (left) and BE 1000 (right) at various angles.

Note that the transmittance is fairly sensitive to angle of incidence. As a result, when the filters were actually installed into the measurement system, care was taken to ensure that they were as close to normal incidence as possible.

As mentioned earlier, one of the critical elements in this experiment was making the best possible use of beam time. Changing the filters by hand would involve shutting down the accelerator, performing the required safety checks, entering the area controlled due to radiation, changing the filter, and then restarting the system. Instead, the filter change was automated by using a filter wheel attached

to a motor that could be controlled from outside of the radiation vault. A CCD camera was mounted near the filter wheel to ensure that the filters were properly in place. Unfortunately, the wheel only had five places for filters. One slot was left open in order to make an unfiltered measurement. Four filters were chosen for the other slots: BE 0805, BE 0600, a two sheet stack of BE 0600, and BM-125-01. These were chosen because they offered a wide variety of filters with center frequencies that seemed appropriate for the experiment. The peak transmission of each of the filters are located at 0.703 THz, 0.967 THz, 0.967 THz (with greater attenuation in the stop band), and 1.56 THz respectively. For convenience, they will be referred to as filters #1, #2, #3, and #4 throughout the rest of this document, and are summarized in Table 5.2.

Reference Number	Material Stock Number	Frequency of Peak Transmittance
#1	BE 0805	0.703 THz
#2	BE 0600	0.967 THz
#3	BE 0600 (Stack of two)	0.967 THz
#4	BM-125-01	1.56 THz

**Table 5.2.** Summary of filters used for terahertz radiation measurements.

### 5.3 Terahertz Radiation Measurements

Measuring the terahertz radiation produced by the pre-modulated electron beams serves not only as a characterization of a source, but also a diagnostic that helps to identify the structure of the electron beam. In this case, the light is produced by transition radiation, and is carried through the light transport system and filters described in the previous sections. The detector is a silicon bolometer built by IR-Labs, which has a responsivity of  $2.7 \cdot 10^5$  V/W<sup>83</sup>, plus a gain of 200 set by a preamplifier. The detector itself is capable of measuring incident light between 2  $\mu\text{m}$  and 3 mm<sup>84</sup>. However, a low pass filter provided by the manufacturer was used to block light at wavelengths shorter than 100  $\mu\text{m}$  or frequencies larger than 3 terahertz. The response of the detector across the spectrum of interest is assumed to be flat<sup>85</sup>.

The energy that reaches the detector at the end of the transport system is given by the following equation,

$$\begin{aligned}
 W_{total} = & \iiint (\sin \theta)(d\theta)(d\phi)(d\omega) \frac{d^2W_1}{d\omega d\Omega} * \\
 & (N_e + N_e(N_e - 1)f_L(\omega, \theta)f_T(\omega, \theta)) * \\
 & T_{air}(\omega)T_{filt}(\omega)T_{guide}(\omega)T_{bend}
 \end{aligned} \tag{5.7}$$

where the radiation from a single electron,  $d^2W_1/d\omega d\Omega$ , is modified by the

longitudinal and transverse form factors,  $f_l(\omega, \theta)$  and  $f_t(\omega, \theta)$ , the number of electrons in the bunch,  $N_e$ , the transmittance due to water absorption in the air,  $T_{air}(\omega)$ , the transmittance due to the waveguide,  $T_{guide}(\omega)$ , the transmittance due to the filters,  $T_{filt}(\omega)$ , and the transmittance due to the bend,  $T_{bend}$ . Finally, the radiated energy is integrated over the appropriate solid angle and the spectral range from DC to 3 terahertz (the cutoff at long wavelength is due to losses at the exit aperture, and this is taken into account in the radiation calculation from a single electron).

$W_{total}$ , as expressed in Equation 5.7, was measured for each initial laser profile, at each charge level, and with each filter available on the filter wheel. In this section, the term "measurement" refers to actual signals detected at the bolometer for these cases. The term "simulation" refers to the results of an analytical calculation used to predict the energy of the terahertz light measured at the bolometer based on the electron beam longitudinal profile predicted by the PARMELA simulation. The term "calculation" also refers to the results of an analytical calculation used to predict the energy of the terahertz light measured at the bolometer, but the calculation is based on the longitudinal profile of the electron beam as measured experimentally with the RF zero phasing technique in combination with the tomographic reconstruction. For each case, the measurements, simulations, and calculations are all compared.

Four different filters were used to measure the terahertz energy at the detector for each of the different charge levels and initial longitudinal distribution. As mentioned in the previous section, the filters chosen for this task were #1, #2, #3,

and #4. During some of the experiments, #3 had not yet been installed on the filter wheel, so in some cases, the data from #3 is missing. Additionally, an unfiltered measurement was taken for each case. Although the bolometer is considered best used as a relative measurement device<sup>86</sup>, the responsivity of the detector was used to estimate absolute energy levels in each pulse.

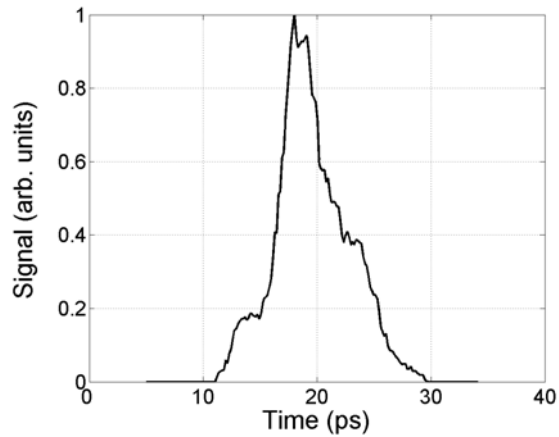
When the experiment was performed, it was arranged as a "charge scan," where a specific laser profile was used at various levels of charge. It is common practice to look at total radiated power as a function of charge, and if the light is coherent, it will exhibit a quadratic dependence on charge since  $W_{\text{total}}$  is proportional to  $f(w)*N^2$ . However, since the longitudinal distribution of the electron beam is a function of charge, the form factor changes as charge goes up. In fact, it was discussed in Chapter 4 that the form factor and its peak frequency fall rather quickly with increasing charge. As a result, not only does the total energy not increase quadratically with charge, it doesn't even increase directly with charge. In fact, when using the filters to probe the higher frequencies, the amount of energy seen at the detector can actually decrease with increasing charge. This occurs because as the charge is increased, the peak modulation frequency scans across the passband of the filter. Combining this effect with the falling amplitude of the form factor lead to this unexpected result.

In addition to the charge scan, the data is also presented as a series of measurements with each of the different filters for a given charge level and initial

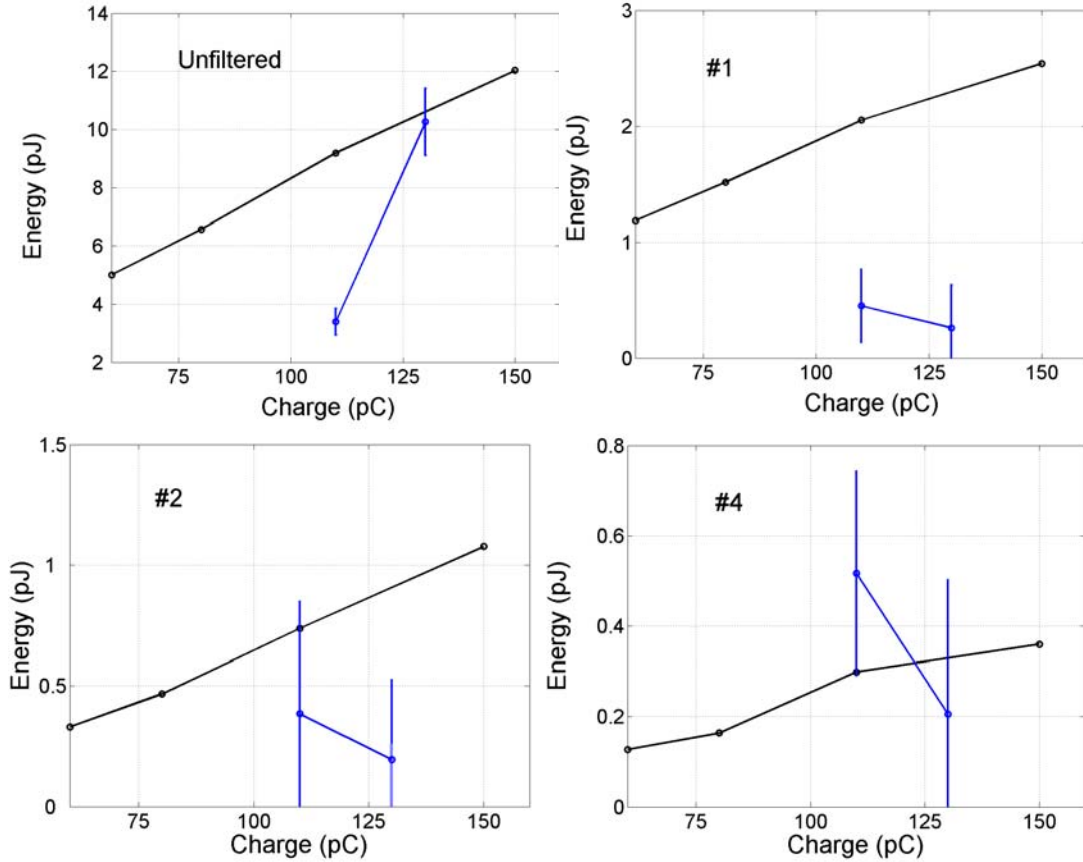
laser profile. This is intended to show how the simulated and calculated predictions compare with the measurements for each electron beam longitudinal distribution. Since a spectrometer was not available to carefully measure the spectrum, a close agreement between the simulations or calculations and the experimental measurements indicate how closely the simulated or calculated spectrum is related to the spectrum actually produced through transition radiation by the electron beam. The spectra generated with the simulation and calculations are presented at the exit aperture of the accelerator, before all of the losses due to the transport system and water absorption take place. In each case, only the spectra that are believed to have been achieved experimentally are shown; spectra predicted by simulations that do not have an experimental data point relating to terahertz radiation measurements are not shown.

Figure 5.20 shows the results of the charge scan for an unmodulated electron beam, for each of the filters, and compares the measured values to simulated and calculated predictions. This unmodulated beam corresponds to laser profile A from Chapter 4, reprinted in Figure 5.19. Each plot is labeled with the filter used to take that particular charge scan. The plots showing the simulation results are separated from those showing the calculated results because the calculated results tend to be much larger than the measurements. Separating the plots allows for as much detail as possible to be seen in both cases. The RF zero phase measurements are not used for these calculations; one could imagine that the predictions from the RF zero phase

measurements alone (i.e. not the reconstructions) would yield unreasonably large signal levels due to the artificially amplified form factor as explained in Chapter 4. Unfortunately, the full extent of this issue was not realized during the experiment, and so only a few data points are available with reconstructions. It is important to point out that experimental measurements of the terahertz radiation were very difficult to make in the unmodulated case. In some cases, the data points have larger error bars than the actual value of the data point itself.



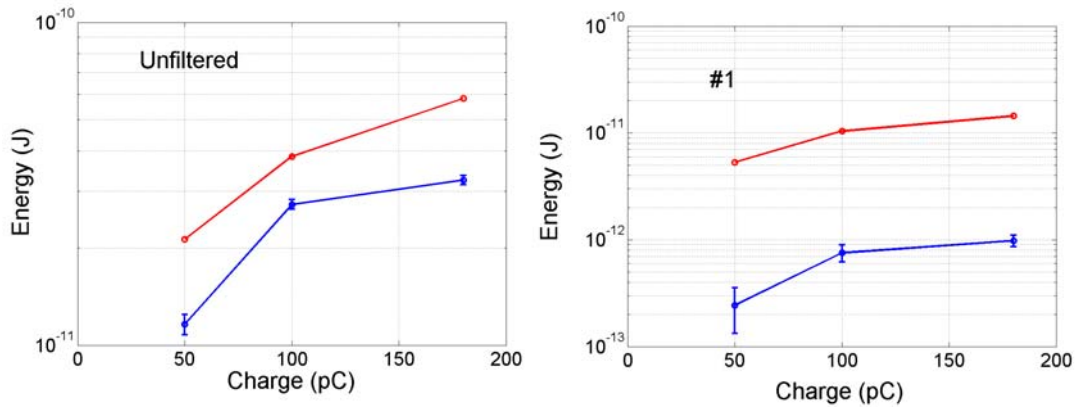
**Figure 5.19.** Laser cross correlation of an unmodulated pulse, corresponding to laser profile A.



**Figure 5.20.** (Blue) Terahertz energy measured at the bolometer (Black) Terahertz energy predicted using simulation.

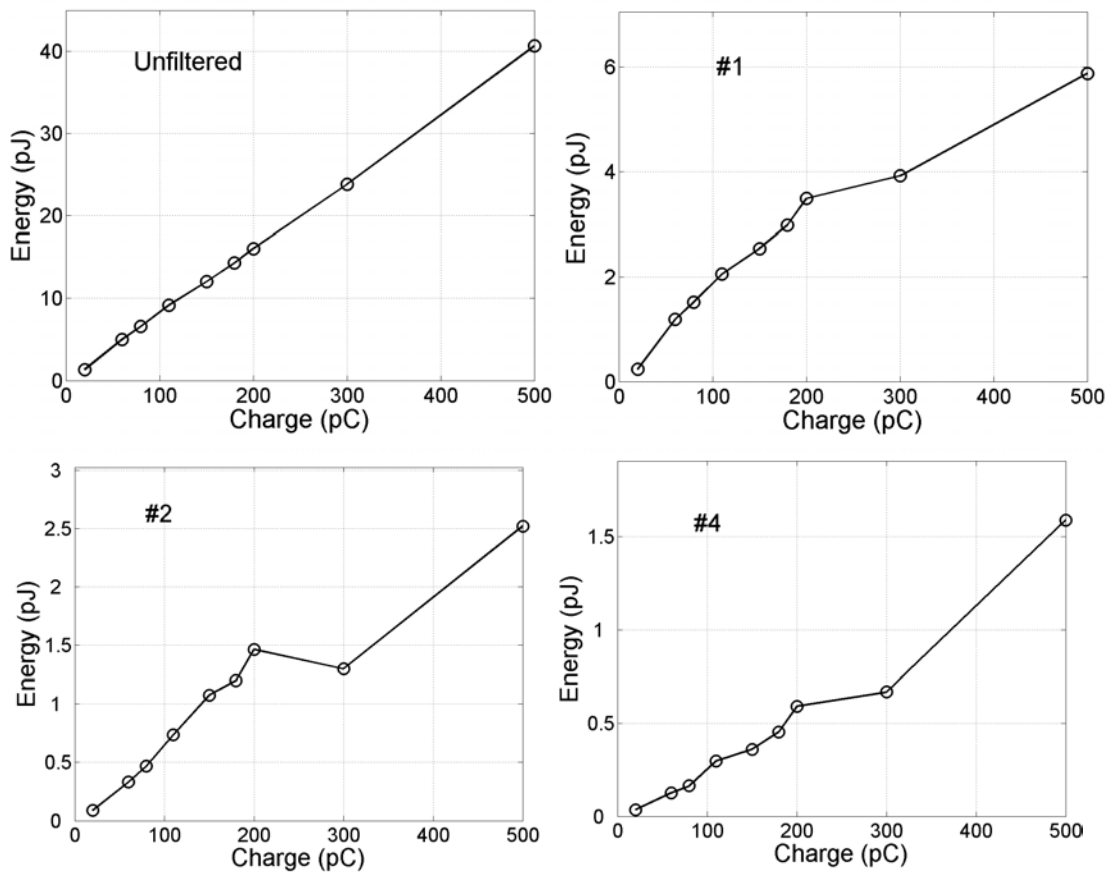
In this case, the error bars in the experimental measurements for all but the unfiltered case are so large it is difficult to draw conclusions from them. However, the simulations seem to indicate that, for an unmodulated beam, as charge increases, the energy measured by each of the filters also increases. In Figure 5.21, a different unmodulated pulse was used to obtain better experimental data. In this case, a good signal could still only be measured for the unfiltered case and for filter #1. Since a tomographic reconstruction for this profile was available, the energy detected at the

bolometer is compared with the calculations based on those. The measurements and calculations in this case also indicate an increase in terahertz energy as a function of charge.



**Figure 5.21.** (Blue) Terahertz energy measured at the bolometer (Red) Terahertz energy predicted using experimentally measured longitudinal electron beam distribution.

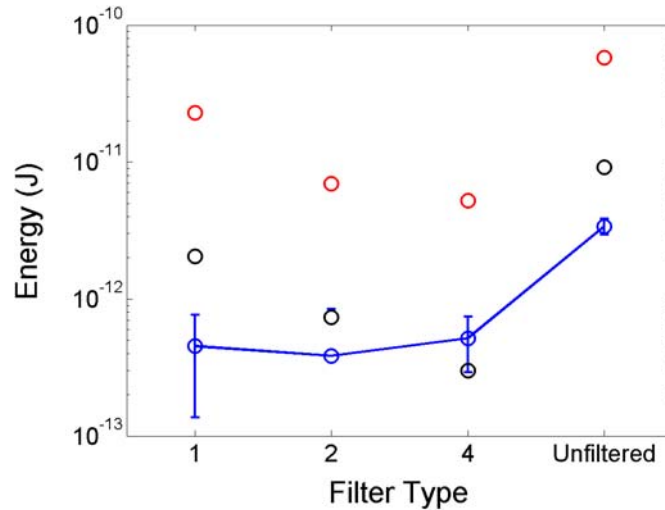
Figure 5.21 also indicates that as charge increases, the amount of energy measured at the bolometer will also increase. The maximum amount of energy measured by the detector was for the 180 pC case, at 32 pJ. Although the maximum amount of charge in any experimental case was limited to less than 200 pC, simulations allow for the exploration of charge levels not achievable experimentally. The simulations were used to predict how the energy measured at the bolometer might change if the charge could be increased to 500 pC. Figure 5.22 shows the simulation results.



**Figure 5.22.** Simulated terahertz measurements for an unmodulated electron beam.

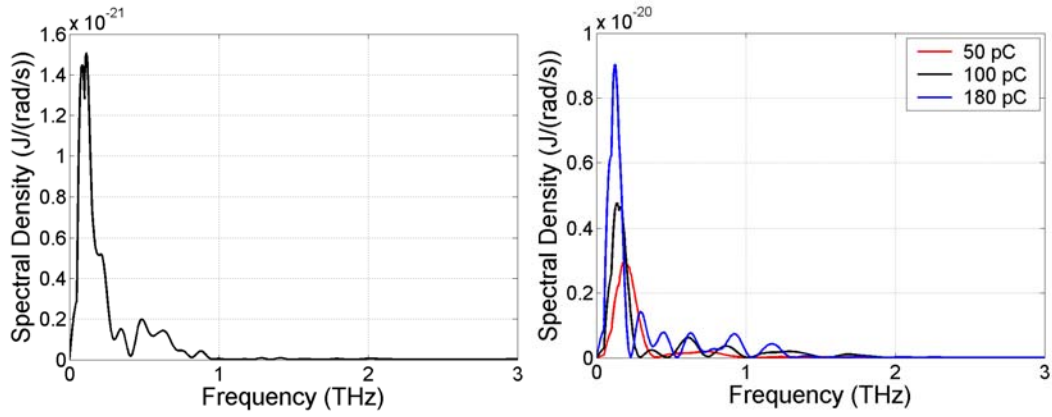
The simulations predict, as expected, that nearly all of the energy radiated by an unmodulated pulse falls near the low frequency end of the spectrum, where the light is more coherent. Each of the filters block more of the light as the edge of the stop band increases in frequency. Recalling that the form factor changes as a function of charge, even for the unmodulated case, the simulations predict the expected result that the total radiated energy should increase directly with charge.

Figure 5.23 compares the measured, simulated, and calculated results for an unmodulated electron beam at 110 pC.



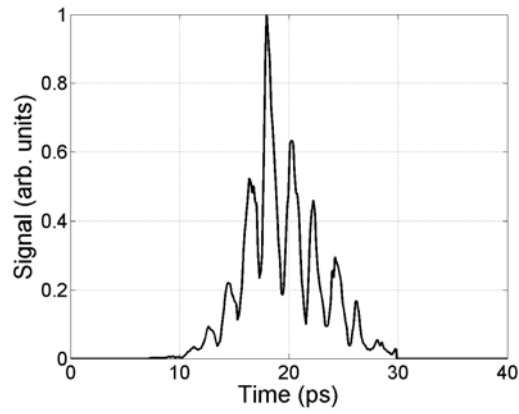
**Figure 5.23.** Comparison of measured (blue), simulated (black), and calculated (red) terahertz measurements for an unmodulated electron beam at 110 pC.

The radiation spectra predicted by simulation and calculation are shown in Figure 5.24. Note that the simulation and calculation result from two different unmodulated cases. While the exact forms of the spectra are different, both the simulation and calculation exhibit the expected large low frequency component which grows smaller with increasing frequency. Note also the low frequency cutoff, which is due to the apertures in the accelerator, as well as the finite radiator effect.

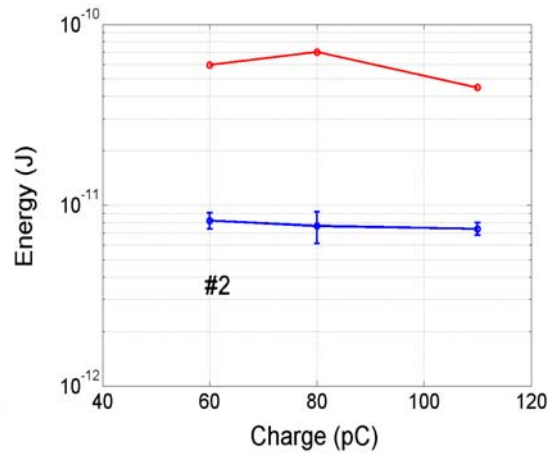
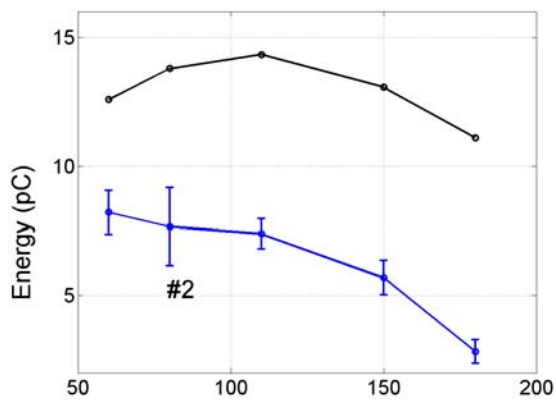
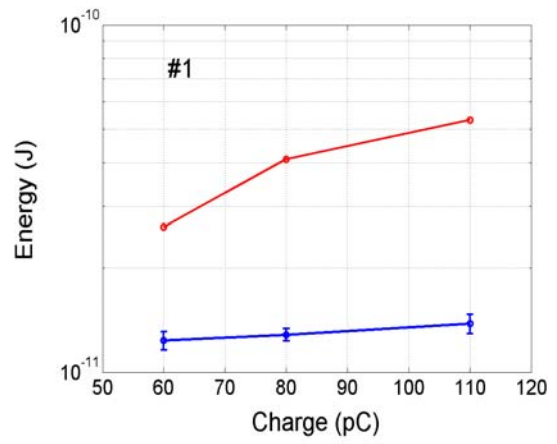
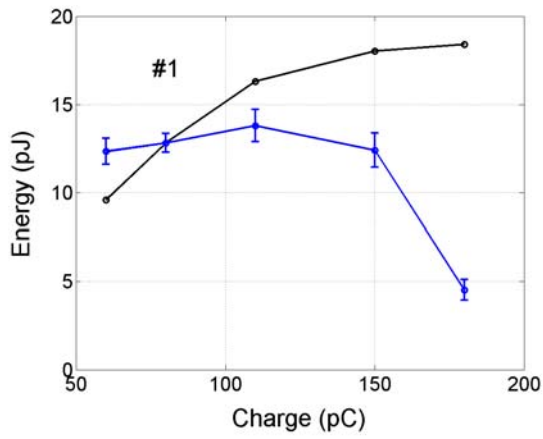
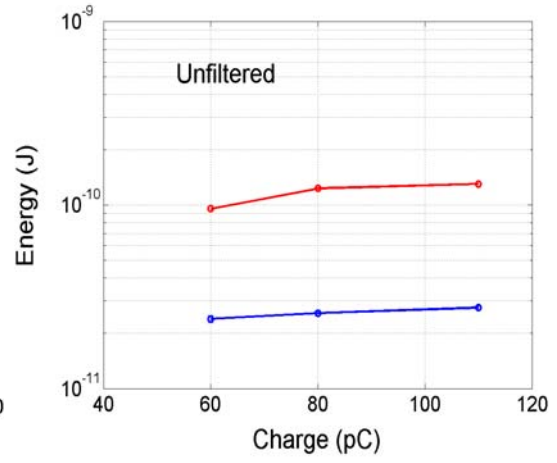
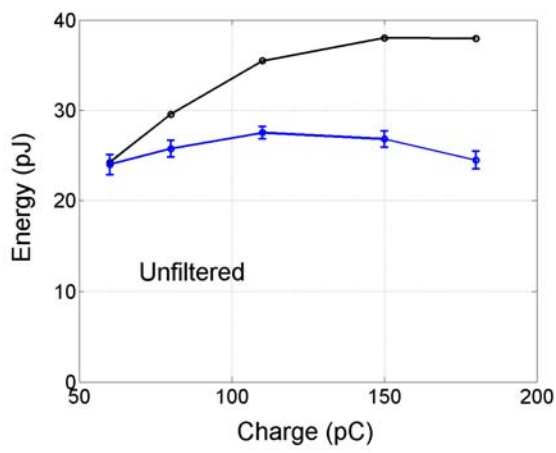


**Figure 5.24.** (Left) Simulated spectrum at 110 pC and (right) calculated spectrum for various charge levels for unmodulated electron beams.

Laser profile B is reprinted in Figure 5.25, and is followed by the charge scan in Figure 5.26.



**Figure 5.25.** Laser cross-correlation of pulse corresponding to laser profile B.



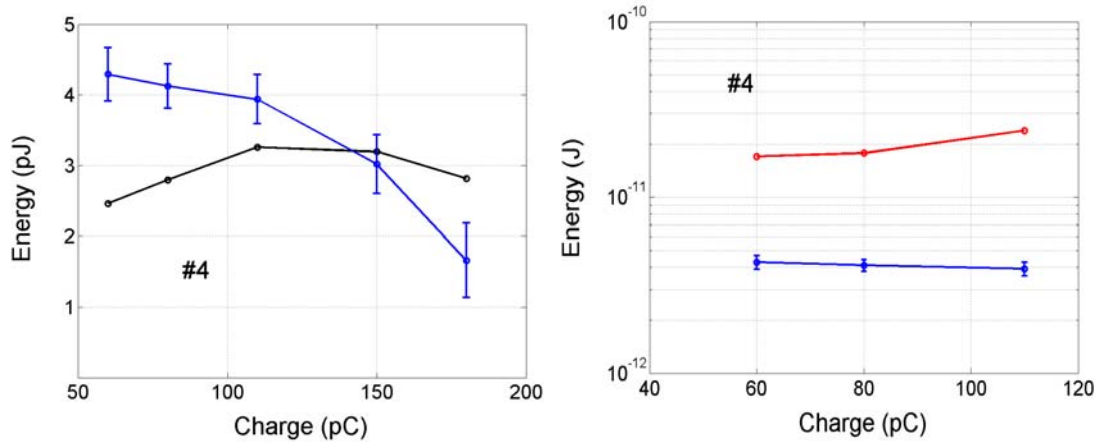


**Figure 5.26.** (Left) Measurements (blue) compared with simulations (black) for each of the filters. (Right) Calculations (red) compared with measurements (blue) for each of the filters.

While the experiment was ongoing, the trends seen in Figure 5.26 were one of the biggest surprises of this work. The fact that the total measured energy might decrease over any portion of the charge domain, with any filter in place, was completely unanticipated, at least at the relatively modest levels of charge used in these experiments. However, this phenomenon is seen in each charge scan for laser profile B, although over different regions depending on which filter is in place. However, as described in Chapter 4, the form factor is very sensitive to the charge in the electron beam, and so this counter-intuitive trend is explained by the washout of the density modulation, which contributes to both a form factor peak and frequency reduction. This effect is also clearly shown in Figure 5.27, which shows simulated charge scans out to 500 pC.

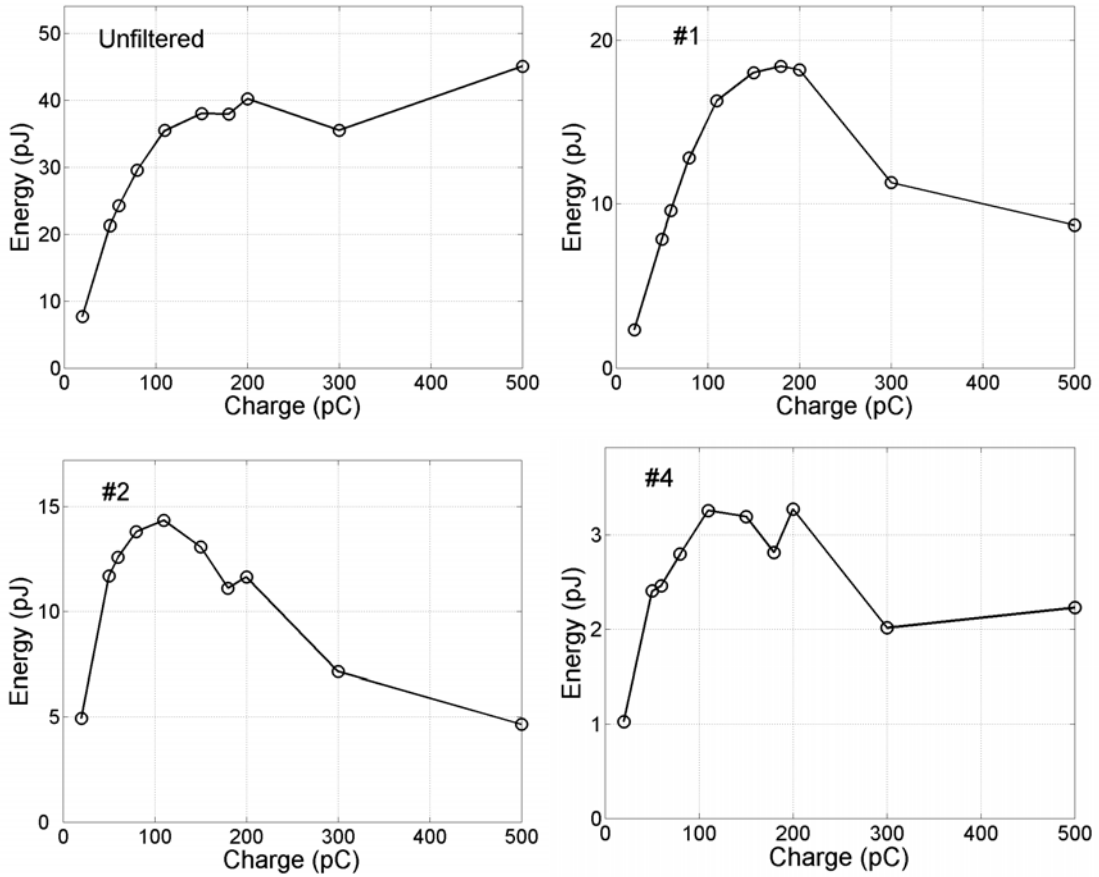


**Figure 5.27.** Simulated terahertz measurements for an unmodulated electron beam.

It is interesting that using Filter #2, approximately the same amount of energy would be detected at the bolometer for a beam with 20 pC as a beam with 500 pC! However, the spectra of these two cases would be vastly different, the one at 500 pC looking more like an unmodulated pulse, since the density modulation has almost completely washed out, whereas at 20 pC, there would be a strong peak at

high frequency. At 20 pC, most of the energy comes from the enhanced form factor. At 500 pC, although the form factor is greatly reduced, an additional order of magnitude of charge makes up for this in total energy. This pre-modulated beam, however, produces more terahertz radiation than the unmodulated case in every configuration. Figure 5.28 is a plot that shows the "enhancement factor" versus filter type. Each point in this plot is calculated by dividing the total energy seen at the detector for laser profile B by the total energy seen at the detector for laser profile A (the unmodulated case), for the simulated, calculated, and measured results.

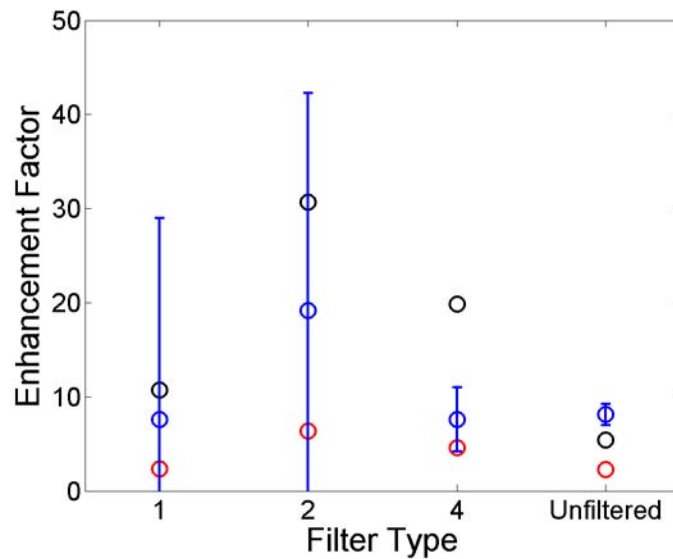
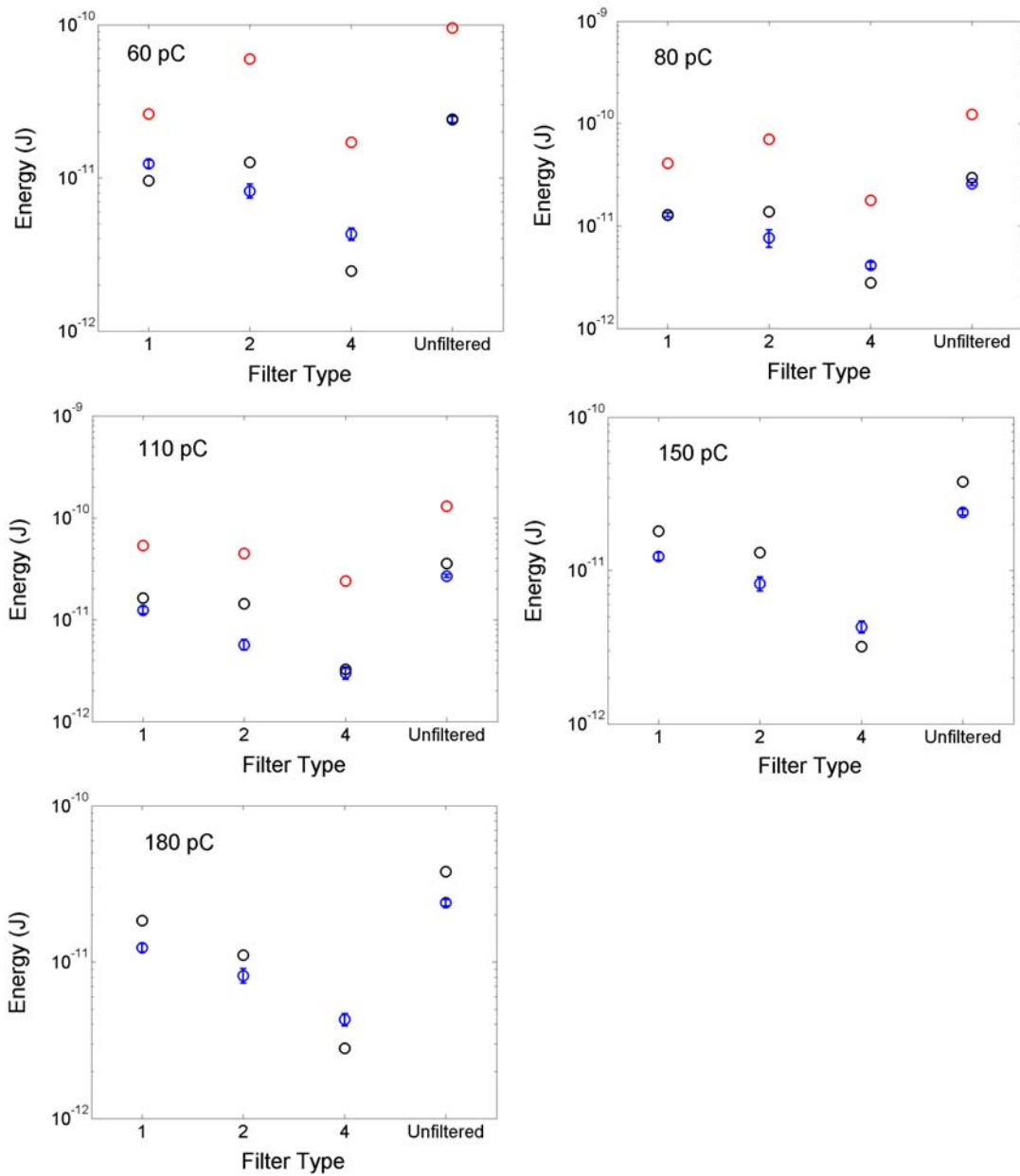


**Figure 5.28.** Enhancement factor for each filter, for (blue) measured, (black) simulated, and (red) calculated results.

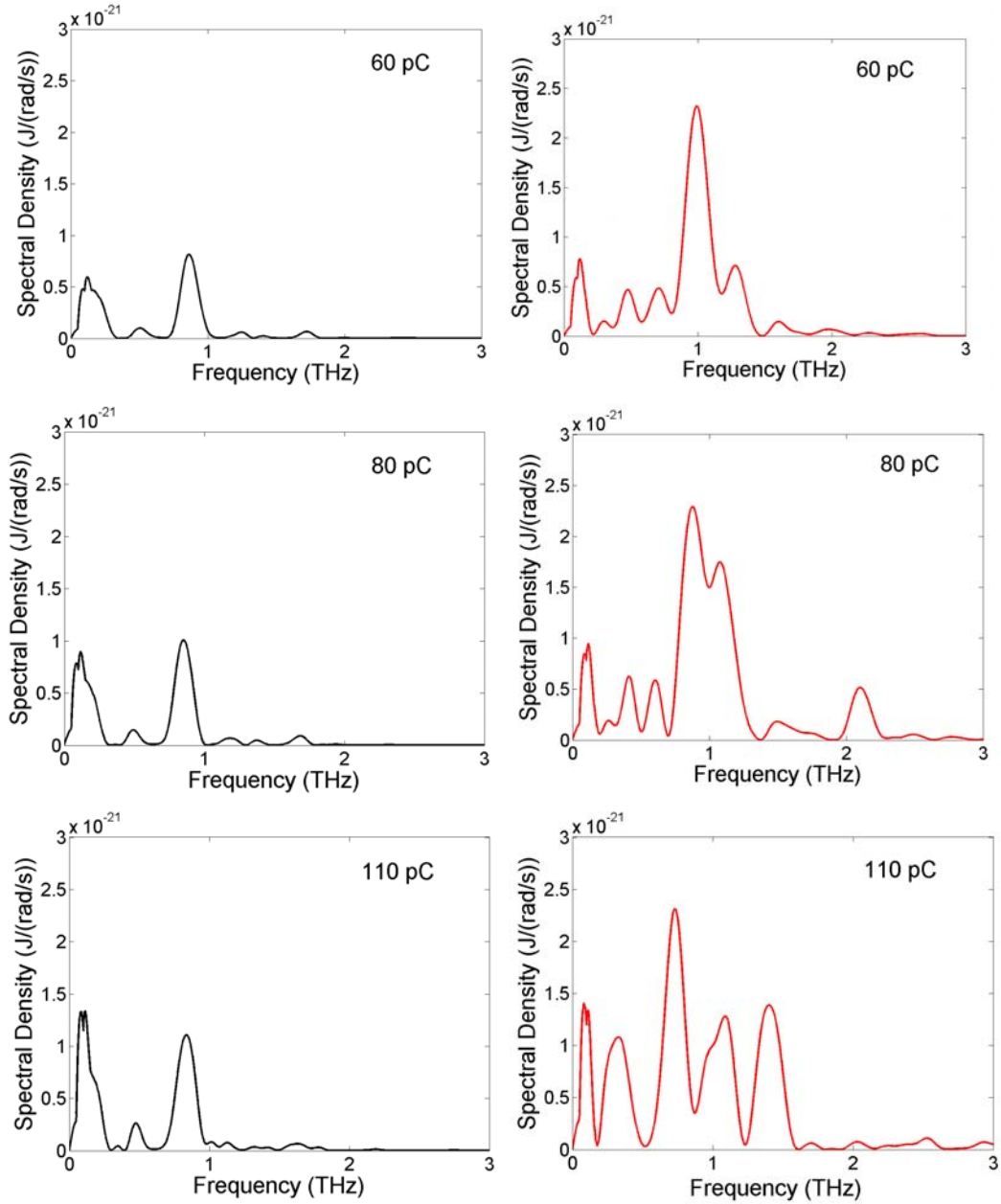
It is not surprising that the largest enhancement factor is seen for filter #2, which has a peak near 1 terahertz. The results in Figure 5.28 are also reminiscent of

the predictions made in Chapter 1; the enhancement seen by the detector is significant, in this case the measured value is near 20 for filter #2, although it is quite far removed from the enhancement factor of  $10^8$ ,  $N_e$ , that might be anticipated from a first look at how bunching affects the generation of radiation. In this case, the direct form factor enhancement, actually of  $\sim 0.02 \cdot 10^8$  for a 20 pC bunch, is realized only in a small bandwidth near the modulation frequency.

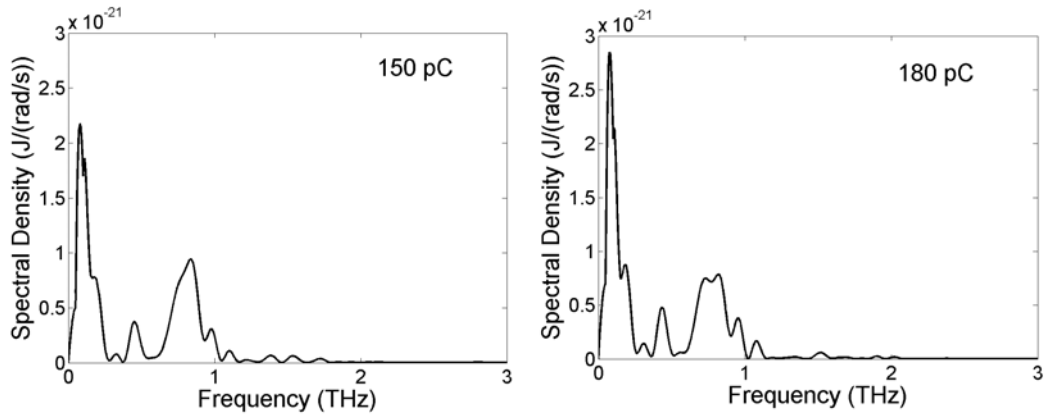
Figure 5.29 shows the calculated, simulated, and measured values of terahertz radiation at the detector for laser profile B at various levels of charge. In this case, the simulation results are much closer to the measured results compared to the calculated results. Following Figure 5.29, Figure 5.30 shows the spectra from the simulations as well as the spectra calculated from the tomographic reconstructions.



**Figure 5.29.** Comparison of measured (blue), simulated (black), and calculated (red) terahertz measurements for modulated electron beams generated by laser profile B.



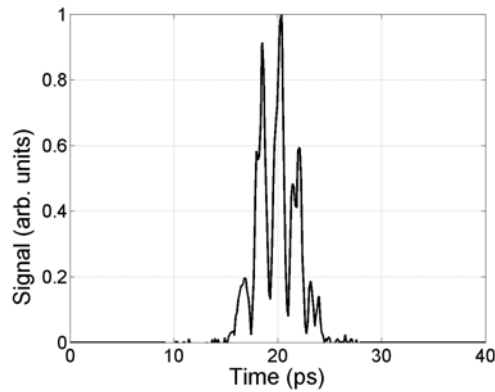
**Figure 5.30.** (Black) Simulated spectra of terahertz radiation generated by electron beams from laser profile B. (Red) Calculated spectra of terahertz radiation generated by electron beams from laser profile B.



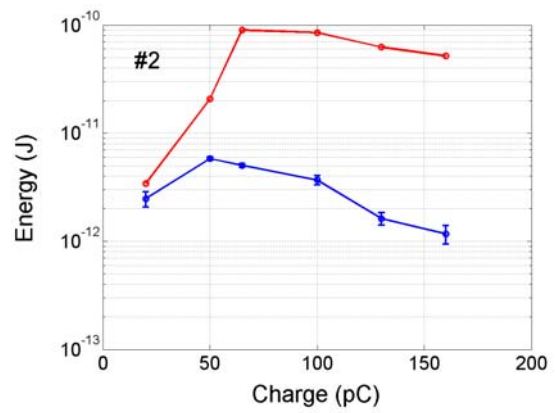
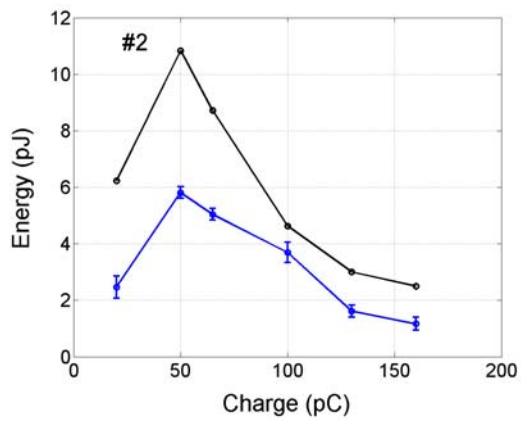
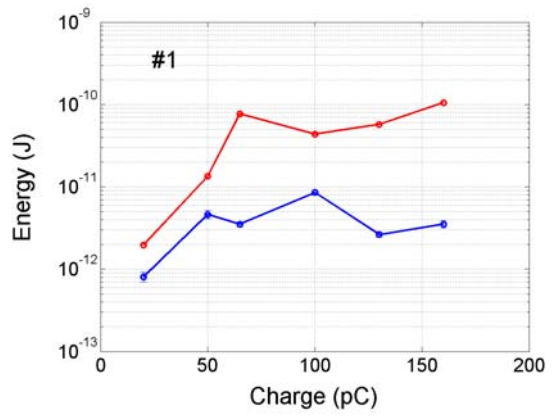
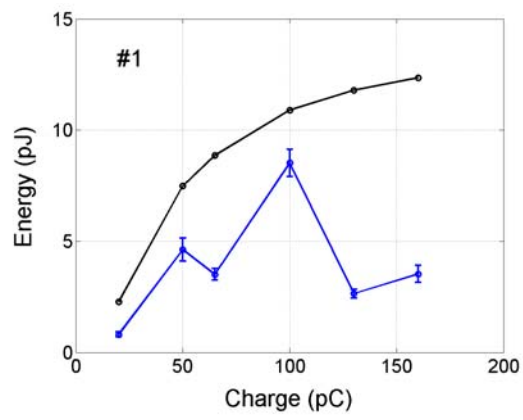
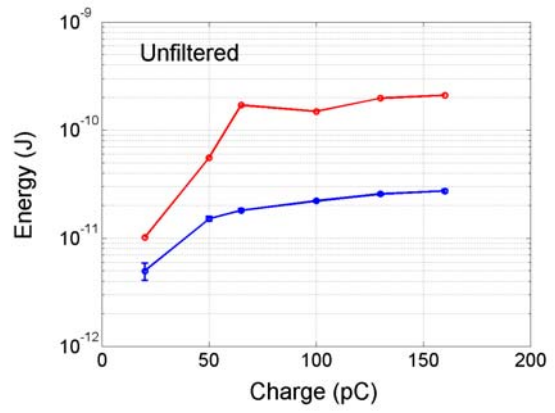
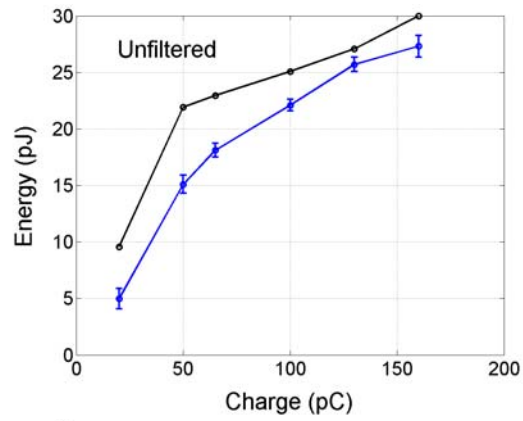
**Figure 5.31.** Additional spectra from simulations of terahertz radiation generated by laser profile B.

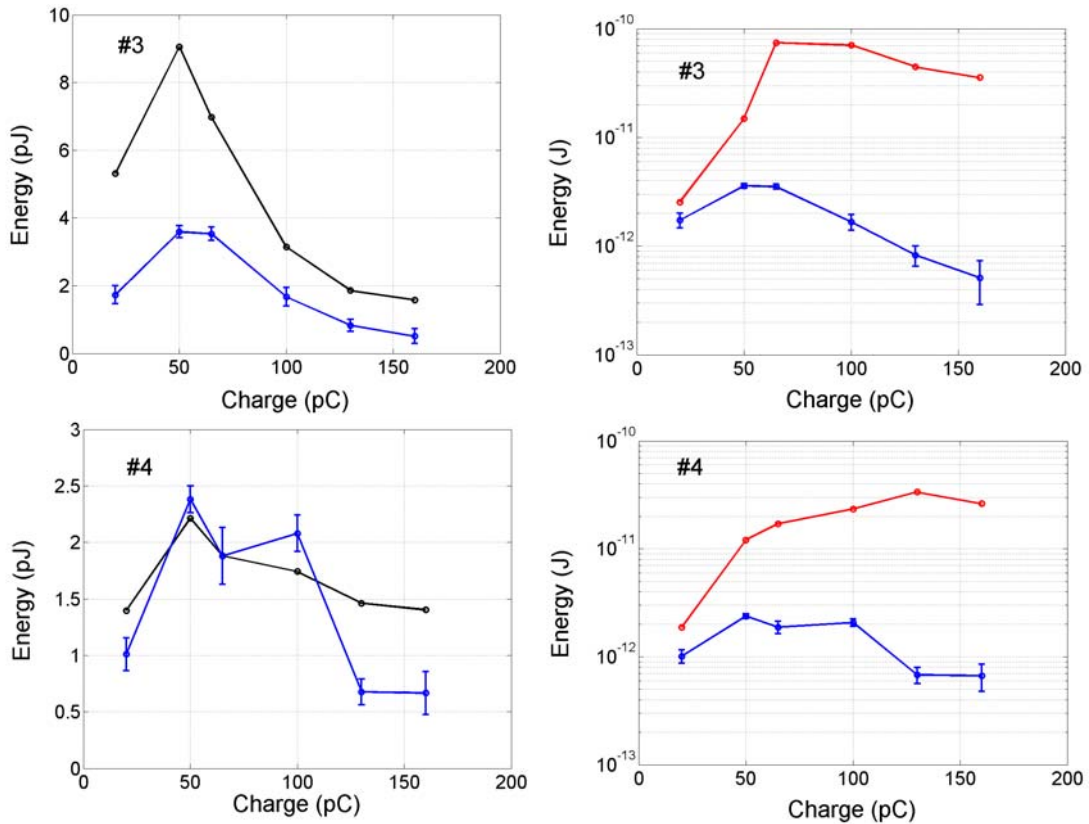
As seen in Figures 5.30-31, as charge goes up, the frequency of the peak in the radiation spectra moves down. Additionally, as charge goes up, more energy accumulates in the low frequency components.

Laser profile C is probably the most well documented case in terms of tomographic reconstructions, simulations, and terahertz measurements. Figure 5.32 is a reprint of laser profile C. The charge scan is shown in Figure 5.33.



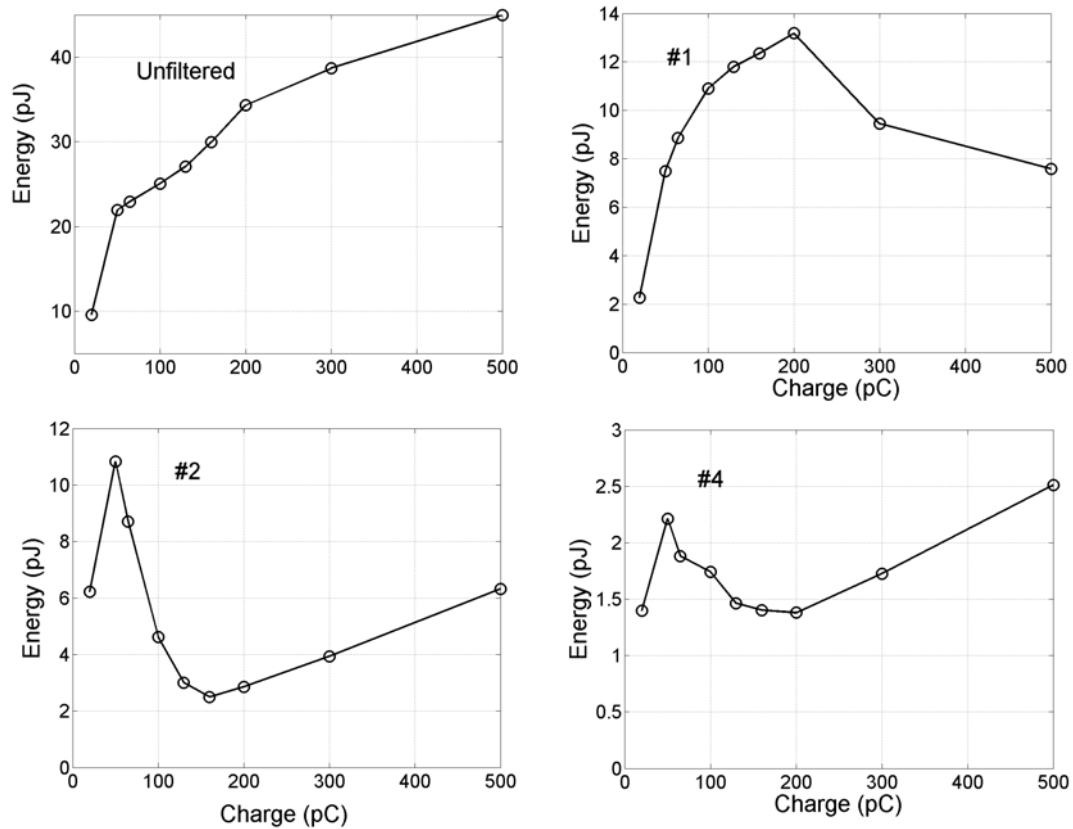
**Figure 5.32.** Laser cross-correlation of pulse corresponding to laser profile C.





**Figure 5.33.** (Left) Measurements (blue) compared with simulations (black) for each of the filters. (Right) Calculations (red) compared with measurements (blue) for each of the filters.

In the charge scan for laser profile C, the effects of the reduction in form factor and peak modulation frequency are clearly seen, especially with filters #2, #3, and #4. Similar to the laser profile B, the total energy rises as a function of charge. The simulations tend to be better predictors of the signal seen at the bolometer than calculations based on the tomography, but some of the general trends are exhibited by both. Figure 5.34 shows results for laser profile C, simulated up to 500 pC.



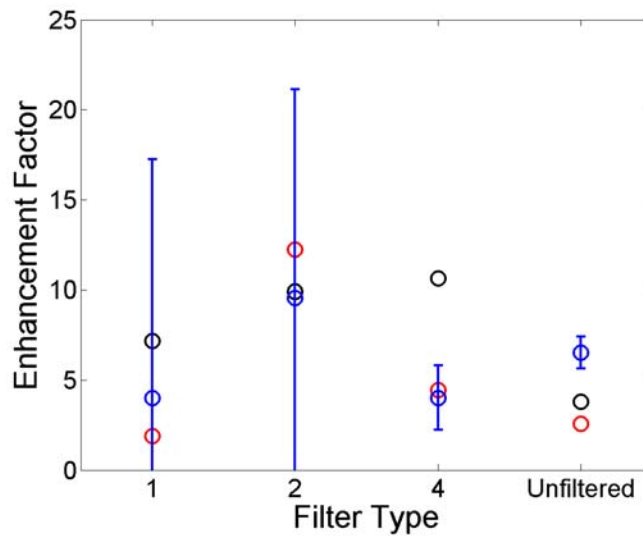
**Figure 5.34.** Simulated terahertz measurements for an unmodulated electron beam.

Figure 5.34 is interesting because it shows that as the charge increases, the beam acts more and more like an unmodulated beam. As charge increases, the form factor decreases, and the peak modulation frequency decreases as well. Eventually, the increase in energy due to increasing charge begins to dominate, and linear growth is seen as a function of charge. One could infer that most, if not all, of the modulation imparted by the laser has been lost at the minimum energy point in these plots. That point changes as different filters are used; this makes sense because as the modulation features wash out, the situation appears to be demodulated at

high frequencies first.

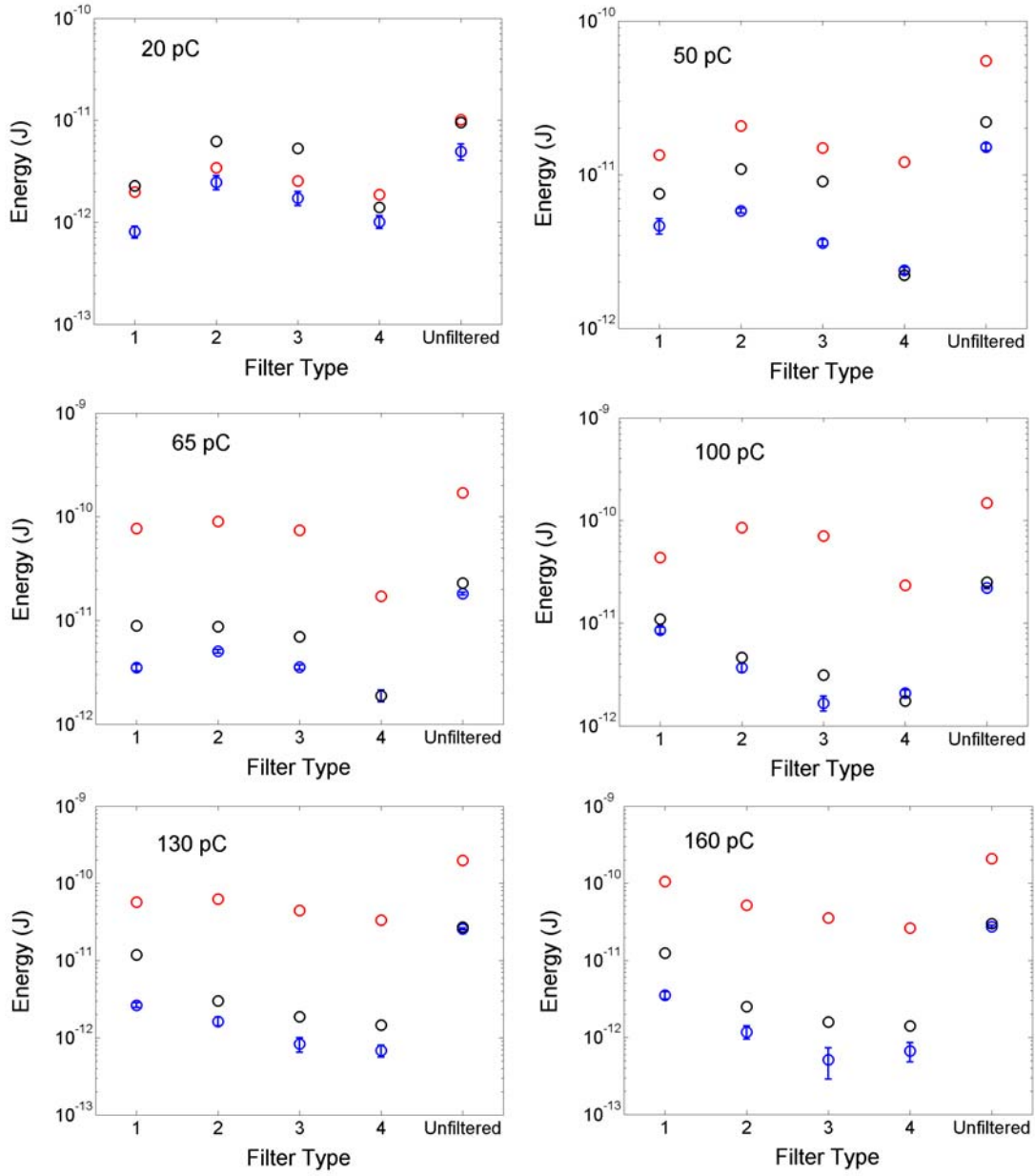
Figure 5.35 shows the enhancement factor for laser profile C at 100 pC.

Similar to the previous case, the enhancement is not astronomical, but is at least an order of magnitude, as in the case of filter #2.

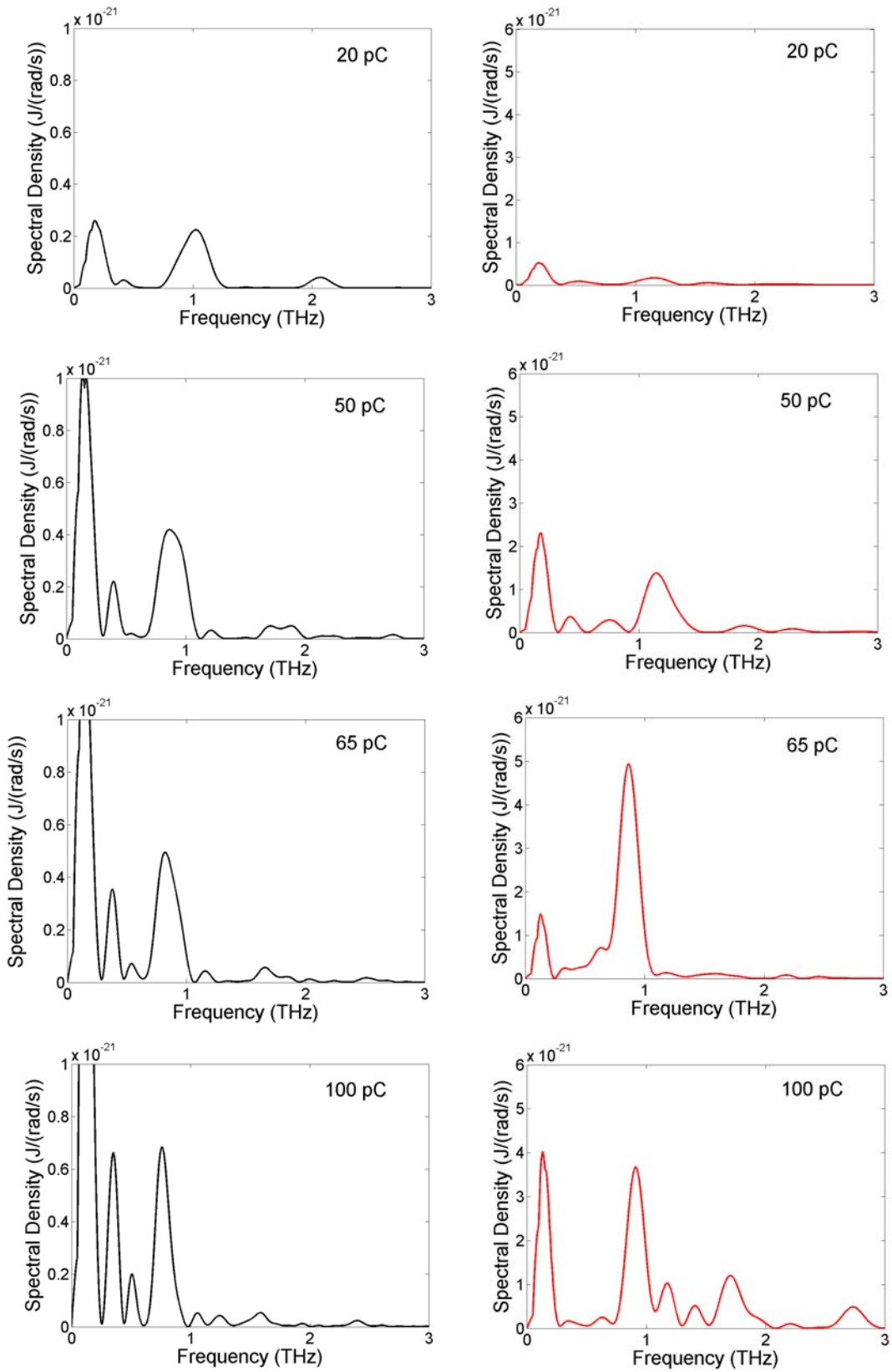


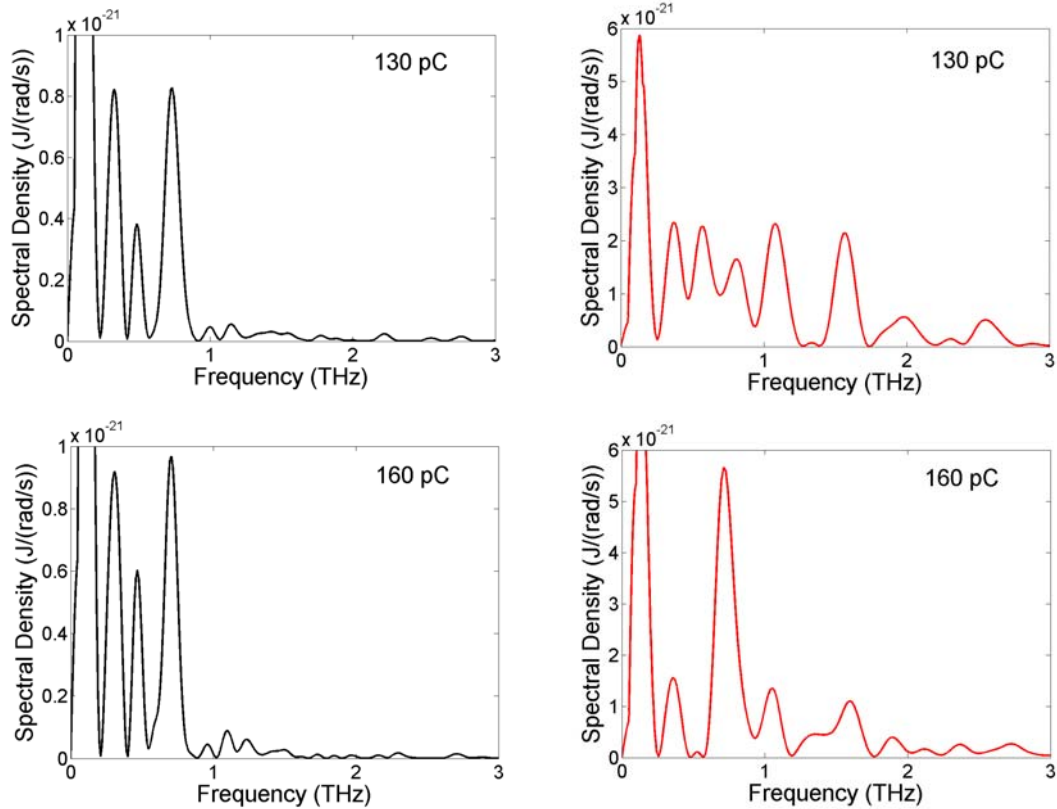
**Figure 5.35.** Enhancement factor for laser profile C at 100 pC.

Figure 5.36 compares the energy measurements, the simulations, and the calculations for each filter at every charge level for laser profile C. Once again, the simulations generally match the measured data better than the results based on the tomographic reconstructions, but the general trends are followed in both cases.



**Figure 5.36.** Comparison of measured (blue), simulated (black), and calculated (red) terahertz measurements for modulated electron beams generated by laser profile C.





**Figure 5.37.** (Left) Spectra generated from simulations for laser profile C. (Right) Spectra generated from tomographic reconstructions for laser profile C.

Although the spectrum is not as clear at the higher charges, the trends established in the previous case prevails for laser profile C, as shown in Figure 5.37. As charge increases, the peak frequency in the spectrum shifts downwards. Although the total energy in the largest peak increases with charge, it does not increase as fast as it would if the form factor were not reducing with charge.

At this point, the general behavior of the system has been demonstrated, but there are a few data points worth examining. Laser profile D, shown in Figure 5.38,

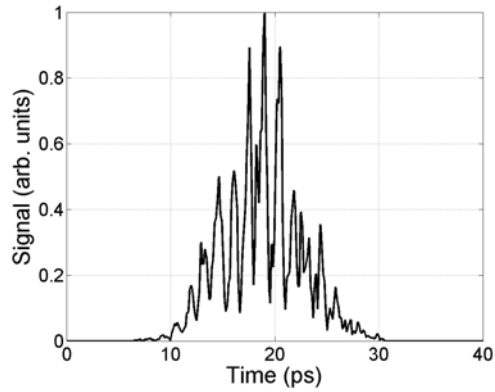


**Figure 5.38.** Cross correlation of laser profile D.

exhibits particular good agreement between simulation and experiment, although there are no tomographic reconstructions available for comparison. Figure 5.39 shows the energy predicted to arrive at the detector for each level of charge and each filter, comparing simulation and measured energy levels. Figure 5.40 follows on with the spectrum for each of these cases. In this particular case, the frequency reduction is not as dramatic in other cases, although the peak at the modulation frequency remains rather stable with charge, rather than increasing.

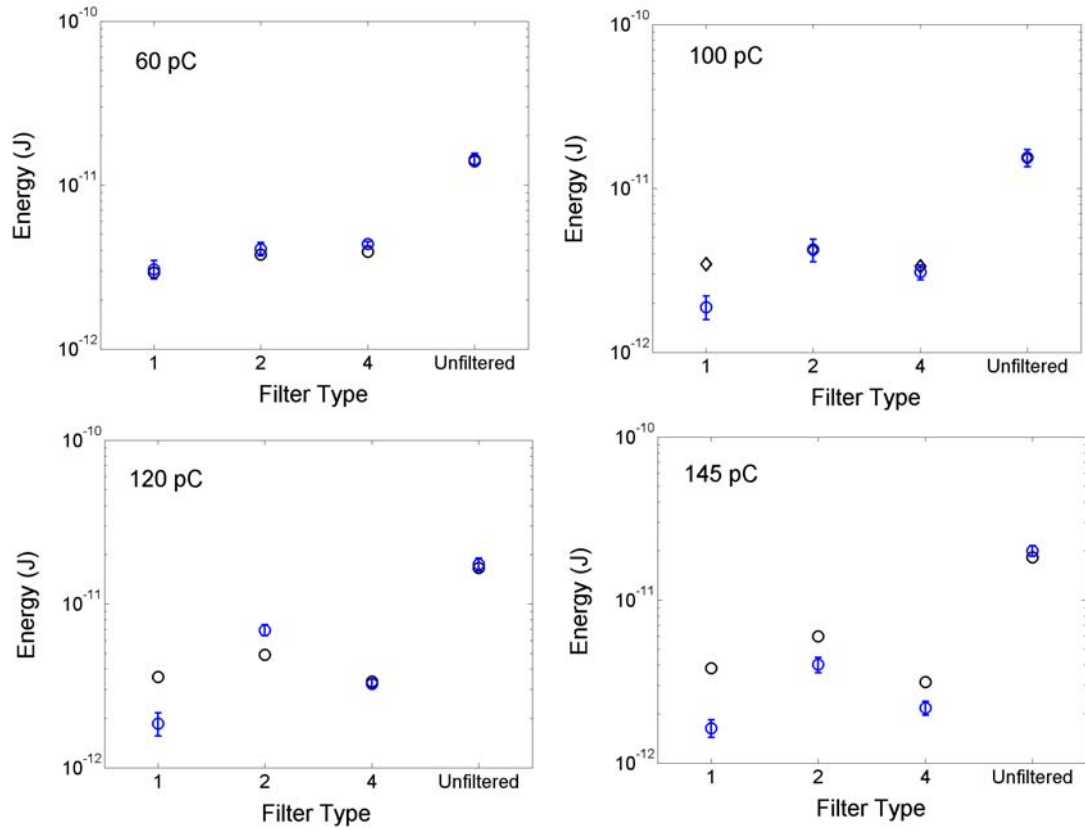


**Figure 5.39.** Comparison of measured (blue), and simulated (black), terahertz measurements for modulated electron beams generated by laser profile D

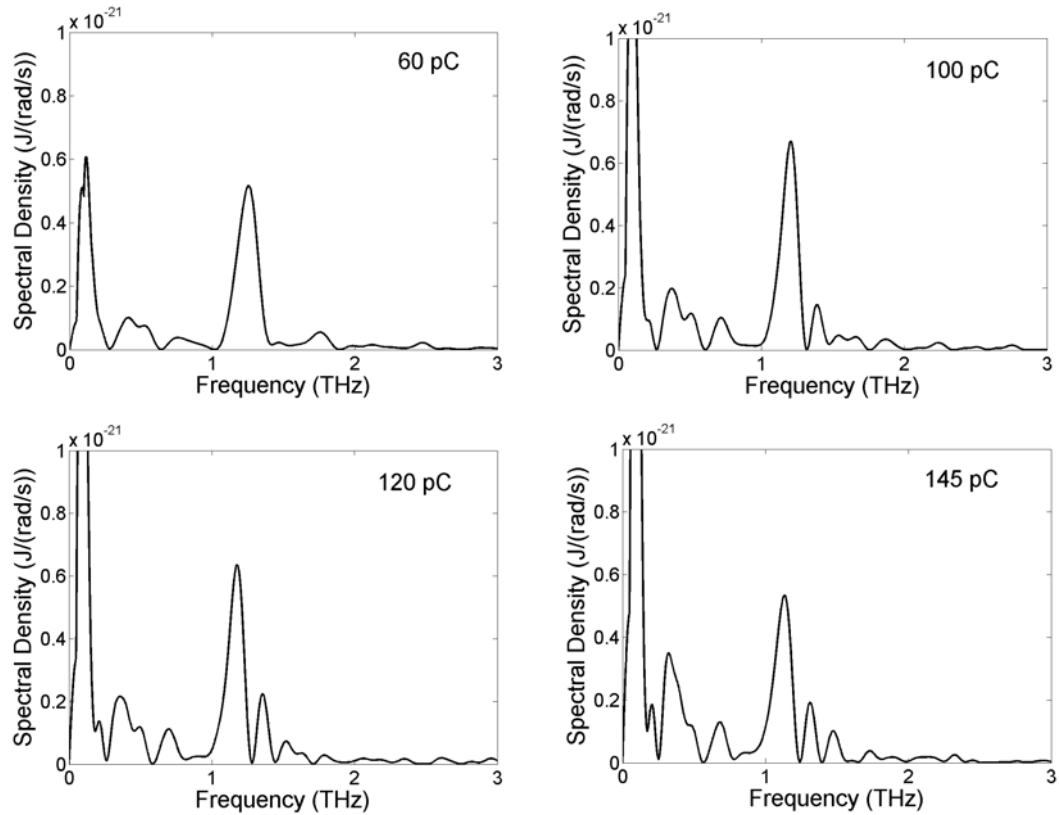


**Figure 5.40.** Spectra generated from simulations for laser profile D.

Laser profiles E and F mostly demonstrate the capabilities of the Fabry-Perot system, and were not particularly well diagnosed in this experiment. Laser profile E is interesting because it marks the highest frequency of modulation that was clearly detectable with the bolometric detector. Laser profile E is shown in Figure 5.41.

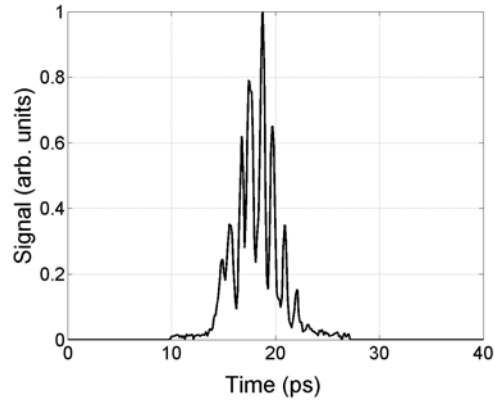


**Figure 5.41.** Cross-correlation of laser profile E.

A comparison between the measured and calculated amounts of terahertz energy, along with the calculated spectrum are shown in Figure 5.42. Besides the low frequency component, the peak of the radiation occurs near 1.5 terahertz. This data was taken only at 180 pC; it would have been interesting to see the results for this profile at a lower charge. Based on the previous cases, it is likely that the result would have peaked at a higher frequency.

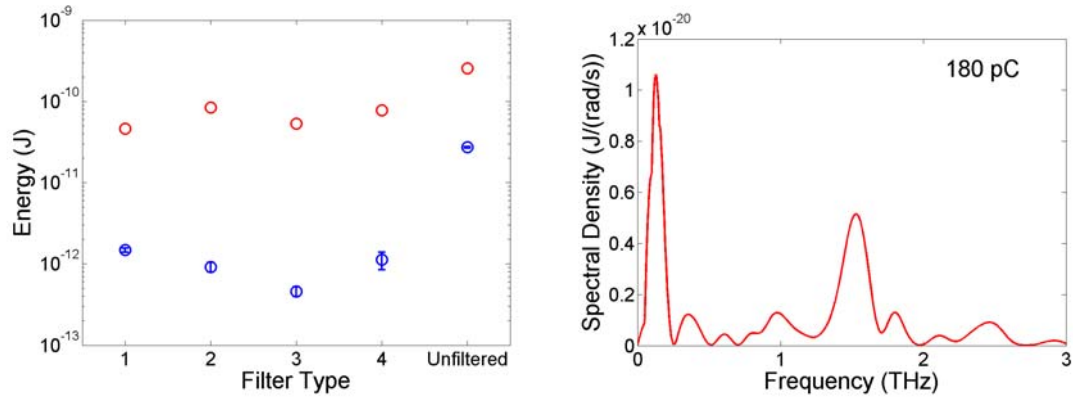


**Figure 5.42.** (Left) Measured (blue) terahertz energy compared with (red) calculated predictions. (Right) Spectrum predicted by the calculations.

Laser profile F may have shown some enhanced radiation due to the modulation above 3 terahertz, but because of the filter installed in the bolometric detector, it was impossible to explore this region. Noting the energy modulation seen in the RF zero phase measurements for this profile, using a bend magnet to recover some of the density modulation might be useful.

In this experiment, it was shown that the measured terahertz energy did not increase quadratically because of density modulation washout due to space charge. If the charge were low enough, however, the washout would not be significant, and the energy would increase with the square of charge. The experimental setup in the experiment would not allow for charge levels below 20 pC, since the charge was too low to measure. However, PARMELA could be used to access this regime. Figure 5.43 shows the form factor for a bunched beam as a function of charge ranging from 10 fC up to 1 nC. The simulations indicate that the form factor is stable up to

approximately 1 pC, and then begins to fall quickly as the space charge driven washout ensues.

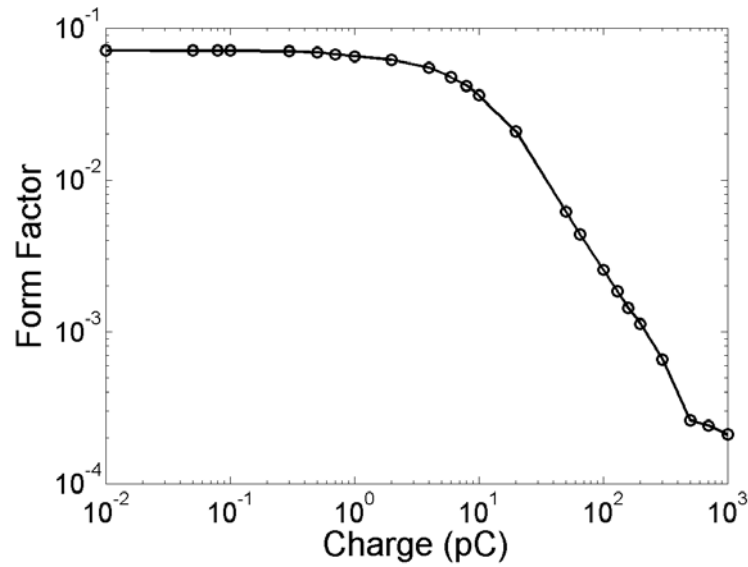


**Figure 5.43.** PARMELA simulation indicating form factor as a function of charge.

Figure 5.44 shows the terahertz radiation that would be generated by the electron beam. The dashed line is a reference that increases with the square of the charge. The diamonds represent the calculations based on the PARMELA simulations, while the crosses represent the calculations based on the tomographic reconstructions, and the circles represent the actual bolometer measurements.

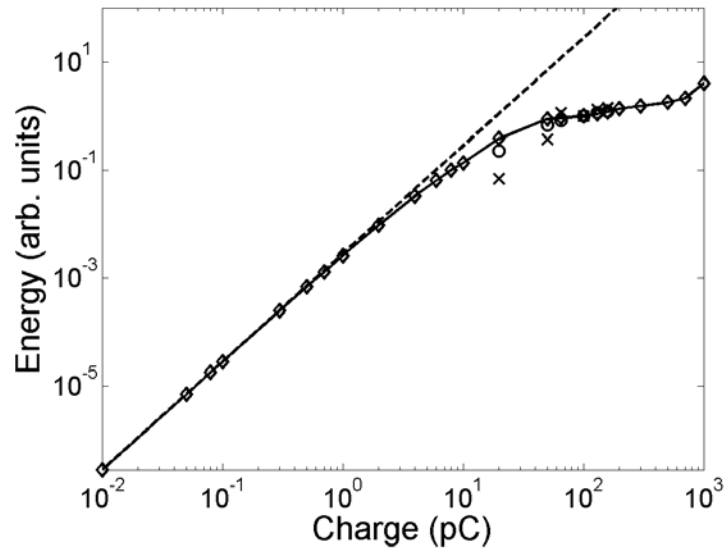


**Figure 5.44.** Total (unfiltered) terahertz energy generated by a modulaed electron beam based on calculations from PARMELA simulations (diamond), calculations from tomographic reconstructions (cross), and actual bolometer measurements (cross). The dashed line is a reference that is defined by a quadratic dependence on charge.

The terahertz energy calculations based on the PARMELA simulations closely match the quadratic reference line until the beam contains approximately 1 pC of charge.

As the charge increases from this point, the total terahertz energy deviates from the quadratic dependence.

## Chapter 6: Conclusions and Future Work

The purpose of this research was to determine whether or not an electron beam could be pre-modulated with a drive laser at the photocathode in a linear accelerator in order to impose a density modulation that would be retained through acceleration. Control over the longitudinal density profile could be used to either smooth the density profile of an electron beam or cause deliberate modulations. This experiment specifically explored the use of density modulation on the electron beam to produce terahertz radiation. The research consisted of three distinct sections: drive laser modulation; electron beam dynamics; and terahertz radiation measurements.

### *6.1 Drive Laser Modulation*

Modulating the drive laser at terahertz frequencies was necessary in order to even begin this experiment. A great deal of time was spent on three different laser modulation techniques. In early experiments, a fixed mask was used to create a time modulation by placing it inside of the laser compressor (See Appendix A). This method worked, and produced four distinct pulses in a single bunch train. Changing the laser profile simply involved using a different mask.

After the early experiments, upgrades to the laser system were sought to obtain higher frequencies, a larger number of bunches, and higher levels of charge. Two techniques were pursued, both of which turned out to be quite successful. The first involved building a "pulse-stacker," where the incident laser pulse could be split into several parts, travel along a delay line, and be reconstructed into a modulated pulse. Waveplates and polarizers were used to control the relative amplitudes of each of the pulses. The system was difficult to align, and so was not used for the experiments at Brookhaven due to limited experimental time, but proved quite successful when used in longitudinal dynamics experiments on the University of Maryland Electron Ring (See Appendix A).

The drive laser modulation method of choice for this experiment was the unique employment of a Fabry-Perot interferometer system. The interferometer was placed in the UV laser beam, and served as a filter that could modulate a chirped pulse in time. This implementation was successful because it was simple. It could be easily inserted or removed into the drive laser system at the Source Development Lab, provided a continuously tunable modulation frequency, and allowed the generation of up to 180 pC of charge at the cathode. The modulation frequency range demonstrated with this system varied between 0.5 THz and 1.6 THz. Although the Fabry-Perot system is very sensitive to self-alignment, it is not sensitive to its alignment with the rest of the laser. A convenient side effect of this was that changing the settings on the interferometer did not require realigning the

rest of the laser. This is in great contrast to the pulse stacker system, which required extensive alignment just to set up.

## *6.2. Electron Beam Dynamics*

The dynamics of the electron beam were explored using the simulation tool PARMELA, and the experimental diagnostic equipment at the Source Development Laboratory. PARMELA proved to be a useful tool, because it allowed investigation into areas not accessible experimentally. For instance, PARMELA was used to determine the state of the electron beam at various points along the accelerator where there were no diagnostics, and also at charge levels that were not attainable experimentally. Initial PARMELA experiments included only the gun area, and the gun model was different from the one used at the SDL. Additionally, it was not possible to simulate the experimentally achieved distribution in the accelerator. Over the last few months, the SDL made a much more accurate model available for use with PARMELA. The results compared very nicely with experimental results, and it is these simulation results that are included in this dissertation.

The RF zero phasing technique was also the only longitudinal diagnostic available at the SDL during early experiments. As it became clear that modulating the drive laser can cause problems with the RF zero phasing measurement technique, the data was supplemented with tomographic reconstructions.

Both the simulations and the experimental measurements indicated that density modulation imposed at the photocathode could be maintained through acceleration. However, space charge affects the details of the beam distribution very strongly. Although the beam starts to stiffen near 9 MeV, the longitudinal distribution appears to change in some cases all the way through the end of the simulation at 34 MeV, and possibly beyond. In all cases, the form factor of the longitudinal distribution was very sensitive to charge. The value of the form factor at the peak modulation frequency tended to fall very quickly with increasing charge. Additionally, the peak modulation frequency also fell with increasing charge. Although these trends are not surprising in and of themselves, it was surprising that they manifested themselves at such modest levels of charge.

Nevertheless, even at the highest laser modulation frequency and highest levels of charge, evidence of the initial modulation remains with the beam all the way through acceleration when compared with an unmodulated case. Although the density modulation may have washed out, energy modulation in the beam phase space still exists. It may be possible to recover the density modulation by manipulating the beam's phase space distribution with additional dispersive segments, even if the projection of the phase space onto the longitudinal coordinate (longitudinal profile) indicates that the modulation has been completely washed out. Electron beam modulation was demonstrated between 712 GHz and 1.66 THz.

### *6.3 Terahertz Radiation Measurements*

One can use an electron beam modulated at terahertz frequencies in order to generate terahertz radiation. In this case, a mirror intercepted the electron beam, and caused transition radiation to be emitted. This light was carried through a transport system to a bolometric detector. Different filters were used to assess the nature of the light.

When the experiment was designed, "rules of thumb" were expected to apply, as explained in Chapter 1. For instance, if the light is coherent, it should increase with the square of the charge. The bandwidth should narrow with increasing numbers of pulses. However, most of these "rules of thumb" generally assume that the shape of the electron bunch is constant as a function of charge. In other words, space charge forces can be neglected. This is clearly not the case for this type of experiment.

As a result of this mindset, a heavy emphasis was placed on designing an experiment that could vary a large number of "knobs". Initially, it was considered important to be able to carefully adjust the number of separate bunches, the frequency of modulation, and the amplitude of the pulse. Each of these parameters would be carefully adjusted, and the results would be measured at the detector. However, space charge forces caused all of these parameters to change as a very sensitive function of charge. The changes in the profile of the electron beam were

most prominently noticed when energy measured at the detector would actually decrease even though the amount of charge in the beam had increased. This was a result of the peak modulation frequency sliding out from the peak of the filter, as well as the reduction in form factor with increasing charge. Although the interferometer provided some convenience with its considerable tunability, the physical laser masks probably would have revealed the same trends uncovered through the course of this work, and allowed for more time to explore the low charge extremes in greater detail.

Generally, even with the low frequency cutoff effects such as the aperture of the accelerator and the finite radiator, the low frequency components were still relatively strong compared with the enhanced frequencies due to the terahertz modulation. The frequency of this peak was variable between 706 GHz and 1.53 THz. The most energy is achieved at the highest levels of charge, but as charge increases, the enhanced part at high frequencies is penalized at the expense of lower frequency components. Typical enhancements as measured at the detector ranged from unity to near a factor of 30. This was not unexpected due to the broad band nature of the detection mechanism. The largest recorded measurement of radiation was 32.5 pJ, but this was for an unmodulated case at high charge. The largest amount of terahertz radiation from a modulated case was 27 pJ, and the peak modulation frequency in this case occurred at 713 GHz.

Comparing these results to those of other devices does not indicate that this

is the best source for terahertz radiation. Even calculating a rough estimate of peak power yields only approximately 5 W. Additionally, the radiation spectrum generated by this source would likely not meet the needs of those who need clean, powerful, narrow band sources. Noting the relative amount of power that goes into generating and accelerating the electron beam, this is also not a very efficient source. However, it is important to remember that using this technique with different radiative mechanisms, specifically an undulator, could be extremely effective, as described in Chapter 1.

In addition to being used as a source, the terahertz radiation measurements can also be used to benchmark the simulations and experimental measurements of the longitudinal beam structure. In this experiment, the simulations tended to have better agreement with the measured data than the calculations that result from the tomographic reconstructions. In this particular case, an argument could be made that the longitudinal profile predicted by the simulations is closer to the actual longitudinal distribution than the tomographic reconstructions. However, recall that there is some qualitative agreement between the tomographic reconstructions and the simulated longitudinal profile. The sensitive dependence of the form factor on the details of the longitudinal structure simply emphasizes these differences. In fact, this sensitive dependence is used by many who seek to use transition radiation alone to completely recover the particle distribution in an electron beam.

## *6.4 Recommendations for Future Work*

Before proceeding with any experimental work, it is probably beneficial to seek a "sweet spot" for operating a device based on this pre-modulation scheme. This work was a proof of principle experiment that has shown the concept is possible, and has clearly shown a trade off between form factor, charge, and frequency. A good next step would be to determine what type of pulse shape and what amount of charge would lead to an ideal source. From this point, a new experiment could be designed to achieve these goals.

One possible way to proceed experimentally with this work would be to design a low energy test stand for this type of device. An electron gun without any additional accelerating sections is probably sufficient. Besides being compact, the beam will have less room to expand and wash out due to space charge. In a transition radiation experiment, the radiation would be clearly in the far field, the distance to which scales as  $2\gamma^2 c/w$ . A 5 MeV electron gun, generating light at 0.5 THz puts this distance at about 6 mm. Coupling a short undulator with such a device could yield the previously mentioned compact, high power terahertz source.

## Appendix A: Other Laser Modulation Methods

During the course of this research, three different drive laser modulation schemes were attempted. The Fabry-Perot interferometer system was used for this particular experiment, and is described extensively in this work. Two other systems, a direct space-to-time mask, and a pulse stacker were also implemented for use with other experiments.

In the case of the direct space-to-time mask, the properties of the chirped pulse amplification were used to achieve laser modulation in the time domain. In this system, the initial laser pulse from the Tsunami titanium:sapphire laser is lengthened using a stretcher, which uses diffraction gratings to introduce dispersion in the beam. The inherent bandwidth in the laser pulse causes "blue" frequencies to diffract at one angle, while "red" frequencies diffract at another angle. Geometric effects result in a path length difference between the various components of the pulse. The disparity in path length causes the pulse to lengthen and creates an energy-time correspondence known as the chirp. In the system at the SDL, the pulse is then amplified and shortened in a compressor, although the pulse is still almost two orders of magnitude longer than the incident 100 fs pulse. The result is that the correspondence between energy and time (chirp) is maintained even after the laser pulse is compressed again. The geometry of the stretcher/compressor system results in certain points where there is a linear correspondence between frequency and

transverse position in the laser spot. At this location, a physical mask is used to block some of the frequency components. Since there is a correspondence between frequency and time after compression, removing these frequency components results in a time modulation that looks qualitatively similar to the frequency modulation after compression. This method is similar to the Fabry-Perot interferometer in that the time modulation is created by using a comb filter; in the case of the Fabry-Perot system, this is done through interference methods. In this case, the filtering is accomplished with a physical mask. The design scheme is shown in Figure A.1.

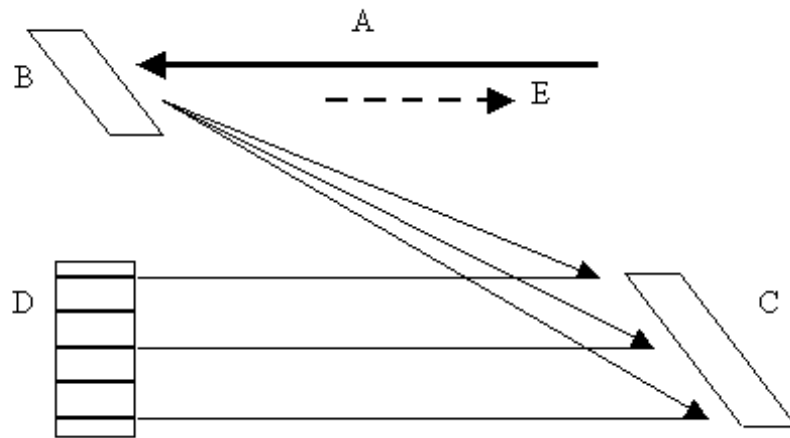


**Figure A.1.** Schematic of modulation using a physical mask. (A) 300ps pulse @ 800 nm is incident from amplifiers (B) Diffraction grating disperses the beam (C) Second diffraction grating collimates the light (D) This mirror is in the Fourier plane; the mask lines remove some of the frequency components (E) The modulated output pulse emerges from the compressor.

The masks were constructed from aluminum using computer controlled Electrical Discharge Machining (EDM) followed by black anodization. Feature size in the aluminum masks was limited by the size of the wire (0.010") in the EDM and the structural integrity of the aluminum. The obstruction sizes included 1/64" (0.396 mm), 1/32" (0.793 mm), 1/16" (1.58 mm), 1/8" (3.175 mm), and 1/4" (6.35 mm). Figure A.2 shows the Tsunami laser in the foreground along with the compressor in the background. The insertion point for the mask is also marked.

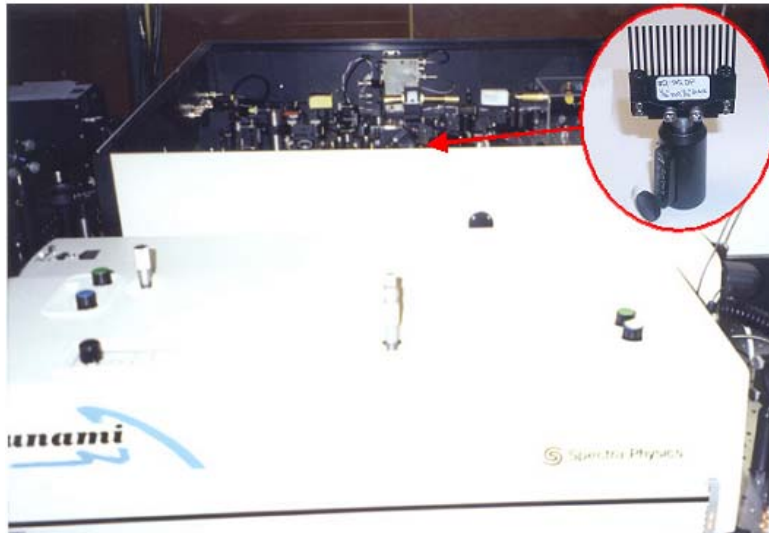


**Figure A.2.** Tsunami Ti:sapphire Laser and Mask

Masking in this way was successful, and was able to produce a modulated laser pulse and a modulated electron beam. Figure A.3 shows an example of laser modulation achieved using this method.

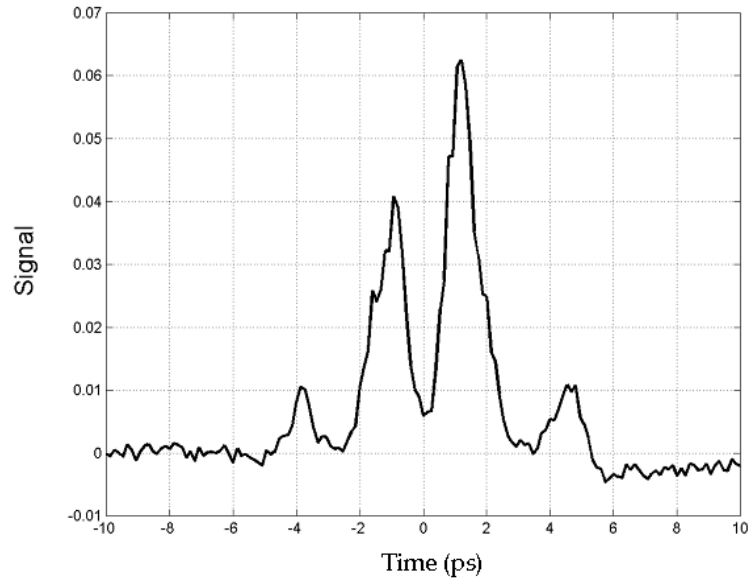


**Figure A.3.** Cross-correlation of UV laser pulse generated with physical masks.

During these experiments, no tomography data was available, but Figure A.4 shows the corresponding RF zero phasing A-slope measurement.

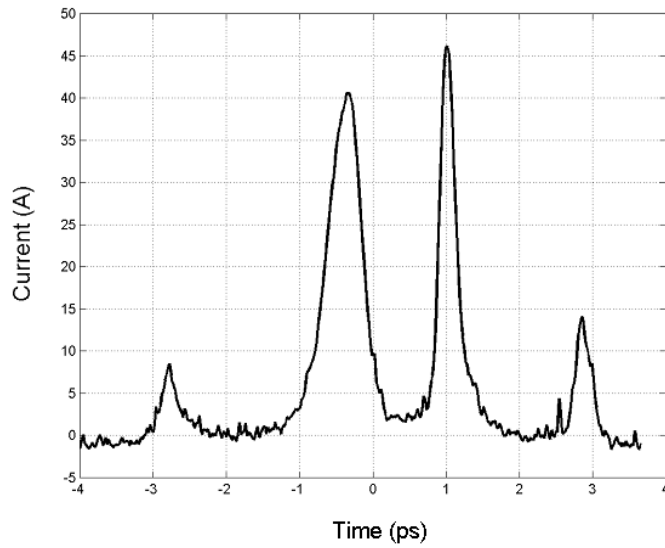


**Figure A.4.** RF Zero Phasing measurement corresponding to Figure A.3.

The aluminum masks were a useful tool for conducting some of the preliminary experiments, but for the later experiments, the interferometer system was used because it provided more control over the laser pulse shape.

The laser pulse stacker provided even more control over the laser profile than the Fabry-Perot interferometer, but was extremely difficult to align. It was not possible to set this system up properly at the Source Development Laboratory due to limited experimental time, but it was used for longitudinal beam dynamics experiments on the University of Maryland Electron Ring (UMER). In this experiment<sup>87</sup>, a low energy space charge dominated beam near 10 keV was modulated using a pulsed Nd:YAG laser. Optical modulation was achieved using a polarizing beam splitters, and delay lines in order to produce perturbations through photoemission. With this setup, four distinct laser pulses could be generated, each with an approximate length of 5 ns. The separation between the pulses and the pulse amplitude could be adjusted independently. A schematic of the pulse stacker system is shown in Figure A.5.

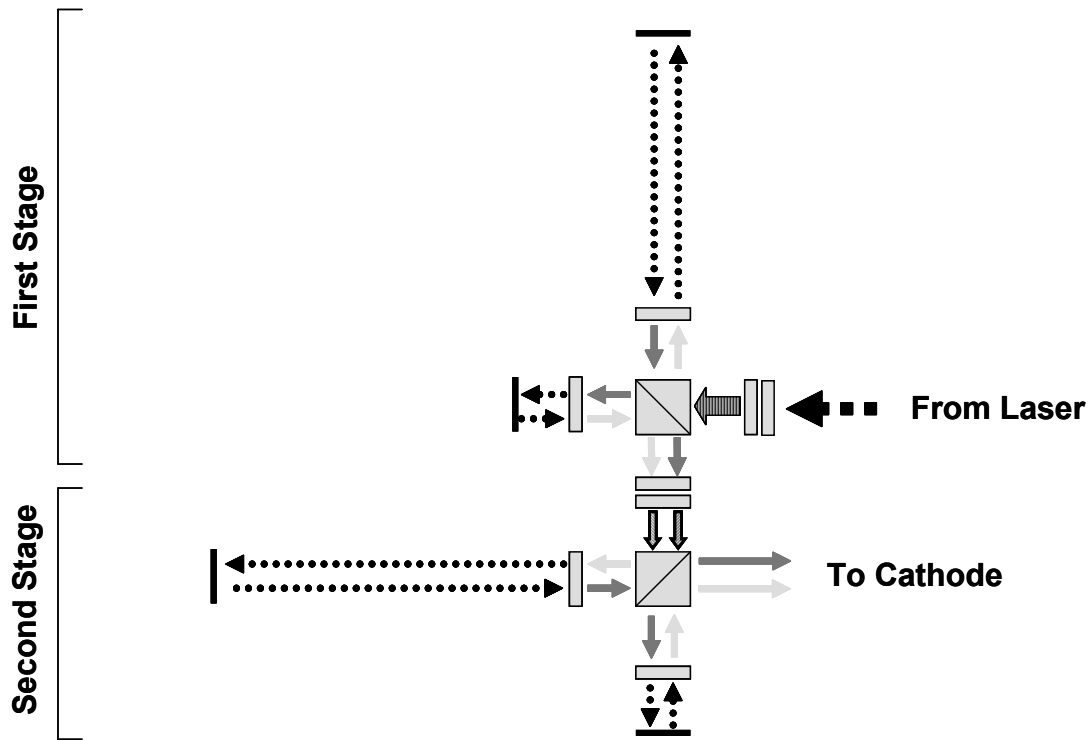
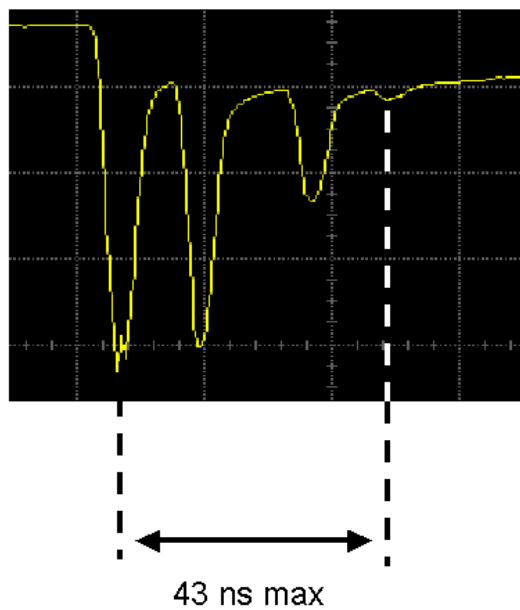


Figure A.5. Schematic of the pulse stacker system

In Figure A.5, the blocks are the polarizing beam splitters, and each small rectangle represents a quarter wave plate. The solid dark shaded arrows refers to horizontal polarization, while the solid light arrow refers to vertical polarization. A dotted line represents elliptical polarization, while a striped line represents a linearly polarized light of an arbitrary polarization.

This system is divided into two stages. In the first stage, the input laser pulse is divided into two pulses by the polarizing beam splitter. A half wave plate controls the amount of light that enters each of the delay lines by controlling the polarization of the incoming light. Delay arms of different lengths cause the pulses

to be separated by the path length difference. In the delay arms, light passes twice through a quarter waveplate, allowing both pulses to emerge from a different face of the beam splitter cube. The second stage works exactly the same way as the first, except two pulses are split into four. These four pulses are sent to the cathode in order to produce the modulated beam. An example of a pulse train generated by this pulse stacker is shown in Figure A.5. Note the different amplitudes of each of the pulses.



**Figure A.5.** Optical pulse train produced by the pulse stacker.

## Appendix B : MATLAB Codes

This appendix contains selected sections of MATLAB code used in support of this dissertation. Only those codes that relate specifically to data analysis or analytical calculations are included. GUI, other graphics, and program control codes are excluded.

### *B.1 Code used to produce test cases for electron beam modulation*

```
function output=longff(fname,slope)

charge=150;
data=load(fname);
type=5;
if (sum(fname((1):(2))=='CC'))~=2
    if type==1
        time=data.handles.timevec.*data.handles.lenscl./10^12;
        timestep=time(2)-time(1);
        time=[min(time)-timestep*(200:-1:1) time max(time)+timestep*(1:200)];
        profile=[zeros(1,200) data.handles.timeprof zeros(1,200)];
    end
    if type==0
        time=data.profs(slope,;,1)/10^12;
        profile=data.profs(slope,;,2);
        timestep=time(2)-time(1);
    end
    if type==5
        time=data.tvec;
        profile=data.timeprof;
        timestep=(data.tvec(2)-data.tvec(1));
    end
else (sum(fname(1:2)=='cc'))==2
    time=data(:,1)./(3*10^8).*2.*10^-6;
    profile=data(:,2)';
    sigma=data(:,3)';
    profile=profile-min(profile);
    profile=profile-mean(profile(1:fix(end/10)));
    time=time-mean(time);
```

```

    timestep=time(2)-time(1);
    figure
    plot(time,profile);
end
jtime=time;
jprof=profile;
len=0.1*10^-12;
numpulse=8;
delay=10^-12;
hold on;
len=1.0*10^-12;
profile=jprof;
hold off
timestep=jtime(2)-jtime(1);
normtime=jprof/(trapz(jprof).*timestep);

%*****normtime must be NOT commented.

samplingrate=1/((max(jtime)-min(jtime))/length(jtime));
f=samplingrate*(0:length(jtime)/2-1)/length(jtime);
w=2*pi.*f;
iow=abs(fft(normtime.*timestep)).^2; % Use this for calculation
figure;
axes('FontSize',20,'XTick',[0 1 2 3]*10^12,'XTickLabel',[0 1 2 3]);
hold on;
plot(f,iow(1:end/2),'k','LineWidth',2);
xlabel('Frequency (THz)','FontSize',24);
ylabel('Form Factor','FontSize',24);
title(fname,'FontSize',10);
axis([0 3*10^12 0 1]);
grid on;

[extra lowend]=min(abs(0.3*10^12-f));
newf=f(lowend:end);
newform=iow(lowend:end/2);
[peak freqpos]=max(newform);
freq=newf(freqpos);
%output=[freq,peak];
nume=100*10^-12/(1.6*10^-19);
output=sum(nume+nume*(nume-1).*iow(20:22));

freqform=f;

*****

function g=testff()

```

```

tvec=linspace(0,10*10^-12,1000);

timeprof=exp(-(tvec-5*10^-12).^2/(2*(5*10^-13)^2));
figure;
plot(tvec,timeprof);
save ex1 tvec timeprof
timeprof=timeprof.*(sin(2*pi*10^12.*tvec)).^2;
hold on;
plot(tvec,timeprof);
save ex2 tvec timeprof

unmod=longff('ex1.mat',1);
mod1=longff('ex2.mat',1);

g=mod1/unmod;

```

## *B.2 Calculation of Fabry-Perot performance*

```

% Jonathan Neumann
% 30 Sep 03
% Calculation of E(t) output after etalon for short/chirped laser pulse

```

```

function y=etalon3()
Ne=10^9;
lambdao=266.4*10^-9;
d=120*10^-6;
co=3*10^8;
counter=1;

zo=376;
n2=0.1815;
%n2=1;
n1=1;
Z2=zo/n2;
Z1=zo;
time=linspace(-20*10^-12,20*10^-12,2^19);
FWHM=6.5*10^-12;
sigma=FWHM/1.1774;
beta=1.2*10^24;
alpha=1/(sigma);
wo1=co*2*pi/(lambdao);
ee=zeros(1,length(time));

inputpulse=real(exp(-((time-10^-12).*alpha).^2).*exp(i.*(wo1.*(time-10^-12)+beta.*(time-10^-

```

```

12).^2));
inputpulse2=inputpulse.*conj(inputpulse);

spectrum=fft(inputpulse);
lpfilter=zeros(1,length(spectrum));
lpfilter(1:length(spectrum)/2)=1;
bspectrum=spectrum.*lpfilter;
input3=ifft(bspectrum);
input3=input3.*conj(input3);
samplingrate=1/((max(time)-min(time))/length(time));
f=samplingrate*(0:length(time)/2)/length(time);
Pff=spectrum.*conj(spectrum);

f2=-fliplr(f(1:length(f)-2));
f=[f f2];
z3pp=zo*(Z2.*cos(2*pi.*f/co*d)+i*Z1.*sin(2*pi.*f/co*d))./(Z1.*cos(2*pi.*f/co*d)+i*Z2.*sin(2*pi.*f.
/co*d));
tt=2.*z3pp./(z3pp+zo);
T=tt.^2.*zo./z3pp;
spectrum=spectrum.*T;
output=ifft(spectrum);
figure;
plot(spectrum.*conj(spectrum));
figure;
output2=output.*conj(output);
plot(time,output2);

spectrum=spectrum.*lpfilter;
output3=ifft(spectrum);
figure;
output4=output3.*conj(output3);
plot(time,output4./max(output4));

```

### *B.3 Code to demonstrate RF zero phasing issues*

```

function cr=crtellipse()

h=0;
k=0;
a=0.5;
b=2;
nx=200;
npx=200*20;
x=linspace(-5,5,nx);
px=linspace(-100,100,npx);

```

```

pixperpx=npx/((max(px)-min(px)));
theta=70;

[zero pxposmin]=min(abs(px+5));
[zero pxposmax]=min(abs(px-5));
z=zeros(npix,nx);
z2=zeros(npix,nx);
m=-10;
m2=5;
theta2=45*2*pi/360;
for xx=1:length(x)
    for yy=pxposmin:pxposmax
        z(yy,xx)=z(yy,xx)+exp(-((sqrt((x(xx)-3)^2/a^2+px(yy)^2/b^2)^2))/(.6));
        z(yy,xx)=z(yy,xx)+exp(-((sqrt((x(xx)-2)^2/a^2+px(yy)^2/b^2)^2))/(.6));
        z(yy,xx)=z(yy,xx)+exp(-((sqrt((x(xx)-1)^2/a^2+px(yy)^2/b^2)^2))/(.6));
        z(yy,xx)=z(yy,xx)+exp(-((sqrt(x(xx)^2/a^2+px(yy)^2/b^2)^2))/(.6));
        z(yy,xx)=z(yy,xx)+exp(-((sqrt((x(xx)+1)^2/a^2+px(yy)^2/b^2)^2))/(.6));
        z(yy,xx)=z(yy,xx)+exp(-((sqrt((x(xx)+2)^2/a^2+px(yy)^2/b^2)^2))/(.6));
        z(yy,xx)=z(yy,xx)+exp(-((sqrt((x(xx)+3)^2/a^2+px(yy)^2/b^2)^2))/(.6));

    end
end
movement=round(sawtooth((x-0.5)*2*pi)*m2*pixperpx);

for xx=1:length(x)
    z(:,xx)=circshift(z(:,xx),movement(xx));
end
realdensity=sum(z);
figure;
colormap(gray);
A=imagesc(x,px,z);
title('intrinsic beam');
figure;
plot(x,realdensity);
title('realdensity');
charge1=sum(sum(z))

for xx=1:length(x)
    movement=round(m*x(xx)*pixperpx);
    z2(:,xx)=circshift(z(:,xx),movement);
end

charge2=sum(sum(z2))
title('chirped beam');
figure
colormap(gray);

```

```

imagesc(x,px,z2);
energy=sum(z2,2);
figure;
theta=atan(m);
plot(px./m,energy/cos(theta),'k');
hold on;
plot(x,realdensity);
title('measured profile');

```

#### B.4 Calculation of filter performance

```

function zz=thzfilt()

% d is hole diameter
% l is plate thickness
% s is spacing between holes
%*****

% GREEN FILTER

lambda=linspace(1*10^-6,2000*10^-6,2000);
figure;
d=277.8167*10^-6;
s=393.383*10^-6;
l=203.2*10^-6;
x=2*pi*d/s/sqrt(3);
nu=1;
bjp=-besselj(nu+1,x)+nu/x*besselj(nu,x);

beta=2*pi./lambda.*sqrt(1-(0.586.*lambda./d).^2);
A=12*sqrt(4/3*(lambda./s).^2-1).*(bjp/(1-(x/1.841)^2))^2;
A=A-(12./sqrt(4/3*(lambda./s).^2-1).*(besselj(1,x)/x)^2);
B=0.21*(s/d)^2*i*beta.*lambda;
trans1=1./(1-i.*(A+B.*tanh(1/2*i.*beta*1)));
trans2=1./(1-i.*(A+B.*coth(1/2*i.*beta*1)));
calctrans=abs(trans1-trans2).^2;
freq=3*10^8./fliplr(lambda);

axis([0.25*10^12 3*10^12 0 1]);
vdiff=1.1547*3*10^8/s

data1=load('930specbe0800.txt');
freq2=3*10^8./(1./(data1(:,1))*0.01);

```

```

hold on;

data2=load('930specbe0800r.txt');
ref1=load('930ref2.txt');
ref2=load('930ref3.txt');
ref=(ref1(:,2)+ref2(:,2))./2;

data3=load('930specbe0800b.txt');
ref3=load('930ref2.txt');
ref4=load('930ref3.txt');
ref5=(ref3(:,2)+ref4(:,2))./2;
ref6=load('930ref7.txt');
ref7=load('930ref8.txt');
ref8=(ref6(:,2)+ref7(:,2))./2;

trans1=data1(:,2)./ref;
trans2=data2(:,2)./ref5;
trans3=data3(:,2)./ref8;

trans4=(trans1+trans2+trans3)./3;

plot(freq2,trans4,'b');
plot(freq,flipr(calctrans),'k');
xlabel('Frequency (THz)',FontSize,24);
ylabel('Transmittance',FontSize,24);
axis([0.25*10^12 3*10^12 0 1]);
title('Green');

```

## *B.5 Theoretical predictions for terahertz emission*

### B.5.1. Angular Spectral Density for a Single Electron and a Finite

#### Radiator

```

function zz=latter()

q=1.6*10^-19;

```

```

restm=.511*10^6;
c=3*10^8;
lt=5000;
eo=8.854*10^-12;
gamma=(restm+73*10^6)/(restm);
beta=sqrt((1-1/gamma^2));
w=linspace(2*pi*0*10^12,2*pi*5*10^12,100);
theta=linspace(0,.1,100);
alpha=linspace(-pi,pi,100);
AA=zeros(length(w),length(theta));
a=.0076;
A1A=zeros(1,length(alpha));
A1B=zeros(1,length(alpha));
astep=alpha(2)-alpha(1);
wstep=w(2)-w(1);
thstep=theta(2)-theta(1);
dWdwdW=q^2*beta^2/pi^3/c/4/eo;
dWdwdW= repmat(dWdwdW,length(w),length(theta));

for ww=1:length(w)
    u=w(ww)*a/c/gamma;
    t=linspace(0.0000000000000001,u*50,lt);
    dt=t(2)-t(1);
    [extra upos]=min(abs(u-t));
    savtim=besselk(1,t).*t;
    for th=1:length(theta)
        for alph=1:length(alpha)
            A1=savtim.*exp(-i.*t.*gamma.*cos(alpha(alph)).*sin(theta(th)));
            A1A(alph)=trapz(A1(1:upos))*dt;
            A1B(alph)=trapz(A1)*dt;
        end
        numerator=A1A.*cos(alpha);
        denom=A1B.*cos(alpha);
        Atop=trapz(numerator)*astep;
        Abot=trapz(denom)*astep;
        AA=(Atop/Abot)^2;
        dWdwdW(ww,th)=dWdwdW(ww,th)*(sin(theta(th))^2)*AA/((1-
beta^2*(cos(theta(th))^2))^2);
    end
    disp('.');
end
size(dWdwdW)

save trans1e dWdwdW

```

## B.5.2. Code for calculating terahertz radiation measured at detector

```

c=3*10^8;
load('D:\My Documents\General Research Data\Latest SDL Data\Latest
Recon2\trans1e2.mat');
lff=longff(fname);
theta=linspace(0,1,100); % REDUCE TO 100 FOR TRANS1E2
thetastep=theta(2)-theta(1);
%str2double(get(handles.edit1,'String'))*10^-12;
beamsize=600*10^-6; %str2double(get(handles.edit2,'String'))*10^-6;
Nume=charge/(1.6*10^-19);
w=linspace(2*pi*0.000000000000001*10^12,2*pi*3*10^12,5000);
wstep=w(2)-w(1);
ft=exp(-(w'/c*beamsize*sin(theta)).^2);
pft=sum(ft,2);
w1=linspace(2*pi*0.000000000000001*10^12,2*pi*5*10^12,100);
lff2=interp1(lff(1,:)*2*pi,lff(2,:),w);
lff2=repmat(lff2,1,length(theta));
lff2=lff2.*ft;
exitapplot=atan(11/150);
exitaperture=atan(6.35/190);
[extra thetapos]=min(abs(exitaperture-theta));
[extra thetapos2]=min(abs(exitaplot-theta));

dWdwdW(1,:)=0;
dWdwdW=dWdwdW(:,[1:length(theta)]);
dWdwdWf=fliplr(dWdwdW);
dWdwdW=[dWdwdWf(:,1:length(theta)-1) dWdwdW];
thetaf=fliplr(theta);
theta2=[-thetaf(1:length(theta)-1) theta];
dWdwdW2=zeros(length(w),length(theta2));
for ivar=1:length(theta2)
    dWdwdW2(:,ivar)=interp1(w1,dWdwdW(:,ivar),w);
end
dWdwdW2(:,100)=0;
lff2i=fliplr(lff2);
lff2=[lff2i(:,1:length(theta)-1) lff2];
dWdwdWf=dWdwdW2.*(Nume+(Nume-1)*Nume.*lff2);
sinth=repmat(theta2,length(w),1);
sinth=abs(sin(sinth));
dWdwdWf=dWdwdWf.*sinth;
dWdw=((trapz(dWdwdWf(:,[(-
thetapos+round(misalign)+length(theta)):(thetapos+round(misalign)+length(theta))]),2)*theta
step))*pi;

```

```

dWdwplot=((trapz(dWdwdWf(:,[-
thetapos2+round(misalign)+length(theta)):(thetapos2+round(misalign)+length(theta))],2)*the
tastep')*pi;
Rs=2.61*10^-7.*sqrt(w./2./pi);
pipea=.5*2.54*10^-2/2;
eta=376.7;
att=1./(exp(Rs./pipea./eta*2*2));
dWdwp(duse,:)=dWdwplot;
dWdw=dWdw.*att;
% Load Filters

% First determine 3 THz pos
[extra terapos]=min(abs((2*pi*3*10^12)-w));

greent=load('greennist.mat');
whitet=load('whitenist.mat');
white2t=load('white2nist.mat');
watert=load('water2.txt');
load blue4sheet.txt
waterx=2*pi*3*10^8./(1./watert(:,1).*0.01);
water=interp1(waterx,watert(:,2),w);
[extra lowpos]=min(abs(2*pi*0.4*10^12-w));
[extra highpos]=min(abs(2*pi*3*10^12-w));
green=interp1(greent.freq2*2*pi,greent.trans4,w);
green(1:lowpos)=green(lowpos);
green(highpos:end)=green(highpos);
white=interp1(whitet.freq2*2*pi,whitet.trans4,w);
white(1:lowpos)=white(lowpos);
white(highpos:end)=white(highpos);
white2=interp1(white2t.freq2*2*pi,white2t.trans4,w);
white2(1:lowpos)=white2(lowpos);
white2(highpos:end)=white2(highpos);
blue=interp1(blue4sheet(:,3)*2*pi,blue4sheet(:,4),w);
blue(1:lowpos)=blue(lowpos);
blue(highpos:end)=blue(highpos);
bend=bendtrans^3;
unfiltered=trapz(dWdw(1:highpos).*water(1:highpos))*wstep*bend;
gfilt=trapz(dWdw(1:highpos).*green(1:highpos).*water(1:highpos))*wstep*bend;
wfilt=trapz(dWdw(1:highpos).*white(1:highpos).*water(1:highpos))*wstep*bend;
w2filt=trapz(dWdw(1:highpos).*white2(1:highpos).*water(1:highpos))*wstep*bend;
bfilt=trapz(dWdw(1:highpos).*blue(1:highpos).*water(1:highpos))*wstep*bend;

if w2flag==1
measured=[gm wm wwm bm unml];

```

```

calc=[gfilt,wfilt,w2filt,bfilt, unfiltered];
end
if w2flag==0
    measured=[gm wm bm unml];
    calc=[gfilt,wfilt,bfilt, unfiltered];
end
gfiltout(duse-startduse+1)=gfilt;
wfiltout(duse-startduse+1)=wfilt;
if w2flag==1
    w2filtout(duse-startduse+1)=w2filt;
end
bfiltout(duse-startduse+1)=bfilt;
unfilteredout(duse-startduse+1)=unfiltered;
figure;
axes('FontSize',20);
hold on;
if w2flag==1
    plot([1 2 3 4 5],calc,'k');
    errorbar([1 2 3 4 5],measured,[L1],'b');
end
if w2flag==0
    plot([1 2 3 4],calc,'k');
    errorbar([1 2 3 4],measured,[L1],'b');
end
title(duse);
xlabel('Filter Type','FontSize',24);
ylabel('Energy (J)','FontSize',24);
errors=calc-measured;
dusecount=1;
errcov(dusecount)=sum(errors.^2)/length(errors);
rr=sum(((measured-mean(measured))/std(measured)).*((calc-
mean(calc))/std(calc)))/(length(measured)-1);
dusecount=dusecount+1;
disp('.');
end
output=sum(errcov.^2)/length(errcov);
bendtrans;
save lastsim dWdwp

```

## References

---

- <sup>1</sup> M. Riordan, P. C. Rowson, and S. L. Wu. *Science*. **291**, no. 5502, 259-260 (2001).
- <sup>2</sup> G. Coutrakon. *Trans. of the American Nuclear Society*. **82**, 20, (2000).
- <sup>3</sup> J. Li, et al. *Nature*. **412**, p. 166-169, (2001).
- <sup>4</sup> I. Osborne. *Science*. **294**, no. 5541, 267. (2001)
- <sup>5</sup> [http://www-ssrl.slac.stanford.edu/research/highlights\\_archive/flat-panel.html](http://www-ssrl.slac.stanford.edu/research/highlights_archive/flat-panel.html)
- <sup>6</sup> J. Stohr, et al. *Science*. **292**, no. 5525, 2299-2302. (2001)
- <sup>7</sup> J.J. Thompson. *Philosophical Magazine*, **44**, 293 (1897).
- <sup>8</sup> P. Rizzi. *Microwave Engineering*. New Jersey: Prentice Hall, 1988.
- <sup>9</sup> P. Rizzi. *Microwave Engineering*. New Jersey: Prentice Hall, 1988.
- <sup>10</sup> V. Granatstein, and I. Alexoff, eds. *High Power Microwave Sources*. Boston: Artech House, 1987.
- <sup>11</sup> S. Choroba, J. Hameister, and S. Jarylkapov *Proc. 1998 Particle Accel. Conf.* 917-919 (1998).
- <sup>12</sup> V. Granatstein, R.K. Parker, and C. M. Armstrong. *Proc IEEE* **87**, 5 (1999).
- <sup>13</sup> <http://www.pbs.org/wgbh/aso/databank/entries/dp31cy.html>
- <sup>14</sup> J. D. Jackson. *Classical Electrodynamics, 3rd ed.* New York: John Wiley & Sons, 1999.
- <sup>15</sup> F. Elder, A. Gurewitsch, R. Langmuir, H. Pollock. *Phys. Rev.* **71**, 829-830 (1947).
- <sup>16</sup> H. Motz, et al. *J. Appl. Phys.* **24**, 826 (1953).
- <sup>17</sup> R.M. Phillips. *IRE Trans. Electron Dev.* **ED-7**, 231-241 (1960)
- <sup>18</sup> J. M. J. Madey. *J. Appl. Phys.* **42**, 1906 (1976).

- 
- <sup>19</sup> D.A.G. Deacon, et al. *Phys. Rev. Lett.* **38**, 892-894 (1977).
- <sup>20</sup> G. R. Neil, S. Benson, et al. *Phys. Rev. Lett.* **84**, 662-665 (2000).
- <sup>21</sup> K. Nguyen, et al. *IEEE Trans. Elec. Dev.* **38**, 10, 2212-2220 (1991).
- <sup>22</sup> D. Priest and M. Shrader. *IEEE Trans. Elec. Dev.* **38**, 10, 2205-2211 (1991).
- <sup>23</sup> W. B. Herrmannsfeldt. *SLAC-PUB-3809* Oct 1985.
- <sup>24</sup> E. L. Garwin, et al. *SLAC-PUB-3650*. April 1985.
- <sup>25</sup> P. Siegel. *IEEE Trans. on Micr. Theory and Tech.* **50**, 3, 910-928 (2002).
- <sup>26</sup> G. L. Carr, et al. *Nature*. **420**. p. 153-156 (2002).
- <sup>27</sup> G.P. Gallerano and S. Biedron. JaCoW.
- <sup>28</sup> Z. Huang, et al. *Phys. Rev. ST - Accel and Beams*, **7**, 074401 (2004).
- <sup>29</sup> C. Limborg-Deprey and P.R. Bolton. *SLAC-PUB-10941*. 2004.
- <sup>30</sup> M. Lampel and M. Tiefenback. *Appl. Phys. Lett.* **43**, 1, 57-58 (1983).
- <sup>31</sup> G. L. Carr, et al. *Nature*. **420**. p. 153-156 (2002).
- <sup>32</sup> C.P. Neuman. Ph. D. thesis, Duke University, 2001.
- <sup>33</sup> C.P. Neuman. Ph. D. thesis, Duke University, 2001.
- <sup>34</sup> V.L. Ginzburg, I. Frank., *J. Phys. USSR* **9**, 353 (1945).
- <sup>35</sup> C. Brau. *Modern Problems in Classical Electrodynamics*. New York: Oxford University Press, 2004.
- <sup>36</sup> C. Brau. *Modern Problems in Classical Electrodynamics*. New York: Oxford University Press, 2004.
- <sup>37</sup> L.C. Steinhauer and W.D. Kimura. *Phys. Rev. ST Accel. and Beams*. **2**, 081301 (1999).

- 
- <sup>38</sup> J. Billen. and L. Young *PARMELA*. LA-UR-96-1835. (2000)
- <sup>39</sup> S. Backus, et al. *Rev. Sci. Instrum.* **69**, 1207-1223 (1998).
- <sup>40</sup> H. Loos, et al. *Proc. 2002 Adv. Accel. Concepts*. AIP Conference Proceedings **647**, no. 1, 849 (2002).
- <sup>41</sup> X. J. Wang, et al. *Nucl. Instrum. and Meth. A.* **375**, 82-86 (1996).
- <sup>42</sup> T. Tsang. *Appl. Phys. Lett.* **63**, 871-873 (1993).
- <sup>43</sup> G.L. Carr, et al. *Proc 2001 Particle Accel. Conf.* 2608-2610. (2001)
- <sup>44</sup> C.P. Neuman. Ph. D. thesis, Duke University, 2001.
- <sup>45</sup> G. L. Carr. Personal communication.
- <sup>46</sup> J. Billen. and L. Young *PARMELA*. LA-UR-96-1835. (2000)
- <sup>47</sup> C. Davis. *Lasers and Electro-Optics*. Cambridge: Cambridge University Press, 1996.
- <sup>48</sup> A. Siegman. *Lasers*. Mill Valley: University Science Books, 1986.
- <sup>49</sup> C. Davis. *Lasers and Electro-Optics*. Cambridge: Cambridge University Press, 1996.
- <sup>50</sup> W.S. Graves, personal communication.
- <sup>51</sup> P. Piot, et al. *Phys. Rev. ST Accel. Beams*, **6**. 033503 (2003).
- <sup>52</sup> P.G. O'Shea, et al. *Nucl. Instrum Meth A*, **331**, 62-68 (1993).
- <sup>53</sup> C.P. Neuman. Ph. D. thesis, Duke University, 2001.
- <sup>54</sup> M. Reiser. *Theory and Design of Charged Particle Beams*. New York: John Wiley & Sons, 1994.
- <sup>55</sup> K. Ricci and T. Smith. *Phys. Rev. STAB*. **3** 032801.1-032801.9 (2000).
- <sup>56</sup> W.S. Graves, et al. *Proc 2001 Particle Accel. Conf.* 2224-2226. (2001)

- 
- <sup>57</sup> Z. Huang and T. Shaftan. *Nucl. Instr. and Meth. A.* **528** 345-349 (2004).
- <sup>58</sup> H. Loos. Personal communication.
- <sup>59</sup> T. Shaftan, et al. *Nucl. Instr. and Meth. A.* **528**, 397-401 (2004).
- <sup>60</sup> A.C. Kak and M. Slaney. *Principles of Computerized Tomographic Imaging*. New York: IEEE Press, 1988.
- <sup>61</sup> A.C. Kak and M. Slaney. *Principles of Computerized Tomographic Imaging*. New York: IEEE Press, 1988.
- <sup>62</sup> H. Loos, et al. *Nucl. Instr. and Meth. A.* **528**, 189-193. (2004)
- <sup>63</sup> A.C. Kak and M. Slaney. *Principles of Computerized Tomographic Imaging*. New York: IEEE Press, 1988.
- <sup>64</sup> T. Shaftan, et al. *Nucl. Instrum. and Meth. A*, **528**, p. 391-401 (2004).
- <sup>65</sup> D.C. Nguyen and B.E. Carlsten. *Nucl. Instrum. and Meth. A.* **375**, p. 597-601 (1996).
- <sup>66</sup> S.N. Dobrovolsky and N.F. Shul'ga. *Physics of Atomic Nuclei.* **64**, 5, p 994-998 (2001).
- <sup>67</sup> H. Loos. Personal communication.
- <sup>68</sup> D. Sutterlin, et al. *Proceedings DIPAC 2003*, 228 (2003).
- <sup>69</sup> S. N. Dobrovolsky and N. F. Shul'ga. *Nucl. Instr. and Meth. B* **201**, 123-132 (2003).
- <sup>70</sup> K.D. Moller and W. Rothschild. *Far-Infrared Spectroscopy*. New York : John Wiley and Sons, 1971.
- <sup>71</sup> J. Neumann, et al. *Nucl. Instrum. and Meth. A.* **507**, 498-501 (2003).

- 
- <sup>72</sup> K.D. Moller and W. Rothschild. *Far-Infrared Spectroscopy*. New York : John Wiley and Sons, 1971.
- <sup>73</sup> S. Ramo, J. Whinnery, T. Van Duzer. *Fields and Waves in Communication Electronics*. New York: John Wiley and Sons, 1965.
- <sup>74</sup> K.D. Moller and W. Rothschild. *Far-Infrared Spectroscopy*. New York : John Wiley and Sons, 1971.
- <sup>75</sup> G.L. Carr. Personal communication.
- <sup>76</sup> D. Plusquellic. Personal communication.
- <sup>77</sup> W.P. Leemans, et al. *Physics of Plasmas*. **11**, 5, 2899-2906. (2004).
- <sup>78</sup> C.C. Chen. *IEEE Trans. Microwave Theory Tech.* **21**, 1 (1973).
- <sup>79</sup> C. Winnewisser, F. Lewen, and H. Helm. *Appl. Phys. A*. **66**, 6, 593-598 (1998).
- <sup>80</sup> C.C. Chen. *IEEE Trans. Microwave Theory Tech.* **21**, 1 (1973).
- <sup>81</sup> [http://www.internetplastic.com/metal\\_etched.htm](http://www.internetplastic.com/metal_etched.htm)
- <sup>82</sup> C. Winnewisser, F. Lewen, and H. Helm. *Appl. Phys. A*. **66**, 6, 593-598 (1998).
- <sup>83</sup> C.P. Neuman. Ph. D. thesis, Duke University, 2001.
- <sup>84</sup> [http://www.irlabs.com/irlabs%20catalog%20pages/catalog\\_frameset.html](http://www.irlabs.com/irlabs%20catalog%20pages/catalog_frameset.html). 1-3-05.
- <sup>85</sup> G.L. Carr. Personal communication.
- <sup>86</sup> C.P. Neuman. Ph. D. thesis, Duke University, 2001.
- <sup>87</sup> J.G. Neumann, et al. *Review of Scientific Instruments*, to be published March 2005.